THE UNIVERSITY
of ADELAIDE

FACULTY OF SCIENCES

SCHOOL OF PHYSICAL SCIENCES

Oscillations and Sterile Neutrinos

Zachary M. Matthews

Supervisors:
Prof. Anthony G. WILLIAMS
Assoc. Prof. Martin WHITE
Dr. Shivani GUPTA
Dr. Pankaj SHARMA

Friday 8th November, 2019

DECLARATION

I certify that this work contains no material which has been accepted for the award of any other degree or diploma in my name, in any university or other tertiary institution and, to the best of my knowledge and belief, contains no material previously published or written by another person, except where due reference has been made in the text. In addition, I certify that no part of this work will, in the future, be used in a submission in my name, for any other degree or diploma in any university or other tertiary institution without the prior approval of the University of Adelaide and where applicable, any partner institution responsible for the joint-award of this degree.

I acknowledge that copyright of published works contained within this thesis resides with the copyright holder(s) of those works.

I also give permission for the digital version of my thesis to be made available on the web, via the University's digital research repository, the Library Search and also through web search engines, unless permission has been granted by the University to restrict access for a period of time.

I acknowledge the support I have received for my research through the provision of an Australian Government Research Training Program Scholarship.

Zachary M. Matthews
November 2019

ACKNOWLEDGEMENTS

I'd like to thank the fantastic physics people of 119 and beyond for all the enjoyable lunches and coffee breaks. Putting up with my constant stream of terrible jokes, impressions and voices for four years straight must have been difficult (not to mention all of the unsolicited car facts and advice)! I don't think I would've made it this far without all of the constant support, friendship and of course, banter. I hope my fellow graduates got as much out of their time spent studying as I did! To those who are still on the journey, make sure you enjoy yourself along the way!

Thanks to Shivani for introducing me to this field and helping me complete my honours what feels like an age ago! Thanks to Pankaj for outlining analyses and helping me publish my first two papers. Finally, thanks to Tony for providing advice over the years, sending me to various conferences and proofreading this behemoth document.

Finally, thanks to my wonderful Mum for making my (rather lengthy) student life as easy and stress-free as possible!

ABSTRACT

In this work I aim to introduce neutrino physics from its fairly mundane beginnings all the way up to the discovery of neutrino oscillations, the latest detectors and theoretical extensions to current models. When viewed individually, many of the detector methods and theories for oscillation seem to make overly specific and somewhat arbitrary assumptions. However, upon knowing the full picture of oscillations, such assumptions become better motivated and a fuller understanding of the modern field can be gained. On the way to understanding the modern field of neutrino oscillations I will make several asides, notably on the specifics of detector types and the concept of neutrino mass. Finally I will introduce GLoBES simulation and present examples of my published work on simulations of oscillation with one light sterile neutrino. These analyses study the effect of adding one light ($\sim$1 eV) sterile neutrino to the current 3-flavour neutrino scenario and the theoretical change in predictive power of certain experiments in this new 4-flavour regime. The main focus for experiment sensitivity is the hierarchy, octant and CP violation detection power of these detectors. Finally, once I have summarised the history, theory and current state of neutrino studies I will comment on the future outlook for neutrino physics in general.

TABLE OF CONTENTS

LIST OF FIGURES

LIST OF TABLES

CHAPTER 1

INTRODUCTION AND HISTORY OF NEUTRINOS

This thesis is aimed to be an introduction to neutrino oscillations in a very general sense. We start with some basic history of neutrino physics and work toward a full understanding of oscillations with short asides discussing other relevant areas. It would be impossible to cover every single extension to basic neutrino theory as the field is indeed broad but I will attempt to outline all of the pieces relevant to my work.

Introducing neutrino physics and later, oscillation phenomena, is most straightforward when we talk about historical experiments. These theories are built from initially simple observations such as observation of deficits in solar neutrinos. Because many other factors could be responsible for a lack of detection, other evidence that neutrinos were changing between active flavours was important. Deficits in rates could also be caused by neutrinos disappearing (e.g. via decay) or otherwise not interacting (e.g. via becoming sterile or flipping to non-interacting helicities). These have been ruled out as at least the primary means of explaining these phenomena by the combined efforts of many highly varied experiments.

Once we've outlined the early history of neutrino experiments we cover the logic of oscillation solutions and derive associated probabilities. Parametrisation of oscillation and matter effects are also covered. Such steps are often glossed over or assumed knowledge in the literature. Most assumptions turn out to be straightforward, but for clarity we present our work in more detail, especially for those new to the field. The sterile neutrino anomalies and corresponding oscillation extensions with an extra mass eigenstate are also introduced. We briefly touch on other extended theories and their relation to oscillations.

We outline the GLoBES software used to simulate oscillations at Long BaseLine (LBL) experiments and how different hypothesis tests are applied. We simulate oscillation probability for various experiments and parameter settings to directly show the idea of degeneracies via overlapping curves. Several example plots are analysed to show how allowed regions change as the best fits are varied and to explain the use of such plots in analyses.

After the theories of oscillation physics and simulation have been discussed we demonstrate our published studies in this field as examples of current areas of research. These studies are intended to evaluate the response of the NOνA, T2K and DUNE detectors to the additional mass splitting introduced to explain neutrino anomalies. We base the core of the analysis on published results and global fits, then vary the parameters which are less certain to see how this affects degeneracy resolution.

My publications:

- Monojit Ghosh, Shivani Gupta, Zachary M. Matthews, Pankaj Sharma, and Anthony G. Williams. Study of parameter degeneracy and hierarchy sensitivity of NOνA in presence of sterile neutrino. *Phys. Rev. D*, 96:075018, Oct 2017

- Shivani Gupta, Zachary M. Matthews, Pankaj Sharma, and Anthony G. Williams. The Effect of a Light Sterile Neutrino at NOνA and DUNE. *Phys. Rev.*, D98(3):035042, 2018

1.1 History of Neutrinos in Physics

Neutrinos have been part of physics for a relatively long time, first postulated (as the neutron) by Wolfgang Pauli in 1930 as the "missing" part of beta decay reactions (required to conserve energy, momentum and spin) and later verified by inverse beta decay

$$\bar{\nu}_e + p \longrightarrow n + e^+ \tag{1.1}$$

in 1956 by several scientists (Clyde Cowan, Frederick Reines, F. B. Harrison, H. W. Kruse, and A. D. McGuire) of whom Frederick Reines was later awarded half of the 1995 Nobel Prize in Physics[1] [3]. Reines et al. performed an initial experiment

---

[1] The other half of this award was for Martin L. Perl for the discovery of the heavy (3500 times electron mass) tau lepton in experiments at the Stanford Linear Accelerator Center (SLAC) between 1974 and 1977.

at Hanford in 1953 intending to view antineutrinos from a nuclear reactor. The antineutrino-proton inverse decay can be detected because the emitted positron will almost immediately annihilate with a nearby electron to produce two back to back photons

$$e^+ + e^- \longrightarrow \gamma + \gamma \tag{1.2}$$

and a couple of microseconds later neutron capture on a nucleus of the detector material (which was Cadmium in this case) will produce an intermediate excited state that decays, emitting a further photon

$$n + {}^{108}\mathrm{Cd} \longrightarrow {}^{109m}\mathrm{Cd} \longrightarrow {}^{109}\mathrm{Cd} + \gamma\,. \tag{1.3}$$

The coincidence of these photons uniquely implies an antineutrino interaction, making candidate events easy to distinguish. The follow up to the Hanford experiment by the same scientists was performed at the Savannah River Plant of the U.S. Atomic Energy Commission. The experimental setup used two large water tanks with approximately 200 L total volume and three metal tanks containing liquid scintillator, all surrounded by a paraffin and lead shield located underground in a reactor room [4]. The arrangement was two scintillator tanks sandwiching the two water tanks which were in turn separated by the third scintillation tank. Each scintillator tank was viewed by an array of 110 5-inch photomultiplier tubes (PMTs). The scintillator tanks were intended to create flashes that the PMTs viewing each one could detect corresponding to one of the photons released. These permitted the observation of the coincident photons from the electron-positron annihilation as well as the neutron capture in cadmium. Analysis of the time delay and dependence on reactor power of interactions allowed the source of the signal to be identified as reactor neutrinos. This definitive experimental result confirmed the existence of a free neutrino.

1.2 Homestake and The Solar Neutrino Problem

Models of the Sun have developed over time, ever since people started attempting to scientifically understand the world around us. We now think of many of the early theories of solar energy as incorrect or very unrealistic. Examples include Lord Kelvin's mid-1800's theories that energy liberated by meteorite impacts, and later gravitational collapse of primordial stellar matter, could cause the heating required [5]. Unfortunately no theories at the time could explain a source of energy that lasted long enough to agree with Charles Darwin's estimated (very old) age of the Earth. In 1904 Ernest Rutherford suggested a contemporary physics explanation based on radioactive decay. It wasn't until 1920 that Sir Arthur Eddington suggested nuclear fusion based on F.W. Aston's discovery that one helium nucleus is more massive than four hydrogen nuclei, combined with Einstein's mass-energy equivalence [6]. From there the field started to develop into what we know of today which involves nuclear burning via various chains of reactions.

The dominant chain in our Sun is the proton-proton or pp-chain from which alpha particles are produced by proton fusion. the pp-chain consists of the following interactions: Two protons fuse to form a deuteron

$$p + p \rightarrow d + e^+ + \nu_e \,, \tag{1.4}$$

$$p + p + e^- \rightarrow d + \nu_e \,. \tag{1.5}$$

Deuteron and proton makes a helium-3 ion

$$d + p \rightarrow {}^3\mathrm{He} + \gamma \,. \tag{1.6}$$

Helium-3 produces alpha particles and beryllium-7

$${}^3\mathrm{He} + p \rightarrow \alpha + e^+ + \nu_e \,, \tag{1.7}$$

$${}^3\mathrm{He} + {}^3\mathrm{He} \rightarrow \alpha + p + p \,, \tag{1.8}$$

$${}^3\mathrm{He} + \alpha \rightarrow {}^7\mathrm{Be} + \gamma \,. \tag{1.9}$$

Beryllium then can produce alpha particles

$${}^7\mathrm{Be} + e^- \rightarrow {}^7\mathrm{Li} + \nu_e \,, \tag{1.10}$$

$${}^7\mathrm{Li} + p \rightarrow \alpha + \alpha \,, \tag{1.11}$$

$${}^7\mathrm{Be} + p \rightarrow {}^8\mathrm{B} + \gamma \,, \tag{1.12}$$

$${}^8\mathrm{B} \rightarrow {}^8\mathrm{Be}^* + e^+ + \nu_e \,, \tag{1.13}$$

$${}^8\mathrm{Be}^* \rightarrow \alpha + \alpha \,, \tag{1.14}$$

where the ${}^8\mathrm{Be}^*$ is an excited state of ${}^8\mathrm{Be}$. From all of these processes the net result is hydrogen fusing into helium, with the by product of positrons, gamma rays and, most importantly, electron neutrinos. The abundance of protons leads the majority of solar neutrinos to be produced by the first reaction. However these are incredibly low energy, as the neutrino spectrum in Fig. 1.1 shows, therefore most experiments will look for the higher energy ones such as those from boron, despite their comparative scarcity.

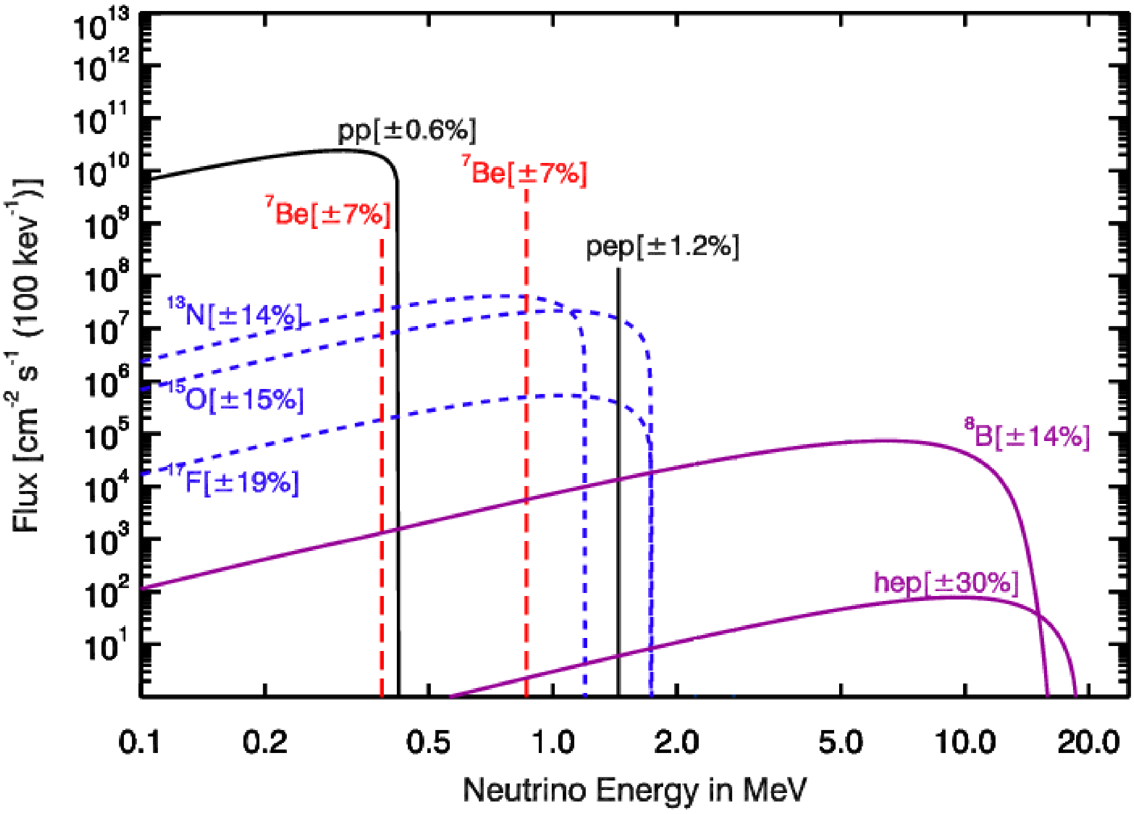

Fig. 1.1 Spectrum of solar neutrino flux as a function of their energy. Each line represents a different reaction in which the neutrinos are produced within the core of the sun, as detailed in the legend. This plot is modified from Fig. 3. from [7].

In the 1960's astrophysicists Raymond Davis, Jr. and John N. Bahcall lead an experiment (known simply as 'Homestake') intended to measure the flux of electron neutrinos from the fusion reactions occurring inside the sun. The detector was set up 1478 m underground in the Homestake Mine in South Dakota to screen out cosmic ray interference and other backgrounds for the several nuclear processes involved. The cross-section of this setup showing the main tank and surrounding rooms is shown in Fig. 1.2. The reaction Homestake measured was the production of radioactive argon by neutrino capture on chlorine atoms

$$\nu_e + {}^{37}\mathrm{Cl} \longrightarrow {}^{37}\mathrm{Ar} + e^- \,. \tag{1.15}$$

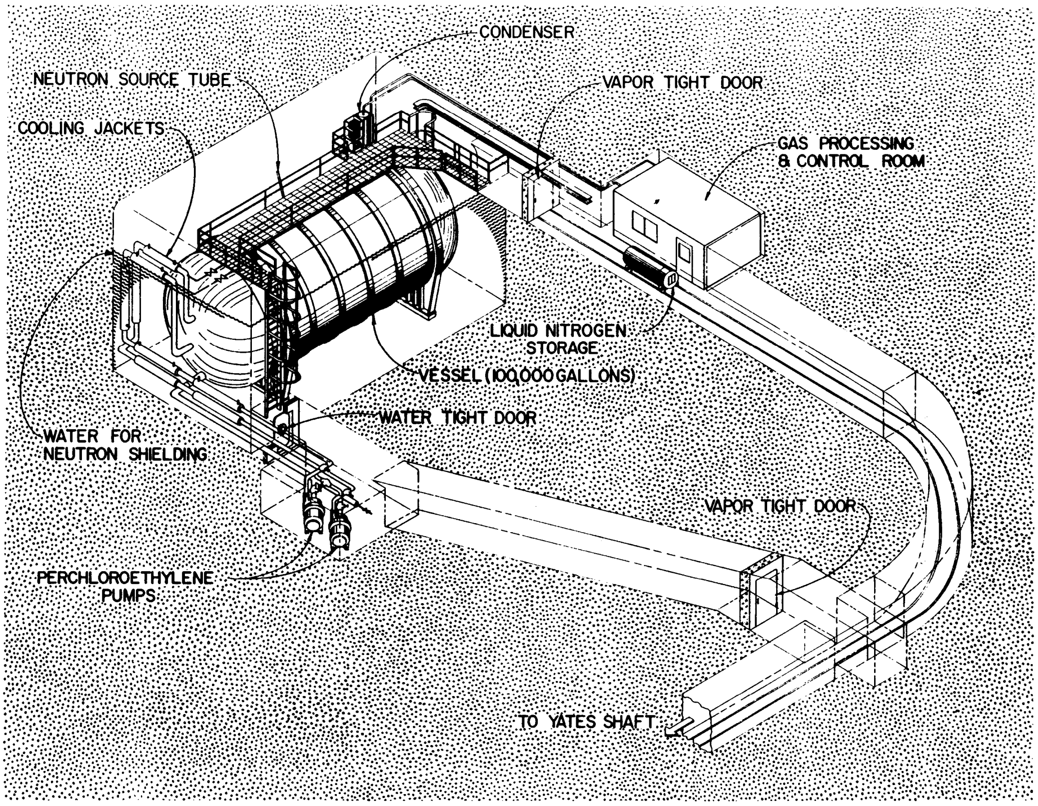

Fig. 1.2 Cross-section of the Homestake neutrino detector cavern, showing the arrangement of the tank and surrounding rooms. Taken from Cleveland et al. 1998 [8].

By measuring the decays of such argon isotopes using a radiation counter (after accounting for reaction rates), the amount created, hence flux of neutrinos could be calculated. From these calculations it was apparent that only one third of the expected number of neutrinos were detected [9] and thus the “solar neutrino problem” was born. The initial response was that the solar model for neutrino production must be wrong or perhaps the detection methodology, after all, these were the simplest solutions. However beginning in the early 1990’s Gallium based radiochemical experiments such as GALLEX [10] and SAGE [11] measured low energy pp-chain neutrinos which hadn’t been directly measured at this point. The method was via the inverse beta radiochemical processes

$$\nu_e + {}^{71}\mathrm{Ga} \rightarrow {}^{71}\mathrm{Ge} + e^- \tag{1.16}$$

and subsequent delayed counting of the $^{71}\mathrm{Ge}$ [12]. This helped verify the accuracy of solar models by confirming the internal mechanisms present as well as validating radiochemical methods of detection[2].

Some years later the deficit was confirmed by several other experiments (mostly using now conventional Cherenkov detectors), which we discuss further in sections 1.3 and 1.4. Given that the solar models were considered verified, theories of how a deficit could appear needed to be tested.

The SNO analysis of NC events using heavy water combined with Super-K measurements made it clear that the solar model flux predictions were correct, yet a deficit in electron flavour was present. Since the total NC flux detected matched up to the neutrino flux emitted by the Sun, the remaining flavour discrepancy lent credence to theories involving some sort of neutrino flavour transformation. These along with other follow-up experiments further validated Homestake and made the search for a solution to this problem a vital area of study.

Despite the plethora of experiments working on it, the solar neutrino problem continued to be of interest for a long time. Meanwhile other oscillation phenomena were being discovered and worked on. This continued until around 2002 when solar experiment SNO and reactor experiment KamLAND [13, 14] finally had the evidence to verify that the LMA-MSW (Large Mixing Angle Mikheyev Smirnov Wolfenstein) solution for solar neutrino transitions was the correct explanation of the lower number of electron neutrino detections (again see sections 1.3 and 1.4). This was a combined effort because the environments in which neutrinos are produced can greatly effect the phenomenology (see section 2.7) but after accounting for these effects both experiments revealed similar mixing and splitting parameters θ_{12} and Δm^2_{21}. Ray Davis and Masatoshi Koshiba each received one quarter of the Nobel Prize in physics in 2002[3] for “for pioneering contributions to astrophysics, in particular for the detection of cosmic neutrinos” [15]. Masatoshi Koshiba was instrumental in early neutrino astronomy, specifically the construction of, and techniques used in Kamiokande-II and Super-Kamiokande which we cover thoroughly in section 1.3.1.

---

[2] When tested with radioactive neutrino sources ^{37}Ar and ^{51}Cr these experiments saw anomalous results. This is discussed in section 3.1.1

[3] The other half of the 2002 prize went to Riccardo Giacconi “for pioneering contributions to astrophysics, which have led to the discovery of cosmic X-ray sources”

1.3 Early Neutrino Experiments

One explanation for the deficit measured by these neutrino experiments was proposed by Bruno Pontecorvo in 1968 (*before* the deficit was discovered), it was simply that the neutrinos weren't missing, but had simply changed into different flavours (such as electron neutrinos changing to muon or tau neutrinos) to which the detector wasn't sensitive. Pontecorvo's original theory involved neutrino-antineutrino oscillations in analogy to neutral Kaon oscillation. Although this proved to be a dead end it is conceptually similar to flavour transitions. The theory of neutrino oscillations evolved from this simple suggestion.

1.3.1 Kamiokande and Super-Kamiokande

Kamiokande (properly KamiokaNDE or Kamioka Nucleon Decay Experiment [16]) was an experiment running from 1983 to 1995. It was constructed by the Institute for Cosmic Ray Research of the University of Tokyo. The full run was split into three phases, Kamiokande-I for 1983-1985, Kamiokande-II for 1985-1990 and Kamiokande-III for 1990-1995. The detector was a 6.0 m height and 15.6 m wide cylinder containing 3,048 metric tons of pure water and about 1,000 PMTs. It's original goal was to search for proton decay via observation of potential daughter particles of such a process, this goal was unsuccessful. Despite it's lack of success with proton decay, Kamiokande-II had many immense successes such as observing the supernova neutrinos from SN 1987A [17–19] as well as being able to view solar neutrinos and provide a check for Homestake [20, 21]. Additionally, during the Kamiokande-II run some of the earliest promising measurements of atmospheric neutrinos were obtained [22] thus beginning to form a more holistic picture of neutrino physics. Atmospheric neutrino detection is possible because the size of the detector and reasonably energetic particles make up for the low flux of such particles. This is in contrast to solar neutrinos where the flux is high and direction of origin is known but the energy, and hence sensitivity, is low. Compared to some earlier radiochemical experiments, an advantage of the water Cherenkov detector is that interactions from neutrinos producing both electrons and muons can be distinguished. The way that this is done is by analysing the Cherenkov rings, for electrons multiple scattering occurs and the ring is 'fuzzy' around the edges while for muon flavour the ring is much more 'sharp' as the muon barely deviates as it travels through the detector.

When cosmic rays produce positive or negative mesons (mostly pions and to a lesser extent kaons), they primarily decay to antimuons or muons respectively [23]

$$\pi^+/K^+ \longrightarrow \mu^+ + \nu_\mu \,, \tag{1.17}$$

$$\pi^-/K^- \longrightarrow \mu^- + \overline{\nu}_\mu \,, \tag{1.18}$$

which in turn decay to electrons or positrons,

$$\mu^+ \longrightarrow e^+ + \nu_e + \overline{\nu}_\mu \,, \tag{1.19}$$

$$\mu^- \longrightarrow e^- + \overline{\nu}_e + \nu_\mu \,, \tag{1.20}$$

all the while producing corresponding neutrinos. Hence atmospheric muon neutrinos were expected to be twice as abundant as atmospheric electron neutrinos.This can also be seen diagrammatically in Fig. 1.3. Thus each meson decay should produce approximately three neutrinos, two of muon flavour with opposite charge and one electron flavour. Thus the ratio of $\nu_\mu + \overline{\nu}_\mu$ to $\nu_e + \overline{\nu}_e$ should be roughly 2:1 [24]. Obviously this did not turn out to be the case, atmospheric muon neutrinos were measured to have a deficit, echoing the earlier solar neutrino problem. The way this was measured was by comparing the ratio of electron to muon flavour to the theoretical value, which was advantageous because it removes a lot of systematics. The anomalous ν_μ/ν_e ratio was referred to as the 'Atmospheric Neutrino Anomaly' [25, 26] with oscillations viewed as a potential underlying cause. Over the next few years oscillations were becoming more considered as a solution [26], though some experiments that confirmed this deficit, such as IMB-3, did not see is as significant enough at the time to warrant neutrino oscillations as an explanation

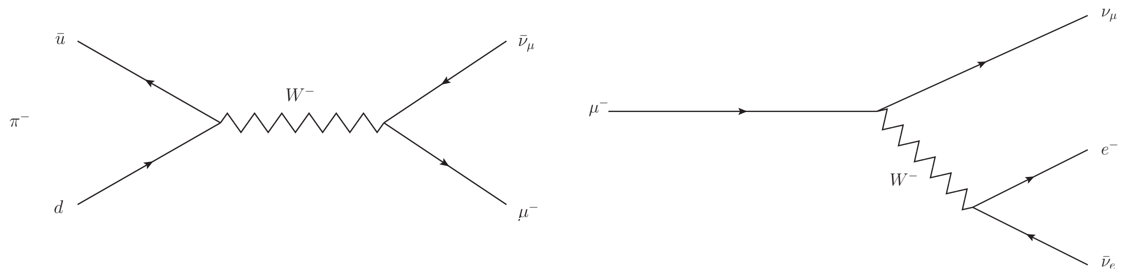

Fig. 1.3 Feynman diagrams involved in neutrino production from meson (in this case pion) decay. Pion decay is depicted in the left diagram and subsequent muon decay in the right. A total of three neutrinos will be emitted by these combined processes.

[27]. Kamiokande's results were verified and improved upon by its successor, Super-Kamiokande.

As mentioned before, in addition to the atmospheric neutrino measurements, Kamiokande-II produced results on solar neutrinos. To reiterate, this was possible due to the sheer size of the experiment, which in the solar neutrino case this allowed the statistics to overcome the tiny interaction cross-section of the high flux, low-energy neutrinos. In addition the water Cherenkov method of detection has several other advantages over delayed-measurement radiochemical experiments like Homestake:

1. events can be seen in real time, hence day/night asymmetry can be measured;
2. produces calorimetric data i.e. energy deposition measurements; and
3. is directional, with recoil paths tracing back towards the source (in this case the Sun).

These properties allowed direct verification of the solar production of neutrinos and more thorough analysis of their energy spectrum than prior experiments. In 1992 Masatoshi Koshiba referred to the development of these modern types of detectors as the birth of 'observational neutrino astrophysics', highlighting the great importance of arrival time, directional information and energy spectrum to astrophysics [28]. The measurement of this solar flux saw a deficit which was different from Homestake. Kamiokande seemed to measure half of the flux predicted by solar models, while Homestake saw only one third. This different deficit was later explained after the Super-Kamiokande run by fact that the detector measures electron recoils from the $\nu_l + e^- \to \nu_l + e^-$ elastic scattering (ES) interaction. This measured process is actually two separate interactions that can occur via CC and NC for ν_e and only NC for ν_μ, ν_τ (Fig. 1.4). Overall then, Kamiokande is sensitive to all flavours but its electron flavour sensitivity is six times higher that muon or tau flavours [29]. Thus a deficit in solar electron flavour neutrinos causes the events measured to decrease but this decrease is smaller than if the detector can *only* see electron flavour CC interactions (as with Homestake).

Super-Kamiokande often known simply as Super-K (where the acronym KamiokaNDE was rightfully changed to Kamioka Neutrino Detector Array), was constructed in the same lead and zinc mine in the Kamioka area of the Gifu prefecture, Japan, as the original Kamiokande. In addition to sharing a location with the original, the design was also similar in that a large water-Cherenkov detector forms the basis of

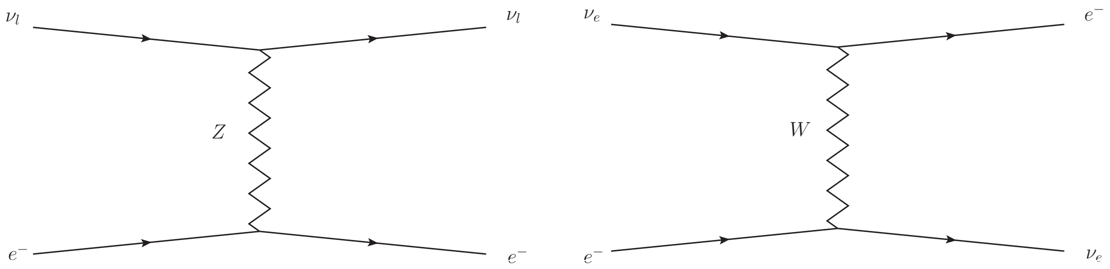

Fig. 1.4 Possible electron quasi elastic scattering interactions showing NC (featuring all active neutrino flavours) on the left and CC (featuring only electron flavour) on the right.

the experiment. Though the fiducial volume was greatly increased to 22.5 kilotons (kt) for Super-Kamiokande versus 1 kt for Kamiokande [23] and the number of PMTs from around 1000 to (eventually in run II) 11,100. Super-Kamiokande started taking data in 1996 with neutrino physics only being part of its goal, the other main (albeit still unsuccessful) goal was to search for proton decay as with the original Kamiokande. The neutrino detection capabilities of the detector are broad, including solar, atmospheric and supernova neutrinos [23]. The specific intention in this sector was

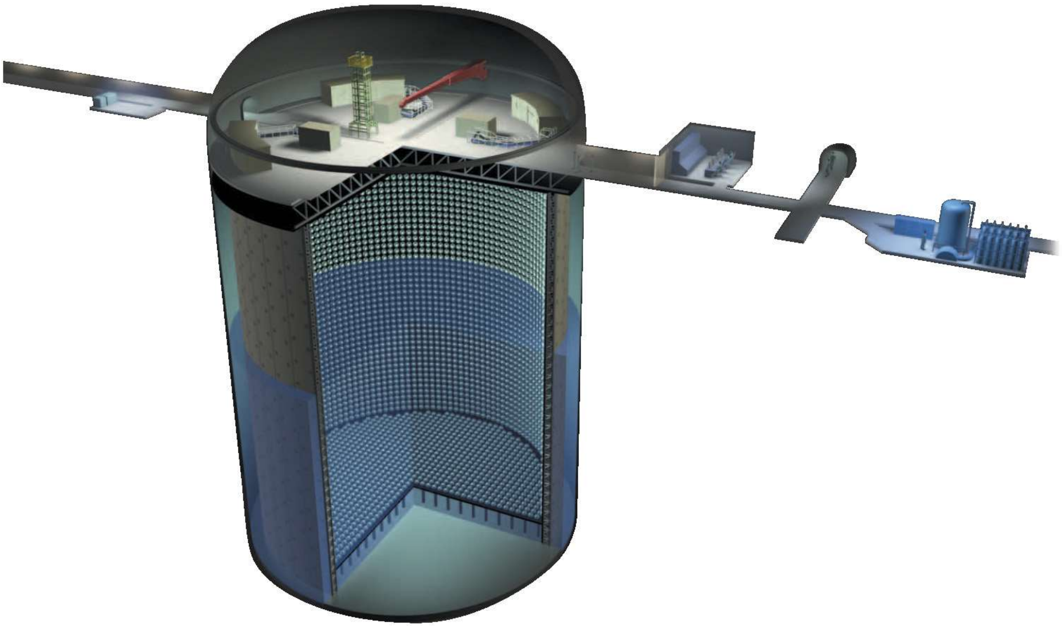

Fig. 1.5 Cross-section of the Super-Kamiokande neutrino detector laboratory, showing the large water tank with PMTs arranged around it as well as access tunnels and rooms. Taken from Kajita et al. 2016 [23].

to investigate the solar neutrino problem as well as the similar Atmospheric Neutrino Anomaly. When investigating muon and electron neutrinos the aforementioned ratio of events is compared with the ratio of flavours

$$R = \frac{(N_\mu/N_e)_{\mathrm{data}}}{(N_\mu/N_e)_{\mathrm{MC}}} \tag{1.21}$$

in the Montecarlo (MC) simulation. So any significant deviation of R from unity will indicate an anomaly, with muon flavour deficit relative to electron flavour giving $R < 1$. The results did come out indicating a muon flavour deficit, of course, as with the original Kamiokande. It was seen as possible that this ratio anomaly came from incorrect flux and cross section predictions or even poor knowledge of water Cherenkov detectors. To test the water Cherenkov performance the KEK (The High Energy Accelerator Research Organization or Kō Enerugī Kasokuki Kenkyū Kikō) laboratory used a test beam on a 1 kt tank and verified the muon to electron separation misidentification percentage of this type of detector to be less than a few percent for particles well inside the detector volume [30]. The conclusion was that the muon neutrino deficit from Kamiokande/Super-Kamiokande could not be an artifact of experimental design and that indeed theory and data could be compared [23]. A few years later in 1998 the Super-Kamiokande Collaboration released their paper on oscillation of atmospheric neutrinos [24] stating that their measurements matched with the familiar two-flavour vacuum oscillation hypothesis

$$P_{\alpha\beta} = \sin^2 2\theta \sin^2 1.27 \frac{\Delta m^2 L}{E_\nu} \tag{1.22}$$

for $\alpha \neq \beta$ which we will cover in more detail later in section 2.3. Note that the number 1.27 is a factor dealing with the unit conversion to put E_ν in GeV, L in km and Δm^2 in eV^2 (see equations 2.59, 2.60 and 2.61) which are convenient units for typical neutrino experiments. The collaboration considered $\nu_\mu \to \nu_e$ and $\nu_\mu \to \nu_\tau$ with the latter being favoured. This distinction can be made because most neutrinos will be well under the 3.5 GeV threshold for tau lepton production so oscillations to tau flavour will cause a mostly pure muon disappearance signal. Oscillations to electron flavour on the other hand can produce electrons due to their low mass, hence the signal of this will be electron flavour appearance above expected. So if, after accounting for all experimental factors, a deficit in muon flavour and an increase (smaller in size than the muon deficit) in electron flavour are seen, then the unseen remainder must go to tau flavour. Super-Kamiokande did observe this, except it turned out that the oscillations to tau flavour were overwhelmingly dominant [31]. The measurements gave values of the measured mixing parameters $\sin^2 2\theta \approx 1$ and $\Delta m^2 \sim 1.5 \times 10^3$.

The fact that tau oscillations were implied to be dominant in the data came from model-dependent predictions and was only explicitly true in the 3ν model. Another possibility considered was that the muon neutrinos were oscillating to a new 'sterile' flavour. Sterile models were mentioned as an alternate solution by the collaboration, but because they would be indistinguishable, no constraints were mentioned initially. It is important to keep in mind that sterile oscillation would cause deficits in NC and CC events, while tau oscillations only cause a deficit in muon NC events. Super-Kamiokande carried out some more thorough analyses based on this fact. Upward going muon flavour neutrinos are exposed to much greater matter effects than downward going ones. So because sterile neutrinos lack matter effects the $\nu_\mu \to \nu_s$ oscillations are suppressed compared to $\nu_\mu \to \nu_\tau$. Analysing zenith angle distortion and upward going muons lead to the muon to sterile oscillation hypothesis being disfavoured [31].

Super-K also helped confirm that vacuum oscillations are not the solution to the solar neutrino problem. To explain this, it is important to consider the characteristic L/E dependence of oscillations. If the deficit in solar neutrinos measured at Earth were a result of vacuum oscillations, then the deficit would vary seasonally due to the eccentricity of Earth's orbit and the L dependence. In contrast, in the LMA-MSW solution for solar neutrinos the neutrinos do not oscillate but will rather transition 'adiabatically' as the matter density slowly changes. As we will see in section 2.7.4, this explanation still involves mass splittings and mixing, but because the mechanism of transition is different, all of these neutrino transitions are complete before they leave the Sun and hence there will be no L dependence. When these neutrinos leave the Sun they are incoherent and cannot oscillate in vacuum, because of this, only a small matter-oscillation effect for up-going neutrinos travelling through the Earth is present. This leads to a day/night asymmetry. Interestingly enough, the mass splitting for which solar neutrinos would propagate coherently ($\Delta m^2 < 10^{-8}\ \mathrm{eV}^2$) is so small that matter effect would be insignificant. Hence observation of either 'day/night' or 'summer/winter' asymmetries was vital for the determination of the nature of the deficit. Super-K saw no such 'summer/winter' asymmetry, which implied that solar neutrinos propagate incoherently and do not oscillate [32] cementing LMA-MSW conversions in the Sun as the solution to the solar neutrino problem.

In addition to observing natural neutrinos, the Super-Kamiokande detector later formed part of the first neutrino long baseline (LBL) experiment. The experiment was known as K2K (KEK To Kamioka) and sent a beam of neutrinos sourced from an accelerator through a 1 kt water Cherenkov near detector 300 m from the neutrino producing proton target, onto the Super-Kamiokande far detector 250 km away [33]. This LBL experiment managed to view oscillations consistent with Super-Kamiokande, and provided further confirmation of atmospheric-scale oscillations [34]. Soon similar experiments were to become the norm with the follow up T2K, which we cover in more detail in section 1.4.1, being one of the pre-eminent experiments for years to come.

A successor experiment to Super-Kamiokande to be called Hyper-Kamiokande is currently in development [35]. It is intended to perform atmospheric studies as well as functioning as a far detector for accelerator neutrinos. The detector design is an cylindrical tank even larger than Super-K that is 60 m tall and 74 m diameter for a fiducial mass of 187 kt. Therefore with two tanks the total fiducial mass is roughly 17 times that of Super-K. The optimal setup involves two identical tanks, with at least one placed in the same location as Super-K while the other may be elsewhere in Japan or even overseas. The current proposed location for the second tank is in Korea, collinear with Super-K and Tokai so it can perform as a second far detector for the J-PARC neutrino beam (see 1.4.1). It is also worth noting that in addition to its neutrino detecting power, Hyper-Kamiokande will be the most sensitive proton decay experiment to date. This has been one of the original goals of the Kamioka experiments since the original Kamiokande and persists as a secondary goal into the future. Construction is planned to begin in April 2020.

1.3.2 SNO

The Sudbury Neutrino Observatory (SNO) was a specifically designed water Cherenkov detector with solar neutrino detection in mind. Originally proposed in 1984 to definitively analyse the solar neutrino problem. It was placed 2 km underground in an active nickel mine near Sudbury, Ontario, Canada. The experimental specification was for a 34 m high and 22m diameter somewhat cylindrical (almost barrel-like) cavity lined with water and radon impermeable Urylon plastic [36]. The spherical vessel of 12 m diameter was constructed out of 5 cm thick clear acrylic and filled with 1000 t of 99.5% pure heavy (deuterated or deuterium-containing) water (D_2O). The cavity surrounding the heavy water vessel was filled with ordinary, high purity water. The 9438 Hamamatsu 20 cm PMTs were attached to a stainless steel geodesic spherical frame and suspended around the heavy water vessel. A further 91 PMTs were arranged facing outward into the cavity to see external events.

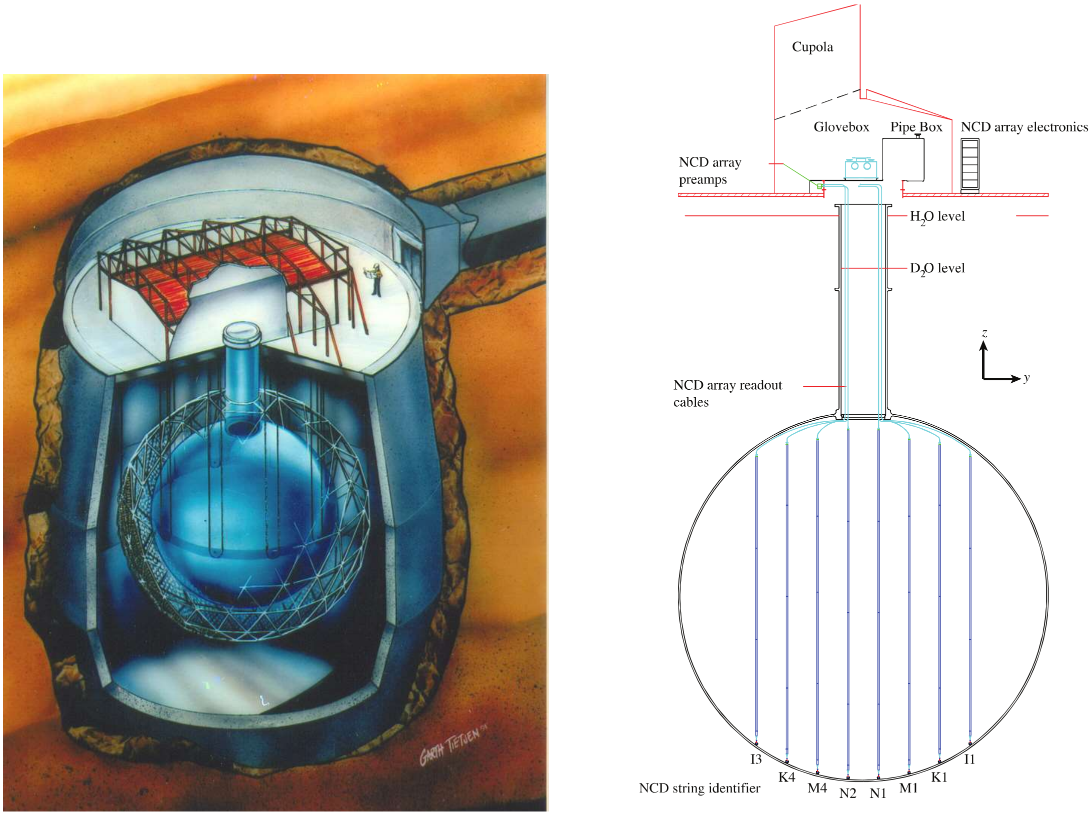

Fig. 1.6 Left: Cross-section of the SNO detector room, showing the main chamber surrounding the inner spherical heavy water chamber and geodesic PMT frame. Right: schematic of the Phase III detector. Taken from Bellerive et al. 2016 [36].

By using heavy water additional effects can be seen in the detector over standard water. This is due to the differing nuclear content between the standard isotope of hydrogen, protium (h) and the isotope with one additional neutron, deuterium (d). The interactions measured involving the extra neutron are the

1. $\nu_e + \mathrm{d} \rightarrow \mathrm{p} + \mathrm{p} + e^-$ CC interaction where a neutron is converted to proton, sensitive only to electron flavour and
2. $\nu_l + \mathrm{d} \rightarrow \mathrm{n} + \mathrm{p} + \nu_l$ NC interaction where the neutron is ejected from the deuteron, sensitive to all flavours equally.

SNO could also measure a third interaction which is the same one that Super-Kamiokande detected using light water.

3. $\nu_l + e^- \rightarrow \nu_l + e^-$ elastic scattering (ES) interaction, recall that electron flavour sensitivity is six times higher that muon or tau flavours due to the additional CC channel (Fig. 1.4).

The CC and ES processes were detected via PMTs picking up on Cherenkov light from the accelerated electron. The way NC reactions were viewed changed over time as the experiment evolved to enhance detection capability. During the initial Phase I run in 1999, the NC reaction was viewed by the neutrino break up of the deuteron. In this case the burst of light is emitted when the free neutron captures on deuterium and releases a γ ray which itself recoils an electron, hence producing a flash viewable by the PMT array.

After about a year and a half of the pure heavy water run, Phase II began (sometimes referred to as the 'Salt Phase' in the literature [37]). Around 2000 kg of NaCl was added to the heavy water to increase neutron capture efficiency. The capture cross section of $^{35}\mathrm{Cl}$ is around five times that of the deuteron and the Cherenkov pattern is more distinctive compared to other processes, leading to greater NC event discrimination [36]. After another three years Phase III began. In this revision, He filled neutrino counters were added to further increase neutral current detection via neutron capture on helium producing deuterium and tritium

$$\mathrm{n} + {}^{3}\mathrm{He} \rightarrow \mathrm{p} + \mathrm{t} + 764\ \mathrm{keV}.$$

These neutrino counters were known as the 'Neutral Current Detection' (NCD) array [36]. In general NC process was viewed via γ rays released upon neutron capture with characteristic energies depending on the target nucleus. By measuring the CC and NC processes, SNO could tell if conversions were occurring by seeing a deficit of CC events over NC events. This conclusion could be made without reference to solar models which was important because, revising the (thought to be incorrect) solar neutrino production model was previously a potential candidate for explaining the solar neutrino problem.

The fluxes can be compared in the ratio corresponding to electron flavour survival [36]

$$P_{\mathrm{SNO}} = \frac{\Phi_e}{\Phi_{\mathrm{NC}}} \tag{1.23}$$

where Φ_e is the electron flavour CC flux and $\Phi_{\rm NC}$ is the total NC flux of all flavours present. If only electron neutrinos are present (i.e. no flavour conversion) then this ratio should be close to 1. However if other flavours are present, then it should be less than 1. After the heavy water phase SNO measured a value of

$$P_{\rm SNO} = 0.340 \pm 0.023^{+0.029}_{-0.031} \tag{1.24}$$

which implies ν_e to ν_μ and ν_τ conversion. In 2001 Super-K and the SNO released results on solar neutrinos [38], both showing a deficit in electron neutrinos. This indicated flavour conversion independent of any possible deficit compared to the predicted solar flux and was very good evidence for solar neutrino mixing.

The understanding of the mechanism for mixing came from the fact that this value was found to be close to the survival probability given by the non-oscillatory 'adiabatic conversion' of neutrinos in the Sun [13] which was found to be

$$P_{\rm non-osc} = \sin^2\theta_{12} = 0.31\,. \tag{1.25}$$

This doesn't fully account for the deficit however, because it predicts *too few* electron events, so the difference between $P_{\rm SNO}$ and $P_{\rm non-osc}$ must be accounted for by some other physics. Remember that we mentioned in 1.3.1 that solar neutrinos lose coherence upon leaving the Sun and as such will not oscillate in space, so vacuum oscillation effects cannot account for a deficit, though MSW effects in the Earth and Sun can. This was found to be due to the combined additional effects of averaged oscillations in the sun and matter oscillations in the Earth. This can be expressed as the sum of these contributions

$$P_{\rm surv} = P_{\rm non-osc} + \Delta P_{\rm osc} + \Delta P_{\rm regen} \tag{1.26}$$

where $\Delta P_{\rm osc}$ and $\Delta P_{\rm regen}$ are the corrections due to averaged Sun oscillations and Earth regeneration oscillations respectively. The averaged oscillations in the Sun will cause overall more electron neutrinos to be emitted. In addition, matter oscillations in Earth provide a regenerative effect, so that neutrinos that had transformed into other flavours have the chance to oscillate back to electron flavour. This can only occur when neutrinos travel inside the Earth before reaching the detector, i.e. at Night. As with Kamiokande, this effect can be calculated from the Night-Day asymmetry factor A_{ND} due to the difference in neutrino path of these cases. From [37] the resulting regeneration probability can be expressed as

$$\Delta P_{\text{regen}} \approx A_{ND} \times P_{\text{non-osc}} \approx \sin^2\theta_{12} \times A_{DN}\,. \tag{1.27}$$

Where the Day-Night asymmetry was measured to be $A_{DN} \sim 5\%$, and the overall regeneration factor found to be [37]

$$\Delta P_{\text{regen}} \approx 0.015\,. \tag{1.28}$$

To get the form of the averaged oscillation component of the Solar transitions we look at the 'averaged adiabatic survival probability' equation which includes both solar effects [37]

$$P = \sin^2\theta + \cos 2\theta \cos^2\theta_M^0 \tag{1.29}$$

where θ will be θ_{12} in this case and θ_M^0 is the matter mixing angle in the production point defined as

$$\theta_M^0 = |\langle\nu_{1M}|\nu(t)\rangle|^2\,. \tag{1.30}$$

Which is the probability to find the ν_{1M} mass eigenstate in the adiabatically propagating state $\nu(t)$. In the limit of no oscillations, (just adiabatic transitions) $\cos 2\theta \cos^2\theta_M^0 = 0$ and $\nu(t) = \nu_{2M}$. Which makes sense because clearly the first term from equation (1.29) is the non-oscillation probability from equation (1.25). The second part of this probability then, is from the averaged oscillation in the Sun, and was found to be

$$\Delta P_{\text{osc}} = \cos 2\theta_{12} \cos^2\theta_M^0 \approx 0.015\,. \tag{1.31}$$

Therefore combining these two factors adds more final electron events which can account for the difference from pure adiabatic conversion.

$$P_{\text{surv}} \approx 0.31 + 0.015 + 0.015 \approx P_{\text{SNO}}\,. \tag{1.32}$$

Confirming that (once all solar effects were accounted for) SNO was providing a good measurement of this phenomenon and a strong constraint on θ_{12}.

This result is the one for which Arthur B. McDonald from SNO received a half share in the 2015 Nobel Prize in Physics [39][4].

---

[4] Takaaki Kajita from Super-K received the other half of the prize for somewhat tangentially related work on atmospheric neutrinos [39]

1.4 Later and Contemporary Experiments

Here we give an overview of a selection of experiments that came around after much of the uncertainty in oscillations and the solar neutrino problem had been figured out. Many of these experiments were (or are) designed to focus on one specific aspect of oscillation physics and perform a very precise analysis. Some areas of analysis that fit this description include: CP phase analysis, matter effects, mass ordering, precision measurements of mixing angles and tau flavour appearance.

1.4.1 T2K

The successor to K2K, Tokai to Kamioka or T2K was proposed to be the first LBL experiment to look for direct electron neutrino appearance in a muon flavour beam [40]. This was important because despite strong evidence for muon flavour oscillation, many early discoveries relied on muon disappearance searches. Electron appearance from atmospheric sources can be seen, but the statistics are less certain. For example, due to wrong flavour corruption from the electron neutrinos present in cosmic ray showers. With a muon neutrino beam source, direct conversion could be verified with almost absolute certainty. T2K experimental commissioning began in 2009 and first physics data was taken in 2010. The experiment uses a proton beam created by the J-PARC accelerator complex to produce neutrinos (at roughly -1° declination) that are then detected 295 km away by the Super-Kamiokande detector which is located 2.5° off-axis. The proton beam produces neutrinos in a similar method to that of atmospheric neutrinos from cosmic rays. The proton beam is directed onto a target which produces (amongst other things) pions and kaons. The charged mesons are then directed by magnetic funnelling horns toward the far detector. These horns also provide switchable charge selection, allowing the detector to run a beam of neutrinos or antineutrinos. This feature is immensely useful for CP violation studies and unique to accelerator experiments. The mesons produced will promptly decay to neutrinos via the same method as the atmospheric case in Fig. 1.3. The off-axis method is chosen because despite lower overall flux, it greatly reduces the width in the peak of the neutrino energy spectrum [41, 42] which for T2K is 0.6 GeV. A discussion of this for the NOνA detector is presented in section 1.4.2 with figures 1.9 and 1.10 though the same concept applies for T2K. For un-oscillated beam studies T2K also has near detectors a mere 280 m from the beam origin. Some of these detectors are on-axis and some of which are off-axis. The on-axis detector is known as INGRID (Interactive Neutrino GRID) and it measures the beam direction and intensity [43]. The off-axis near detector known as ND280 (i.e. Near Detector 280 metres) is considered part of T2K itself and is used to measure the muon neutrino flux and energy spectrum as well as intrinsic electron neutrino contamination which is important for the electron-flavour appearance search. A two detector layout allows comparison between oscillated to unoscillated measurements as well as analysis of near and far detector signals to eliminate backgrounds that cannot be easily ruled out when only using one detector. This is in contrast to other types of experiments which usually compare one set of measurements to previous fits or theory. Because these may not reflect identical experimental circumstances or accurate modelling, such comparisons can obviously carry errors. Hence most LBL experiments have this layout because it massively advantageous for the (relatively) low cost of a smaller secondary detector. The approximate arrangement of the T2K experiment, including the J-PARC beam, ND280 near detector and Super-KAMIOKANDE itself can be seen in figure 1.7. In 2011 T2K reported confirmation of ν_e appearance and put early limits on $\theta_{13} \neq 0$, δ_{13} and $|\Delta m^2_{31}|$ under the assumption that $\sin^2 2\theta_{23} = 1$ [44].

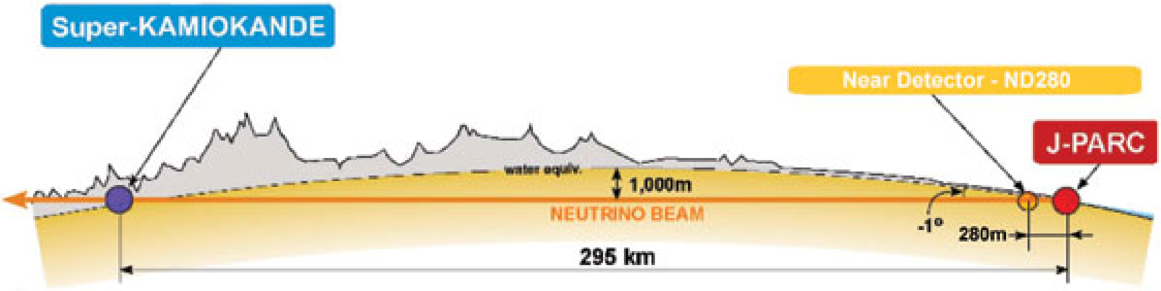

Fig. 1.7 Side profile illustrating the distances between the beam and detector of T2K, taken from [40].

A major extension has been proposed and developed to further extend the T2K physics program it involves directing the Tokai beam to the upcoming Hyper-Kamiokande detector (as mentioned in 1.3.1) to form T2HK (Tokai To Hyper-Kamiokande) with the same 295 km baseline as T2K. The Hyper-Kamiokande tank is designed to greatly increase the statistics over Super-Kamiokande so that the sensitivity to CP phases will increase, despite having the same level of matter effects due to the identical baseline. If the second Hyper-K tank is placed even further along the beamline in Korea then we will have a second far detector with a 1100 km baseline, hence T2HKK (Tokai To Hyper-Kamiokande and Korea). Due to the further detector being further away, yet receiving the same beam with identical peak neutrino energies, it will be placed in the second oscillation maximum. The other tank and Super-K are at the first as is normal for such experiments. This would allow T2HKK to compete with NOνA and DUNE in the mass ordering space as well as allowing good CP resolution.

1.4.2 MINOS and NOνA

The MINOS (Main injector neutrino oscillation search) collaboration proposed a two detector experiment in 1995 [45]. The neutrinos were to originate at Fermilab Illinois via the NuMI (Neutrinos at the Main Injector) beam, travel 1.04 km to the near detector, then another 735 km onto a far detector in the Soudan mine in Minnesota. The MINOS detectors are magnetized steel-scintillator tracking calorimeters. Near and far detectors are functionally identical with total masses of 0.98 kt and 5.4 kt respectively. The neutrino source is similar in style to the J-PARC accelerator for T2K, with 120 GeV protons from the Fermilab Main Injector accelerator being directed onto a graphite target.

MINOS was operated from 2005 to 2016 with an upgrade to MINOS+ taking place between 2012 and 2013. Early measurements were able to reject the no-oscillation hypothesis at 98% confidence level [46]. Confirmation of muon neutrino disappearance in a beam was published soon after [47]. Early parameter best fits were found to be consistent with Super-K results. In terms of oscillation parameters MINOS primarily published measurements of $|\Delta m^2_{32}|$ and θ_{23} [48].

Controversially MINOS reported potential evidence (only 1.8σ significance) for superluminal neutrino velocities in 2007 [49]. In this measurement the central value of the velocity measurement was greater than c but with large uncertainties. Later the ICARUS experiment (in response to the superluminal velocity anomaly seen by OPERA) measured Neutrino velocity rejected neutrino velocities above the speed of light at 90% confidence [50], in agreement with accepted physics.

NuMI Off-axis ν_e Appearance or NOνA is a neutrino experiment which was originally intended to supersede MINOS using the same NuMI beam [51]. The NOνA proposal and development process began before MINOS had even taken data. The intention was to explore expanded regions of oscillation physics while utilising some of the same equipment [52]. One of the main goals of NOνA compared to MINOS is to observe the θ_{13} mixing angle via muon to electron oscillations at the atmospheric oscillation L/E scale [52]. NOνA began full operation in 2014 and ran alongside MINOS+ [53] until the latter was shut down in 2016.

The neutrinos for NOνA travel from Fermilab through 810 km through the Earth's crust and onto the far detector in Ash River Minnesota. The main detector is located 14.6 mrad off-axis due to the way this affects the energy spectrum of the neutrinos. This is in contrast to MINOS+, which is on-axis. A rough idea of the geometry of this arrangement can be seen in figure 1.8. To explain the off-axis behaviour we look at

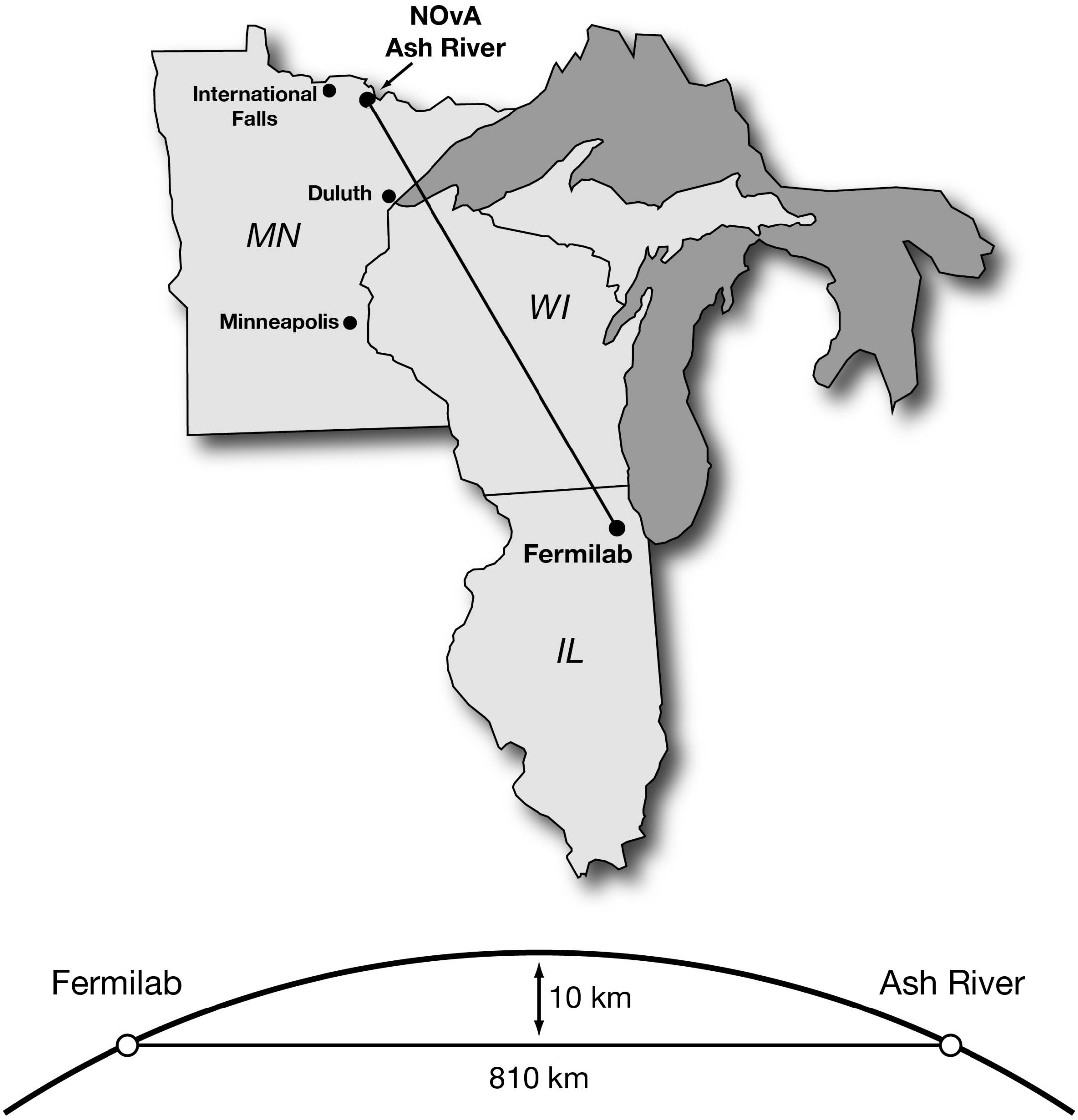

Fig. 1.8 Side profile illustrating the distances between the beam and detector of NOνA as well as the depth it reaches within the Earth.

the flux and energy of neutrinos in relation to the angle between them and the initial pion beam. The flux for highly boosted pions decaying to neutrinos in the lab frame is

$$F = \left(\frac{2\gamma}{1+\gamma^2\theta^2}\right)^2 \frac{A}{4\pi z^2} \tag{1.33}$$

where θ is the (small) angle between the pion and the produced neutrino, $\gamma = E_\pi/m_\pi$ is the ratio of pion energy to mass, z is the distance and A is detector area. The corresponding neutrino energy is

$$E_\nu = \frac{0.43E_\pi}{1+\gamma^2\theta^2} \tag{1.34}$$

where for kaons rather than pions $0.43 \rightarrow 0.96$. These equations are from The NOvA Technical Design Report, Ayres et al. [51]. This broadens the neutrino energy spectrum due to the kaon's greater mass. Neutrino flux and energy can be plotted versus pion energy for various angles to get an idea of what different detector placements will see for a given accelerator energy. From Fig. 1.9 it can be seen that the curve for 14 mrad has a balance of having without high enough flux that statistics do-not suffer and a peak in neutrino energy at 2 GeV over range of pion energies. This ensures that neutrino energies are primarily around the oscillation maximum of 1.6 GeV. CC event rates and neutrino energies corresponding to detectors at several angles receiving the NuMI beam can be seen in Fig. 1.10. These plots reinforce the choice of 14 mrad off-axis as a compromise between event rates and narrowness of the peak in terms of energy while being close to the oscillation maximum value.

Unlike T2K the NOνA far detector uses a lattice of cells filled with liquid scintillator as the detector medium rather than a large water tank. While compared to MINOS the far detector mass is increased from 5.4 kt to 14 kt. The original proposal called for a 30 kt far detector which would've resulted in approximately 10 times more sensitivity to $P_{\mu e}$ than MINOS [52]. After accounting for detector factors, the overall primary difference between NOνA and T2K are their different baselines. The longer baseline of NOνA allows for greater matter-induced CP effects, hence stronger constraints on the mass ordering. The results in 2012 indicating that θ_{13} is non-zero [44, 54–57] (and relatively large compared to early predictions) were very promising for NOνA because this means that terms dependent on CP phases (including some extra θ_{23} terms) do not vanish for three (and four) flavour probabilities. Combined data between NOνA and T2K recently has given promising early hints towards best fits

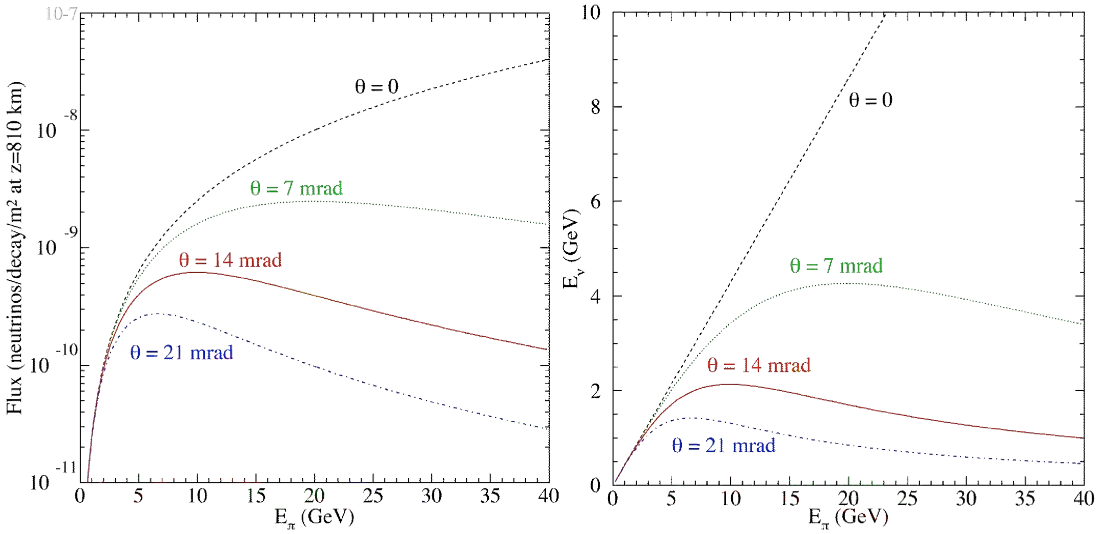

Fig. 1.9 Plot of neutrino flux and neutrino energy vs pion energy at NOνA's baseline. Taken from The NOvA Technical Design Report, Ayres et al. 2007 [51].

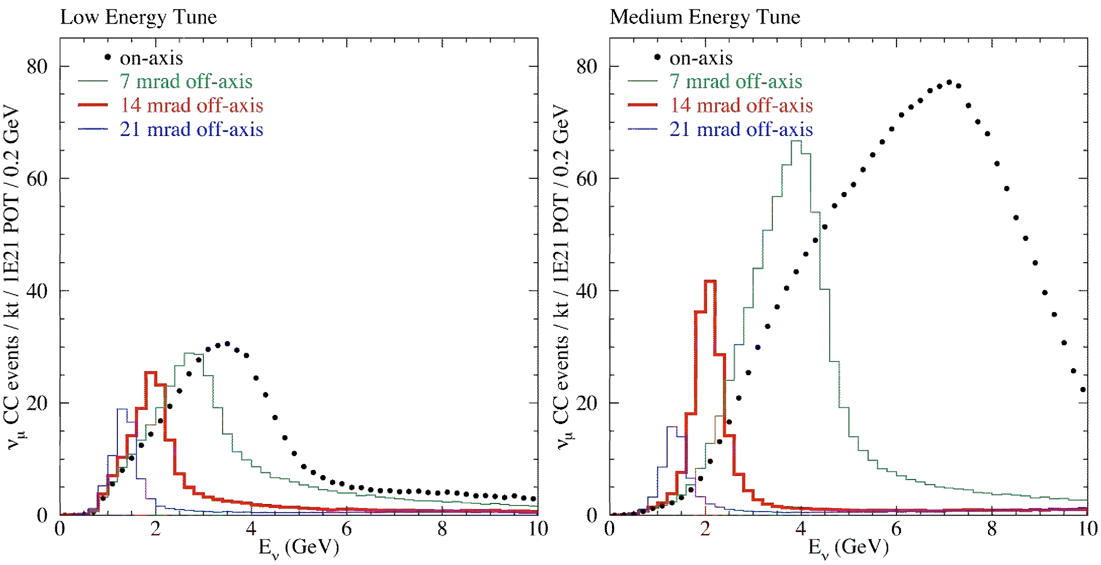

Fig. 1.10 Plot of event rates of neutrinos vs neutrino energy for the NuMI beam low and medium energy configurations. Taken from The NOvA Technical Design Report, Ayres et al. 2007 [51].

for mass ordering and CP phases as well as constraints on θ_{23} [58–60]. The NOνA Collaboration released their first combined neutrino and antineutrino analysis in 2019 [61].

1.4.3 DUNE

DUNE is a future very long baseline experiment that will further expand upon the studies that T2K and NOνA are currently working on. DUNE has the lofty but achievable goals of solving the mass ordering (MO) and octant degeneracies as well as determining the level of leptonic CP violation (see section 1.9 for an introduction to mass eigenstates and their ordering, and section 4.3 for an overview of degeneracies). Other goals include the ever-present search for proton decay, observation of supernova neutrinos and dark matter searches [62]. DUNE also has the potential to resolve extra degeneracies induced by extra mass splittings from extended neutrino theories (see 6 for theoretical analyses in the extended $3+1$ case) . The baseline is 1300 km which is larger than any extant or proposed accelerator type experiment. The intention is to exploit even more matter effects to increase the asymmetry between normal and inverted hierarchy solutions. The beam for DUNE originates at the LBNF (Long Baseline Neutrino Facility) "near site" at Fermilab which is a new beamline and near detector cavern, constructed specifically for this experiment. The far detector is located at SURF (Sanford Underground Research Facility) which is in the same mine as the original Homestake experiment. DUNE is not in the Homestake cavern but instead in the LBNF "far site" cavern [63]. Contrary to T2K and NOνA the DUNE detector is located on-axis. DUNE is currently intended to start running under partial detector install in 2026 [64]. Although the primary purpose of DUNE is to study $P_{\mu e}$ it can also directly probe $P_{\mu\tau}$ as the tau production energy is within the neutrino energy spectrum of the LBNF beam [65]. Unfortunately the threshold production energy is well past that of the first few tau oscillation maxima at DUNE. This would mean that the calculation of the probability would be rather imprecise, limiting the physics potential. Predictions do show that it is likely that sensitivity to this channel will not increase DUNE's 3ν sensitivity, but can significantly increase the NSI (Non-Standard Interactions) and $3+1$ sensitivity parameters related to tau flavour [66]. NSI parameter cover potential matter effects that occur with the non-electron flavours of neutrinos. If present, such interactions will affect oscillation and can potential lead to phenomena that differ greatly from standard oscillations. For a short overview see Appendix C. However, the advantage is that whatever signal can be gleaned is practically independent of other channels and complementary to overall information collection.

1.4.4 OPERA

Final confirmation of muon to tau oscillation was accomplished by OPERA (Oscillation Project with Emulsion-tRacking Apparatus) which ran between 2008-2012. This experiment used the CNGS (Cern Neutrinos to Gran Sasso) beam which sent muon neutrinos 730 km from Geneva, Switzerland to the detector in Gran Sasso, Italy. The objective of OPERA was to search for tau neutrino appearance via direct tau production to prove directly that muon to tau flavour oscillation occurs, and is the dominant transition channel, at atmospheric neutrino energy scales. Up until then all experiments in this energy range only inferred indirectly that oscillations to tau flavour were occurring. The CNGS beam was created at CERN by impacting the SPS (Super Proton Synchrotron) proton beam onto a target to produce pions and kaons, which subsequently decay to neutrinos. OPERA detected tau candidates using nuclear emulsion detector ‘bricks’ interleaved with lead, with a scintillation trigger system to indicate and roughly locate each detection. The trigger system was necessary to locate where and when events occurred in the detector. This is important because emulsion detectors work somewhat like photographic film, with the bricks being removed and processed after an event is tagged to view the permanent tracks left inside by particles. OPERA detected its first (potentially oscillation sourced) tau candidate in 2010 [67]. A final analysis of the four years of data in 2018 indicated *ten* tau candidates, with a predicted background of two tau events, from a total of 5603 fully reconstructed neutrino events [68]. This completed the three flavour picture of neutrino oscillations, with all possible active-flavour oscillations directly confirmed to occur.

In 2011 OPERA published data pertaining to neutrino velocities exceeding the speed of light [69]. Compared to the earlier MINOS anomalies, the significance was much higher (6.0σ). Problems in the experimental setup were discovered in 2012 with the net effect of decreasing apparent neutrino travel time [70]. This fact, along with measurements by ICARUS refuted the faster than light neutrino hypothesis [50].

1.4.5 Daya Bay, RENO and Double-CHOOZ

Reactor neutrino experiments have been important throughout the years of neutrino physics. As mentioned in section 1.1, the first neutrinos directly seen came from a reactor [4]. Reactor experiments look for deficits in $\overline{\nu}_e$ appearance from β^+ decay chains reactions coming from heavy elements including: ^{235}U, ^{239}Pu, ^{238}U and ^{241}Pu.

Many of the modern detectors intended to see oscillations use a two-scale detection method. The idea is that the near detector will measure unoscillated flux which can be compared with that of a far detector further away. Here we summarise three reactor experiments which were crucial to the determination of the full oscillation parameter set.

The Daya Bay experiment is named after its location at the Daya Bay nuclear power plant in Daya Bay, China. The complex is situated in southeast China approximately 52 kilometers northeast of Hong Kong and 45 kilometers east of Shenzhen. Daya Bay uses a total of eight detectors spaced apart in three underground detector halls all within 2 km of the sources. Two of these sites are 'near sites' (between 363 m and 526 m from the clusters) with two detectors each while the remaining four are in the 'far site' (1615 m from one reactor cluster and 1985 from the other). These receive neutrinos from initially two, now three reactor clusters, each with two cores [71]. These detectors contain 20 t each of liquid scintillator surrounded by PMTs.

The RENO (Reactor Experiment for Neutrino Oscillation) reactor experiment is located in the west coast of South Korea, about 250 km from Seoul. It features two 16 t liquid scintillator detectors, situated 'near' and 'far' at 290 m and 1.4 km baselines respectively [72]. Additionally these detectors are 70 m and 260 m underground respectively. The neutrinos are produced by six reactors at the Hanbit (previously Yonggwang) Nuclear Power Plant located in-between the detectors.

Double-CHOOZ was developed to be the successor to the CHOOZ experiment which put limits on $\sin^2 2theta_{13}$. The name comes from adopting a two-detector approach with one at $\sim$150 m and the other at 1.05 km [73]. The neutrino source are the two CHOOZ neutrino reactors located northeast of France in the Ardennes region, close to the Belgian border.

The burn-up of such nuclear fuel is accounted for in the interaction rate but is not fully understood. Some experiments have reported rate inconsistencies unexplained by current oscillation parameters. Such anomalies have been variously attributed to fuel burn-up, as well as potential short range anomalous oscillations. We summarise these in the context of oscillation anomalies in section 3.1.1. For a more thorough overview of reactor neutrino detectors, physics and anomalies see the review [74].

In the era of oscillation physics, the short (metre scale) or medium (kilometre scale) baseline, low energy neutrino experiments possible at reactors were developed to measure the mixing angle θ_{13}. This mixing angle was often thought to be incredibly small, if not zero. As we will alter see in section 2.2.2 this would lead to a much simplified mixing matrix and hence simpler oscillation probabilities, devoid of genuine three flavour interactions. This assumption persisted until the early 2010's when experiments Daya Bay [54], RENO [55], Double-CHOOZ [56], MINOS [57] and T2K [44] (alongside MINOS [57] and the newly launched T2K [44]) all published results determining that θ_{13} is non-zero and indeed is surprisingly large. This development has motivated much of the recent physics development in T2K and NOνA.

1.5 Overview of Experimental Oscillation Measurement

We present an overview of the basic mathematics and logic of applying an oscillation probability to an experimental phenomenon to highlight some key points. Now, any given neutrino experiment has a method of detection, the two main cases are: real-time detection utilising PMTs and/or scintillation of some sort, such as the current generation experiments NOνA and T2K, and delayed chemical-based methods based on the statistical analysis of isotopes extracted which are produced in neutrino interactions e.g. Homestake, SAGE and GALLEX. Depending on the energy of the neutrinos, some transitions will be unmeasurable due to the high threshold energy required to produce the observable leptons associated. An example of this is in the case of reactor antineutrinos, these only have sufficient energy to produce positrons, so oscillations to antimuon and antitau flavour will only be seen in a lowered rate of positron appearance. So depending on the neutrino source it may not be viable to have a detector that is sensitive to muons and taus, in a case like this disappearance will be the channel of choice. Regardless of method, these experiments will produce some number of events which we can relate to an 'oscillation'/'appearance', 'disappearance' or 'survival' probability

$$P \propto N_{\text{events}} \,. \tag{1.35}$$

We somewhat confusingly use 'appearance' and 'oscillation' interchangeably despite ascribing all of these behaviours to oscillation phenomena. This is due to different flavour appearance being the smoking gun signal for oscillation. Other phenomena that only involve one flavour can feasibly correspond to other physics. In these cases L/E dependence will indicate a preference for oscillation solutions.

We consider an appearance probability when we expect an amount of neutrinos of a certain flavour to be small above the background e.g. ν_e's at NOνA. In this case the NUMI beam produces a strong beam of ν_μ's with a very small contamination of ν_e. We account for this in our background statistical analysis and then perform a search for ν_e events above background. We attribute this to an oscillatory effect so we write the general expression

$$P_{\text{osc}} = \sin^2 2\theta \sin^2 \Delta \tag{1.36}$$

with oscillation factor $\Delta = \Delta m^2 L/4E$ encompassing the L/E dependence and related to the mass squared splitting Δm^2 (see section 1.9 for related terminology). We derive this equation in section 2.3.

A survival probability is usually thought of when we measure a deficit in our detection channel. For example, Homestake expected a certain rate of neutrinos emitted from the sun based on solar models. The experiment then detected far too few $^{37}\mathrm{Ar}$ isotopes once the gas was flushed out and radioactively counted. After exhausting all possible mistakes with the flux calculation the eventual explanation for this was that due to relatively large mixing between flavours and the MSW effect inside the sun, transitions occur and as such less ν_e than expected are detected. In a similar sense, NOνA can search for ν_μ CC events in the far detector because it can tell e and μ tracks apart, therefore it can perform a ν_μ disappearance scan as well as the aforementioned appearance check. The general survival probability expression can be written

$$P_{\text{surv}} = 1 - \sin^2 2\theta' \sin^2 \Delta' \tag{1.37}$$

and related to the number of events we see. The corresponding disappearance probability can be calculated

$$\begin{aligned} P_{\text{disapp}} &= 1 - P_{\text{survival}} \\ &= \sin^2 2\theta' \sin^2 \Delta' \,. \end{aligned} \tag{1.38}$$

In a two flavour neutrino case where a given type can only disappear by becoming the other, an experiment that can measure both appearance and disappearance channels would show that $\theta = \theta'$ and $\Delta = \Delta'$. These can be equated because (as we will see in section 2.3) we are fitting data so can choose the quadrant of the angle θ and sign of Δ because these are merely effective parameters. So we don't need to write $\theta = \theta' + n\pi$ and $\Delta = \pm\Delta'$. So because we can equate these, we can essentially measure the same thing two ways. This also makes sense due to the trivial unitarity of this two flavour only case (also assuming this isn't broken by some other new physics). So we have

$$P_{\text{surv}}^{(2\nu)} = 1 - P_{\text{osc}}^{(2\nu)} \tag{1.39}$$

hence

$$P_{\text{osc}}^{(2\nu)} = P_{\text{disapp}}^{(2\nu)} \tag{1.40}$$

which makes intuitive sense, because the chance of a neutrino to disappear from one channel must be the chance it has to appear in the other channel. But is is very important to note that this it not true in general, only in the simple two flavour case. For example, with NOνA, assuming we only have three neutrino flavours, the expressions for ν_e appearance (oscillation), ν_μ survival and hence ν_μ disappearance are defined

$$P_{\text{osc}} = P_{\mu e} \tag{1.41}$$

$$P_{\text{surv}} = P_{\mu\mu} \tag{1.42}$$

$$P_{\text{disapp}} = 1 - P_{\mu\mu} \tag{1.43}$$

which can be parametrised in turn as

$$P_{\mu e} = \sin^2 2\theta_{\mu e} \sin^2 \Delta_{\mu e} \tag{1.44}$$

$$P_{\mu\mu} = 1 - \sin^2 2\theta_{\mu\mu} \sin^2 \Delta_{\mu\mu} \tag{1.45}$$

$$1 - P_{\mu\mu} = \sin^2 2\theta_{\mu\mu} \sin^2 \Delta_{\mu\mu} \,. \tag{1.46}$$

Now if we think about the physics going on to produce such probabilities, the ν_e appearance is entirely based on the chance for a muon neutrino to oscillate to an electron neutrino, while the ν_μ disappearance is dependent on the chance for a muon neutrino to oscillate to an electron *or* tau flavour hence these will only coincide for vanishing tau mixing. We therefore expect that for three flavours:

$$1 - P_{\mu\mu} = P_{\mu\tau} + P_{\mu e} \tag{1.47}$$

due to unitarity. Early global fits to neutrino data had θ_{13} consistent with zero, and that simple two flavour approaches were valid in atmospheric oscillations (see the θ_{13} dependence of matrix elements in section 2.2.2 to get an idea). In the late 2000's it was hinted that $\theta_{13} \neq 0$ meaning that *none* of the standard mixing angles are vanishingly small [75, 76]. This was confirmed definitively in the early 2010's by combined fits of accelerator and reactor data [77, 78], implying that three flavour effects should be accounted for in approximations. Although this is good to keep in mind, a simplified probability can usually be calculated due to certain oscillation parameters dominating at a given baseline. Regardless it's important to fully understand what exact process is being examined.

In the previous examples it can be seen that for this simple parametrisation of appearance and disappearance the generic mixing terms have sign ambiguity built in and the probabilities are degenerate under sign flips of the Δ terms i.e.

$$P_{\mu e}(+\Delta_{\mu e}) = P_{\mu e}(-\Delta_{\mu e}) \tag{1.48}$$

$$P_{\mu\mu}(+\Delta_{\mu\mu}) = P_{\mu\mu}(-\Delta_{\mu\mu})\,. \tag{1.49}$$

This allows the definition of two orderings for each measurement of P and value of θ which is the source of the 'Mass-Hierarchy Degeneracy' which we will discuss further in section 4.3. It can also be seen that degeneracies associated with θ are possible as it is also symmetric about $\pm\theta$ and $\theta = 45^\circ$ etc. these concepts are covered in more detail later on in 4.3.

1.6 Summary of Neutrino Experiments and History

Here we will present summaries of detector types, outlining several useful features for each. Clearly separating the types of experiments can be somewhat confusing, especially since some detectors operate in multiple modes. A timeline of neutrino physics is included in Table 1.1 of section 1.6.5 to show how the physics progressed over the years.

1.6.1 Solar

- The Sun is a source of neutrinos dominated by the pp chain with a small contribution from the CNO cycle and other such solar processes [79].

- Several characteristic neutrino energies are available via different steps in the chain.

- Energy peaks from all possible nuclear reactions are well below production threshold for muon or tau leptons.

- Low wrong-sign contamination due to nature of production and some detectors (like Homestake) are not sensitive to antineutrinos.
- Transformations occur via LMA-MSW, including adiabatic conversion, averaged oscillations in the Sun and the Earth-matter regeneration effect.

1.6.2 Atmospheric

- Neutrinos from the upper atmosphere are created by cosmic ray impacts and subsequent particle decays.
- Neutrinos are primarily muon flavour from pion and kaon decay.
- Flavour ratio $(\nu_\mu + \overline{\nu}_\mu)/(\nu_e + \overline{\nu}_e)$ is at roughly 2 for neutrino energies below 1 GeV and increases from there [80].
- Oscillations to tau flavour will be below threshold for production, hence invisible.
- Lack of observation of additional electron flavour flux implied that tau or sterile flavour oscillations dominate.
- Later constrained to show tau channel is primary for atmospheric oscillations.
- Most detectors are non-magnetised so have poor to no lepton sign determination power. This is because particle charge cannot be distinguished based on path deflection in a magnetic field.
- A magnetised detector such as the proposed ICAL (Iron CALorimeter) at the INO (India-based Neutrino Observatory) [81] could have strong sign determination.
- Oscillations have zenith angle dependency due to differing matter effects and baseline. Sometimes divided into up going/down going.
- Potential anomalies exist in short range experimental data (see SBL section 3.1.1).

1.6.3 Reactor

- Sources of neutrinos of <10 MeV energy on Earth must be produced from β decays.

- Nuclear reactors are a source of 2-8 MeV antineutrinos from β^+ decay chains of elements such as: ^{235}U, ^{239}Pu, ^{238}U and ^{241}Pu.
- These neutrinos are created as purely e-flavour.
- $\bar{\nu}_e$'s produced at a reactor may be detected by observing e^+ appearance via CC interactions in a detector.
- The e-flavour appearance channel is the only one because the neutrino energies are below μ (let alone τ) production threshold.
- Oscillation is therefore detected in the $\bar{\nu}_e$ disappearance channel.
- Examples include Daya Bay, Double-CHOOZ and RENO as well as the upcoming JUNO.

1.6.4 Accelerator

- Beams sourced by accelerators can produce neutrinos of varying initial flavour.
- Accelerator sourced beams have widely varying energies amd are often purpose built/tuned for a specific detector.
- Low energy neutrinos (53 MeV) can be created by pion and muon decay at rest (DAR) decay chain (e.g. LSND) $\pi^+ \to \mu^+\nu_\mu$ and $\mu^+ \to e^+\bar{\nu}_\mu\nu_e$.
- In this low energy case, the opposite sign pion chain can be suppressed by ensuring that π^- are captured preferentially in the target.
- The contamination of $\bar{\nu}_e$'s in the resulting beam is small, allowing the $\bar{\nu}_\mu \to \bar{\nu}_e$ channel to be observed.
- High energy (100 MeV-hundreds of GeV) sources use a proton beam and target (commonly beryllium or carbon) to produce highly boosted mesons (such a J-PARC or NUMI).
- These charged pions and kaons which decay in flight (DIF) down the decay pipe to appropriately charged lepton-neutrino pairs.
- Because of this, the choice of neutrino(antineutrino) can be selected by steering the positive(negatively) charged mesons using magnets. This leads to only a few percent wrong sign contamination.

- These accelerator-based beams are primarily utilised for $\nu_\mu \to \nu_e$ and $\bar{\nu}_\mu \to \bar{\nu}_e$ appearance processes.
- Accelerator experiments can be divided into Short and Long BaseLine (SBL/LBL) due to differing oscillation paradigms.
- **Short BaseLine (SBL):**
  - Can probe potential sterile oscillations? In this case NC events important.
  - It is also important that CC events can be classified, that is, the outgoing lepton must be identified.
  - LSND was a DAR experiment using a $\bar{\nu}_\mu$ beam, it detected an excess of $\bar{\nu}_e$ appearances interpreted as oscillation.
  - Typical baselines are tens of metres with energies being of order tens of MeV.
  - Reactor experiments and accelerator SBL experiments may have complimentary L/E ranges depending on setup.
- **Long BaseLine (LBL):**
  - Often utilise near and far detectors.
  - OPERA is an example of a tau appearance search from a muon neutrino beam using the CNGS (Cern Neutrinos to Gran Sasso) 730km baseline beam.
  - Popular current detectors include: T2K, NOνA.
  - Proposed future detectors include: DUNE, T2HK.
  - Typical baselines are between a few hundred kilometres to over a thousand with energies in the order of magnitude of a few GeV.
  - L/E values will usually be of similar scale to atmospheric oscillations but clearly are more precisely controlled.

1.6.5 Timeline of Neutrino Physics

In Table 1.1 we present a rough timeline of neutrino physics from 1930 to 2019. The timeline is useful for contextualising theories and discoveries because it is easy to forget that not all particles were discovered at once and detector technology in 1960 was *very* different to that of 1990.

TABLE 1.1 Timeline of Neutrino Physics

1930	Neutrinos are postulated by Pauli as the ‘neutron’ as a way to conserve E, p and spin in β decay [82].
1932	Neutron discovered by James Chadwick. Fermi introduces ‘neutrino’ after hearing it (jokingly) from Eduardo Amaldi.
1933	Neutrino name in common use, including by Pauli. Fermi’s theory of β decay implies the interaction: $n^0 \rightarrow p^+ + e^- + \tilde{\nu}^0$ where the $\tilde{\nu}^0$ is not known to be ν_e at this time.
1935	Yukawa postulates that all fundamental interactions revolve around boson exchange and that the boson corresponding to Fermi’s neutrino interaction should be extremely heavy.
1942	Wang Ganchang proposes β capture to detect neutrinos.
1956	Clyde Cowan, Frederick Reines, F. B. Harrison, H. W. Kruse and A. D. McGuire published confirmation that they had seen $\overline{\nu}_e + p^+ \rightarrow n + e^+$ [4].
1957	Pontecorvo publishes early work on $\nu \leftrightarrow \overline{\nu}$ oscillations in analogy to neutral kaon oscillation. Over the next 10 years he develops the modern oscillation formulation.
1962	Leon M. Lederman, Melvin Schwartz and Jack Steinberger show that more than one type of neutrino exists by detecting the hypothesised ‘neutretto’ i.e. ν_μ.
1969	Homestake experiment begins.
1970	First evidence of ‘solar neutrino problem’.
1975	τ lepton observed at SPEAR (originally named Stanford Positron Electron Asymmetric Rings).
1978	Lincoln Wolfenstein publishes early works on neutrino mass effect.
1981	ν_τ directly established with some significance from $\tau \rightarrow \nu$ decays.
1983	Original Kamiokande-I run begins.

1985	Stanislav Mikheyev and Alexei Smirnov refine Wolfenstein's work to create MSW effect.
1988	Leon M. Lederman, Melvin Schwartz, Jack Steinberger win the Nobel Prize in Physics for their work on neutrino beams, lepton doublet structure and hence discovery of ν_μ [83].
1995	Nobel Prize in Physics awarded to Martin L. Perl for discovery of the τ and Frederick Reines for detection of ν's [3].
1996	LSND publishes first controversial evidence for $\sim \mathrm{eV}^2$ scale oscillations.
1998	SNO NC data shows evidence that no solar neutrino deficit exists when all flavours are accounted for, solving the solar neutrino problem.
1998	KamLAND identified $\overline{\nu}_e$ oscillations and MINOS confirmed ν_μ oscillations from reactor and accelerator sources respectively.
2000	DONUT (Direct Observation of the Nu(ν) Tau) directly observes ν_τ via CC interaction.
2002	Nobel Prize in physics for Raymond Davis Jr. and Matoshi Koshiba for detection of astrophysical neutrinos [15].
2005	Super-K publishes evidence confirming the LMA-MSW model for the solar neutrino transformations [32].
2005	Z width analyses started in 1990 (with $2 < N_\nu < 4$) culminate to show $N_\nu = 2.984 \pm 0.008$, leaving no room for more than three light active neutrinos.
2008	OPERA begins operation to directly observe ν_τ in a ν_μ beam.
2010	T2K Begins taking physics data. Aims to observe ν_e in a ν_μ beam [40].
2012	Experiments Daya Bay [54], RENO [55], Double-CHOOZ [56], MINOS [57] and T2K [44] combine to determine that θ_{13} is non-zero.
2014	Full operation of NOνA begins in October.
2015	Nobel Prize in physics goes to Takaaki Kajita for the detection of atmospheric neutrino oscillations at Super-K and Arthur B. McDonald for the solution of the solar neutrino problem at SNO [39].
2018	MiniBooNE collaboration publishes controversial new results indicating preference for an additional large mass splitting at high significance [161].
2019	KATRIN collaboration publishes new improved upper bound on the absolute mass scale for active neutrinos [206].

1.7 Neutrino Mixing Terminology

In the field of neutrino mixing there is a lot of terminology involved and it often can become confusing to separate what terms actually mean. For example, technically neutrino mixing refers specifically to neutrino flavour and mass eigenstates not coinciding i.e. the mass matrix for such particles is non-diagonal. Neutrino oscillations are specific phenomena exhibiting L/E dependence that are a consequence of this mixing as well as the existence of non-zero mass splittings. Often oscillation phenomena will be referred to as mixing, this is relatively harmless due to being somewhat correct, as oscillation is a consequence of physical mixing properties. However sometimes mixing related but non-oscillatory phenomena will be referred to as oscillation. This is incorrect and can lead to confusion due to the specific behaviour that the label 'oscillation' implies. For example the conversions seen in the sun (see Section 2.7). The problem with this conflation is it can lead to confusion on what formalism can be used to explain a given phenomenon and could lead to incorrect equations being applied to try and explain phenomena.

Similarly, when discussion neutrino masses, the terms hierarchy and ordering are used to describe the arrangement of the masses of the eigenstates. Often the term hierarchy is used to describe whether the arrangement is so-called normal (ascending in numerical order) or inverted (where one or more masses are lower than those of lower numbered states) but ordering is the better term to use in this case because it explicitly refers to the ordering of numerical states. Hierarchy is better used to describe the overall mass scale of these states, how they are grouped and if any or all states are quasi-degenerate (approximately equal mass). The conflation of hierarchy and ordering is less problematic and more of a technicality because context is usually very clear and it will rarely introduce any errors (for more details see section 1.9). We will deliberately use these interchangeably later on in section due to some confusing acronyms used in analysis papers. We explain this more thoroughly in section 4.3.

Sometimes models add a 'heavy sterile neutrino' when they should really refer to such a particle as an additional 'predominantly sterile, heavy neutrino mass eigenstate', though this is clearly a mouthful! As with active flavours, a general sterile neutrino with non-zero mixing to all mass eigenstates does not have one mass. Conversely the introduced heavy mass eigenstate will have (usually very small) mixing to the active flavours, thus can't be called truly sterile. As such we should probably keep 'heavy neutrino' and 'sterile neutrino' separate. Similarly we'll often say ‘light sterile neutrino’ when referring to eV scale eigenstates for SBL oscillation. Usually in this case there is less confusion what we mean but the same logic still applies in terms of what the proper terminology should be (‘eV-scale predominantly sterile neutrino mass eigenstate’ doesn’t exactly sound great though). Due to the convenience and brevity of these terms we will inevitably use them out of necessity, hopefully whilst being fully aware of the context and potential ambiguities involved.

So in a similar manner, it’s also worth noting that sterile neutrinos and right-handed neutrinos are often conflated. Again, these shouldn’t be confused because a sterile flavour doesn’t usually correspond explicitly to ν_{eR}, ν_{μ_R} or $\nu_{\tau R}$. Usually we deal with the sterile neutrino in an agnostic sense. For example we can add an additional mass eigenstate to account for short range oscillation anomalies. Other examples might include adding a mostly sterile neutrino as the solution for a specific mass dark matter candidate etc. To ensure that such a particle doesn’t interfere with active neutrino physics we require that this eigenstate has small mixing to the active flavours and must therefore be mostly mixed with something that never interacts in any SM process, hence ‘sterile’. But other than predominantly sterile mixing and some mass we don’t require specific properties of such a particles. Right handed neutrinos are covered briefly in section 1.10 as well as in pedagogical detail in the review [84]. More information on sterile neutrinos (at least the part we are concerned with) is presented in chapter 3 as well as in thorough detail in [85–87].

1.8 Mass and Flavour Eigenstates

Once we are sure that neutrino mixing exists we introduce terminology to deal with specifying all of our individual states. Because we only ‘see’ which flavour a neutrino is when it interacts with a weak charged-current (CC) we decide to refer to neutrino flavours in physics by their weak flavour, so we use “weak eigenstates” and “flavour eigenstates” interchangeably. For the active neutrinos these names come from the corresponding charged lepton present in the CC interaction: e, μ or τ. Note that this is in contrast to down type quarks which are referred to in mass-eigenstate form as d, s, b. When dealing with the interactions of the W boson, weak (“Cabbibo-rotated”) eigenstates for the quarks have to be used and are often depicted as primed i.e. d', s',

b'. This can be seen by comparing the weak doublets of the quarks:

$$\begin{pmatrix} u \\ d' \end{pmatrix}, \quad \begin{pmatrix} c \\ s' \end{pmatrix}, \quad \begin{pmatrix} t \\ b' \end{pmatrix}. \tag{1.50}$$

with the weak doublets of the leptons:

$$\begin{pmatrix} e \\ \nu_e \end{pmatrix}, \quad \begin{pmatrix} \mu \\ \nu_\mu \end{pmatrix}, \quad \begin{pmatrix} \tau \\ \nu_\tau \end{pmatrix}. \tag{1.51}$$

The conversions between mass and weak eigenstates for the down-type quarks are defined as

$$\begin{pmatrix} d' \\ s' \\ b' \end{pmatrix} = \begin{pmatrix} V_{ud} & V_{us} & V_{ub} \\ V_{cd} & V_{cs} & V_{cb} \\ V_{td} & V_{ts} & V_{tb} \end{pmatrix} \begin{pmatrix} d \\ s \\ b \end{pmatrix} \tag{1.52}$$

using the CKM (Cabibbo–Kobayashi–Maskawa) mixing matrix V for quarks and correspondingly or neutrinos

$$\begin{pmatrix} \nu_e \\ \nu_\mu \\ \nu_\tau \end{pmatrix} = \begin{pmatrix} U_{e1} & U_{e2} & U_{e3} \\ U_{\mu 1} & U_{\mu 2} & U_{\mu 3} \\ U_{\tau 1} & U_{\tau 2} & U_{\tau 3} \end{pmatrix} \begin{pmatrix} \nu_1 \\ \nu_2 \\ \nu_3 \end{pmatrix} \tag{1.53}$$

using the PMNS (Pontecorvo–Maki–Nakagawa–Sakata) mixing matrix U. In summary, it can be seen that what we refer to as down type quark flavours are the mass states on the right hand side of equation (1.52) while the what we call neutrinos are the flavour states on the left side of equation (1.53). Both of these matrices are often parametrised in the form

$$V, U = \begin{pmatrix} c_{12}c_{13} & s_{12}c_{13} & s_{13}e^{-i\delta_{13}} \\ -s_{12}c_{23} - c_{12}s_{23}s_{13}e^{i\delta_{13}} & c_{12}c_{23} - s_{12}s_{23}s_{13}e^{i\delta_{13}} & s_{23}c_{13} \\ s_{12}c_{23} - c_{12}s_{23}s_{13}e^{i\delta_{13}} & -c_{12}s_{23} - s_{12}c_{23}s_{13}e^{i\delta_{13}} & c_{23}c_{13} \end{pmatrix} \tag{1.54}$$

where we have abbreviated $\sin\theta_{ij} = s_{ij}$ and $\cos\theta_{ij} = c_{ij}$. Of course, mixing angles θ_{ij} and CP phase δ_{13} are particular to both V and U. The details and derivation of which will be explored later in section 2.1. Another worthwhile comparison is the ‘amount’ of mixing present in these sectors, this can be compared by looking at the size of the elements of V and U and how close to diagonal the matrix is, for example

$$|V_{\alpha\beta}| \approx \begin{pmatrix} 0.974 & 0.225 & 0.004 \\ 0.224 & 0.974 & 0.042 \\ 0.009 & 0.041 & 0.999 \end{pmatrix}, \tag{1.55}$$

which clearly has much larger components on the main diagonal than off-diagonal, while

$$|U_{\alpha\beta}| \approx \begin{pmatrix} 0.820 & 0.552 & 0.150 \\ 0.362 & 0.564 & 0.713 \\ 0.414 & 0.597 & 0.678 \end{pmatrix}, \tag{1.56}$$

on the other hand, has much larger off diagonal components, indicating more significant mixing between neutrino states than quarks. The size of such elements can be evaluated directly from experimental measurements or from fits of mixing parameters. Note that we have rounded the answers to three significant figures and excluded errors for illustrative purposes. The full results on which we have based these examples on can be found in: the PDG [88] for V, and the global fits [89] for U (where we averaged the extremes of the 3σ range of both datasets to find a rough centrepoint for comparison to V).

From the above quark mixing it can be seen that weak and mass eigenstates can be somewhat closely associated, so using a similar name for weak and mass eigenstates makes sense. Another comparison and example of common confusion is that statements about quarks such as “the down quark is the lightest down-type quark in the standard model” can be made with little ambiguity, however similar statements about flavour neutrinos are impossible as no flavour mixes entirely with only one mass state. The mixing in the neutrino case is much greater and in some cases it is not clear which flavour mixes predominantly with each mass eigenstate, not to mention the mass ordering is uncertain. An example of this is the proportion of ν_μ and ν_τ in ν_3 and its mass, as seen later on in figure 1.11. Therefore we can say that a statement such as “the electron neutrino is the lightest neutrino” is vague and incorrect, though “in the normal hierarchy the lightest neutrino eigenstate mixes predominantly with the electron flavour state” is reasonable, albeit long winded and perhaps not useful. Overall the distinction is that when we are referring to any propagating physical particle we are talking about its mass eigenstate(s), so when quoting neutrino particle properties such as mass and charge, we should always be referring to $\nu_1, \nu_2, \cdots$ etc. the reason these statistics are less useful than they are in the cases of other particles is because of the aforementioned high level of mixing and the purely weak nature of neutrino interactions.

To summarise the notation for neutrino flavour eigenstates is quite simple, the neutrino flavour associated with a $W^{\pm}$ CC interaction must correspond to the charged lepton in the same vertex. So for three flavours we have ν_e, ν_μ and ν_τ defined by such CC interactions. If sterile neutrinos exist, then their characteristic is that they do not interact weakly (and as such do not have corresponding charged leptons), because of this they cannot be labelled using corresponding lepton flavours and are usually referred to as the singlet state(s): ν_s, or $\nu_{s_1}, \nu_{s_2}, \cdots, \nu_{s_n}$, in the case of n sterile states.

We now want a robust definition of the mass eigenstate notation to ensure there is no confusion when changing between different orderings or sterile models as up until now we have only considered the trivial normal hierarchy three flavour case. To start with, the neutrino mass eigenstates ν_1 and ν_2 represent respectively the lighter and heavier states in the smaller mass splitting (Δm^2_{21}). The third mass eigenstate ν_3 is defined as either the heaviest or lightest of the first three mass eigenstates, depending respectively on whether the ordering is normal or inverted. Further mass eigenstates are defined in reference to these (being numbered $\nu_4, \nu_5, \cdots, \nu_N$ where $N = 3 + n$ is the total number of neutrino masses), usually being placed heavier than all three though occasionally sitting below ν_3 (ν_1) in an otherwise standard normal (inverted) hierarchy. In section 3.3 we will introduce a common extension of recent interest, where ν_4 exists and is the heaviest mass eigenstate with large mixing to a sterile state ν_s and only small mixings to the active neutrino flavours ν_e, ν_μ and ν_τ. In section 3.4.2 we show as an aside, several different examples of more outlandish hierarchies and orderings to demonstrate how they would affect measurements of mass splittings compared to our standard choice.

1.9 Neutrino Mass Splittings, Ordering and Hierarchy

The mass eigenstates of neutrinos are usually not referred to individually in oscillations. This is due to oscillations being agnostic to the individual neutrino masses and in fact only dependent on the squared-mass splittings defined as

$$\Delta m^2_{ij} \equiv m^2_i - m^2_j \,. \tag{1.57}$$

Which is clearly antisymmetric under the exchange $i \leftrightarrow j$

$$\Delta m^2_{ij} = -\Delta m^2_{ji} \tag{1.58}$$

so if we included all permutations in our analysis we'd merely be over-specifying our parameters. We also clearly enforce $i \neq j$ because trivially $\Delta m^2_{ii} = 0, \forall i$. In the standard 3ν case we use the conventional Δm^2_{21}, Δm^2_{31} and Δm^2_{32} not Δm^2_{12}, Δm^2_{13} and Δm^2_{23} or any other such combination of these six possible pairs of states. Note that these explicit splittings are not defined with any intention of the order or scale of the masses and are not positive definite in general. Unlike the effective splittings or oscillation factors in measured probabilities. Also note that not all of the possible splittings can be expressed independently as the relationship

$$\Delta m^2_{ij} = \Delta m^2_{ik} - \Delta m^2_{kj} \tag{1.59}$$

so we usually choose a few independent splittings to fully specify the oscillation case, then only refer to the non-independent ones when necessary. For example, for three flavours we choose Δm^2_{21} and Δm^2_{31} to be independent and hence $\Delta m^2_{32} = \Delta m^2_{31} - \Delta m^2_{21}$. This implies that the inputs to our equations and simulations will be the former two while the latter is dependent. Note that is it still relatively common that Δm^2_{21} and Δm^2_{32} are used as the independent splittings due to the similar size of Δm^2_{31} and Δm^2_{32}, though it is simple to translate between the two. We could also use Δm^2_{31} and Δm^2_{32} together as our independent pair, but this is a lot less useful because it doesn't give us a straightforward comparison between the 'solar' (small splitting) and 'atmospheric' (large splitting) scales of oscillation.

Once we start grouping the masses into mass splittings, we must develop terminology to discuss different scales and orderings of them more compactly. Recall that we explicitly define the ordering $m_1 < m_2$ as we have the freedom of labelling these in 2ν. From 3ν onwards we need to be much more careful how we label our states, starting with the 2ν convention of a pair of closely spaced states labelled ν_1 and ν_2 with masses in ascending order $m_1 < m_2$. This disallows orderings such as $m_1 < m_3 < m_2$ because either these wouldn't be labelled this way in the first place, or if we did label them this way but have defined $|\Delta m^2_{31}| > |\Delta m^2_{21}|$ then $m_3 \notin (m_1, m_2)$ i.e. m_3 can't fit in that range if we have the splittings sized this way. The 'ordering' refers to the numerical order of the states relative to their increasing mass order. Here normal ordering (NO) implies that the numerical ordering corresponds to the mass ordering so in 3ν we have $m_1 < m_2 < m_3$. Similarly, inverted ordering (IO) implies at least one anomaly in this counting so that at least one state is lighter than another state with a lower numerical label e.g. in 3ν the standard IO considered is $m_3 < m_1 < m_2$. So it can be seen that we'll only ever have one NO for a given number of states but many potential IO cases. Whether these are reasonable to model with depends on the oscillation physics present and the scale of the splittings.

The term 'hierarchy' refers to the overall mass scale of these splittings i.e. how apart they are, whether there are any close pairs, quasidegenerate (roughly equal) pairs or even if the lightest neutrino mass is zero or not. This becomes more important as we extend beyond three flavours because the number of combinations grows dramatically (see 3.4.2). As mentioned when we covered terminology in section 1.7 we often refer to the NO and IO cases for a given hierarchy as normal hierarchy (NH) and inverted hierarchy (IH) respectively. This is somewhat erroneous as the mass scales between splitting should be the same, just the ordering of some states flipped. Remember that for the standard 3ν oscillation case we chose one small independent mass splitting corresponding to the original 2ν parameter Δm^2_{21} and one larger independent mass splitting Δm^2_{31} to match the measured solar deficit and atmospheric oscillations respectively. Now that we have knowledge of mass and flavour eigenstates, mixing, hierarchy and ordering, we can draw a schematic encompassing much of this information. The schematic of this hierarchy with NO and IO is illustrated qualitatively in Fig. 1.11. Here the vertical height of the bars represents absolute scale of the mass eigenstates, the spacing between states represents the splittings and the amount of colour in each bar represents the favour admixture. the IO case is similar but with the large mass splitting flipped and it should be noted that the absolute masses of ν_1 (NO) and ν_3 (IO) are not equal in general so the plots do not necessarily 'zero' at the same height. We are unconcerned with this anyway as oscillations do not care for the absolute masses as long as the neutrinos can propagate coherently and ultrarelativistically.

It should be noted that the change in ordering for set mixings *can* feasibly produce a change in hierarchy, for example in the 3ν case where, for NO we have a light pair ν_1, ν_2 and one heavier state ν_3 while for IO we have one light state ν_3 and a heavy pair ν_1, ν_2. If the absolute mass of the lightest state in NO and IO are assumed to be the same then the overall mass scale (or hierarchy) is skewed higher in IO, hence the sum of masses would be larger. This can potentially affect constraints from cosmology for example. This specific case seems to return us to the problem that ordering and

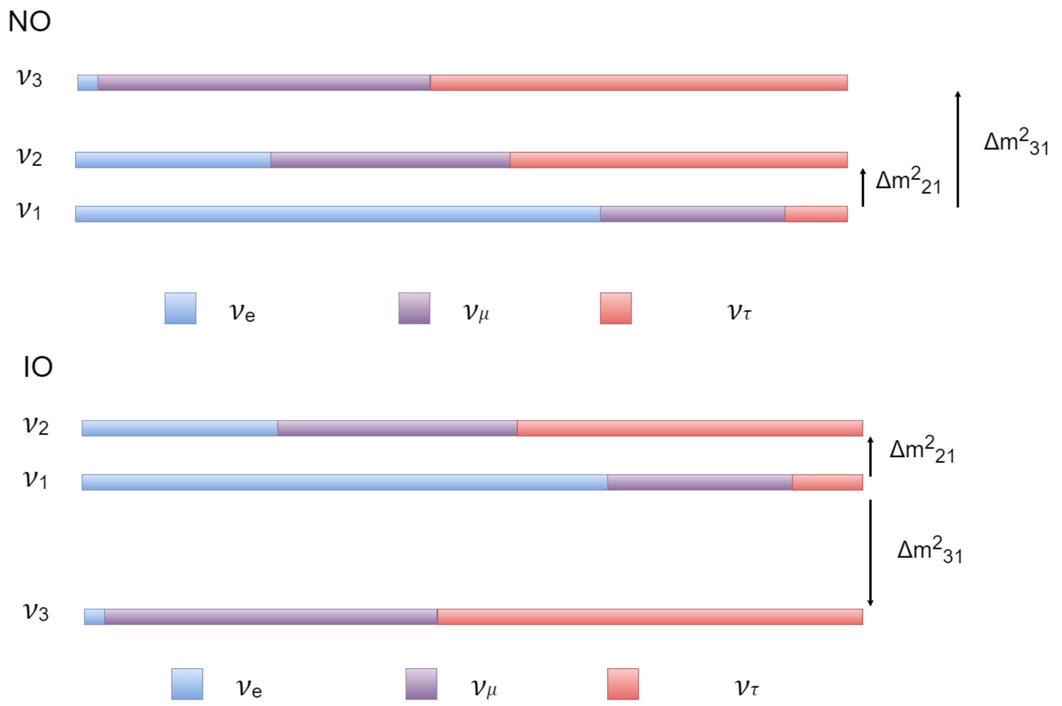

FIG. 1.11 Schematic of mass splittings and flavour content of mass eigenstates in the standard 3ν case with both orderings that fit current physics.

hierarchy terminology seem to coincide. Don't worry, we can show that this is not true. Imagine we have a different specific 3ν case where the lightest IO state $\nu_3^{\rm IO}$ is a lot lighter than the corresponding $\nu_1^{\rm NO}$ in NO (as long as $\nu_1^{\rm NO}$ isn't massless), such that the sum of masses is the same. Now no hierarchy change occurs if we perform an ordering change. Overall, neither of these cases is true in general and there is usually little ambiguity of what is being referred by NO/IO or NH/IH, so in practice these statements are still mostly interchangeable (at least when discussing simple cases).

It should now be clear that there are a potentially infinite number of different 3ν hierarchies which we do not consider due to them not lining up with the physics we observe. Some examples are: the quasidegenerate case where $m_1 \approx m_2 \approx m_3$ which results in no oscillations, the case where the masses of states are evenly spaced out such that $\Delta m^2_{21} \approx \Delta m^2_{32}$ which would have two almost identical small splittings and one large Δm^2_{31} in contrast to the standard case, or even the case where $\Delta m^2_{21} \approx \Delta m^2_{31}, \Delta m^2_{32} \approx 0$ such that there would only be one macroscopic oscillation length observable over distance despite having three masses. The quasidegenerate case also gives us a clear example of terminology being important because in this case the masses are non-hierarchical but can still be ordered in many ways.

1.10 The Standard Model and Neutrino Mass

The standard model (SM) Lagrangian is a single expression that encompasses the majority of physics development in particle physics over the last hundred years. However it still has several known issues i.e. lack of a feasible dark matter candidate to resolve the long standing galaxy rotation curve problem and no mechanism for neutrino mass, and hence nothing to drive oscillations. Technically we have been discussing beyond the standard model (BSM) physics this whole time! We follow the introductory materials from [84] to explain the nomenclature of RH neutrinos and their place in the extended SM.

Lets revise the aspects of Dirac and Majorana fermions and associated mass terms. Firstly we define the four-component spinors $\Phi_L = (\phi_L, 0)^T$ and $\Phi_R = (\phi_R, 0)^T$. We consider sets of LH and RH spinors $\Phi_{L,i}$ and $\Phi_{R,j}$ where the individual fields are 'flavours'. Indices i and j run from 1 to n and m respectively. So n and m are the number of LH and RH flavours respectively. The most general free Lagrangian for fermions is

$$\mathcal{L} = \frac{i}{2}\left(\overline{\Psi_L}\partial\!\!\!/\Psi_L + \overline{\Psi_R}\partial\!\!\!/\Psi_R\right) - \overline{\Psi_L}m_D\Psi_R - \frac{1}{2}\left(\overline{\Psi_L}m_M\Psi_L^c + \overline{\Psi_R}M_M\Psi_R\right) + h.c. \quad (1.60)$$

[84] where flavour indices have been suppressed. It can be seen that the m_D, m_M and M_M terms can be combined into a matrix, which will be the mass matrix $\mathfrak{M}$. The isolated mass term will be

$$\frac{1}{2}\left(\overline{\Psi_L}\,\overline{\Psi_R^c}\right)\mathfrak{M}\begin{pmatrix}\Psi_L^c \\ \Psi_R\end{pmatrix} + h.c. \quad (1.61)$$

Where $\mathfrak{M}$ will be

$$\mathfrak{M} \equiv \begin{pmatrix} m_M & m_D \\ m_D^T & M_M^\dagger \end{pmatrix}. \quad (1.62)$$

The size of $\mathfrak{M}$ will be $(n+m)\times(n+m)$ and the eigenvalues of $\mathfrak{M}\mathfrak{M}^\dagger$ will be the squared physical masses. The m_D term represents the Dirac masses created by the Higgs mechanism, while m_M and M_M are 'Majorana mass terms'. The Dirac nature can also be seen in the fact that if $m_M = 0$ and $M_M = 0$ then the LH and RH fields in the Lagrangian (1.60) can be combined into Dirac spinors $\Psi = \Psi_L + \Psi_R$ to give $\mathcal{L} = \overline{\Psi}(i\partial\!\!\!/ - m_D)\Psi$.

In the case where $m_M \neq 0$ and $M_M \neq 0$ we can instead form Majorana spinors. The simplest case is where $m_D = 0$ i.e. particles are 'entirely Majorana' and the mass submatrices m_M and M_M are diagonal. In this case we will define the Majorana spinors $\chi_i = \Psi_{L,i} + \Psi^c_{L,i}$ and $\Upsilon_j = \Psi_{R,j} + \Psi^c_{R,j}$. Similar to before the Lagrangian can be rewritten to resemble the Dirac equation $\frac{1}{2}(\overline{\chi}(i\partial\!\!\!/ - m_M)\chi + \overline{\Upsilon}(i\partial\!\!\!/ - M_M)\Upsilon)$ but with Majorana conditions $\chi_i = \chi^c_i$ and $\Upsilon_i = \Upsilon^c_i$. This has the clear implication of making these neutral fermions their own antiparticles thus allowing them to annihilate with themselves. It is important to note that outside of the special cases above there is little correlation between non-zero Majorana or Dirac mass terms and the appearance of particles with Majorana or Dirac properties this is further outlined in Appendix B of [84]. Note that charged leptons cannot be Majorana due to electric charge but neutrinos are neutral so have no such restriction.

Now that we have discussed a general SM fermion, let's focus on the neutrinos and charged leptons. Neutrinos are the only particles in the SM that have not been observed with RH chirality. Some theories why are that RH equivalents of LH neutrinos (or LH of RH antineutrinos) simply do not exist or that they interact so weakly with other matter that such observation is impossible. In the standard model neutrinos exist as massless fermions, as feature we now assume to be incorrect, given the oscillation solution of several neutrino problems implies that at least two neutrino mass eigenstates (maybe three) have non-zero mass, while still allowing the lightest of them to be massless. Some possible mass models are discussed in section 3.6.

The left-handed leptons in the SM are arranged into three $SU(2)_L$ doublets

$$\begin{pmatrix} \nu_e \\ e \end{pmatrix}_L , \quad \begin{pmatrix} \nu_\mu \\ \mu \end{pmatrix}_L , \quad \begin{pmatrix} \nu_\tau \\ \tau \end{pmatrix}_L . \tag{1.63}$$

these are the pairs that participate in the W boson vertex. The corresponding right-handed particles (including right handed neutrinos, if they exist) are grouped into singlets which do not feel the weak force due to its handedness. We now will explicitly add n RH fermions to the SM that are singlet under all gauge interactions and couple to the LH neutrinos via Yukawa interactions in the same way RH charged leptons couple to their LH counterparts. These will of course be referred to as the RH neutrinos with the notation $\nu_{R,\alpha}$ or $(\nu_R)_\alpha$ depending on what is more convenient. The labelling index will be a flavour index. This gives the RH lepton content as the singlets (under the SM gauge group)

$$\begin{matrix}(\nu_e)_R \\ (e)_R\end{matrix}, \quad \begin{matrix}(\nu_\mu)_R \\ (\mu)_R\end{matrix}, \quad \begin{matrix}(\nu_\tau)_R \\ (\tau)_R\end{matrix}. \tag{1.64}$$

Where we have used the same flavour indices as the LH case, which may be a bit misleading due to the lack of coupling between the RH charged leptons and neutrinos. This construction leaves the right-handed neutrinos with no SM interaction vertices and as such fits with our observation of only left-handed neutrinos and right-handed antineutrinos. Keep in mind that RH particles can still have interactions in general, for example right-handed quarks in QCD interact no-differently to left-handed quarks. This is of course because QCD is insensitive to chirality while the weak force is and directly violates parity symmetry. Once such particles are introduced we can write a minimal extension to the SM Lagrangian, the νMSM (Neutrino Minimal Standard Model), where the only additional fields are the ν_R ones [84]

$$\mathcal{L}_{\nu MSM} = \mathcal{L}_{SM} + i\overline{\nu_R}\not{\partial}\nu_R - \overline{l_L}F\nu_R\tilde{\Phi} - \overline{\nu_R}F^\dagger l_L\tilde{\Phi}^\dagger - \frac{1}{2}\left(\overline{\nu_R^c}M_M\nu_R + \overline{\nu_R}M_M^\dagger\nu_R^c\right). \tag{1.65}$$

Where we have again suppressed flavour and isospin indices and $\mathcal{L}_{SM}$ is the standard model Lagrangian. F is a matrix of Yukawa couplings and M_M are Majorana masses of the RH neutrinos as seen before in the generic fermion Lagrangian (1.60). $l_L = (\nu_L, l_L)^T$ are the SM LH lepton doublets, and we have defined $\tilde{\Phi} = (\epsilon\Phi)^\dagger$, where ϵ is the $SU(2)$ antisymmetric tensor and Φ is the Higgs doublet. $\nu_R^c = C\overline{\nu_R}^T$, where the charge conjugation matrix is $C = i\gamma_2\gamma_0$ (in the Weyl representation).

We go no further with neutrino masses in this section but it is of supreme interest to find out if the Yukawa couplings in F, Majorana masses M_M or even something stranger are responsible for the physical neutrino masses. More possible ideas are covered in section 3.6.

1.11 CP Violation in the SM

What follows is a short proof of how complex phases from the PMNS (or CKM) matrix (see section 2.1) can lead to CP (Charge-Parity) violation in the SM, hence are known commonly as ‘CP violating phases’.

Define a process, e.g. neutrino oscillation between two flavours $\nu_\alpha \to \nu_\beta$, and a corresponding antiparticle process $\bar{\nu}_\alpha \to \bar{\nu}_\beta$ with amplitudes M and $\bar{M}$ respectively.

If a phase term is introduced (from the PMNS matrix for example,) it can be pulled out of its corresponding amplitude to give

$$M = Ae^{i\delta} \tag{1.66}$$

for some A. Now if $\bar{M}$ corresponds to antiparticles then it involves the conjugate phase term, so we have

$$\bar{M} = \bar{A}e^{-i\delta}\,, \tag{1.67}$$

again, with some $\bar{A}$. But without CP violation i.e. if $\delta = 0^\circ, 180^\circ$, the particle and antiparticle processes must have the same probability. Hence in the CP conserving case $M_{\text{cons}} = A$, $\bar{M}_{\text{cons}} = \bar{A}$ and $M_{\text{cons}} = \bar{M}_{\text{cons}}$ which implies that $A = \bar{A}$. We can further split these A terms into phases and amplitudes, writing $A = |A|e^{i\theta}$. Hence after all this we can rewrite both of the amplitudes

$$M = |A|e^{i\theta}e^{i\delta}\,, \tag{1.68}$$

$$\bar{M} = |A|e^{i\theta}e^{-i\delta}\,. \tag{1.69}$$

It should be noted that the δ phase changes sign between the process and antiprocess while the θ doesn't. So δ parametrises the CP behaviour of the process while θ just represents the phase angle of the complex number A. Even more importantly, any measurement of a process of this form will depend on the absolute magnitude squared of these amplitudes, this means that the phase will disappear regardless of δ. Hence CP violation cannot be seen in a process with such a simple form.

Now we can consider the same oscillation process as before but allow for the possibility that there are multiple paths e.g. $\nu_\alpha \xrightarrow{1} \nu_\beta$ and $\nu_\alpha \xrightarrow{2} \nu_\beta$ by which the process can occur. In our oscillation example these paths correspond to two possible intermediate mass eigenstates ν_1 and ν_2. We can write out the total amplitude as a superposition of the amplitudes corresponding to each of the two paths:

$$M = |A_1|e^{i\theta_1}e^{i\delta_1} + |A_2|e^{i\theta_2}e^{i\delta_2}\,, \tag{1.70}$$

$$\bar{M} = |A_1|e^{i\theta_1}e^{-i\delta_1} + |A_2|e^{i\theta_2}e^{-i\delta_2}\,, \tag{1.71}$$

with the subscripts corresponding to each path. Multiplying M and $\bar{M}$ with $e^{-i\delta_1}$ and $e^{i\delta_1}$ respectively gives

$$Me^{-i\delta_1} = |A_1|e^{i\theta_1} + |A_2|e^{i\theta_2}e^{i(\delta_2-\delta_1)}\,, \tag{1.72}$$

$$\bar{M}e^{i\delta_1} = |A_1|e^{i\theta_1} + |A_2|e^{i\theta_2}e^{-i(\delta_2-\delta_1)}\,. \tag{1.73}$$

Note that in general we can absorb one phase into a redefinition of the quantum state (further explained in 2.1). Because of this phase ambiguity we can ignore the phases on the LHS because $|M| = |Me^{i\phi}|,\ \forall\phi$. We then redefine $\delta_2 - \delta_1 \equiv \delta$ to simplify these amplitudes to

$$M = |A_1|e^{i\theta_1} + |A_2|e^{i\theta_2}e^{i\delta}\,, \tag{1.74}$$

$$\bar{M} = |A_1|e^{i\theta_1} + |A_2|e^{i\theta_2}e^{-i\delta}\,. \tag{1.75}$$

We can calculate the probabilities where $P = |M|^2$ and $\bar{P} = |\bar{M}|^2$. Firstly for the neutrino process

$$\begin{aligned} P &= |M|^2 \\ &= MM^* \\ &= \left(|A_1|e^{i\theta_1} + |A_2|e^{i\theta_2}e^{i\delta}\right)\left(|A_1|e^{-i\theta_1} + |A_2|e^{-i\theta_2}e^{-i\delta}\right) \\ &= |A_1|^2 + |A_2|^2 + |A_1||A_2|\left(e^{i(\theta_1-\theta_2)}e^{-i\delta} + e^{-i(\theta_1-\theta_2)}e^{i\delta}\right)\,, \end{aligned} \tag{1.76}$$

and similarly for the antineutrino case,

$$\begin{aligned} \bar{P} &= |\bar{M}|^2 \\ &= \bar{M}\bar{M}^* \\ &= \left(|A_1|e^{i\theta_1} + |A_2|e^{i\theta_2}e^{-i\delta}\right)\left(|A_1|e^{-i\theta_1} + |A_2|e^{-i\theta_2}e^{i\delta}\right) \\ &= |A_1|^2 + |A_2|^2 + |A_1||A_2|\left(e^{i(\theta_1-\theta_2)}e^{i\delta} + e^{-i(\theta_1-\theta_2)}e^{-i\delta}\right)\,. \end{aligned} \tag{1.77}$$

From here we can compare the probabilities of process M to $\bar{M}$ by taking the difference between them $P - \bar{P}$.

$$P - \bar{P} = |A_1||A_2|\left(e^{i(\theta_1-\theta_2)}e^{-i\delta} + e^{-i(\theta_1-\theta_2)}e^{i\delta} - e^{i(\theta_1-\theta_2)}e^{i\delta} - e^{-i(\theta_1-\theta_2)}e^{-i\delta}\right)\,. \tag{1.78}$$

We can group the terms in this equation by $e^{-i\delta}$ and $-e^{i\delta}$ to get

$$P - \bar{P} = |A_1||A_2| \left(\left[e^{i(\theta_1-\theta_2)} - e^{-i(\theta_1-\theta_2)} \right] e^{-i\delta} - \left[e^{i(\theta_1-\theta_2)} - e^{-i(\theta_1-\theta_2)} \right] e^{i\delta} \right) . \tag{1.79}$$

Now note that from Euler's formula $\sin\phi = (e^{i\phi} - e^{-i\phi})/2i \implies e^{i\phi} - e^{-i\phi} = 2i\sin\phi$. Hence $e^{i(\theta_1-\theta_2)} - e^{-i(\theta_1-\theta_2)} = 2i\sin(\theta_1 - \theta_2)$. Which allows us to rearrange the square bracketed exponential terms in the equation (1.79) to give

$$\begin{aligned} P - \bar{P} &= |A_1||A_2| \left(2i\sin(\theta_1-\theta_2)e^{-i\delta} - 2i\sin(\theta_1-\theta_2)e^{i\delta} \right) \\ &= |A_1||A_2| 2i\sin(\theta_1-\theta_2) \left(e^{-i\delta} - e^{i\delta} \right) \\ &= |A_1||A_2| 2i\sin(\theta_1-\theta_2) \left(-2i\sin\delta \right) , \end{aligned} \tag{1.80}$$

so we finally have

$$P - \bar{P} = 4|A_1||A_2| \sin(\theta_1-\theta_2)\sin\delta \, . \tag{1.81}$$

Thus it is demonstrated by this example that in the case of a process with multiple paths, such CP-breaking phases can cause an asymmetry between particle and antiparticle effects hence indirect CP-breaking.

To see a real example of a CP sensitive observable we can look at a term known as the 'Jarlskog Invariant' after Cecilia Jarlskog [90]. This term can be defined for both quarks and leptons. It is a parametrisation-invariant measure of the 'amount' of CP-violation measured in the mixing of such particles. We can define

$$J_{CP}^{\text{leptons}} \equiv \Im \left[U_{\alpha i} U_{\beta j} U^*_{\alpha j} U^*_{\beta i} \right] , \tag{1.82}$$

$$J_{CP}^{\text{quarks}} \equiv \Im \left[V_{us} V_{cb} V^*_{ub} V^*_{cs} \right] . \tag{1.83}$$

It's clear from this that $J = 0$ would indicate CP conservation, while $J \neq 0$ indicates CP violation. In both sectors these invariants are related to their maximum values and the CP phases present in their respective matrix elements by

$$J \equiv J^{(\text{max})} \sin\delta_{CP} \, . \tag{1.84}$$

The maximal possible value (i.e. if CP phases are maximally violating), can be calculated from the relatively well known mixing parameters from recent best fits in [89] to be

$$J_{CP}^{\text{lepton(max)}} = 0.333 \pm 0.0006 \, . \tag{1.85}$$

The best fit for δ_{13} from the same source gives the leptonic Jarlskog invariant best fit central value of

$$J_{CP}^{\text{leptons}} = -0.019\,, \tag{1.86}$$

which can be compared with the quark equivalent from the 2018 PDG review [91]

$$J_{CP}^{\text{quarks}} = (3.18 \pm 0.15) \times 10^{-5}\,. \tag{1.87}$$

So it can be seen that the 'size' of CP violation in the lepton sector, if phases are close to maximal, is roughly three orders of magnitude larger than in the quark sector. Even with the current non-maximal best fit for δ_{13}, J_{CP}^{leptons} is still around 600 times larger than J_{CP}^{quarks}. However the current significance of this is still low, and will be explored thoroughly in the next few years.

CHAPTER 2

NEUTRINO OSCILLATION BASICS

In this section we aim to introduce the parametrisation of oscillation cases, the two flavour approximation and derivate the general oscillation probability. Once we have the framework we also present several examples of specific cases to highlight some key features and methods used in deriving such expressions.

2.1 Oscillation Parametrisation

In all cases we must at some point define the PMNS matrix, as defined by Ziro Maki, Masami Nakagawa and Shoichi Sakata to explain Bruno Pontecorvo's neutrino mixing theories. This matrix is often referred to as the 'neutrino mixing matrix' or more correctly the 'leptonic mixing matrix' and is analogous to the CKM matrix in the quark sector. We saw a brief preview of this in section 1.8 when we introduced the idea of separate mass and flavour eigenstates. We will eventually derive the matrix we stated without proof in equation (1.54).

So from our statements in section 1.8 and the equation (1.53) we know that the PMNS matrix $n \times n$ matrix where n is the number of eigenstates and it relates mass to flavour. We write the equivalent version of equation (1.53) for n flavours in index form as

$$|\nu_\alpha\rangle = \sum_{i=0}^{n} U_{\alpha i} |\nu_i\rangle \tag{2.1}$$

where the flavour indices are $\alpha = e, \mu, \tau, \cdots, \alpha_n$ and the mass indices $i = 1, 2, 3, \cdots, n$. Where l_n is just some n^{th} neutrino flavour. Note that occasionally this is defined without the complex conjugate. This just puts the conjugate on the inverse terms and doesn't really change much except flip any potential CP phases. As long as one is self consistent this is just a matter of convention. Because the relation in equation (2.1) corresponds to a change in basis we can perform n rotations to transform between our n flavour and mass eigenstates. This implies that we can construct the mixing matrix out of n individual 2×2 rotation matrices each corresponding to one axis rotation. We embed these rotations in $n \times n$ identity matrices to get the correct form and multiply them in a specific order that we keep track of. These rotation matrices are defined as

$$R(\theta_{ij}, \delta_{ij}) = \begin{pmatrix} 1 & \cdots & 0 & \cdots & 0 & \cdots & 0 \\ \vdots & & \vdots & & \vdots & & \vdots \\ 0 & \cdots & c_{ij} & \cdots & s_{ij}e^{i\delta_{ij}} & \cdots & 0 \\ \vdots & & \vdots & & \vdots & & \vdots \\ 0 & \cdots & -s_{ij}e^{i\delta_{ij}} & \cdots & c_{ij} & \cdots & 0 \\ \vdots & & \vdots & & \vdots & & \vdots \\ 0 & \cdots & 0 & \cdots & 0 & \cdots & 1 \end{pmatrix} \tag{2.2}$$

with the sine and cosine abbreviations

$$c_{ij} = \cos\theta_{ij},\ s_{ij} = \sin\theta_{ij}\,. \tag{2.3}$$

For the rotation matrices with no CP phase we define the shorthand

$$R(\theta_{ij}) = R(\theta_{ij}, 0)\,. \tag{2.4}$$

Note that we can alternatively define $R(\theta_{ij}, \delta_{ij})$ elementwise as

$$[R(\theta_{ij}, \delta_{ij})]_{ab} = \hat{\delta}_{ab} + (c_{ij} - 1)(\hat{\delta}_{ai}\hat{\delta}_{bi} + \hat{\delta}_{aj}\hat{\delta}_{bj}) + s_{ij}(e^{-i\delta_{ij}}\hat{\delta}_{ai}\hat{\delta}_{bj} - e^{i\delta_{ij}}\hat{\delta}_{aj}\hat{\delta}_{bi})\,, \tag{2.5}$$

where $\hat{\delta}_{ij}$ is the Kronecker Delta Function notated as $\hat{\delta}$

$$\hat{\delta}_{ij} = \begin{cases} 1 & \text{if} \quad i = j \\ 0 & \text{if} \quad i \neq j \end{cases} \tag{2.6}$$

to explicitly differentiate it from CP phases δ_{ij} in the exponential terms.

We will write the generic $n \times n$ PMNS matrix as the product of R matrices

$$U = \prod_{j>i}^{n} R(\theta_{ij}, \delta_{ij})\,, \tag{2.7}$$

where the order of these rotations and placement of the δ terms varies between different parametrisations. Without loss of generality we can choose all mixing angles to be in the first quadrant i.e. between $0°$ and $90°$ while the CP phases can be in the full $0°$ to $360°$ range. This is fine because the angles themselves are unphysical and therefore never measurable directly, only levels of mixing between 0 and 1 need to be allowed. Such angles can be interpreted as geometric Euler angles relating to the positions of the flavour states in the mass state basis or vice-versa. The former can be seen graphically in Fig. 2.1.

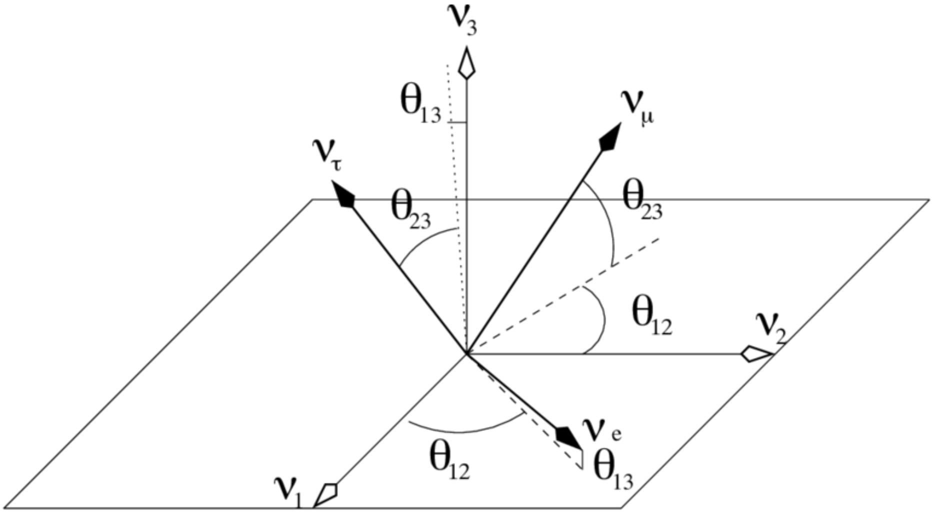

FIG. 2.1 Euler angle representation of neutrino mixing angles showing the relationship between flavour and mass eigenstates, in this case arranged to see flavour states in the mass basis. Taken from Stephen F. King. 2015 [92].

As briefly mentioned in section 1.8, the CKM and PMNS matrices can and often are parametrised the same way, albeit with differing mixing angles. In fact, the size of the smallest leptonic mixing angle is roughly of the same order as the largest quark mixing angle. This would imply that a similar diagram to Fig. 2.1 but for mass and flavour mixing of quarks (see equations (1.50), (1.52) and (1.55)) would feature very small deviation between the massive d, s, b states and flavoured d', s', b' axes respectively.

2.1.1 Parametrisation of a Unitary Mixing Matrix

To understand how many free parameters we need to fully parametrise this we start with a general $n \times n$ complex matrix U. Each element of a complex matrix is a complex number and hence can be parametrised by 2 real numbers, therefore since we have $n \times n = n^2$ matrix elements, we need $2n^2$ real numbers to fully parametrise U. But we have the unitarity property

$$U^\dagger U = UU^\dagger = \mathbb{I} \tag{2.8}$$

for our $n \times n$ unitary matrix U. We can express this in index form as

$$\sum_{k=1}^{n} U_{ik} U_{kj}^\dagger = \sum_{k=1}^{n} U_{ik} U_{jk}^* = \delta_{ij} \,. \tag{2.9}$$

So for the $i = j$ components we have the simplified equation

$$\sum_{k=1}^{n} U_{ik} U_{ik}^* = \sum_{k=1}^{n} |U_{ik}|^2 = 1 \,, \tag{2.10}$$

which implies n constraints corresponding to the diagonal of $U^\dagger U$. Similarly, for $i \neq j$ we have

$$\sum_{k=1}^{n} U_{ik} U_{jk}^* = 0 \,, \tag{2.11}$$

which will have C_2^n possible equations from this, where C_k^n is the binomial coefficient

$$C_k^n = \frac{n!}{k!(n-k)!} \,. \tag{2.12}$$

So the number of equations we have is

$$\begin{aligned} C_2^n &= \frac{n!}{2!(n-2)!} \\ &= \frac{n(n-1)(n-2)!}{2(n-2)!} \\ &= \frac{n(n-1)}{2} \,. \end{aligned} \tag{2.13}$$

This will also be the number of associated complex constraints, twice of which gives the number of real constraints, which is $2C_2^n = n(n-1)$. This is due to the two real degrees of freedom of a complex number. So equation (2.9) imposes $n + n(n-1)$ constraints overall, which evaluates to give a total of n^2. This reduces the minimum necessary number of real parameters to specify U from $2n^2$ to n^2. It is important to note that we will be multiplying this matrix with quantum mechanical states when relating flavour and mass via $|\nu_\alpha\rangle = \sum_i U_{\alpha i}^* |\nu_i\rangle$, we can now take advantage of the fact that to further reduce the available degrees of freedom. We know that global phase shifts in quantum states, such as

$$|\psi\rangle \longrightarrow e^{i\phi}|\psi\rangle \tag{2.14}$$

are unphysical, so can be discarded. Each mass and flavour state can be written multiplied by a phase pulled from the matrix U, this can be done to all n mass and n flavour states for a total of $2n$. The form of this can be expressed via the transform

$$|\nu_\alpha\rangle = \sum_i U^*_{\alpha i}|\nu_i\rangle \longrightarrow e^{i\phi_\alpha}|\nu_\alpha\rangle = \sum_i U^*_{\alpha i}e^{i\phi_i}|\nu_i\rangle\,. \tag{2.15}$$

We can rearrange the transformed state to

$$\begin{aligned}|\nu_\alpha\rangle &= \sum_i U^*_{\alpha i}e^{-i\phi_\alpha}e^{i\phi_i}|\nu_i\rangle \\ &= \sum_i U^*_{\alpha i}e^{-i(\phi_\alpha-\phi_i)}|\nu_i\rangle \\ &= \sum_i U^*_{\alpha i}e^{-i\Delta\phi_{\alpha i}}|\nu_i\rangle\,,\end{aligned} \tag{2.16}$$

where we have defined $\phi_\alpha - \phi_i \equiv \Delta\phi_{\alpha i}$. In matrix form for $n = 3$ the relationship between mass and flavour eigenstates looks like

$$\begin{pmatrix}\nu_e\\ \nu_\mu\\ \nu_\tau\end{pmatrix} = \begin{pmatrix}U^*_{e1} & U^*_{e2} & U^*_{e3}\\ U^*_{\mu 1} & U^*_{\mu 2} & U^*_{\mu 3}\\ U^*_{\tau 1} & U^*_{\tau 2} & U^*_{\tau 3}\end{pmatrix}\begin{pmatrix}\nu_1\\ \nu_2\\ \nu_3\end{pmatrix}\,. \tag{2.17}$$

As before with equation (2.15), we can re-write our generic matrix elements by pulling out specific phase factors with the exact form we want, this gives

$$\begin{pmatrix}\nu_e\\ \nu_\mu\\ \nu_\tau\end{pmatrix} = \begin{pmatrix}U^*_{e1}e^{-i\Delta\phi_{e1}} & U^*_{e2}e^{-i\Delta\phi_{e2}} & U^*_{e3}e^{-i\Delta\phi_{e3}}\\ U^*_{\mu 1}e^{-i\Delta\phi_{\mu 1}} & U^*_{\mu 2}e^{-i\Delta\phi_{\mu 2}} & U^*_{\mu 3}e^{-i\Delta\phi_{\mu 3}}\\ U^*_{\tau 1}e^{-i\Delta\phi_{\tau 1}} & U^*_{\tau 2}e^{-i\Delta\phi_{\tau 2}} & U^*_{\tau 3}e^{-i\Delta\phi_{\tau 3}}\end{pmatrix}\begin{pmatrix}\nu_1\\ \nu_2\\ \nu_3\end{pmatrix} \tag{2.18}$$

which can be re-written

$$\begin{pmatrix}\nu_e\\ \nu_\mu\\ \nu_\tau\end{pmatrix} = \begin{pmatrix}e^{-i\phi_e} & & \\ & e^{-i\phi_\mu} & \\ & & e^{-i\phi_\tau}\end{pmatrix}\begin{pmatrix}U^*_{e1} & U^*_{e2} & U^*_{e3}\\ U^*_{\mu 1} & U^*_{\mu 2} & U^*_{\mu 3}\\ U^*_{\tau 1} & U^*_{\tau 2} & U^*_{\tau 3}\end{pmatrix}\begin{pmatrix}e^{i\phi_1} & & \\ & e^{i\phi_2} & \\ & & e^{i\phi_3}\end{pmatrix}\begin{pmatrix}\nu_1\\ \nu_2\\ \nu_3\end{pmatrix}. \tag{2.19}$$

Now taking the flavour phase factors to the other side

$$\begin{pmatrix}\nu_e\\ \nu_\mu\\ \nu_\tau\end{pmatrix}\begin{pmatrix}e^{i\phi_e} & & \\ & e^{i\phi_\mu} & \\ & & e^{i\phi_\tau}\end{pmatrix} = \begin{pmatrix}e^{i\phi_1} & & \\ & e^{i\phi_2} & \\ & & e^{i\phi_3}\end{pmatrix}\begin{pmatrix}U^*_{e1} & U^*_{e2} & U^*_{e3}\\ U^*_{\mu 1} & U^*_{\mu 2} & U^*_{\mu 3}\\ U^*_{\tau 1} & U^*_{\tau 2} & U^*_{\tau 3}\end{pmatrix}\begin{pmatrix}\nu_1\\ \nu_2\\ \nu_3\end{pmatrix}. \tag{2.20}$$

Note, however that we can multiply both sides of this equation by $e^{-i\phi_e}$ and define new phases $\phi'_x \equiv \phi_x - \phi_e$ to get

$$\begin{pmatrix}\nu_e\\ \nu_\mu\\ \nu_\tau\end{pmatrix}\begin{pmatrix}1 & & \\ & e^{i\phi'_\mu} & \\ & & e^{i\phi'_\tau}\end{pmatrix} = \begin{pmatrix}e^{i\phi'_1} & & \\ & e^{i\phi'_2} & \\ & & e^{i\phi'_3}\end{pmatrix}\begin{pmatrix}U^*_{e1} & U^*_{e2} & U^*_{e3}\\ U^*_{\mu 1} & U^*_{\mu 2} & U^*_{\mu 3}\\ U^*_{\tau 1} & U^*_{\tau 2} & U^*_{\tau 3}\end{pmatrix}\begin{pmatrix}\nu_1\\ \nu_2\\ \nu_3\end{pmatrix}. \tag{2.21}$$

which reduces the number of phases we can remove to $2n-1$. It is clear if we decide to divide again by another phase term, say $e^{i\phi'_\mu}$, that while the ν_μ phase term will become $e^0 = 1$, the ν_e phase term will be $e^{-i\phi'_\mu}$, hence we will still have $2n-1$ phases to absorb. So it can be surmised that this can always be done to one phase for all possible n. We can then absorb these phases

$$\begin{pmatrix}1 & & \\ & e^{i\phi'_\mu} & \\ & & e^{i\phi'_\tau}\end{pmatrix}\begin{pmatrix}\nu_e\\ \nu_\mu\\ \nu_\tau\end{pmatrix} = \begin{pmatrix}\nu_e e^{i\phi'_e}\\ \nu_\mu e^{i\phi'_\mu}\\ \nu_\tau e^{i\phi'_\tau}\end{pmatrix} \longrightarrow \begin{pmatrix}\nu_e\\ \nu_\mu\\ \nu_\tau\end{pmatrix} \tag{2.22}$$

for the flavour states and similarly

$$\begin{pmatrix}e^{i\phi'_1} & & \\ & e^{i\phi'_2} & \\ & & e^{i\phi'_3}\end{pmatrix}\begin{pmatrix}\nu_1\\ \nu_2\\ \nu_3\end{pmatrix} = \begin{pmatrix}\nu_1 e^{i\phi'_1}\\ \nu_2 e^{i\phi'_2}\\ \nu_3 e^{i\phi'_3}\end{pmatrix} \longrightarrow \begin{pmatrix}\nu_1\\ \nu_2\\ \nu_3\end{pmatrix} \tag{2.23}$$

for the mass eigenstates. So performing this reverse process illustrates how we can absorb these $2n-1$ degrees of freedom. It is important to note however that we are not removing all of the complexity from each element. We are simply removing some possible phase factors that exist in such a matrix and thus degrees of freedom, each $U^*_{\alpha i}$ element remains complex in general. Each of these phases can then be absorbed into a redefinition of its corresponding state, as with equation (2.14). This implies that we can absorb degrees of freedom from U into state re-definitions without changing the physics. So in summary, we can only remove $2n-1$ degrees of freedom with these phase ambiguities because we can always have one overall phase which cannot be constrained away. The number of necessary real parameters is now reduced to $n^2-(2n-1)=n^2-2n+1=(n-1)^2$.

We wish to know how many of the remaining free parameters correspond to the real and imaginary parts of U individually. This will allow us to know how many CP affecting terms we will have. Because $\Re\left\{U\right\}^\dagger = \Re\left\{U\right\}^T$, the real component of U will be an $n \times n$ orthogonal matrix, which we define as

$$O \equiv \Re\left\{U\right\} \,. \tag{2.24}$$

The minimal number of parameters in the real part of U is equivalent to the number of real parameters required to parametrise O which is $n(n-1)/2$. To get this number we wish to narrow down the total n^2 real elements in O to get its remaining degrees of freedom the same way we have been proceeding for U so far. We start with the the property of orthogonal matrices

$$O^T O = O O^T = \mathbb{I}\,, \tag{2.25}$$

which can written

$$O_{ij}O_{ji} = O_{ji}O_{ij} = \delta_{ij}\,, \tag{2.26}$$

so we have the diagonal constraints from

$$O^2_{ii} = 1 \tag{2.27}$$

and the off-diagonal constraints from

$$O_{ji}O_{ij} = 0, \text{ for } i \neq j. \tag{2.28}$$

So this gives n constraints along the diagonal leaving n^2-n potential off-diagonal constraints. These are double counted due to $i \leftrightarrow j$ symmetry as the orthogonal properties tell us $O_{ij}O_{ji} = O_{ji}O_{ij}$. Therefore we have $(n^2-n)/2$ actual constraints from the off diagonal parts of the equation. This gives the total number of constraints as $n+(n^2-n)/2 = n(n+1)/2$. Finally we subtract this number from the total number of elements to give the degrees of freedom as $n^2 - n(n+1)/2 = n(n-1)/2$, this is the number of parameters needed to fully specify O. To check that this number makes sense we can think of n neutrino masses, between each pair of which we have a mixing, therefore again we have C_2^n separate mixings between two flavours, i.e. $n(n-1)/2$. This makes sense because if all CP phases are zero then the PMNS matrix is real, hence orthogonal and is parametrised purely with mixing angles e.g. for $n = 3$ and no CP violation the number of parameters is 3 i.e. the three mixing angles.

We can now return to the complex matrix U. From the analysis of O we can say that clearly the parameters for the real part of U will be the mixing angles. We can subtract the number of these from the total number of parameters for U to find the number needed to parametrise the imaginary part. This is equal to $(n-1)^2 - n(n-1)/2 = (n-1)(n-2)/2$. By inspection these are what we will eventually call the Dirac phases.

The other parameters we are interested in for oscillations are the independent mass splittings, though these obviously do not come in until the probability is evaluated. Clearly because these are the *differences* between the squared values not the individual masses, we therefore have one less than we have total mass eigenstates i.e. $n-1$.

We can now summarise the formulae for the number of angles, mass differences and phases to parametrise a specific oscillation case:

$$\begin{aligned} N_{\Delta \mathrm{m}^2} &= n-1 \\ N^{\mathrm{total}}_{\mathrm{params}} &= (n-1)^2 \\ N_{\mathrm{angles}} &= \frac{n(n-1)}{2} \\ N^{\mathrm{Dirac}}_{\mathrm{phases}} &= \frac{(n-1)(n-2)}{2} \end{aligned} \tag{2.29}$$

We can also in general add an additional phase for each mass splitting. We will call these 'Majorana phases' because they come into the physics of neutrinos of Majorana nature (see section 3.6.2). These phases are added by multiplying U by a matrix of the form $P_{\mathrm{Maj}} = \mathrm{diag}\,\{1, e^{i\alpha_1}, e^{i\alpha_2}, \cdots, e^{i\alpha_{n-1}}\}$

$$N^{\mathrm{Maj}}_{\mathrm{phases}} = n-1 \tag{2.30}$$

$$N_{\text{phases}}^{\text{total}} = \frac{n(n-1)}{2}$$

however, note that only the Dirac phases are important in oscillation. Majorana phases are important for physics such as neutrinoless double beta decay (see section 3.7), but do not affect oscillations because of the way that matrix elements enter oscillation probabilities.

2.1.2 Parameter conventions

To be consistent with our parameters once we have multiple of each type, we define the index conventions for angles, phases and mass-squared differences to be:

$$\theta \to \theta_{ij} \tag{2.31}$$

$$\delta_{\text{CP}} \to \delta_{ij} \tag{2.32}$$

$$\Delta m^2 \to \Delta m^2_{ji} = m^2_j - m^2_i \tag{2.33}$$

where we always number such that $i < j$.

2.2 Example Parametrisations

We can now specify some example parametrisations and resulting PMNS matrix elements for various numbers of neutrinos. The two flavour case is almost trivial, with only one mixing matrix and no CP phase, this changes hugely when we go from two to three flavours. The complexity of the PMNS matrices in three and four flavours are such that to write the matrix elements out fully we must list them. If we were to put them in matrix form we will struggle to fit these on a page. The parametrisations we derive here will be used extensively throughout the rest of the thesis.

2.2.1 Two Flavour Parametrisation

The two flavour formalism is the earliest formalism for oscillation, because it is the minimal necessary to explain appearance/disappearance phenomenon with L/E dependence. This case relies only on two states having some non-zero mixing and mass splitting. Despite knowing that at least one more mass and flavour exist in nature, we will see later in section 2.3 that the two flavour framework can be applied in many cases to check proof of concept and to simplify analyses. Using the previous formalism we defined in section 2.1 and the generic rotation matrix from equation (2.2), the (somewhat trivial) two flavour mixing matrix

$$U = R(\theta_{12})\,. \tag{2.34}$$

Which contains 1 mixing angle and 0 Dirac phases. Clearly:

$$U = \begin{pmatrix} U_{e1} & U_{e2} \\ U_{\mu 1} & U_{\mu 2} \end{pmatrix} = \begin{pmatrix} \cos\theta_{12} & \sin\theta_{12} \\ -\sin\theta_{12} & \cos\theta_{12} \end{pmatrix} . \tag{2.35}$$

2.2.2 Three Flavour Parametrisation

We now have the tools to express the standard three flavour case in our oscillation language. Our choice of parametrisation is fairly standard, though some variation exists, for example the placement of the CP-phase. Obviously the physics cannot change between different parametrisations measuring the same phenomena, some care just needs to be maintained when comparing results. We again use the formalism from section 2.1 and equation (2.2) but this time the a CP phase must be included as $N^{\mathrm{Dirac}}_{\mathrm{phases}} = 1$ for $n = 3$. The parametrisation defined by

$$U = R(\theta_{23}) R(\theta_{13}, \delta_{13}) R(\theta_{12}) \equiv U_{3\nu} \tag{2.36}$$

gives the mixing matrix

$$U = \begin{pmatrix} U_{e1} & U_{e2} & U_{e3} \\ U_{\mu 1} & U_{\mu 2} & U_{\mu 3} \\ U_{\tau 1} & U_{\tau 2} & U_{\tau 3} \end{pmatrix} \tag{2.37}$$

with elements:

$$\begin{aligned} U_{e1} &= \cos\theta_{12}\cos\theta_{13}\,, \\ U_{\mu 1} &= -\cos\theta_{23}\sin\theta_{12} - \cos\theta_{12}\sin\theta_{13}\sin\theta_{23}e^{i\delta_{13}}\,, \\ U_{\tau 1} &= \sin\theta_{12}\sin\theta_{23} - \cos\theta_{12}\cos\theta_{23}\sin\theta_{13}e^{i\delta_{13}}\,, \\ U_{e2} &= \cos\theta_{13}\sin\theta_{12}\,, \\ U_{\mu 2} &= \cos\theta_{12}\cos\theta_{23} - \sin\theta_{12}\sin\theta_{13}\sin\theta_{23}e^{i\delta_{13}}\,, \\ U_{\tau 2} &= \cos\theta_{13}\sin\theta_{23}\,, \\ U_{e3} &= \sin\theta_{13}e^{-i\delta_{13}}\,, \end{aligned} \tag{2.38}$$

$$\begin{aligned}
U_{\mu 3} &= -\cos\theta_{12}\sin\theta_{23} - \cos\theta_{23}\sin\theta_{12}\sin\theta_{13}e^{i\delta_{13}}\,,\\
U_{\tau 3} &= \cos\theta_{13}\cos\theta_{23}\,.
\end{aligned}$$

These elements correspond to what we saw earlier in equation (1.54) which we repeat here for convenience

$$V, U = \begin{pmatrix} c_{12}c_{13} & s_{12}c_{13} & s_{13}e^{-i\delta_{13}} \\ -s_{12}c_{23} - c_{12}s_{23}s_{13}e^{i\delta_{13}} & c_{12}c_{23} - s_{12}s_{23}s_{13}e^{i\delta_{13}} & s_{23}c_{13} \\ s_{12}c_{23} - c_{12}s_{23}s_{13}e^{i\delta_{13}} & -c_{12}s_{23} - s_{12}c_{23}s_{13}e^{i\delta_{13}} & c_{23}c_{13} \end{pmatrix} \tag{1.54}$$

recalling that we have abbreviated $\sin\theta_{ij} = s_{ij}$ and $\cos\theta_{ij} = c_{ij}$ and used $\delta_{CP} = \delta_{13}$ to be explicit and to anticipate introducing more phases in the four flavour case.

2.2.3 Four Flavour Parametrisation

The importance of four flavour models will be more evident later in chapter 3 when we begin to discuss more complicated theories. There are several possible extensions into four flavours but all must have $N_{\text{angles}} = 6$ and $N^{\text{Dirac}}_{\text{phases}} = 3$. Following conventions we introduce mixing angles: θ_{14}, θ_{24} and θ_{34} and CP phases: δ_{14} and δ_{34}. We use the parametrisation defined by:

$$U = R(\theta_{34}, \delta_{34})R(\theta_{24})R(\theta_{14}, \delta_{14})R(\theta_{23})R(\theta_{13}, \delta_{13})R(\theta_{12}) \tag{2.39}$$

which can also be written involving our usual three flavour matrix as:

$$U = R(\theta_{34}, \delta_{34})R(\theta_{24})R(\theta_{14}, \delta_{14})U_{3\nu}\,. \tag{2.40}$$

This gives the matrix

$$U = \begin{pmatrix} U_{e1} & U_{e2} & U_{e3} & U_{e4} \\ U_{\mu 1} & U_{\mu 2} & U_{\mu 3} & U_{\mu 4} \\ U_{\tau 1} & U_{\tau 2} & U_{\tau 3} & U_{\tau 4} \\ U_{s1} & U_{s2} & U_{s3} & U_{s4} \end{pmatrix} \tag{2.41}$$

with elements:

$$\begin{aligned}
U_{e1} &= c_{12}c_{13}c_{14}\,, \qquad (2.42)\\
U_{\mu 1} &= \left(-s_{24}s_{14}c_{13}e^{i\delta_{14}} - c_{24}s_{23}s_{13}e^{i\delta_{13}}\right)c_{12} - c_{24}c_{23}s_{12}\,,
\end{aligned}$$

$$\begin{aligned}
U_{\tau 1} &= c_{12}\left[-s_{34}s_{14}c_{13}e^{-i(\delta_{34}-\delta_{14})} - s_{13}e^{i\delta_{13}}\left(c_{34}c_{23} - s_{34}s_{24}s_{23}e^{-i\delta_{34}}\right)\right] \,, \\
&\quad + s_{12}\left(s_{34}s_{24}c_{23}e^{-i\delta_{34}} + c_{34}s_{23}\right) \,, \\
U_{s1} &= c_{12}\left[-c_{34}s_{14}c_{13}e^{i\delta_{14}} + s_{13}e^{i\delta_{13}}\left(s_{34}c_{23} + c_{34}s_{24}s_{23}\right)\right] \,, \\
&\quad - s_{12}\left(-c_{34}s_{24}c_{23}e^{i\delta_{34}} + s_{34}s_{23}\right) \,, \\
U_{e2} &= c_{13}c_{14}s_{12} \,, \\
U_{\mu 2} &= c_{12}c_{23}c_{24} - s_{12}\left(s_{14}s_{24}c_{13}e^{i\delta_{14}} + c_{24}s_{13}s_{23}e^{i\delta_{13}}\right) \,, \\
U_{\tau 2} &= -c_{12}\left(c_{23}s_{24}s_{34}e^{-i\delta_{34}} + c_{34}s_{23}\right) \,, \\
&\quad - s_{12}\left[c_{24}s_{13}s_{14}s_{34}e^{-i(\delta_{34}-\delta_{14})} + s_{13}e^{i\delta_{13}}\left(c_{23}c_{34} - s_{23}s_{24}s_{34}e^{-i\delta_{34}}\right)\right] \,, \\
U_{s2} &= c_{12}\left(-c_{23}c_{34}s_{24} + s_{23}s_{34}e^{i\delta_{34}}\right) \,, \\
&\quad - s_{12}\left[c_{13}c_{24}c_{34}s_{14}e^{i\delta_{14}} - s_{13}e^{i\delta_{13}}\left(c_{23}s_{34}e^{i\delta_{34}} + c_{34}s_{23}s_{24}\right)\right] \,, \\
U_{e3} &= c_{14}s_{13}e^{-\delta_{14}} \,, \\
U_{\mu 3} &= c_{13}c_{24}s_{23} - c_{13}s_{14}s_{24}e^{i(\delta_{14}-\delta_{13})} \,, \\
U_{\tau 3} &= c_{13}\left(c_{23}c_{34} - s_{23}s_{24}s_{34}e^{-i\delta_{34}}\right) - c_{24}s_{13}s_{14}s_{34}e^{i(\delta_{34}-\delta_{14}+\delta_{13})} \,, \\
U_{s3} &= -c_{13}\left(c_{23}s_{34}e^{i\delta_{34}} + c_{34}s_{23}s_{24}\right) - c_{24}c_{34}s_{13}s_{14}e^{i(\delta_{14}-\delta_{13})} \,, \\
U_{e4} &= s_{14}e^{-i\delta_{14}} \,, \\
U_{\mu 4} &= c_{14}s_{24} \,, \\
U_{\tau 4} &= c_{14}c_{24}s_{34}e^{-i\delta_{34}} \,, \\
U_{s4} &= c_{14}c_{24}c_{34} \,.
\end{aligned}$$

Clearly this would be difficult to fit on the page in 4×4 matrix notation so the raw matrix for $n > 3$ is rarely written out in full.

2.3 Two Flavour Oscillation

In this section we aim to derive the form of simple two flavour oscillations with L/E dependence. In this section we demonstrate the 'standard' quantum mechanical plane-wave derivation for neutrino oscillations. This approach has several flaws which may not seem apparent at first. These are due to poorly justified (but well intentioned) mathematical hand-waving in regards to energy and momentum. Miraculously the results turn out correct! This is due to the fact that when properly accounted for, the true solution includes several extra factors which are so small as to be vanishingly important.We will re-visit this afterwards in section 2.4. Also worth mentioning is the fact that in general, a two flavour approach will only ever be approximate when modelling real 3ν physics. Despite these shortcomings this approach is useful in specific cases as well as to explain basic phenomena. We will also see in section 3.4, that with appropriate *effective* mixing parameters, this approach is a useful tool for highlighting degeneracies.

Two flavour formalisms were often used historically because genuine 3ν were not important or unable to be observed. The vastly different scales available in 3ν and smallness of θ_{13} are responsible for this fact. So if we compare the sizes of the two characteristic mass splittings and evaluate $\sin^2\theta_{13}$ we see

$$\frac{\Delta m^2_{21}}{\Delta m^2_{31}} \approx 0.03 \quad \text{and/or} \quad \sin^2\theta_{13} \leq 0.10. \tag{2.43}$$

It may not be clear from above but these numbers indicate that oscillations can be broadly split into two separate two-flavour regimes.

To begin with two flavours properly, firstly lets step back and derive the minimal oscillation case. So choosing the oscillation between two flavours, ν_e and ν_μ we write two linear combinations,

$$\nu_1 = \cos\theta\nu_e - \sin\theta\nu_\mu, \quad \nu_2 = \sin\theta\nu_e + \cos\theta\nu_\mu. \tag{2.44}$$

Where ν_1 and ν_2 are the mass eigenstates, ν_e and ν_μ are the flavour eigenstates and the $\sin\theta$ and $\cos\theta$ terms are normalisation constants defined so that unitarity is preserved. From these equations we define θ as the “mixing angle” between the ν_e and ν_μ flavour states, because it determines the level of flavour mixing in the mass eigenstates. Note these mass eigenstates must also obey the Schrödinger equation, therefore we have:

$$\nu_1(t) = \nu_1(0)e^{-iE_1t/\hbar}, \quad \nu_2(t) = \nu_2(0)e^{-iE_2t/\hbar}\,. \tag{2.45}$$

It is also simple to rearrange equation (2.44) to express the flavour eigenstates as linear combinations of the mass eigenstates,

$$\nu_e(t) = \cos\theta\nu_1(t) + \sin\theta\nu_2(t) \quad \text{and} \quad \nu_\mu(t) = -\sin\theta\nu_1(t) + \cos\theta\nu_2(t)\,, \tag{2.46}$$

all eigenstates have also been promoted to time dependent versions. From equations (2.44) and (2.46) it becomes obvious that we can express these equations using a unitary matrix along with state vectors i.e. for the mass eigenstates from equation (2.44)

$$\begin{pmatrix} \nu_1 \\ \nu_2 \end{pmatrix} = \begin{pmatrix} \cos\theta & -\sin\theta \\ \sin\theta & \cos\theta \end{pmatrix} \begin{pmatrix} \nu_e \\ \nu_\mu \end{pmatrix} . \tag{2.47}$$

We can rearrange in terms of the flavour state vector (where our matrix can just be transposed because of the unitary property $U^{-1} = U^\dagger$) to get the familiar form,

$$\begin{pmatrix} \nu_e \\ \nu_\mu \end{pmatrix} = \begin{pmatrix} \cos\theta & \sin\theta \\ -\sin\theta & \cos\theta \end{pmatrix} \begin{pmatrix} \nu_1 \\ \nu_2 \end{pmatrix} , \tag{2.48}$$

which clearly gives the flavour eigenstate equations (2.46). This matrix representation is especially useful as it generalises to the three flavour case (the PMNS matrix), where it immensely simplifies things. Now that we have the transformation between flavour and mass states, we can calculate an oscillation probability equation for these two flavours e.g. for an initial ν_e to turn into a ν_μ. For the initial electron flavour example we have the initial ($t = 0$) conditions:

$$\nu_e(0) = 1, \;\; \nu_\mu(0) = 0 \quad \therefore \; \nu_1(0) = \cos\theta, \;\; \nu_2(0) = \sin\theta \, , \tag{2.49}$$

which come from (2.44) or (2.47). Substituting these conditions into equation (2.44) we get the time dependent mass states:

$$\nu_1(t) = \cos\theta e^{-E_1 t/\hbar} \quad \text{and} \quad \nu_2(t) = \sin\theta e^{-E_2 t/\hbar} \, , \tag{2.50}$$

which can be substituted into equation (2.46) to give the following expression for $\nu_\mu(t)$:

$$\nu_\mu(t) = \sin\theta\cos\theta\Big(- e^{-iE_1 t/\hbar} + e^{-iE_2 t/\hbar}\Big) . \tag{2.51}$$

Therefore to calculate the probability that our initial ν_e has changed flavour to a ν_μ after time t is the modulus squared of the above expression. So we have the probability of the transition after time t:

$$P_{\nu_e \longrightarrow \nu_\mu} \equiv |\nu_\mu(t)|^2 \, , \tag{2.52}$$

where to shorten the left hand side further we define the convenient notation:

$$P_{\nu_\alpha \longrightarrow \nu_\beta} \equiv P_{\alpha\beta} \, . \tag{2.53}$$

So expanding the probability using our time dependent states gives:

$$\begin{aligned}
P_{e\mu} &= (\sin\theta\cos\theta)^2 \Big(- e^{-iE_1 t/\hbar} + e^{-iE_2 t/\hbar} \Big) \Big(- e^{iE_1 t/\hbar} + e^{iE_2 t/\hbar} \Big) \\
&= \frac{\sin^2(2\theta)}{4} \Big(1 - e^{i(E_2 - E_1)t/\hbar} - e^{-i(E_2 - E_1)t/\hbar} + 1 \Big) \\
&= \frac{\sin^2(2\theta)}{4} \left(2 - 2\cos\frac{(E_2 - E_1)t}{\hbar} \right) \\
&= \frac{\sin^2(2\theta)}{4} 4\sin^2\left(\frac{E_2 - E_1}{2\hbar} t \right) , \\
\therefore \; P_{e\mu} &= \sin^2 2\theta \sin^2\left(\frac{E_2 - E_1}{2\hbar} t \right) .
\end{aligned} \tag{2.54}$$

From equation (2.54) it can clearly be seen that the ν_μ probability is sinusoidal in time which is where the term ‘oscillation’ comes from. This implies that the neutrinos will ‘oscillate’ between ν_e and ν_μ and back again. But what are the energies E_1 and E_2? This is where we make some problematic assumptions involving equal momentum but unequal energy of eigenstates. We briefly discuss why these momentum and energy assumptions are invalid (but lead to the correct answers) at the end of section 2.4. So returning to our equations, we know that neutrinos are highly relativistic, and from special relativity we have $E^2 - |\mathbf{p}|^2 c^2 = m^2 c^4$, therefore,

$$\begin{aligned}
E_i^2 &= |\mathbf{p_i}|^2 c^2 + m_i^2 c^4 \\
&= |\mathbf{p_i}|^2 c^2 \left(1 + \frac{m_i^2 c^2}{|\mathbf{p_i}|^2} \right) , \\
\Longrightarrow \; E_i &\approx |\mathbf{p_i}| c \left(1 + \frac{1}{2} \frac{m_i^2 c^2}{|\mathbf{p_i}|^2} \right) \\
\therefore \; E_i &= p_i c + \frac{m_i^2 c^3}{2 p_i} \, .
\end{aligned} \tag{2.55}$$

So, making the (problematic) assumption that $p_1 = p_2$ and substituting m_1 and m_2 gives E_1 and E_2 respectively, then subtracting E_2 from E_1 gives:

$$E_2 - E_1 \approx \frac{m_2^2 c^3 - m_1^2 c^3}{2p} \approx \frac{m_2^2 - m_1^2}{2E} c^4 = \frac{\Delta m^2}{2E} c^4 \, , \tag{2.56}$$

where

$$\Delta m^2 = m_2^2 - m_1^2 \tag{2.57}$$

and the E and p in the denominator with no subscripts will be the average neutrino energy and momentum. We can now substitute equation (2.56) into (2.54) to get the probability in terms of the neutrino mass squared difference:

$$P_{e\mu} = \sin^2 2\theta \sin^2 \left(\frac{\Delta m^2 c^4}{4\hbar E} t \right) . \tag{2.58}$$

It can also be useful to express the oscillation probability in terms of distance the neutrinos have travelled L using $L \approx ct$:

$$P_{e\mu} = \sin^2 2\theta \sin^2 \left(\frac{\Delta m^2 c^3}{4\hbar E} L \right) . \tag{2.59}$$

Note that this is also sometimes written (usually in experimental context) as

$$P_{\alpha\beta} = \sin^2 2\theta \sin^2 1.27 \frac{\Delta m^2 L}{E_\nu} , \tag{2.60}$$

where 1.27 is a conversion factor dealing with the unit conversion to put E in GeV, L in km and Δm^2 in eV^2 defined from

$$\frac{\Delta m^2 c^3 L}{4\hbar E} = \frac{\mathrm{GeV fm}}{4\hbar c} \times \frac{\Delta m^2}{\mathrm{eV}^2} \frac{L}{\mathrm{km}} \frac{\mathrm{GeV}}{E} \approx 1.27 \times \frac{\Delta m^2}{\mathrm{eV}^2} \frac{L}{\mathrm{km}} \frac{\mathrm{GeV}}{E} . \tag{2.61}$$

From equation (2.59) we can also calculate the distance over energy (L/E) required to operate an experiment at the first oscillation maximum which is useful in experiment design:

$$\left[\frac{L}{E} \right]_{max} = \frac{2\pi\hbar}{\Delta m^2 c^3} . \tag{2.62}$$

Note: the L/E for NOνA is ≈ 405 km/GeV which is close to maximum, while the SBL experiment LSND is ≈ 0.75 km/GeV also from an accelerator neutrino source hence will measure a different, non-maximal part of the oscillation curve. To fully simplify our equation we express these probabilities using natural units:

$$P_{e\mu} = \sin^2 2\theta \sin^2 \frac{\Delta m^2}{4E} L , \tag{2.63}$$

then define a more compact parameter that encompasses the L/E and splitting size dependence:

$$\Delta = \frac{\Delta m^2}{4E} L \,, \tag{2.64}$$

which is known as an ‘oscillating factor’. This further simplifies our expression to:

$$P_{e\mu} = \sin^2 2\theta \sin^2 \Delta \,. \tag{2.65}$$

This is the key form of an oscillation probability. From all of these equations there are two main features to note: $P_{e\mu} \neq 0$ if and only if $\theta \neq 0$ and $m_1 \neq m_2$. So for oscillations to occur there *must* be some mixing (θ) *and* a mass difference (Δm^2). We now can illustrate the shape of oscillations by looking at the oscillation probabilities for initial muon neutrinos from a source such as NOνA.

2.4 Deriving the General Oscillation Probability

Using the framework for flavour mixing in terms of the PMNS matrix, we can work out the general oscillation probability expression in terms of the neutrino mixing parameters. This is important because it allows us to get probabilities for cases with any number of neutrinos for various parametrisations. It is important to note that the previous derivation of two flavour oscillation probability in section 2.3 required some ‘hand-waved’ equating of momenta between propagating neutrino mass eigenstates. This weakly-motivated process eliminates two additional phases, one associated with these wave functions being displaced in time and the other with them decohering over distance. We can treat neutrinos thoroughly using a wavepacket type analysis and show that these phases are indeed small and thus show why the naive approximation still gives the correct answer.

We begin by constructing our states. For single-particle eigenstate expressed in the momentum state basis $|\nu_k, \mathbf{p}\rangle = |\mathbf{p}\rangle \otimes |\nu_k\rangle$ we construct the initial state at $t = 0$ as

$$|\psi_k(0)\rangle \equiv \int d^3p \, \psi_k(\mathbf{p}) |\nu_k, \mathbf{p}\rangle \tag{2.66}$$

for a some function $\psi_k(\mathbf{p})$. At time t we have

$$|\psi_k(t)\rangle = e^{-i\hat{H}t} |\psi_k(0)\rangle \tag{2.67}$$

as usual. Hence we have

$$|\psi_k(t)\rangle = \int d^3p\, \psi_k(\mathbf{p}) e^{-iE_k(p)t} |\nu_k, \mathbf{p}\rangle \tag{2.68}$$

where $E_k(p) = \sqrt{\mathbf{p}^2 + m_k^2}$. We can also express our state in coordinate space as $|\nu_k, \mathbf{x}\rangle = |\mathbf{x}\rangle \otimes |\nu_k\rangle$ and hence write, in coordinate space representation:

$$\psi_k(\mathbf{x}, t)|\nu_k\rangle = \langle \mathbf{x}|\psi_k(t)\rangle = \int \frac{d^3p}{(2\pi)^{3/2}} \psi_k(\mathbf{p}) e^{i(\mathbf{p}\cdot\mathbf{x} - E_k(p)t)} |\nu_k\rangle\,, \tag{2.69}$$

where $\langle \mathbf{x}|\mathbf{p}\rangle = e^{(i\mathbf{p}\cdot\mathbf{x})}/(2\pi)^{3/2}$. From this we will follow the derivation of oscillation via wavepackets first brought up by Boris Kayser in 1981 [93]. To get this to work we want $\psi_k(\mathbf{p}) = f_k(\mathbf{p} - \mathbf{p}_k)$ where $f_k(\mathbf{p} - \mathbf{p}_k)$ is to be sharply peaked around $\mathbf{p} = \mathbf{p}_k$ for example $f(\mathbf{p})$ can be a narrow gaussian. Therefore we can write a broad spatial wavepacket:

$$\psi_k(\mathbf{x}, t) = \int \frac{d^3p}{(2\pi)^{3/2}} f_k(\mathbf{p} - \mathbf{p}_k) e^{i(\mathbf{p}\cdot\mathbf{x} - E_k(p)t)} \tag{2.70}$$

with mean momentum $\bar{\mathbf{p}} \sim \mathbf{p}$. We can take f_k to be symmetric, i.e. $f_k(\mathbf{p}) = f_k(-\mathbf{p})$ to make $\bar{\mathbf{p}} = \mathbf{p}_k$. Though this case is simple the arguments made can be generalised for the asymmetric case.From experiment specifications and the scale of neutrino masses we have: $E_i \gtrapprox 1$ MeV and because $m_i \lessapprox 1$ eV we have $|\mathbf{p}_i| \gg m_i$ so from relativity $E_i \simeq |\mathbf{p}_i|$. This implies that all mass eigenstates will be ultrarelativistic, hence are travelling close to the speed of light. This ensures little wavepacket dispersion over reasonable distances. We write the truncated Taylor expansion of $E_k(p)$ about the $p = p_k$ point

$$\begin{aligned} E_k(p) &= E_k(p_k) + (p - p_k)^i \left.\frac{\partial E_k}{\partial p^i}\right|_{\mathbf{p}=\mathbf{p}_k}\,, \\ &= E_k(p_k) + (\mathbf{p} - \mathbf{p}_k)\cdot \mathbf{v}_k, \end{aligned} \tag{2.71}$$

where $p = |\mathbf{p}|$, $p_k = |\mathbf{p}_k|$ and $\mathbf{v}_k = p_k/E_k(p)$. So overall we have the wavepacket group velocity $\mathbf{v}_k \sim c$ and a stable wavepacket shape over oscillation distances. Therefore, by pulling out a factor of $\exp(-iE_k(p_k)t)$, the wavepacket can be rewritten as:

$$\psi_k(\mathbf{x}, t) = e^{-iE_k(p_k)t} \int \frac{d^3p}{(2\pi)^{3/2}} f_k(\mathbf{p} - \mathbf{p}_k) e^{i(\mathbf{p}\cdot\mathbf{x} - [E_k(p) - E_k(p_k)]t)}\,. \tag{2.72}$$

Hence using equation (2.71)

$$\begin{aligned}
\psi_k(\mathbf{x},t) &= e^{-iE_k(p_k)t}\int\frac{d^3p}{(2\pi)^{3/2}}f_k(\mathbf{p}-\mathbf{p}_k)e^{i(\mathbf{p}\cdot\mathbf{x}-[\mathbf{p}-\mathbf{p}_k]\cdot\mathbf{v}_k t)} \\
&= e^{i[\mathbf{p}_k\cdot\mathbf{x}-E_k(p_k)t]}\int\frac{d^3p}{(2\pi)^{3/2}}f_k(\mathbf{p})e^{i\mathbf{p}\cdot(\mathbf{x}-\mathbf{v}_k t)} \\
&\equiv e^{i[\mathbf{p}_k\cdot\mathbf{x}-E_k(p_k)t]}g_k(\mathbf{x}-\mathbf{v}_k t),
\end{aligned} \tag{2.73}$$

with a change of variables ($\mathbf{p}\to\mathbf{p}+\mathbf{p}_k$) in the second line and the function $g_k(\mathbf{x}-\mathbf{v}_k t)$ is defined as the ‘preserved wavepacket shape factor’.

Typical neutrino mass eigenstates created in charged-current nuclear processes have energies $\mathcal{O}$(1-10) MeV and are ultrarelativistic. Note that, except under highly specific cases, non-relativistic neutrinos can be disregarded as they cannot oscillate due to lack of coherence [94]. These processes result in linear superpositions of all three mass eigenstates, $m_1, m_2, m_3 \lessapprox 1$ eV (can be generalised to n mass eigenstates in non-standard mixing scenarios later). The production of these eigenstates is extended over a small region of space and a short time interval so we can make the assumptions that the wavepacket shape factors and group velocities are roughly the same for all three eigenstates ($g_1 = g_2 = g_3 \equiv g$ and $\mathbf{v}_1 = \mathbf{v}_2 = \mathbf{v}_3 \equiv \mathbf{v}$). The assumption on group velocities works for distances L such that the different eigenstates do not significantly lose overlap and is most certainly valid in studied oscillation cases. So we now define the wavepacket shape of the neutrino source as $g^S(\mathbf{x}-\mathbf{v}t)$. Its spatial midpoint is initially ($t=0$) set at $\mathbf{x}=0$ and the shape such that it decreases rapidly away from $\mathbf{x}-\mathbf{v}t=0$. So now we can write the neutrino flavour eigenstate ν_α created in a region centred at $\mathbf{x}$ at $t=0$ as:

$$\begin{aligned}
|\nu_\alpha(\mathbf{x},t)\rangle &\equiv \sum_i U^*_{\alpha i}\psi_i(\mathbf{x},t)|\nu_i\rangle \\
&= \sum_i U^*_{\alpha i}e^{i[\mathbf{p}_i\cdot\mathbf{x}-E_i(p_i)t]}g^S_i(\mathbf{x}-\mathbf{v}_i t)|\nu_i\rangle \\
&\simeq g^S(\mathbf{x}-\mathbf{v}t)\sum_i U^*_{\alpha i}e^{i[\mathbf{p}_i\cdot\mathbf{x}-E_i(p_i)t]}|\nu_i\rangle.
\end{aligned} \tag{2.74}$$

If we have a detector at $\mathbf{L}$ where $|\mathbf{L}| = L$ is the distance from the source of neutrinos or the experimental baseline. We are only considering neutrinos heading straight to our detector, so $\mathbf{L}$ is parallel to $\mathbf{v}$. For experiments such as T2K (section 1.4.1) and NOνA (section 1.4.2) this is not entirely true due to their detectors being located off the centre axis of the neutrino beam. In these cases however, because the angles involved are small, the probability will be approximately the same. If L is not too large for the given neutrino energies/velocities, as is usually specified in the case of reactor and accelerator experiments, then the centres of the wavepackets arrive at the detector approximately simultaneously and thus will be strongly overlapping. Given that $|\mathbf{v}| \simeq c$, the arrival time is $t \simeq L/|\mathbf{v}| \simeq L/c$ for all eigenstates. We define the detected wavepacket similarly to the source wavepacket, with detected flavour ν_β and shape $g^D(\mathbf{x}-\mathbf{L})$ which peaks at $\mathbf{x}=\mathbf{L}$ not $\mathbf{x}=0$ this time, as

$$|\nu_\beta(\mathbf{x}-\mathbf{L})\rangle \simeq g^D(\mathbf{x}-\mathbf{L}) \sum_i U^*_{\beta i} e^{i[\mathbf{p}_i\cdot(\mathbf{x}-\mathbf{L})]} |\nu_i\rangle. \tag{2.75}$$

We can then calculate the oscillation amplitude $\nu_\alpha \to \nu_\beta$ as

$$\begin{aligned} A_{\alpha\beta}(\mathbf{L},t) &= \int d^3x \langle \nu_\beta(\mathbf{x}-\mathbf{L})|\nu_\alpha(\mathbf{x},t)\rangle \\ &= G(\mathbf{L}-\mathbf{v}t) \sum_i U^*_{\alpha i} U_{\beta i} e^{-i[E_i(p_i)t - \mathbf{p}_i\cdot\mathbf{L}]}\,, \end{aligned} \tag{2.76}$$

where $G(\mathbf{L}-\mathbf{v}t)$ is an ‘effective shape factor’ defined as

$$G(\mathbf{L}-\mathbf{v}t) \equiv \int d^3x\, g^D(\mathbf{x}-\mathbf{L})^* g^S(\mathbf{x}-\mathbf{v}t)\,. \tag{2.77}$$

The emission and absorption times are not measured for neutrinos so the probability of ν_α to ν_β being observed at position $\mathbf{L}$ is

$$\begin{aligned} P_{\alpha\beta}(\mathbf{L}) &= \int_{-\infty}^{\infty} dt |A_{\alpha\beta}(\mathbf{L},t)|^2\,, \\ &= \sum_{i,j} U_{\beta i} U^*_{\beta j} U^*_{\alpha i} U_{\alpha j} I_{ij}(\mathbf{L}), \end{aligned} \tag{2.78}$$

with an integral term defined as

$$I_{ij}(\mathbf{L}) \equiv \int_{-\infty}^{\infty} |G(\mathbf{L}-\mathbf{v}t)|^2 e^{-i\Delta\phi_{ij}(\mathbf{L},t)} \tag{2.79}$$

with term in the exponential

$$\begin{aligned} \Delta\phi_{ij}(\mathbf{L},t) &= [E_i(p_i) - E_j(p_j)]\,t - [p_i - p_j]L\,, \\ &\equiv \Delta E_{ij} t - \Delta p_{ij} L. \end{aligned} \tag{2.80}$$

Clearly we have now arrived at a somewhat familiar probability. We can now see that the properties of this expression are the same as in our standard derivation. Firstly that $P_{\alpha\beta} = P^*_{\alpha\beta}$ i.e. is real (as a probability must be), this works because conjugation exchanges i and j, both of which are summed over. Additionally it's clear that if there are no CP-breaking phases in the oscillation terms, then the PMNS matrix is real and hence $P_{\alpha\beta} = P_{\beta\alpha}$. Similarly, if we consider antineutrinos then our implicit assumption of CPT invariance implies $P_{\bar{\alpha}\bar{\beta}} = P_{\beta\alpha}$. Returning to our probability, we can take the limit of entirely degenerate neutrino masses i.e. $m_i \approx m_j, \forall i, j$ to check the normalisation. This case implies $E_i(p_i) = E_j(p_j)$ hence $p_i = -p_j$, giving $\Delta\phi_{ij}(\mathbf{L}, t) = 0$ and $I_{ij}(\mathbf{L}) = 1$. So we have

$$I_{ij}(\mathbf{L}) = 1 = \int_{-\infty}^{\infty} |G(\mathbf{L} - \mathbf{v}t)|^2 e^0 \tag{2.81}$$

and therefore we have the normalisation of the shape factor term in the integral

$$\int_{-\infty}^{\infty} |G(\mathbf{L} - \mathbf{v}t)|^2 = 1\,. \tag{2.82}$$

Similarly for degenerate masses we also have $P_{\alpha\beta}(\mathbf{L}) = (\delta_{\alpha\beta})^2 = \delta_{\alpha\beta}$ implying the oscillations do not take place if the neutrino masses are degenerate. From the unitarity property in equation (2.96) we have $\sum_\beta U_{\beta i} U^*_{\beta j} = \delta_{ij}$ so

$$\begin{aligned} \sum_\beta P_{\alpha\beta}(\mathbf{L}) &= \sum_i U^*_{\alpha i} U_{\alpha i} I_{ii}(\mathbf{L})\,, \\ &= \sum_i U^*_{\alpha i} U_{\alpha i}\,, \\ &= 1\,, \end{aligned} \tag{2.83}$$

for any $\mathbf{L}$. This allows $P_{\alpha\beta}(\mathbf{L})$ to be interpreted as the oscillation probability $\nu_\alpha \to \nu_\beta$. We now look to simplify the exponential term. The standard relativistic energy expression gives

$$E_i(p_i) = \sqrt{p_i^2 + m_i^2} \tag{2.84}$$

and in the ultrarelativistic limit can be expanded

$$E_i(p_i) \simeq p_i + \frac{m_i^2}{2p_i} \simeq p_i + \frac{m_i^2}{2p} \simeq p_i + \frac{m_i^2}{2E}. \tag{2.85}$$

Similarly

$$\begin{aligned}\Delta E_{ij} &\equiv E_i(p_i) - E_j(p_j)\,,\\ &\simeq (p_i - p_j) + \frac{m_i^2 - m_j^2}{2p}\,,\\ &\equiv \Delta p_{ij} + \frac{\Delta m_{ij}^2}{2p}\,,\end{aligned} \tag{2.86}$$

defining p and E as the average neutrino momentum and energy. Regarding p as a function of E in the mass-energy relation $p(E, m^2) = \sqrt{E^2 - m^2}$ allows us to write

$$\begin{aligned}\Delta p &= \left.\frac{\partial p}{\partial E}\right|_{\Delta m^2} \Delta E + \left.\frac{\partial p}{\partial m^2}\right|_{E} \Delta m^2\,,\\ &= \frac{1}{v}\Delta E - \frac{1}{2p}\Delta m^2\,.\end{aligned} \tag{2.87}$$

We then simplify equation (2.80).

$$\begin{aligned}\Delta\phi_{ij}(\mathbf{L}, t) &= \Delta E_{ij} t - \Delta p_{ij} L\,,\\ &= \frac{\Delta m_{ij}^2}{2p} L - \frac{1}{v}(L - vt)\Delta E_{ij}\,,\end{aligned} \tag{2.88}$$

which then allows us to pull part of this phase outside the integral term from equation (2.79)

$$I_{ij}(\mathbf{L}) = e^{-i\Delta m_{ij}^2 L/2p} \int_{-\infty}^{\infty} dt |G(\mathbf{L} - \mathbf{v}t)|^2 e^{i(L - vt)\Delta E_{ij}/v}\,, \tag{2.89}$$

hence the new probability expression

$$P_{\alpha\beta}(\mathbf{L}) = \sum_{i,j} U_{\beta i} U_{\beta j}^* U_{\alpha i}^* U_{\alpha j} e^{-i\Delta m_{ij}^2 L/2p} F_{ij}\,, \tag{2.90}$$

which looks almost like the standard expression but with an additional factor

$$F_{ij} \equiv \int_{-\infty}^{\infty} dt |G(\mathbf{L} - \mathbf{v}t)|^2 e^{i(L - vt)\Delta E_{ij}/v}\,, \tag{2.91}$$

which is independent of L. Because we have ultrarelativistic motion then $v \simeq c = 1$ and so if $(L - vt)\Delta E_{ij} \ll 1$ then the exponential in the integrand of F_{ij} becomes unity and then $F_{ij} = 1$. Hence, after interchanging p and E, which are equal at first order due to the ultrarelativistic limit, we recover the standard neutrino oscillation formula

$$P_{\alpha\beta}(\mathbf{L}) = \sum_{i,j} U_{\beta i} U^*_{\beta j} U^*_{\alpha i} U_{\alpha j} e^{-i\Delta m^2_{ij} L/2E} . \tag{2.92}$$

To get this probability into a less obscure form we add a term that is zero overall and drop the (from now on, implicit) **L**-dependence from the left hand side.

$$\begin{aligned} P_{\alpha\beta} &= \sum_{i=0}^{n}\sum_{j=0}^{n} \left[(1-1) U_{\beta i} U^*_{\beta j} U^*_{\alpha i} U_{\alpha j} + U_{\beta i} U^*_{\beta j} U^*_{\alpha i} U_{\alpha j} e^{-i\frac{\Delta m^2_{ij}}{2E}L} \right] , \\ &= \sum_{i=0}^{n}\sum_{j=0}^{n} \left[U_{\beta i} U^*_{\beta j} U^*_{\alpha i} U_{\alpha j} + U_{\beta i} U^*_{\beta j} U^*_{\alpha i} U_{\alpha j} \left(e^{-i\frac{\Delta m^2_{ij}}{2E}L} - 1 \right) \right] . \end{aligned} \tag{2.93}$$

We will pull the terms outside of the brackets into separate sums to give

$$P_{\alpha\beta} = \sum_{i=0}^{n}\sum_{j=0}^{n} U_{\beta i} U^*_{\beta j} U^*_{\alpha i} U_{\alpha j} + \sum_{i=0}^{n}\sum_{j=0}^{n} U_{\beta i} U^*_{\beta j} U^*_{\alpha i} U_{\alpha j} \left(e^{-i\frac{\Delta m^2_{ij}}{2E}L} - 1 \right) . \tag{2.94}$$

Now recall the properties of unitary matrices from equation (2.9) in section 2.1.1 which can be re-written in the specific neutrino mixing case to give:

$$\sum_{j=0}^{n} U^*_{\beta j} U_{\alpha j} = \delta_{\alpha\beta} , \tag{2.95}$$

$$\sum_{\alpha=0}^{n} U^*_{\alpha i} U_{\alpha j} = \delta_{ij} . \tag{2.96}$$

We want to use this to simplify equation (2.94) but first we will write the double sum as a product of each individual sum

$$\sum_{i=0}^{n}\sum_{j=0}^{n} U_{\beta i} U^*_{\alpha i} U^*_{\beta j} U_{\alpha j} = \left(\sum_{i=0}^{n} U_{\beta i} U^*_{\alpha i} \right) \left(\sum_{j=0}^{n} U^*_{\beta j} U_{\alpha j} \right) . \tag{2.97}$$

Where we now have two factors that resemble equation (2.95). It is now clear that we can use one the unitarity to further simplify the double sum in equation (2.94) as

$$\therefore \sum_{i=0}^{n}\sum_{j=0}^{n} U_{\beta i} U^*_{\alpha i} U^*_{\beta j} U_{\alpha j} = \delta_{\alpha\beta}\delta_{\alpha\beta} = \delta_{\alpha\beta} , \tag{2.98}$$

and our probability becomes

$$P_{\alpha\beta} = \delta_{\alpha\beta} + \sum_{i,j=0}^{n} U_{\beta i} U^*_{\beta j} U^*_{\alpha i} U_{\alpha j} \left(e^{-i\frac{\Delta m^2_{ij}}{2E}L} - 1 \right) . \tag{2.99}$$

Using Euler's formula the exponential can be separated into sine and cosine parts

$$P_{\alpha\beta} = \delta_{\alpha\beta} + \sum_{i,j=0}^{n} U_{\beta i} U^*_{\beta j} U^*_{\alpha i} U_{\alpha j} \left(\cos\left(\frac{\Delta m^2_{ij}}{2E} L \right) + i \sin\left(\frac{\Delta m^2_{ij}}{2E} L \right) - 1 \right) . \tag{2.100}$$

We then use the double angle formula

$$\cos 2\theta = 1 - 2\sin^2\theta, \tag{2.101}$$

for the cosine term, and introduce the shorthand terms

$$\Delta_{ij} = \frac{\Delta m^2_{ij}}{4E} L \, . \tag{2.102}$$

and

$$\mathbb{U}^{\alpha\beta}_{ij} = U_{\beta i} U^*_{\beta j} U^*_{\alpha i} U_{\alpha j} \tag{2.103}$$

With these we can now write a shorthand version of equation (2.100)

$$P_{\alpha\beta} = \delta_{\alpha\beta} + \sum_{i,j=0}^{n} \mathbb{U}^{\alpha\beta}_{ij} \left(-2\sin^2\Delta_{ij} + i\sin 2\Delta_{ij} \right) . \tag{2.104}$$

Now we note that because $\Delta_{ii} = 0$ for all i the second and third terms in equation (2.100) vanish for $i = j$ so we can instead split the sum into $i > j$ and $i < j$ parts.

$$\begin{aligned} P_{\alpha\beta} = \delta_{\alpha\beta} &+ \sum_{i>j}^{n} \mathbb{U}^{\alpha\beta}_{ij} \left(-2\sin^2\Delta_{ij} + i\sin 2\Delta_{ij} \right) \\ &+ \sum_{i<j}^{n} \mathbb{U}^{\alpha\beta}_{ij} \left(-2\sin^2\Delta_{ij} + i\sin 2\Delta_{ij} \right) . \end{aligned} \tag{2.105}$$

We now re-label the second sum using $i \leftrightarrow j$ to get both sums over the same limits

$$\begin{aligned} P_{\alpha\beta} = \delta_{\alpha\beta} &+ \sum_{i>j}^{n} \mathbb{U}^{\alpha\beta}_{ij} \left(-2\sin^2\Delta_{ij} + i\sin 2\Delta_{ij} \right) \\ &+ \sum_{i>j}^{n} \mathbb{U}^{\alpha\beta}_{ji} \left(-2\sin^2\Delta_{ji} + i\sin 2\Delta_{ji} \right) . \end{aligned} \tag{2.106}$$

We now use equations (2.103) and (2.102) to show that

$$\Delta_{ji} = \frac{\Delta m^2_{ji}}{4E} L = -\Delta_{ij} \, . \tag{2.107}$$

and

$$\mathbb{U}_{ji}^{\alpha\beta} = U_{\beta j}U_{\beta i}^{*}U_{\alpha j}^{*}U_{\alpha i} = \overline{\mathbb{U}_{ij}^{\alpha\beta}}\,, \tag{2.108}$$

with the overbar representing the complex conjugate. Substituting these into equation (2.106) gives

$$\begin{aligned} P_{\alpha\beta} = \delta_{\alpha\beta} - &\sum_{i>j}^{n} \mathbb{U}_{ij}^{\alpha\beta}\left(2\sin^2\Delta_{ij} - i\sin 2\Delta_{ij}\right) \\ -&\sum_{i>j}^{n} \overline{\mathbb{U}_{ij}^{\alpha\beta}}\left(2\sin^2\Delta_{ij} + i\sin 2\Delta_{ij}\right)\,. \end{aligned} \tag{2.109}$$

We can now group up the sine and cosine terms using linearity of sums

$$\begin{aligned} P_{\alpha\beta} = \delta_{\alpha\beta} - 2&\sum_{i>j}^{n} \left(\mathbb{U}_{ij}^{\alpha\beta} + \overline{\mathbb{U}_{ij}^{\alpha\beta}}\right)\sin^2\Delta_{ij} \\ +i&\sum_{i>j}^{n} \left(\mathbb{U}_{ij}^{\alpha\beta} - \overline{\mathbb{U}_{ij}^{\alpha\beta}}\right)\sin 2\Delta_{ij}\,. \end{aligned} \tag{2.110}$$

The terms inside the brackets can be recognised to correspond to real and imaginary parts of $\mathbb{U}_{ij}^{\alpha\beta}$ via the relations $\Re[z] = (z+\bar{z})/2$ and $\Im[z] = (z-\bar{z})/2i$.

$$\begin{aligned} P_{\alpha\beta} = \delta_{\alpha\beta} - 4&\sum_{i>j}^{n} \Re\left[\mathbb{U}_{ij}^{\alpha\beta}\right]\sin^2\Delta_{ij} \\ -2&\sum_{i>j}^{n} \Im\left[\mathbb{U}_{ij}^{\alpha\beta}\right]\sin 2\Delta_{ij}\,. \end{aligned} \tag{2.111}$$

Now note that $\Re\left[az\right] = a\Re\left[z\right]$ and $\Im\left[az\right] = a\Im\left[z\right]$ for $a \in \mathbb{R}$ and $z \in \mathbb{C}$. Using this property of complex numbers and the fact that the sine function is real, we pull the real and imaginary signs outside of the sums and expand our shorthand to give the common form of the probability

$$\begin{aligned} P_{\alpha\beta} = \delta_{\alpha\beta} - 4\Re&\sum_{i>j} U_{\beta i}U_{\beta j}^{*}U_{\alpha i}^{*}U_{\alpha j}\sin^2\left(\frac{\Delta m_{ij}^2}{4E}L\right) \\ -2\Im&\sum_{i>j} U_{\beta i}U_{\beta j}^{*}U_{\alpha i}^{*}U_{\alpha j}\sin\left(\frac{\Delta m_{ij}^2}{2E}L\right)\,. \end{aligned} \tag{2.112}$$

Note that the sign on the imaginary term will depend of the definition of Δ_{ij} and whether the element U translating from mass to flavour (all the way back in equation (2.1)) is defined as the conjugate or not. Sometimes this differs depending on convention, especially in older references. The real and imaginary term formalism is useful because the imaginary part vanishes when all CP phases are $0°$ or $180°$.

The conditions necessary for oscillation, which are 'hand-waved' away in non-wavepacket based approaches are:

1. The no-decoherence condition, which requires that the loss of overlap of the different mass wavepackets at the detector is negligible,
2. The localisation condition $(L - vt)\Delta E_{ij} \ll 1$.

No-decoherence will be satisfied if the shift in the wavepacket centres due to the difference in group velocities is small relative to the effective wavepacket size i.e. $\Delta v\, t_L = (\Delta v/v)L \ll \sigma_x$, where $t_L \equiv L/v$ is the average time taken for a wavepacket to reach the detector. The localisation condition can be rewritten as $\sigma_x \Delta m^2_{ij}/p \ll 1$, using the fact that $|G(\mathbf{L} - \mathbf{v}t)|^2$ goes to zero rapidly when $(L - vt) \gtrapprox \sigma_x$ and also $\Delta E_{ij} \sim \Delta m^2_{ij}/p$.

An overview of the difference between the plane wave approximation and wavepacket derivation is that in the plane wave case we make a choice that the propagating mass eigenstates have either: equal energy and differing momentum or vice versa. Neither of these assumptions are good but they do get the right answer. The reason why these assumptions work can be seen in the wavepacket case where we explicitly define coherence and localisation conditions. These conditions allow the formalism to be the same when the energies and momenta are not equal but close within some range.

Once we have a specific probability we can find the relevant antineutrino version of it denoted $P_{\bar{\alpha}\bar{\beta}} \equiv P(\overline{\nu}_\alpha \to \overline{\nu}_\beta)$, by performing the transformation $P_{\alpha\beta} \to P_{\bar{\alpha}\bar{\beta}}$: $\delta_{ij} \to -\delta_{ij}$ for all CP phases δ_{ij}. Once we get to this point we can substitute specific flavours for α and β, hence, using the PMNS matrix elements we can get an expression for a specific probability in terms of mixing parameters. So for example for standard 3 flavour $\nu_\mu \longrightarrow \nu_e$:

$$\begin{aligned} P_{\mu e} = \quad & s^2_{23} \sin^2 2\theta_{13} \sin^2 \frac{\Delta m^2_{31} L}{4E} + c^2_{13} c^2_{23} \sin^2 2\theta_{12} \sin^2 \frac{\Delta m^2_{21} L}{4E} \\ & + 8 c^2_{13} s_{13} c_{12} s_{12} c_{23} s_{23} \sin \frac{\Delta m^2_{21} L}{4E} \sin \frac{\Delta m^2_{31} L}{4E} \cos \left(\frac{\Delta m^2_{21} L}{4E} + \delta_{13} \right) \\ & - 2 s^2_{12} s^2_{23} \sin^2 2\theta_{13} \sin \frac{\Delta m^2_{21} L}{4E} \sin \frac{\Delta m^2_{31} L}{4E} \cos \frac{\Delta m^2_{21} L}{4E} \\ & + 4 c^2_{13} s^2_{12} s_{13} s_{23} \left(s_{23} s_{13} s_{12} - 2 c_{12} c_{23} \cos \delta_{13} \right) \sin^2 \frac{\Delta m^2_{31} L}{4E} \, . \end{aligned} \tag{2.113}$$

2.5 Quantum Field Theory Derivation of Oscillations

This section is a summary of the difference between QM and QFT wavepackets. We summarise the key changes that arise in the approach presented by Akhmedov, E. K. and Kopp, J. in [95]. In this work the authors analyse oscillation theory with wavepackets using QM and QFT approaches and compare the two. An unconventional but somewhat enlightening way to express neutrino oscillations is to use QFT, this is unconventional as we usually skirt the description of production and detection processes together and treat them somewhat abstractly once it can be seen that they fit the wavepacket oscillation condition. Using a QFT versus QM wavepackets is even more proper, but the improvement in terms of assumptions removed is small. The QFT approach starts with the generic interaction seen in the figure 2.2 including production and detection of a neutrino.

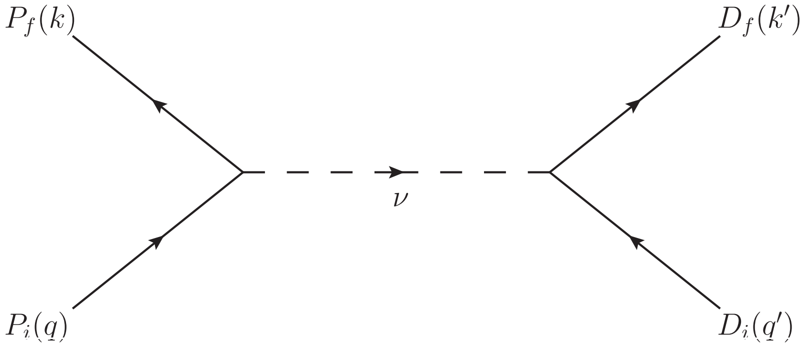

FIG. 2.2 Generic Feynman diagram encompassing production and detection of a neutrino.

The resulting wavepacket from this QFT amplitude can be compared with that of the QM wavepacket, from this the explicit parameters from the QFT approach can be related to the QM case. The differences in the QFT case from the QM case can be summarised:

- Momentum uncertainties are effective ones.
- Mean momentum $\mathbf{P}$ is modified to an effective value defined as $\mathbf{P}_{\text{eff}} = \mathbf{P} + \delta$. Where the δ term describes the shift away from the naive momentum expectation $\langle \mathbf{p} \rangle = \mathbf{P}$.
- The wavepacket is modified by an extra factor $N_j = \exp\left[-\tilde{\gamma}_j\right]$ which modifies the normalisation of the neutrino wave function.

The full forms of δ and $\tilde{\gamma}_j$ are in Appendix A of [95]. The explicit definitions are in equations (58) and (59) of [95]. The matching between QM and QFT is similar for production and detection. The QFT approach in the case of ultrarelativistic neutrinos (or quasi-degenerate, which we neglect) can show the conditions in which the standard probability $P_{\alpha\beta}(L/E)$ is well defined and gives the correct normalisation. With the condition on the mass splittings

$$|p_i - p_j| \simeq \frac{\Delta m_{ij}^2}{2p} \ll \sigma_p \,, \tag{2.114}$$

where σ_p is an effective momentum uncertainty dominated by the smallest out of σ_{pP} and σ_{pD}. These are furthermore related to the energy uncertainties σ_{eP} and σ_{eD} which have the condition

$$|E_i - E_j| \simeq \frac{\Delta m_{ij}^2}{2\bar{E}} \ll \sigma_{eP} \,. \tag{2.115}$$

The QFT approach adds little over the QM wavepacket explanation given that wavepackets already remove the more egregious equal momentum or equal energy approximations. The main ambiguity that the QFT approach removes is that of wavepacket shape. This is not a bad approximation though as any arbitrary wavepacket with the right properties should work fine. So the main draw of the QFT explanation is one of completeness.

2.6 Expressions for Various Oscillation Paradigms

In this section we cover certain specific approximate mixing probabilities that are commonly used in the literature and experimental analyses. Often these are glossed over or presented without explicit derivation. Here the aim is to show a few examples and to give an idea what logic is used to approximate and simplify the often complicated probabilities involved in oscillation. Some of these examples involve a fourth mass eigenstate and corresponding mass splitting which we will introduce thoroughly in chapter 3.

2.6.1 Appearance Probabilities

Here we present examples of appearance probabilities such as those seen by experiments like LSND and NOνA. Both of these examples involve an additional mass eigenstate which is the primary source of oscillation at SBL and a small additional effect at LBL. In the LBL case we introduce averaging over fast oscillations.

Probabilities for MiniBooNE and LSND

We wish to show that the SBL appearance probability can be approximated as

$$P_{\mu e} = \sin^2 2\theta_{\mu e} \sin^2 \Delta_{41} \,, \tag{2.116}$$

where

$$\sin^2 2\theta_{\mu e} \approx 4|U_{\mu 4}|^2 |U_{e4}|^2 = 4 \sin\theta_{14} \cos\theta_{14} \sin\theta_{24}. \tag{2.117}$$

To start, recall the full $\nu_\alpha \longrightarrow \nu_\beta$ oscillation probability

$$\begin{aligned} P_{\alpha\beta} = \delta_{\alpha\beta} - 4\Re \sum_{i>j} U_{\beta i} U^*_{\beta j} U^*_{\alpha i} U_{\alpha j} \sin^2 \Delta_{ij} \\ -2\Im \sum_{i>j} U_{\beta i} U^*_{\beta j} U^*_{\alpha i} U_{\alpha j} \sin 2\Delta_{ij} \,. \end{aligned} \tag{2.118}$$

Then we have

$$P_{\mu e} = -4\Re \sum_{i>j} U_{ei} U^*_{ej} U^*_{\mu i} U_{\mu j} \sin^2 \Delta_{ij} - 2\Im \sum_{i>j} U_{ei} U^*_{ej} U^*_{\mu i} U_{\mu j} \sin 2\Delta_{ij} \,, \tag{2.119}$$

but we know that due to the extremely short range of SBL experiments, oscillation due to Δ_{21} and Δ_{31} are insignificant. Hence for $ij = 21, 31, 32$ we make the approximations that $\sin^2 \Delta_{ij} \approx 0$ and $\sin 2\Delta_{ij} \approx 0$. Setting $i = 4$ in our sum will neglect these terms, leaving

$$P_{\mu e} = -4\Re \sum_{j=1}^{3} U_{e4} U^*_{ej} U^*_{\mu 4} U_{\mu j} \sin^2 \Delta_{4j} - 2\Im \sum_{j=1}^{3} U_{e4} U^*_{ej} U^*_{\mu 4} U_{\mu j} \sin 2\Delta_{4j} \,. \tag{2.120}$$

Note also $\Delta_{41} \gg \Delta_{31} > \Delta_{21}$, hence we also approximate $\Delta_{41} \approx \Delta_{42} \approx \Delta_{43}$. This leaves

$$P_{\mu e} = -4\Re \sum_{j=1}^{3} U_{e4} U^*_{ej} U^*_{\mu 4} U_{\mu j} \sin^2 \Delta_{41} - 2\Im \sum_{j=1}^{3} U_{e4} U^*_{ej} U^*_{\mu 4} U_{\mu j} \sin 2\Delta_{41}. \tag{2.121}$$

We assume that the SBL experiments we are concerned with operate at the short range oscillation maximum associated with ν_4, implying $\sin^2 \Delta_{41} \approx 1$, hence $\sin 2\Delta_{41} \approx 0$, thus we drop the imaginary term to leave the real probability

$$P_{\mu e} = -4\Re\left[U_{e4}U_{\mu 4}^{*}\sum_{j=1}^{3}U_{ej}^{*}U_{\mu j}\right]\sin^{2}\Delta_{41}. \tag{2.122}$$

From the unitarity property of $U(4\times 4)$ we know

$$\sum_{i=1}^{4}U_{\alpha i}U_{\beta i}^{*} = \delta_{\alpha\beta}. \tag{2.123}$$

So for $\alpha = e$ and $\beta = \mu$ we have

$$\begin{aligned} \sum_{i=1}^{4}U_{ei}^{*}U_{\mu i} &= 0\,, \\ \therefore\, U_{e4}^{*}U_{\mu 4} + \sum_{i=1}^{3}U_{ei}^{*}U_{\mu i} &= 0\,. \end{aligned} \tag{2.124}$$

Therefore the remaining sum in Eq. (2.122) can be written

$$\sum_{j=1}^{3}U_{ej}^{*}U_{\mu j} = -U_{e4}^{*}U_{\mu 4}. \tag{2.125}$$

Therefore by substituting equation (2.125) into (2.122) the probability reduces to

$$P_{\mu e} = -4\Re\left[-|U_{e4}|^{2}|U_{\mu 4}|^{2}\right]\sin^{2}\Delta_{41}. \tag{2.126}$$

Hence we reach the concise expression

$$P_{\mu e} = 4|U_{e4}|^{2}|U_{\mu 4}|^{2}\sin^{2}\Delta_{41} \tag{2.127}$$

as required.

LBL With Fast Sterile Oscillations

Experiments such as NOνA and T2K have the ν_e from ν_μ appearance channel as one of their detection methods. To look at these probabilities we make the assumptions:

1. Can assume $\sin^2\Delta_{21}$ and $\sin 2\Delta_{21}$ are small for this L/E.
2. Δ_{31} and Δ_{32} terms will predominantly shape the curves and we operate near maximal mixing.

3. All sterile mass splittings are roughly the same, hence: $\Delta_{41} \approx \Delta_{42} \approx \Delta_{43}$.

4. Δ_{41} terms will be averaged due to fast oscillations and limited detector resolution, giving: $\sin^2 \Delta_{41} \approx 1/2$ and $\sin 2\Delta_{41} = 0$.

After averaging over the sterile oscillations the standard probability reduces to:

$$\begin{aligned} P_{\mu e} = &-4\sum_{i>j}^{3} \Re\left[U_{ei}U^*_{ej}U^*_{\mu i}U_{\mu j}\right]\sin^2\Delta_{ij} \\ &-2\sum_{i>j}^{3} \Im\left[U_{ei}U^*_{ej}U^*_{\mu i}U_{\mu j}\right]\sin 2\Delta_{ij} \\ &-4\sum_{j=1}^{3} \Re\left[U_{e4}U^*_{ej}U^*_{\mu 4}U_{\mu j}\right]\frac{1}{2}. \end{aligned} \tag{2.128}$$

Expanding the sums and neglecting Δ_{21} terms gives:

$$\begin{aligned} P_{\mu e} = &-4\Re\left[U_{\mu 3}U^*_{e3}\left(U^*_{\mu 1}U_{e1}\sin^2\Delta_{31} + U^*_{\mu 2}U_{e2}\sin^2\Delta_{32}\right)\right] \\ &-2\Im\left[U_{\mu 3}U^*_{e3}\left(U^*_{\mu 1}U_{e1}\sin 2\Delta_{31} + U^*_{\mu 2}U_{e2}\sin 2\Delta_{32}\right)\right] \\ &-2\Re\left[U_{e4}U^*_{\mu 4}\sum_{j=1}^{3}U^*_{ej}U_{\mu j}\right]. \end{aligned} \tag{2.129}$$

We do not go any further here because these expressions get quite tedious but we do present some probabilities derived this way in section 3.3 where we truncate to some order in small parameters to further simplify. Such modified LBL probabilities are also relevant in our areas of study in sections 5 and 6.

2.6.2 Disappearance and Survival Probabilities

Here we present the generic disappearance and survival properties which we can then adapt for specific baselines. We later present the SBL example and show how the effective short range sterile mixing is derived. This effective mixing is commonly used in the experimental literature to constrain the size of the sterile mixing angles.

For $\alpha = \beta$ the general probability reduces to:

$$P_{\alpha\alpha} = 1 - 4\Re\left[\sum_{i>j}|U_{\alpha i}|^2|U_{\alpha j}|^2\right]\sin^2\Delta_{ij} - 2\Im\left[\sum_{i>j}|U_{\alpha i}|^2|U_{\alpha j}|^2\right]\sin 2\Delta_{ij} \tag{2.130}$$

but trivially: $\Im(|z|^2) = 0$ and $\Re(|z|^2) = |z|^2$ for all complex numbers z. So we have the “survival probability” for the α flavour:

$$P_{\alpha\alpha} = 1 - 4\sum_{i>j} |U_{\alpha i}|^2 |U_{\alpha j}|^2 \sin^2 \Delta_{ij} \tag{2.131}$$

and the “disappearance probability” for the α flavour:

$$1 - P_{\alpha\alpha} = 4\sum_{i>j} |U_{\alpha i}|^2 |U_{\alpha j}|^2 \sin^2 \Delta_{ij}. \tag{2.132}$$

Electron Flavour Oscillations for SBL Reactors

Reactors experiments such as DANSS [96] and SoLi∂ [97] are recent experiments explicitly designed to look for short range ν_e and $\nu_{\bar{e}}$ oscillations, with the survival probability:

$$P_{ee} = 1 - 4\sum_{i>j} |U_{\alpha i}|^2 |U_{\alpha j}|^2 \sin^2 \Delta_{ij}\,. \tag{2.133}$$

Then dropping the non-Δ_{41} terms due to them being small at short range and making the same approximations as in section 2.6.1 gives

$$P_{ee} = 1 - 4|U_{e4}|^2 \left[|U_{e1}|^2 + |U_{e2}|^2 + |U_{e3}|^2\right] \sin^2 \Delta_{41}. \tag{2.134}$$

To simplify this we use the unitarity condition from equation (2.123) with $\alpha = \beta = e$

$$\sum_{i=1}^{4} |U_{ei}|^2 = 1. \tag{2.135}$$

Which we can write out fully and then rearrange

$$\begin{gathered} |U_{e1}|^2 + |U_{e2}|^2 + |U_{e3}|^2 + |U_{e4}|^2 = 1\,, \\ \therefore |U_{e1}|^2 + |U_{e2}|^2 + |U_{e3}|^2 = 1 - |U_{e4}|^2. \end{gathered} \tag{2.136}$$

So using equation (2.136) the bracketed term in equation (2.134) simplifies to give

$$P_{ee} = 1 - 4|U_{e4}|^2 \left[1 - |U_{e4}|^2\right] \sin^2 \Delta_{41}. \tag{2.137}$$

Substituting in the explicit matrix element from section 2.2.3 gives the electron flavour disappearance probability

$$P_{ee} = 1 - 4\sin^2\theta_{14}\left(1 - \sin^2\theta_{14}\right)\sin^2\Delta_{41}. \tag{2.138}$$

We can equate this to the effective disappearance probability

$$P_{ee} = 1 - \sin^2 2\theta_{ee}\sin^2\Delta_{ee} \tag{2.139}$$

to solve for the effective parameters:

$$\Delta_{ee} = \Delta_{41}, \tag{2.140}$$

$$\sin^2 2\theta_{ee} = 4\sin^2\theta_{14}\left(1 - \sin^2\theta_{14}\right) \tag{2.141}$$

$$\approx 4\sin^2\theta_{14}, \tag{2.142}$$

for small θ_{14}.

SBL Muon Neutrino Survival/Disappearance

Similarly, if we have an experiment to measure muon neutrinos in SBL (this is unlikely due to the low energy sources and muon production threshold)

$$\sin^2 2\theta_{\mu\mu} = 4|U_{\mu4}|^2(1 - |U_{\mu4}|^2) \approx |U_{\mu4}|^2, \tag{2.143}$$

for small $|U_{\mu4}|^2$.

2.6.3 Summary of Probabilities for SBL

Turns out we can generalise the effective two flavour transition and survival probabilities at SBL detectors:

$$P_{\alpha\beta}^{\text{SBL}} \approx \sin^2 2\theta_{\alpha\beta}\sin^2\Delta_{41},\ \text{for } \alpha \neq \beta\,, \tag{2.144}$$

$$P_{\alpha\alpha}^{\text{SBL}} \approx 1 - \sin^2 2\theta_{\alpha\alpha}\sin^2\Delta_{41}\,, \tag{2.145}$$

where the transition amplitudes are:

$$\sin^2 2\theta_{\alpha\beta} = 4|U_{\alpha4}|^2|U_{\beta4}|^2\,, \tag{2.146}$$

$$\sin^2 2\theta_{\alpha\alpha} = 4|U_{\alpha 4}|^2 \left(1 - |U_{\alpha 4}|^2\right) , \tag{2.147}$$

with the constraint:

$$\sin^2 2\theta_{\alpha\beta} \approx \frac{1}{4} \sin^2 2\theta_{\alpha\alpha} \sin^2 2\theta_{\beta\beta} . \tag{2.148}$$

These probabilities only depend on Δ_{41} and the absolute values of the 4^{th} column of the PMNS matrix. No CP phases in this column imply that the neutrino and antineutrino probabilities are equal.

2.7 The MSW effect

For neutrinos travelling through dense media, such as the Earth we have to consider the effect of matter interactions on the oscillation probabilities. Unlike space or the atmosphere, the electron density in Earth is high enough to be considered a dense medium even for weakly interacting particles. The effect of this on propagating neutrinos is known as the Mikheyev-Smirnov-Wolfenstein (MSW) effect [98, 99] after the physicists who helped pioneer the theory. What is often confused is the fact that matter effects provide two important phenomena, both of which are commonly referred to as the MSW effect:

1. Resonance enhancement of oscillation in constant density i.e. 'matter oscillation' (see sections 2.7.1, 2.7.2 and 2.7.3),
2. Non-oscillatory 'adiabatic conversion' in slowly varying density (see section 2.7.4).

It is important not to get these two phenomena mixed up (as Smirnov himself is quick to point out [13]) because they are important in different regimes despite initially being described together in the literature. Resonance enhancement, for example, is important for LBL experiments like NOνA and DUNE, as well as for atmospheric neutrinos coming from below in detectors like Super-K and Icecube. Adiabatic conversion, on the other hand, is important for neutrinos produced in the solar core and is responsible for the deficits in solar neutrinos measured by Homestake and SNO. Simply put, the reason these interactions change the oscillation probabilities is that the mass eigenstates which are stationary in vacuum, are modified in the resonance case and in the adiabatic case, are non stationary.

In the mid to late 1970's Wolfenstein proposed that coherent neutrino forward scattering should be accounted for when neutrinos travel through matter [98]. The development of this idea and it's relation to the MSW effect is outlined by Smirnov in [14]. This forward scattering results in a potential V related to the difference of potentials between ν_e and ν_l flavours [100] (due to the extra interactions present for electron flavour on matter electrons)

$$V \equiv V_e - V_l = \sqrt{2} G_F N_e \,, \tag{2.149}$$

where G_F is the Fermi coupling constant of the weak interaction and N_e is the number density of electrons. This potential is often referred to as the 'Wolfenstein Matter Potential'. A full derivation is presented in the thorough analysis by J Linder [101]. A related refraction length can be defined by inverting the potential

$$l_0 \equiv \frac{2\pi}{V} \,, \tag{2.150}$$

which determines the scales at which this effects occur.

After showed that oscillations of massive neutrinos are modified in matter, Wolfenstein also stated that, under the specific condition where the vacuum oscillation length equals the refraction length of the medium, oscillation probabilities are *highly* modified. This was presented with little discussion and somewhat pre-empted work on the resonance phenomenon which was fleshed out by Mikheyev and Smirnov. It's important to note that Wolfenstein originally considered massless neutrinos, which cannot oscillate in vacuum, but *can* oscillate in matter.

For neutrinos in the MeV-GeV range potential, mass splitting and Earth radius are related by

$$\frac{\Delta m^2_{21}}{2E} \sim V \sim \frac{1}{R_E} \,, \tag{2.151}$$

where R_E is the radius of the Earth. Smirnov refers to this coincidence (the remarkable fact that we can see matter effects at all despite the smallness of V), as a "conspiracy of small quantities" [13].

Mikheyev and Smirnov are better known for discovering the full form of the resonance phenomenon and adiabaticity conditions [14]. Properties of these two phenomena were also discussed in detail and a graphical representation was developed. Sometime after the combination of all development in this area became known as the MSW effect.

A feature of these interactions that can be utilised in detectors such as NOνA and DUNE is that the corrections due to resonance enhancement have opposite signs for neutrinos and antineutrinos. So because these detectors can provide either, the value of the corrections can be determined by running an experiment with neutrinos and antineutrinos. The signs of the corrections will also flip depending on whether the mass ordering is normal or inverted, hence running neutrinos and antineutrinos in these detectors allows even greater ability to constrain NO/IO solutions.

2.7.1 Mixing Parameters in Matter

In matter, the mixing angles become a function of density thus making the flavour eigenstates also density dependent. So in vacuum we treat the mixing angles as fundamental parameters of the vacuum Hamiltonian (H_0), while in matter the mixing angles become variables [13]. We denote the general Hamiltonian as

$$H_M = H_0 + V \, , \tag{2.152}$$

where we have added a matrix of potentials V, which account for matter effects. The mass eigenstates of the matter Hamiltonian H_M are ν_M and are different to the vacuum mass eigenstates ν for H_0. We now wish to see how this affects mixing angles. In the two flavour approximation we will therefore have flavour eigenstates made of *different* mixtures of *different* eigenstates which can be written

$$\nu_e = \quad \cos\theta_{12}^M \nu_{1M} + \sin\theta_{12}^M \nu_{2M} \, , \tag{2.153}$$

$$\nu_a = -\sin\theta_{12}^M \nu_{1M} + \cos\theta_{12}^M \nu_{2M} \, , \tag{2.154}$$

with the mass eigenstates in matter denoted ν_{iM} and the mixing angle in matter generally differing from the angle in vacuum, that is $\theta_M \neq \theta$. Similarly the matter eigenstates can be written

$$\nu_{1M} = \cos\theta_{12}^M \nu_e - \sin\theta_{12}^M \nu_\mu \, , \tag{2.155}$$

$$\nu_{2M} = \sin\theta_{12}^M \nu_e + \cos\theta_{12}^M \nu_\mu \, . \tag{2.156}$$

So the mixing angle determines the flavour composition of the mass eigenstates as usual, though the mixing angle becomes a dynamical variable in matter, dependent on density and energy. So we have

$$\theta_M = \theta_M \left(n(t), E \right) \tag{2.157}$$

with density $n(t)$ and energy E. So for constant density, this appears similar to vacuum mixing, with the size of the dip in the oscillations being $\sin^2\theta_M$. There also exists an energy such that for a particular density, the depth of oscillations will become maximal ($\sin^2\theta_M = 1$, hence $\theta_M(n, E) = \pi/4$) and total conversion between flavours will occur. This is know as the resonance energy and is denoted E_R. When the density becomes incredibly high, well above resonance for any reasonable energy, the mixing angle saturates at $\theta_M(n, E) = \pi/2$ and the mixing disappears. So as the density decreases from this saturated value the mixing angle will move towards resonance then eventually on to the vacuum mixing angle $\theta_M \approx \theta$ when the density is much less than resonance.

2.7.2 Matter Oscillation Parametrisation

We want to verify how the MSW resonance enhancement effect modifies our oscillation theory at the probability level and how we can relate it to our vacuum equations. In this section we will see an illustrative two flavour oscillation example confirming that matter oscillations can be dealt with by simply using the standard parametrisation and replacing the standard mixing parameters with matter ones. We approach this from the Schrödinger equation with the knowledge of two flavour mixing from section 2.3. For the vacuum oscillations in the two flavour case ($\Delta m^2_{21} = \Delta m^2$) we can write out the Schrödinger equation

$$i\frac{d}{dt}\begin{pmatrix}\nu_e\\ \nu_\mu\end{pmatrix} = H_0\begin{pmatrix}\nu_e\\ \nu_\mu\end{pmatrix}\ , \tag{2.158}$$

where H_0 is the vacuum Hamiltonian. We eventually want this in terms of θ and Δm^2 so we can relate the matter case to the the vacuum case using effective versions of these parameters. We derive this Hamiltonian using the time evolution of the *mass* eigenstates

$$i\frac{d}{dt}\begin{pmatrix}\nu_1\\ \nu_2\end{pmatrix} = \begin{pmatrix}E_1 & 0\\ 0 & E_2\end{pmatrix}\begin{pmatrix}\nu_1\\ \nu_2\end{pmatrix}\ . \tag{2.159}$$

Substituting the approximation for ultrarelativistic energy of eigenstates $E_i = p_i + \frac{m_i^2}{2E}$ from equation (2.85) and making the naive $p_1 \approx p_2 \equiv p$ from section 2.3 we get

$$i\frac{d}{dt}\begin{pmatrix}\nu_1\\ \nu_2\end{pmatrix} \approx \begin{pmatrix}\frac{m_1^2}{2E} & 0\\ 0 & \frac{m_2^2}{2E}\end{pmatrix}\begin{pmatrix}\nu_1\\ \nu_2\end{pmatrix} + \begin{pmatrix}p & 0\\ 0 & p\end{pmatrix}\begin{pmatrix}\nu_1\\ \nu_2\end{pmatrix}\ ,$$

$$= \left[\begin{pmatrix} \frac{m_1^2}{2E} & 0 \\ 0 & \frac{m_2^2}{2E} \end{pmatrix} + p \begin{pmatrix} 1 & 0 \\ 0 & 1 \end{pmatrix} \right] \begin{pmatrix} \nu_1 \\ \nu_2 \end{pmatrix} . \tag{2.160}$$

Note that terms which are constant multiples of the identity will only introduce constant phase factors into the Hamiltonian. These will cancel out for oscillations and therefore may be omitted [102]. This is why we are able to remove the momentum term, leaving

$$i\frac{d}{dt} \begin{pmatrix} \nu_1 \\ \nu_2 \end{pmatrix} = \begin{pmatrix} \frac{m_1^2}{2E} & 0 \\ 0 & \frac{m_2^2}{2E} \end{pmatrix} \begin{pmatrix} \nu_1 \\ \nu_2 \end{pmatrix} . \tag{2.161}$$

Now substituting in the two flavour mixing matrix from the two flavour section, equation (2.47)

$$i\frac{d}{dt} \begin{pmatrix} -\sin\theta & \cos\theta \\ \cos\theta & \sin\theta \end{pmatrix} \begin{pmatrix} \nu_e \\ \nu_\mu \end{pmatrix} = \frac{1}{2E} \begin{pmatrix} m_1^2 & 0 \\ 0 & m_2^2 \end{pmatrix} \begin{pmatrix} -\sin\theta & \cos\theta \\ \cos\theta & \sin\theta \end{pmatrix} \begin{pmatrix} \nu_e \\ \nu_\mu \end{pmatrix} . \tag{2.162}$$

Then, knowing that this two flavour mixing matrix is it’s own inverse (from the two flavour section 2.3), we can modify equation (2.162) by taking the matrix on the left hand side over to the right.

$$\begin{aligned} \Rightarrow i\frac{d}{dt} \begin{pmatrix} \nu_e \\ \nu_\mu \end{pmatrix} &= \frac{1}{2E} \begin{pmatrix} -\sin\theta & \cos\theta \\ \cos\theta & \sin\theta \end{pmatrix} \begin{pmatrix} m_1^2 & 0 \\ 0 & m_2^2 \end{pmatrix} \begin{pmatrix} -\sin\theta & \cos\theta \\ \cos\theta & \sin\theta \end{pmatrix} \begin{pmatrix} \nu_e \\ \nu_\mu \end{pmatrix} , \\ &= \frac{1}{2E} \begin{pmatrix} -\sin\theta & \cos\theta \\ \cos\theta & \sin\theta \end{pmatrix} \begin{pmatrix} -m_1^2\sin\theta & m_1^2\cos\theta \\ m_2^2\cos\theta & m_2^2\sin\theta \end{pmatrix} \begin{pmatrix} \nu_e \\ \nu_\mu \end{pmatrix} . \end{aligned} \tag{2.163}$$

Now we multiply out these matrices

$$i\frac{d}{dt} \begin{pmatrix} \nu_e \\ \nu_\mu \end{pmatrix} = \frac{1}{2E} \begin{pmatrix} m_1^2\sin^2\theta + m_2^2\cos^2\theta & m_2^2\sin\theta\cos\theta - m_1^2\sin\theta\cos\theta \\ m_2^2\sin\theta\cos\theta - m_1^2\sin\theta\cos\theta & m_1^2\cos^2\theta + m_2^2\sin^2\theta \end{pmatrix} \begin{pmatrix} \nu_e \\ \nu_\mu \end{pmatrix} . \tag{2.164}$$

To simplify this we substitute $\Delta m^2 = m_2^2 - m_1^2$ and $m_2^2 = \Delta m^2 + m_1^2$, and use $\sin^2\theta + \cos^2\theta = 1$ to give

$$i\frac{d}{dt} \begin{pmatrix} \nu_e \\ \nu_\mu \end{pmatrix} = \frac{1}{2E} \begin{pmatrix} m_1^2 + \Delta m^2\cos^2\theta & \Delta m^2\sin\theta\cos\theta \\ \Delta m^2\sin\theta\cos\theta & m_1^2 + \Delta m^2\sin^2\theta \end{pmatrix} \begin{pmatrix} \nu_e \\ \nu_\mu \end{pmatrix} . \tag{2.165}$$

Then removing the constant multiple of the identity matrix, $m_1^2\mathbb{I}$ and pulling out constants further simplifies our expression to

$$i\frac{d}{dt}\begin{pmatrix}\nu_e\\ \nu_\mu\end{pmatrix} = \frac{\Delta m^2}{2E}\begin{pmatrix}\cos^2\theta & \sin\theta\cos\theta\\ \sin\theta\cos\theta & \sin^2\theta\end{pmatrix}\begin{pmatrix}\nu_e\\ \nu_\mu\end{pmatrix}. \tag{2.166}$$

Therefore, using the double angle formulae, $\cos^2\theta = \frac{1}{2}(\cos 2\theta + 1)$, $\sin^2\theta = \frac{1}{2}(-\cos 2\theta + 1)$ and $\sin\theta\cos\theta = \frac{1}{2}\sin 2\theta$ we find

$$\begin{aligned} i\frac{d}{dt}\begin{pmatrix}\nu_e\\ \nu_\mu\end{pmatrix} &= \frac{\Delta m^2}{4E}\begin{pmatrix}\cos 2\theta + 1 & \sin 2\theta\\ \sin 2\theta & -\cos 2\theta + 1\end{pmatrix}\begin{pmatrix}\nu_e\\ \nu_\mu\end{pmatrix},\\ &= \frac{\Delta m^2}{4E}\left[\begin{pmatrix}\cos 2\theta & \sin 2\theta\\ \sin 2\theta & -\cos 2\theta\end{pmatrix} + \begin{pmatrix}1 & 0\\ 0 & 1\end{pmatrix}\right]\begin{pmatrix}\nu_e\\ \nu_\mu\end{pmatrix}, \end{aligned} \tag{2.167}$$

so again we remove the constant multiple of the identity matrix, leaving

$$i\frac{d}{dt}\begin{pmatrix}\nu_e\\ \nu_\mu\end{pmatrix} = \frac{\Delta m^2}{4E}\begin{pmatrix}\cos 2\theta & \sin 2\theta\\ \sin 2\theta & -\cos 2\theta\end{pmatrix}\begin{pmatrix}\nu_e\\ \nu_\mu\end{pmatrix}, \tag{2.168}$$

which is clearly the form of the Schrödinger equation with the vacuum Hamiltonian

$$H_v = \frac{\Delta m^2}{4E}\begin{pmatrix}\cos 2\theta & \sin 2\theta\\ \sin 2\theta & -\cos 2\theta\end{pmatrix}. \tag{2.169}$$

This Hamiltonian clearly gives the standard 2ν oscillation probability for $\nu_e \to \nu_\mu$ from equation (2.65)

$$P_{e\mu} = \sin^2 2\theta \sin^2\Delta\,. \tag{2.170}$$

We can then write a similar Hamiltonian for neutrinos travelling through matter by adding a CC potential term that will interact with the electron flavour state due to the electron content of matter

$$\begin{aligned} H_M &= H_0 + \mathrm{diag}(V, 0) \qquad (2.171)\\ &= \frac{\Delta m^2}{4E}\begin{pmatrix}\cos 2\theta & \sin 2\theta\\ \sin 2\theta & -\cos 2\theta\end{pmatrix} + \begin{pmatrix}V & 0\\ 0 & 0\end{pmatrix}, \end{aligned}$$

the extra potential term is the Wolfenstein Matter Potential from equation (2.149) in section 2.7

$$V = \pm\sqrt{2}G_F N_e\,, \tag{2.172}$$

where the $+(-)$ signs are for electron neutrinos(antineutrinos), G_F is the Fermi constant and N_e is the electron density in matter. An explanation of the sign change between neutrinos and antineutrinos is explained in [101] and is to do with the relative sign between creation and annihilation operators changing for neutrinos and antineutrinos. Note that we can also add an NC potential affecting all flavours. Because such a term would be of the form $V_{\mathrm{NC}}\mathbb{I}$ it would not affect oscillation due to being a constant multiple of the identity so we simply leave it out. Equation (2.171) can be rewritten by subtracting a constant multiple of the identity, $(1/2)V\mathbb{I}$, without modifying the physics (see section 2.3 where we did the reverse of this). So we write

$$H_M = \frac{\Delta m^2}{4E}\begin{pmatrix}\cos 2\theta & \sin 2\theta\\ \sin 2\theta & -\cos 2\theta\end{pmatrix} + \begin{pmatrix}V & 0\\ 0 & 0\end{pmatrix} - \frac{1}{2}\begin{pmatrix}V & 0\\ 0 & V\end{pmatrix}, \tag{2.173}$$

and collect terms to obtain

$$H_M = \frac{\Delta m^2}{4E}\begin{pmatrix}\cos 2\theta + \frac{2VE}{\Delta m^2} & \sin 2\theta\\ \sin 2\theta & -\cos 2\theta - \frac{2VE}{\Delta m^2}\end{pmatrix}. \tag{2.174}$$

We then define a term to simplify this expression

$$A = \frac{2VE}{\Delta m^2} = \pm\frac{2\sqrt{2}G_F N_e E}{\Delta m^2}, \tag{2.175}$$

and our Hamiltonian becomes

$$H_M = \frac{\Delta m^2}{4E}\begin{pmatrix}\cos 2\theta + A & \sin 2\theta\\ \sin 2\theta & -\cos 2\theta - A\end{pmatrix}. \tag{2.176}$$

We then write the Hamiltonian in a similar form to before but with *effective* (subscript M for matter) mass squared differences and mixing angles

$$H_M = \frac{\Delta m_M^2}{4E}\begin{pmatrix}\cos 2\theta_M & \sin 2\theta_M\\ \sin 2\theta_M & -\cos 2\theta_M\end{pmatrix}. \tag{2.177}$$

Clearly this Hamiltonian leads to a similar oscillation probability to the vacuum case albeit with the parameters exchanged for the effective ones,

$$(P_{e\mu})_M = \sin^2 2\theta_M \sin^2\left(\frac{\Delta m_M^2}{4E}L\right). \tag{2.178}$$

Equating (2.176) and (2.177) to get the relationship between the effective terms and the vacuum terms gives us:

$$\Delta m_M^2 = C\Delta m^2, \tag{2.179}$$

$$\sin^2 2\theta_M = \frac{\sin^2 2\theta}{C^2}, \tag{2.180}$$

where C is a term relating the vacuum mixing terms to the A matter term

$$C = \sqrt{(\cos 2\theta - A)^2 + \sin^2 2\theta}. \tag{2.181}$$

We can see from above that for small values of A the probabilities approach the vacuum approximation, therefore we need a long baseline (hence high E and high A) to observe matter effects. There also exists a resonance condition that enhances oscillation, $\cos 2\theta = A$, this occurs regardless of the true mixing angle. If we rearrange this resonant condition using the expression for A, equation (2.175), we can obtain an equation giving the energy at which this resonance occurs for neutrinos [103]

$$E_R = \Delta m^2 \frac{\cos 2\theta}{2\sqrt{2}G_F N_e}. \tag{2.182}$$

The energy window in which oscillations are enhanced is

$$\Delta E_R = E_R \tan 2\theta\,. \tag{2.183}$$

These two factors are important in experiment design because they can be used to optimise the baseline and neutrino energies to increase the chance of detecting an oscillation signal. Also of note is the fact that, even if neutrinos do not experience CP violation (i.e. allowing neutrino and antineutrino oscillation probabilities to be equal in vacuum), the difference between neutrino and antineutrino probabilities in matter can still be non-zero due entirely to matter effects.

2.7.3 MSW Effect in the 3+1 Case

Recall that the potential (V) associated with the MSW effect is added to the vacuum Hamiltionian to give the matter Hamiltonian. For three flavours it is

$$V^{3\nu} = \begin{pmatrix} V_{CC} & 0 & 0 \\ 0 & 0 & 0 \\ 0 & 0 & 0 \end{pmatrix}, \tag{2.184}$$

where V_{CC} is the same Wolfenstein matter term seen before in sections 2.3 and 2.7.2. This three flavour matter Hamiltonian will modify the oscillation probabilities similar to how the two flavour example does. We add the label CC for charged current to make it explicitly clear what relationship leads to this potential. To obtain this potential we previously subtracted off the neutral current (NC) component in the Hamiltonian because it effects all active flavours equally. However, in the 3+1 case, the fourth sterile flavour does not have either of these interactions so the total potential term would look like

$$V^{4\nu}_{\text{total}} = \begin{pmatrix} V_e & 0 & 0 & 0 \\ 0 & V_\mu & 0 & 0 \\ 0 & 0 & V_\tau & 0 \\ 0 & 0 & 0 & V_s \end{pmatrix}, \tag{2.185}$$

with the explicit potentials $V_e = V_{CC} + V_{NC}$, $V_\mu = V_\tau = V_{NC}$ and $V_s = 0$. So after we subtract non-contributing constant identity multiple ($V_{NC}\mathbb{I}$) off our potential there will be a left over negative term in the fourth position, therefore we have

$$V^{4\nu} = \begin{pmatrix} V_{CC} & 0 & 0 & 0 \\ 0 & 0 & 0 & 0 \\ 0 & 0 & 0 & 0 \\ 0 & 0 & 0 & -V_{NC} \end{pmatrix}. \tag{2.186}$$

So whereas before we didn't care about the NC (Z-boson mediated) potential, we now need to include it. It has a similar form to the CC term

$$V_{NC} = -\frac{1}{\sqrt{2}} G_F N_n. \tag{2.187}$$

but is negative for neutrinos and based on the neutron density (N_n). Interestingly enough the proton and electron NC contributions cancel themselves out full details are explored in [101]. We do not calculate the corresponding probabilities here because they will be complicated. In our studies this step is approximated by GLoBES (see chapter 4) so we do not have to do the hard work ourselves!

2.7.4 MSW in Varying Density: Adiabatic Conversion

Up until now when discussing matter effects we have only considered matter of uniform density. While this is a good approximation of the outer Earth crust, it is not a good approximation of the centre of the Sun. Unfortunately we must consider the high density solar core if we are going to accurately analyse solar neutrinos. The key property here is the fact that the density varies with radius, starting extremely high in the core and gradually decreasing towards the surface. This affects oscillations because as the density changes, the matter mixing angle will change. Under conditions where this change is slow the system can transition adiabatically, leading to so-called 'adiabatic conversion' of neutrinos which will be explained here using the methods pioneered by Mikheev and Smirnov in the mid to late 80's [99, 104, 105][1]. Under these conditions L/E dependent oscillation itself is *almost* irrelevant. Such an effect that is still important is the small ν_e regenerative effect on solar neutrinos propagating up through Earth, where ν_μ and ν_τ that originally transformed from ν_e can oscillate *back* into ν_e. As we discussed earlier in sections 1.3.1 and 1.3.2, this effect would show a *slight* day/night asymmetry in detectors that can measure event timing such as Super-K, or an overall *slightly* smaller disappearance in a 'collect and count' experiment such as Homestake.

Returning to adiabatic conversion, we consider a medium of decreasing density $\rho_R(E)$ with minimum density close to zero (i.e. empty space), then

$$\rho_{\min} \sim 0 \ll \rho_{\mathrm{R}}(E) \ll \rho_{\max}\,. \tag{2.188}$$

Supposing that the neutrinos are produced at the location of maximum density $\rho_{\max}$ implies that the initial mixing angle will be maximal which by definition implies

---

[1] Smirnov has released many useful retrospective publications, for example [13, 14], to help explain the principles behind these works and to debunk some of the confusion surrounding the MSW effect and so called solar 'oscillations'.

$\theta_M \approx \pi/2$. So for initial electron flavour we have

$$\nu_{\text{initial}} = \nu_e \approx \nu_{2M}(\rho_{\text{max}}) \tag{2.189}$$

i.e. the flavour eigenstate ν_e almost coincides with the heaviest involved mass eigenstate, which in this case is the particular matter mass eigenstate ν_{2M} at this specific maximum density. Note that in principle, if only a single mass eigenstate propagates there will be no oscillation because there is no interference. Hence if electron neutrinos are being roughly produced in one mass state due to the density of the surrounding medium, then flavour transitions must happen via another method.

We assume the adiabatic condition, which is that density varies slowly and implies that transitions between mass eigenstates $\nu_{2M} \leftrightarrow \nu_{1M}$ can be neglected [13]. So we assume that over the course of adiabatic propagation

$$\nu(\rho) \approx \nu_{2M}(\rho) \longrightarrow \nu_{2M}(\rho_{\text{min}})\,. \tag{2.190}$$

that is, if this change is indeed adiabatic then only the ν_{2M} eigenstate is involved and no ν_{1M} state is produced [13]. This implies that the change in flavour will directly correspond to changes in the mass eigenstate due to slowly varying density, with no interference-driven oscillation occurring. A visualisation of this $\nu_{2M} \rightarrow \nu_2$ transition and the changing flavour composition can be seen in figure 2.3. So as the density changes in the adiabatic transition case, the mixing angles change and hence the flavour content of the mass eigenstates will change. We can therefore have transformation of neutrino flavour because the mass eigenstate adiabatically transforms from almost entirely ν_e to (for example) a mixture of ν_e and ν_μ. So the survival probability of ν_e will be reduced and the appearance probability of ν_μ will become non-zero similar to standard oscillations. Note that this phenomenon can even cause transitions if there is no mixing in vacuum i.e. $\theta = 0$.

The final density is assumed to be zero $\rho_{\text{min}} = 0$, i.e. a perfect vacuum, hence the final mixing angle will be equivalent to the vacuum mixing angle $\theta_M(\rho_{\text{min}}) = \theta$ this will then imply that the final version of the mass eigenstate will also be equivalent to the vacuum case $\nu_{\text{final}} = \nu_{2M}(\rho_{\text{min}}) = \nu_2$. So the electron flavour amplitude in the final state is

$$\langle \nu_e | \nu_{\text{final}} \rangle = \langle \nu_e | \nu_2 \rangle = \sin\theta\,, \tag{2.191}$$

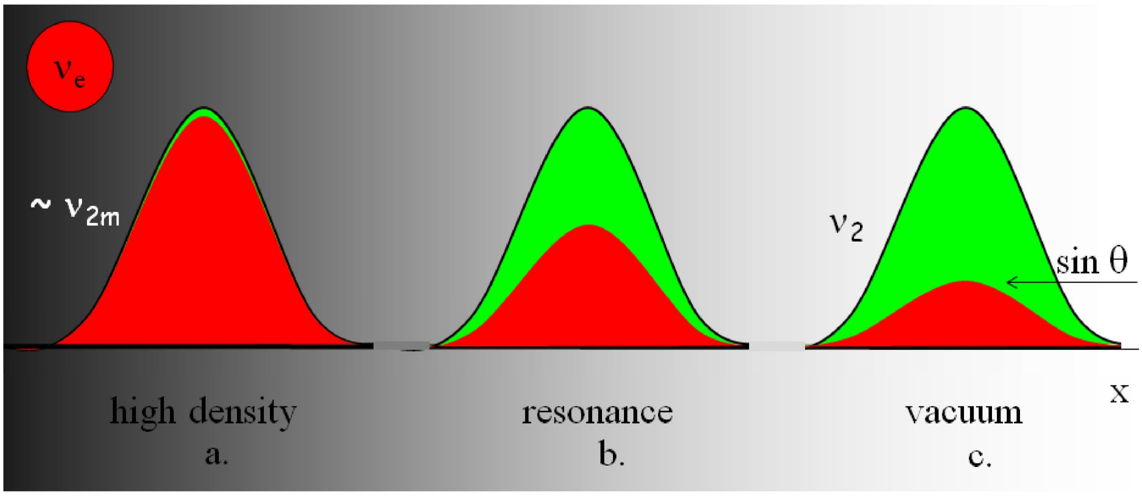

FIG. 2.3 Wavepacket picture of adiabatic conversion in a medium decreasing from incredibly high density to vacuum. In this case we make the approximation that initially there is just one neutrino mass eigenstate and it is almost entirely electron flavour. Taken from A. Yu. Smirnov 2016 [13].

which is the height of the ν_e component of the neutrino wavepacket in figure 2.3 c. The survival probability for electron flavour after this non-oscillatory adiabatic conversion is

$$P = |\langle\nu_e|\nu_2\rangle|^2 = \sin^2\theta\,, \tag{2.192}$$

which is the same as equation (1.25) from section 1.3.2. A more general example where the initial density is not overly large (so initially $\nu_{2M} \not\approx \nu_e$) with two mass eigenstates transitioning ($\nu_{2M} \to \nu_2$ and $\nu_{1M} \to \nu_1$) is shown in figure 2.4. In this case the ν_{1M} in the initial case can not be ignored and initial mixing (θ_M^0) will not be maximal. In this case, if the density still changes adiabatically, then a combination of oscillation and adiabatic transition will occur. This leads to the averaged adiabatic survival probability that SNO calculated (see section 1.3.2), which we repeat here

$$P = \sin^2\theta + \cos 2\theta\cos^2\theta_M^0\,. \tag{1.29}$$

Recall also, that θ_M^0 is the matter mixing angle in the production point from equation (1.30) which we also repeat here

$$\theta_M^0 = |\langle\nu_{1M}|\nu(t)\rangle|^2\,. \tag{1.30}$$

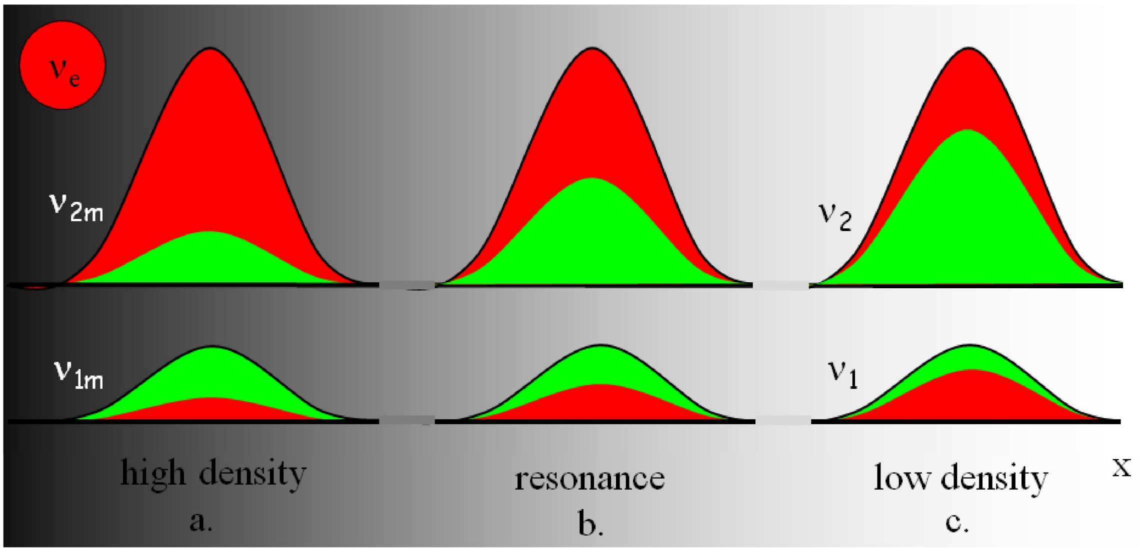

FIG. 2.4 A general wavepacket picture involving two mass eigenstates showing adiabatic conversion in a medium decreasing from high to low density. Taken from A. Yu. Smirnov 2016 [13]. Oscillation will also take place in this case but is not shown here.

The initial matter mixing $\sin\theta_M^0$ and $\cos\theta_M^0$ correspond respectively to the electron flavour components of ν_{1M} and ν_{2M} in figure 2.4. This clearly reduces to the idealised case of figure 2.3 for maximal initial mixing, because if $\sin\theta_M^0 \approx 1$ then $\cos\theta_M^0 \approx 0$, so the second term of equation (1.29) goes to zero leaving us with equation (2.192).

Note that there is an energy dependence on the survival probability in this decreasing density regime, for particularly low energies the probability instead is given purely by averaged oscillations

$$P(E_{\text{low}}) = 1 - \sin^2 2\theta \langle \sin^2 \Delta \rangle = 1 - \frac{1}{2}\sin^2 2\theta \,, \tag{2.193}$$

where $\langle \sin^2 \Delta \rangle = 1/2$ is the L/E average of $\sin^2\Delta$. Similarly for energies above that of the adiabatic conversion case, a non-adiabatic conversion occurs and the survival probability approaches unity as energy increases i.e. no oscillations occur.

CHAPTER 3

STERILE NEUTRINOS AND OTHER EXTENSIONS

Theories involving extra neutrinos beyond the known three have existed for a long time as potential solutions for various problems including oscillations, dark matter and light neutrino masses. The term ‘sterile’ introduced in most of these cases is used to denote that such neutrinos are singlets and therefore lack the weak interaction characteristics of the active neutrinos. This implies that there are no Z and $W^{\pm}$ vertices involving ν_s leaving such neutrinos with very few possible interactions with the rest of physics, at least in the standard model. Due to the lack of weak interaction these additional flavours will not contribute to the invisible decay width of the Z boson and its relationship to the number of active neutrino flavours. Despite all of this, because these neutrinos may be massive they can still potentially oscillate as well as contribute to dark matter.

The relationship between such sterile and right-handed neutrinos is also of interest because both are singlets with regards to the weak interaction. But it should be noted that they aren’t necessarily one and the same.

3.1 Constraints on Number of Neutrinos

What constraints do we have on the number of neutrinos? Is there even room for another neutrino flavour? How can sterile neutrinos get around these constraints? Light active neutrinos are constrained by post Big Bang processes as well as the invisible decay width of the Z boson. An example of the former is the process $e^{+} + e^{-} \rightarrow \nu + \overline{\nu}$ if Fig 3.1, which should, due to universality, portion energy from nuclear processes amongst neutrino flavours in an even fashion. The resulting proportion of energetic electron neutrinos helps fuel processes such as $\nu_e + n \rightarrow p + e^{-}$

so the rate of this reaction is modified by the number of neutrino flavours the Z boson interacts with.

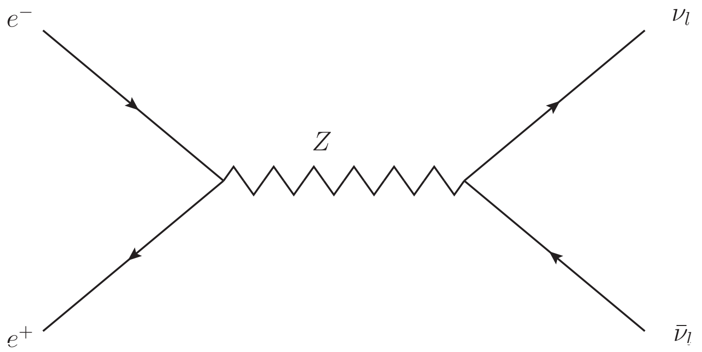

FIG. 3.1 $e^+ + e^- \rightarrow \overline{\nu}_l + \nu_l$ interaction used to constrain the invisible width of the Z boson. Where the subscript l indicates that the neutrinos can be of any *active* flavour.

Similarly the LEP (Large Electron-Positron collider) measured the Z resonance by colliding electrons and positrons. Eventually, a global fit containing data from multiple collaborations produced a high-precision constraint on the number of light active neutrino flavours as $N_\nu = 2.9841 \pm 0.0082$ [106].

This would seem to preclude the addition of an additional flavour eigenstate to the neutrino picture. However this constraint can be dodged with additional flavours that have corresponding large masses (i.e. predominantly mix with very large mass eigenstates) or flavours that lack the weak interaction or even both. This comes from the fact that if the neutrinos have a large enough mass such that the decays and interactions are unavailable. In the case of Z decay this will be true for $m_\nu > m_Z/2$. So if the we have an eigenstate with mass over half that of the Z boson then it will not contribute to these decay widths. Similarly, if they are sterile they will not participate in the first place, hence not adding to these numbers. Recall that this is where the term ‘sterile’ in reference to neutrinos comes from, denoting neutrinos that lack the weak interaction and as such only interact with active neutrinos via some sort of mixing. Returning to the description of chiralities from Sec. 1.10 we see that if the neutrinos are sterile, then we expect them to be singlets and they may or may not be right-handed. If sterile neutrinos exist as left-handed singlets (that somehow lack weak interactions) then the standard formalism becomes broken, while right-handed singlets fit rather normally with the current understanding.

Overall the main motivations for extra neutrinos can be summarised as

- Short Baseline (SBL) anomalies (see Chapter 3.1.1)

- Dark Matter candidate(s)
- See-saw mechanism for small active ν masses from large ν_S masses.

3.1.1 SBL Anomalies

Sterile neutrino models are motivated in a large way by the anomalies present in SBL neutrino data. At short baselines the addition of at least one extra mass eigenstate causes additional high-frequency oscillations, these can potentially explain the anomalies. Such an eigenstate is assumed to be sterile to fit with the rest of our knowledge of charged leptons.

LBL experiments are not directly sensitive to these high frequency oscillations because they tend to be averaged out of the data, this leaves these experiments with poor discovery potential. However, if the presence of a sterile neutrino can be confirmed (or denied) then LBL experiments have a much greater ability to measure the CP phases and to distinguish if any degeneracies are present due to much higher matter effects. This is especially important if more than one CP phase is non-zero.

Reactor Neutrino Anomaly

This anomaly is a deficit in the $\bar{\nu}_e$ rate observed at several SBL reactor experiments compared to revised flux calculations [107]. The preference for new mass splitting is around $|\Delta m^2_{\rm new}| \approx 1.5~{\rm eV}^2$ [108]. It has also been argued that statistical uncertainties in antineutrino fluxes are too large to infer an 'anomaly' in this sector [109].

Gallium Neutrino Anomaly

The Gallium anomaly refers to the deficit in the ν_e rate measured by radioactive source experiments using gallium in the detectors, specifically the GALLEX and SAGE solar neutrino detectors. The detection method is the observation of specific gallium to germanium inverse beta decays corresponding to electron neutrino capture (repeated from section 1.2):

$$\nu_e + {}^{71}{\rm Ga} \to {}^{71}{\rm Ge} + e^- \,. \tag{1.16}$$

When tested with radioactive neutrino sources ^{37}Ar and ^{51}Cr for calibration purposes, these experiments produced anomalous results compared to predicted rates [12, 110]. Particularly, measurement of the aforementioned electron-capture decays showed a deficit in electron neutrinos. The combined significance of this anomaly from

GALLEX and SAGE was found to be around $\sim 3\sigma$ [111]. Recent analyses show lower significance (reduced from 3.0σ to 2.3σ) but are still compatible with a sterile oscillation solutions to reactor $\overline{\nu}_e$ disappearance [112] and a new $\sim \mathrm{eV}^2$ scale mass splitting.

LSND Neutrino Anomaly

The Liquid Scintillator Neutrino Detector at the Los Alamos Neutron Science Center or LSND, observed an excess of $\bar{\nu}_e$ in a $\bar{\nu}_\mu$ from a muon decay at rest source using stopped pions [113]. This was inconsistent with standard mixing so could be interpreted as evidence for a fourth mass splitting in the neutrino sector. The similar KARMEN experiment, however, saw no excess [114].

The MiniBooNE experiment is an accelerator source able to produce ν_μ and $\overline{\nu}_\mu$ and intended to provide follow up measurements of the SBL $\nu_\mu \to \nu_e$ channel probed by LSND. The results from MiniBooNE were originally thought to be inconclusive, but recent analysis has since yielded significant excesses (total 4.8σ) in ν_e (4.5σ) and $\bar{\nu}_e$ (2.8σ) channels [115]. These results seem somewhat consistent with LSND and combined statistics gives 6.1σ significance to the existence of these excesses with a mass splitting $\Delta_{41} \approx 1\ \mathrm{eV}^2$. It has been mentioned that the MiniBooNE data for energies below 475 MeV correspond to L/E values outside the LSND range. The authors of [116] consider the MiniBooNE low-energy excess to be potentially separate from the corresponding LSND anomaly. They call this the “MiniBooNE low-energy anomaly” to distinguish it.

Summary of SBL Anomalies

These anomalies can be summarised by the different effective mixings involved and the PMNS matrix elements they depend on. The probability at short baseline assuming that $\Delta m^2_{41} \gg |\Delta m^2_{31}|, \Delta m^2_{21}$ can be simplified to

$$P_{\alpha\beta} = \delta_{\alpha\beta} - 4|U_{\alpha\beta}|^2 \left(\delta_{\alpha\beta} - |U_{\alpha\beta}|^2\right) \sin\Delta_{41}\,. \tag{3.1}$$

Hence substituting in α and β for each experimental channel and comparing to the effective mixing probability $P_{\alpha\beta} = \sin^2 2\theta_{\alpha\beta} \sin^2 \Delta_{\alpha\beta}$ gives a different value for the effective mixing parameter $\theta_{\alpha\beta}$,

$$\nu_e \longrightarrow \nu_e : \sin^2 2\theta_{ee} \ \equiv 4|U_{e4}|^2 \left(1 - |U_{e4}|^2\right) \quad (\text{Reactor},\ \text{Gallium anomalies})\,, \tag{3.2}$$

$$\nu_\mu \longrightarrow \nu_\mu : \sin^2 2\theta_{\mu\mu} \equiv 4|U_{\mu 4}|^2 \left(1 - |U_{\mu 4}|^2\right) \quad \text{(no anomaly observed)}\,, \tag{3.3}$$

$$\nu_\mu \longrightarrow \nu_e : \sin^2 2\theta_{\mu e} \equiv 4|U_{\mu 4}|^2 |U_{e4}|^2 \quad \text{(LSND, MiniBooNE anomalies)}\,. \tag{3.4}$$

See alternate explicit derivations in sections 2.6.1 and 2.6.2. Note that for SBL oscillations $\Delta_{\alpha\beta} \approx \Delta_{41}$ for all α and β. An important note is that tension still persists between the appearance (LSND, MiniBooNE) and disappearance (Reactor, Gallium) anomalous measurements [87, 116].

3.2 Extensions Featuring 4 Neutrino Mass Eigenstates

Neutrino models with an additional ν_4 eigenstate are the minimal extension to the SM neutrino model. This model can offer explanations for the SBL anomalies. This model, known as $3+1$, adds one mass eigenstate (ν_4) primarily composed of a new sterile flavour (usually denoted ν_s) with minor mixing to the standard 3 flavours of neutrino. As with the standard neutrino oscillation case this introduces a new mass difference ($\Delta m^2_{41} \approx 10^{-5}$-$10^2$ eV^2) which can be positive or negative. In this case however the positive case is usually taken to be true as otherwise the three standard mass eigenstates must be more massive than estimated. The comparatively large value of this mass difference allows the two flavour approximation to be used when calculating active-sterile mixing. Other theorised extensions are introduced in section 3.4.2 but these are less important in the main cases we consider.

It is also worth noting that extra neutrinos are often brought up when discussing dark matter (DM), however the $3+1$ case is usually not suitable for this. Models with a light sterile neutrino do not provide a DM candidate that fits with current constraints, instead these prefer other light WIMPS (Weakly Interacting Massive Particles) such as the neutralino [117] which are the SUSY (SUper-SYmmetric) partners of the neutral electroweak gauge bosons and Higgs bosons. Experimental data and models place limits on the potential WIMP mass and nucleon cross sections [118] as well as multi-component cases where DM is not just one type of particle [119]. Despite current fits, it is possible that neutrinos may contribute in some manner. For an overview see the 2018 review by Boyarsky et al. [120].

Adding a new flavour does complicate the model somewhat, as the mixing matrix is now 4×4. Therefore we have some new parameters which we saw in section 2.2.3:

- Mixing angles: θ_{14}, θ_{24} and θ_{34}.

- CP phases: δ_{14} and δ_{34} (recall these are labelled as such to denote where they occur in the mixing matrix).
- Mass-squared difference: Δm^2_{41}.

Also recall the mixing matrix parametrisation with rotation matrices R

$$U^{3+1}_{\text{PMNS}} = R(\theta_{34},\delta_{34})R(\theta_{24},0)R(\theta_{14},\delta_{14})R(\theta_{23},0)R(\theta_{13},\delta_{13})R(\theta_{12},0)\,. \tag{2.39}$$

3.3 LBL Oscillations With One Light Sterile Neutrino

When an extra neutrino flavour is added, the oscillation probability equations become more complex due to the additional mixing parameters, despite this, they are obtained in the same way as before. In this section we will explicitly differentiate the n flavour cases by writing the oscillation probabilities in the form

$$P^{n\nu}_{\alpha\beta} \tag{3.5}$$

for a neutrino of α flavour oscillating to a neutrino of β flavour and where n is obviously the total number of flavours. We do this because some of these probabilities will be related to the standard three flavour ones and we do not want to mix them up. We will perform several simplifications too because this makes it easier to see what the major contributions to the probabilities are, especially the behaviour related to $\pm\Delta_{ij}$ and $\pm\delta_{ij}$ terms. To do this we follow the approach of [121].

In the vacuum, 3ν case, it can be seen that the $\nu_\mu \longrightarrow \nu_e$ oscillation probability can be expressed as a series expansion up to α^2 in $\alpha = \Delta m^2_{21}/\Delta m^2_{31}$ and is given by the sum of three terms

$$P^{3\nu}_{\mu e} = P^{\text{ATM}}_{3\nu} + P^{\text{SOL}}_{3\nu} + P^{\text{INT}}_{3\nu}\,, \tag{3.6}$$

where the first two terms are introduced by the atmospheric and solar mass squared differences respectively and the third term is the related interference term. Note that the first two terms are positive-definite while the third is not. We now want to start throwing away small terms. To do this we make the approximation that $\alpha \approx s_{13} \approx \epsilon$, for some small parameter epsilon. This is not entirely valid as $\alpha \approx \pm 0.03$ while $s_{13} \approx 0.15$ implying $\alpha \approx \epsilon^2$. The authors of [121] mention this, alluding to a different expansion in [122] that accounts for the different order of these terms. However, due to the smallness of these parameters, this naive but simple second-order expansion in ϵ will be fine. The three flavour expressions for these terms to second order in the small parameter ϵ are:

$$P_{3\nu}^{\mathrm{ATM}} \approx 4s_{23}^2 s_{13}^2 \sin^2\Delta, \tag{3.7}$$

$$P_{3\nu}^{\mathrm{SOL}} \approx 4c_{12}^2 c_{23}^2 s_{12}^2 \sin^2(\alpha\Delta), \tag{3.8}$$

$$P_{3\nu}^{\mathrm{INT}} \approx 8s_{13}s_{12}c_{12}s_{23}c_{23}(\alpha\Delta)\sin\Delta\cos(\Delta+\delta_{13}), \tag{3.9}$$

where we rewrite the oscillation terms:

$$\alpha = \frac{\Delta_{21}}{\Delta_{31}} \tag{3.10}$$

$$\Delta = \Delta_{31} \tag{3.11}$$

$$\therefore \alpha\Delta = \Delta_{21} \tag{3.12}$$

with the usual relation between oscillation factor and mass-squared splitting,

$$\Delta_{ij} = \frac{\Delta m_{ij}^2 L}{4E}, \tag{3.13}$$

and the splittings have the usual sign convention

$$\Delta m_{ij}^2 = m_i^2 - m_j^2. \tag{3.14}$$

Because the ratio α is smaller than the smallest mixing-dependent term s_{13}, the probabilities $P^{\mathrm{ATM}}, P^{\mathrm{SOL}}$ and P^{INT} have different contributions to the probability. This comes from choosing the order of our parameters loosely but it will not drastically change our results.

The four flavour equivalent of equation (3.6) can be obtained from (2.129) by filling in the matrix elements and again removing any terms second order in ϵ. SBL best fit values for s_{14} and s_{24} are similar in size to s_{13} so they are assumed to be of order ϵ. The four flavour expression can be written

$$\begin{aligned} P_{\mu e}^{4\nu} \approx\ & (1 - s_{14}^2 - s_{24}^2)P_{\mu e}^{3\nu} \\ & +4s_{14}s_{24}s_{13}s_{23}\sin\Delta\sin(\Delta+\delta_{13}-\delta_{14}) \\ & -4s_{14}s_{24}c_{23}s_{12}c_{12}(\alpha\Delta)\sin\delta_{14} \\ & +2s_{14}^2 s_{24}^2\,, \end{aligned} \tag{3.15}$$

remembering that we have averaged over the high frequency oscillations due to Δ_{41} using $\sin^2\Delta_{41} \approx 0.5$ and $\sin 2\Delta_{41} \approx 0$. The first term in this expression is merely the three flavour probability multiplied by a factor of $1 - \mathcal{O}(\epsilon^2)$. So, similar to before, the four flavour case can be written in terms of *six* separate terms, three from mass splittings and three interference terms, three of these will essentially be the three terms from the three flavour case (though modified by the order ϵ terms). Thus

$$\begin{aligned} P^{4\nu}_{\mu e} = \quad & P^{\mathrm{ATM}} + P^{\mathrm{SOL}} + P^{\mathrm{STR}} \\ & + P^{\mathrm{INT}}_{\mathrm{I}} + P^{\mathrm{INT}}_{\mathrm{II}} + P^{\mathrm{INT}}_{\mathrm{III}}, \end{aligned} \tag{3.16}$$

where P^{ATM}, P^{SOL} and $P^{\mathrm{INT}}_{\mathrm{I}}$ are modified from the three flavour probability terms by the factor $(1 - s^2_{14} - s^2_{24})$, i.e.,

$$P^{\mathrm{ATM}} = (1 - s^2_{14} - s^2_{24}) P^{\mathrm{ATM}}_{3\nu}, \tag{3.17}$$

$$P^{\mathrm{SOL}} = (1 - s^2_{14} - s^2_{24}) P^{\mathrm{SOL}}_{3\nu}, \tag{3.18}$$

$$P^{\mathrm{INT}}_{\mathrm{I}} = (1 - s^2_{14} - s^2_{24}) P^{\mathrm{INT}}_{3\nu}. \tag{3.19}$$

The new terms from equation (3.15) are

$$P^{\mathrm{STR}} \approx \quad 2 s^2_{14} s^2_{24}, \tag{3.20}$$

$$P^{\mathrm{INT}}_{\mathrm{II}} \approx \quad 4 s_{14} s_{24} s_{13} s_{23} \sin\Delta \sin(\Delta + \delta_{13} - \delta_{14}), \tag{3.21}$$

$$P^{\mathrm{INT}}_{\mathrm{III}} \approx -4 s_{14} s_{24} c_{23} s_{12} c_{12} (\alpha\Delta) \sin\delta_{14}. \tag{3.22}$$

However, in the case of T2K and NOνA we can simplify this with further approximations. From SBL anomalies (and in the case where $s^2_{14} = s^2_{24}$) we have a constraint on the parameter $s^2_{14} + s^2_{24} = 2 s^2_{14} = 2 s_{14} s_{24}$ (often denoted $\sin 2\theta_{\mu e}$, called the "effective appearance mixing angle") on which all terms are dependent. The allowed range is roughly: $\sin 2\theta_{\mu e} \in (0.030, 0.065)$. In this range the absolute values for P^{SOL}, P^{STR} and $P^{\mathrm{INT}}_{\mathrm{III}}$ are less than 0.003 so can be neglected [121], while the rest of the terms are larger and will contribute, leaving the probability

$$P^{4\nu}_{\mu e} \approx P^{\mathrm{ATM}} + P^{\mathrm{INT}}_{\mathrm{I}} + P^{\mathrm{INT}}_{\mathrm{II}}. \tag{3.23}$$

Finally, as in section 2.7.2 we must modify this again to account for the MSW effect. The ratio

$$v = \frac{V}{k} \equiv \frac{2VE}{\Delta m_{31}^2}, \tag{3.24}$$

where V is the usual Wolfenstein matter term we covered in section 2.7

$$V = \pm\sqrt{2}G_F N_e\,, \tag{3.25}$$

a thorough derivation of which is in [101]. To obtain the matter probability from the vacuum probability we make the substitution

$$P_M^{\mathrm{ATM}} \approx (1+2v)P^{\mathrm{ATM}}. \tag{3.26}$$

This incorporates third order matter corrections. The corrections to the interference terms however, are fourth order, thus when truncating to third order we can drop the corrections to them. Note that the full matter effect may be more complicated but this works for this specific case. For some extra details on matter potentials in $3+1$ see section 2.7.3.

So in summary we have an approximation of the four flavour probability we are interested in

$$P_{\mu e}^{4\nu} \approx P_M^{\mathrm{ATM}} + P_{\mathrm{I}}^{\mathrm{INT}} + P_{\mathrm{II}}^{\mathrm{INT}}. \tag{3.27}$$

This is useful because the Δ, δ_{13} and δ_{14} behaviour and the size of such effects in these approximate terms is a lot more obvious than in the full probability. We can summarise these properties:

$$P_M^{\mathrm{ATM}} \propto \sin^2\Delta, \tag{3.28}$$

$$P_{\mathrm{I}}^{\mathrm{INT}} \propto \sin\Delta\cos(\Delta+\delta_{13}), \tag{3.29}$$

$$P_{\mathrm{II}}^{\mathrm{INT}} \propto \sin\Delta\sin(\Delta+\delta_{13}-\delta_{14}). \tag{3.30}$$

The usefulness will be especially evident when we start to analyse parameter degeneracies in these complicated probabilities in section 4.3 as well as chapters 5 and 6.

3.4 Two-Flavour Approximations of 3ν and 4ν Cases

In section 2.3 we mentioned that for some cases it is simpler to analyse the oscillations a detector sees in the framework of an effective two-flavour oscillation due to the fact that detector channels are usually limited to one or two of the active neutrino flavours. Measuring the neutrino mass hierarchy is one of the key goals of the current and future detectors, often in simulations this comes down to determining whether the sign of Δm^2_{31} is positive (Normal Hierarchy or NH) or negative (Inverted Hierarchy or IH). This is incorrect however, for two reasons, firstly because, as it can be seen from figure 3.2 that the magnitude *and* sign of the mass difference we use in simulations (Δm^2_{31}) must change when the hierarchy change. We can therefore write formulae

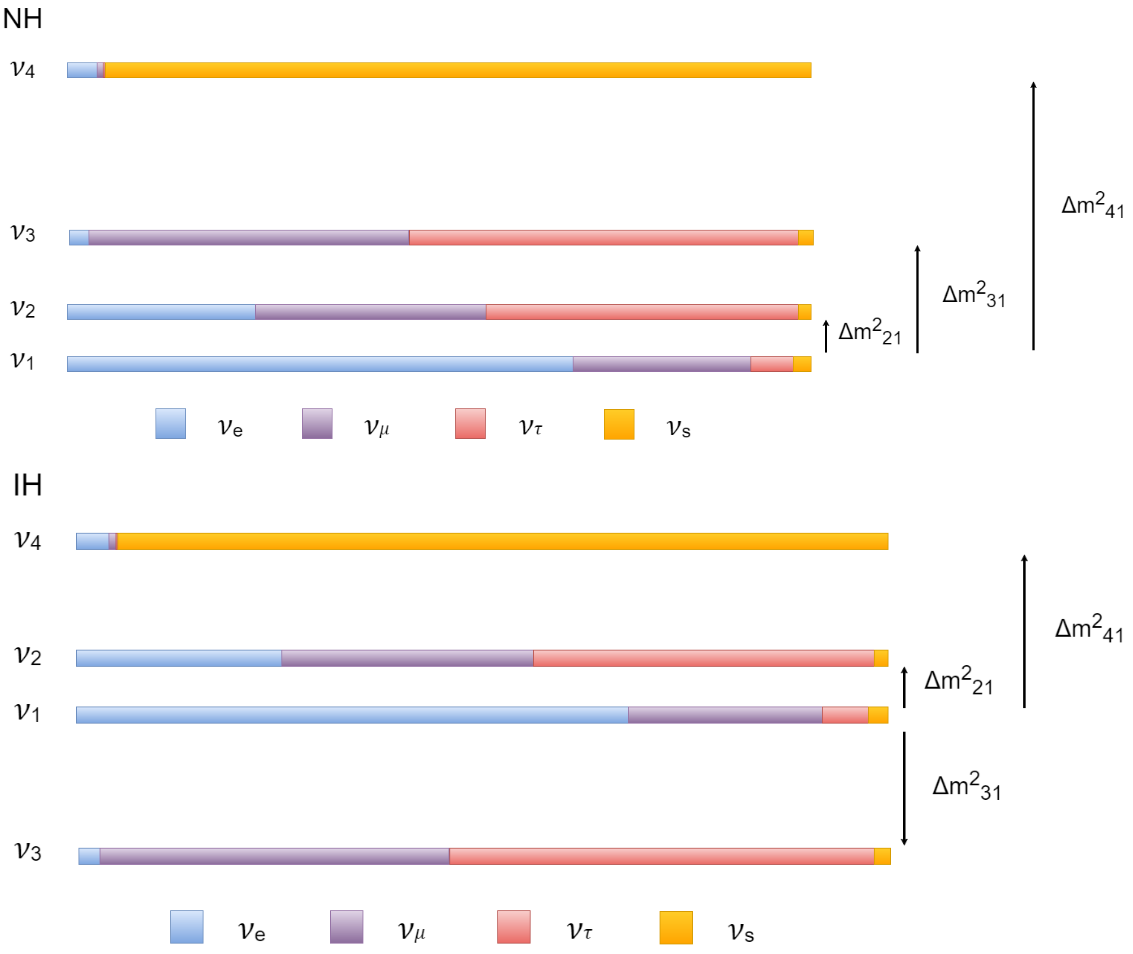

FIG. 3.2 Schematic of normal and inverted 3+1 hierarchies of the 4ν case with mixings of each flavour indicated by amount of each colour in each mass state (not-to scale).

defining these in terms of the magnitudes of the NH differences:

$$\begin{aligned}
\Delta m^2_{31}(\text{NH}) &\equiv \quad |\Delta m^2_{31}|\,, && (3.31)\\
\Delta m^2_{32}(\text{NH}) &= \quad |\Delta m^2_{31}| - \Delta m^2_{21}\,, && (3.32)\\
\Delta m^2_{31}(\text{IH}) &= -|\Delta m^2_{31}|\,, && (3.33)\\
\Delta m^2_{32}(\text{IH}) &= -|\Delta m^2_{31}| - \Delta m^2_{21}\,. && (3.34)
\end{aligned}$$

Firstly we note that, as the small mass difference is positive and unchanged by hierarchy

$$\Delta m^2_{21}(\text{NH}) = \Delta m^2_{21}(\text{IH}) = |\Delta m^2_{21}| = \Delta m^2_{21}\,. \tag{3.35}$$

We take the first splitting (3.31) as a definition. That is we define the size of the 3-1 splitting by the measured NH value and write equations for the other splittings in terms of the NH values. So overall we have

$$\begin{aligned}
|\Delta m^2_{31}| &= |\Delta m^2_{32}| + \Delta m^2_{21} \quad \text{for NH}\,, && (3.36)\\
|\Delta m^2_{31}| &= |\Delta m^2_{32}| - \Delta m^2_{21} \quad \text{for IH}\,. && (3.37)
\end{aligned}$$

If we assume that the largest mass difference we measure corresponds to Δm^2_{31} in NH and Δm^2_{32} in IH and that the sizes are are equal, then

$$|\Delta m^2_{31}|(\text{NH}) = |\Delta m^2_{32}|(\text{IH})\,, \tag{3.38}$$

which also implies

$$|\Delta m^2_{32}|(\text{NH}) = |\Delta m^2_{31}|(\text{IH})\,. \tag{3.39}$$

So we will often then define the Δm^2_{31} oscillation mass difference we are interested in terms of the NH mass differences:

$$\begin{aligned}
\Delta m^2_{31}(\text{NH}) &= \quad |\Delta m^2_{31}(\text{NH})|\,, && (3.40)\\
\Delta m^2_{31}(\text{IH}) &= -|\Delta m^2_{31}(\text{NH})| + \Delta m^2_{21}. && (3.41)
\end{aligned}$$

As we will see however, defining our oscillation case based on these splittings is not the best method when we are trying to make fits or perform simulations.

Because there are two closely spaced mass eigenstates, two of the mass-squared differences, Δm^2_{31} and Δm^2_{32} have similar magnitudes. This implies that the oscillations they cause will have similar frequencies and as such, individual peaks and troughs may be indistinguishable. Because of this only one peak will actually be seen by an experiment at the oscillation maximums and hence the measured mass difference (for ν_μ disappearance experiments) $\Delta m^2_{\mu\mu} \neq \Delta m^2_{31}$ and is instead some linear combination of Δm^2_{31} and Δm^2_{32}. In fact the form of this combination has been shown to be 'flavour weighted' averages of the two large mass splittings [123]. The α flavour weighted average for an α disappearance experiment can be expressed as

$$\Delta m^2_{\alpha\alpha} = \frac{|U_{\alpha 1}|^2 \Delta m^2_{31} + |U_{\alpha 2}|^2 \Delta m^2_{32}}{|U_{\alpha 1}|^2 + |U_{\alpha 2}|^2} \,, \tag{3.42}$$

or alternatively,

$$\Delta m^2_{\alpha\alpha} = \Delta m^2_{31} - \frac{|U_{\alpha 2}|^2}{|U_{\alpha 1}|^2 + |U_{\alpha 2}|^2} \Delta m^2_{21} \,, \tag{3.43}$$

depending on which two mass splittings used to specify this 3ν case. This implies that at different flavour disappearance experiments, a different effective splitting is measured. These equations lead to the corresponding disappearance effective mass splittings:

$$\Delta m^2_{ee} = \Delta m^2_{31} - \sin^2\theta_{13} \Delta m^2_{21} \,, \tag{3.44}$$

$$\Delta m^2_{\mu\mu} = \Delta m^2_{31} + \left(\cos\delta_{13} \sin\theta_{13} \sin 2\theta_{12} \tan\theta_{23} - \cos^2\theta_{12}\right) \Delta m^2_{21} \,, \tag{3.45}$$

$$\Delta m^2_{\tau\tau} = \Delta m^2_{31} - \left(\cos\delta_{13} \sin\theta_{13} \sin 2\theta_{12} \tan\theta_{23} - \cos^2\theta_{12}\right) \Delta m^2_{21} \,, \tag{3.46}$$

which correspond to what an atmospheric/LBL scale experiment will actually measure in these channels.

So because neither Δm^2_{31} or Δm^2_{32} are what detectors themselves truly measure, for our simulations we must consider an effective two-flavour approximation related to the three flavour parametrisation to find the correct effective parameters. An important note is that this will also give us an effective mixing angle $\theta_{\mu\mu}$ which will replace θ_{23} in our two flavour approximation giving us

$$P_{\mu\mu} = 1 - \sin^2 2\theta^{4\nu}_{\mu\mu} \sin^2 \Delta^{4\nu}_{\mu\mu} \,. \tag{3.47}$$

This will also ensures that the degeneracies are exact in the effective parameter space, i.e.,

$$P_{\mu\mu}(\Delta m^2_{\mu\mu}) = P_{\mu\mu}(-\Delta m^2_{\mu\mu})\,, \tag{3.48}$$

$$P_{\mu\mu}(\theta_{\mu\mu}) = P_{\mu\mu}(90^\circ - \theta_{\mu\mu})\,. \tag{3.49}$$

Now because the three neutrino case has been done before we intend to try and find a four flavour equivalent.

3.4.1 2ν Effective Parametrisation of 4ν case

So can we deduce what the muon disappearance version of this would be in four flavour? To attempt this we start with the probability and simplify as much as possible. Note that working with splittings (Δm^2_{ij}) or oscillation factors (Δ_{ij}) give the same effective parametrisations because they are linearly related. In the 4ν case the μ-flavour disappearance probability (divided by 4 for convenience) is

$$\begin{aligned}\frac{1-P^{4\nu}_{\mu\mu}}{4} = \; & |U_{\mu3}|^2|U_{\mu1}|^2\sin^2\Delta_{31} \\ & +|U_{\mu3}|^2|U_{\mu2}|^2\sin^2\Delta_{32} \\ & +|U_{\mu2}|^2|U_{\mu1}|^2\sin^2\Delta_{21} \\ & +|U_{\mu4}|^2|U_{\mu1}|^2\sin^2\Delta_{41} \\ & +|U_{\mu4}|^2|U_{\mu2}|^2\sin^2\Delta_{42} \\ & +|U_{\mu4}|^2|U_{\mu3}|^2\sin^2\Delta_{43}\,,\end{aligned} \tag{3.50}$$

where: $\Delta_{ij} = \frac{\Delta m^2_{ij}L}{4E}$. Because we know $\Delta_{41} \gg \Delta_{31}, \Delta_{21}$, $\Delta_{42} = \Delta_{41} - \Delta_{21}$ and $\Delta_{43} = \Delta_{41} - \Delta_{31}$, (and knowing we will later average over trigonometric terms involving Δ_{41}) we can approximate $\Delta_{41} \approx \Delta_{42} \approx \Delta_{43}$. Therefore the probability becomes

$$\begin{aligned}\frac{1-P^{4\nu}_{\mu\mu}}{4} = \; & |U_{\mu3}|^2|U_{\mu1}|^2\sin^2\Delta_{31} \\ & +|U_{\mu3}|^2|U_{\mu2}|^2\sin^2\Delta_{32} \\ & +|U_{\mu2}|^2|U_{\mu1}|^2\sin^2\Delta_{21} \\ & +|U_{\mu4}|^2\left(|U_{\mu1}|^2+|U_{\mu2}|^2+|U_{\mu3}|^2\right)\sin^2\Delta_{41}\,.\end{aligned} \tag{3.51}$$

Then as $\Delta_{21} \ll \Delta_{31}$ at the baselines we are considering and as our detector is near the Δ_{31} oscillation maximum, $\sin^2 \Delta_{31} \approx 1$, we let $\sin^2 \Delta_{21} \to 0$. So we lose the Δ_{21} term

$$\begin{aligned} \frac{1 - P^{4\nu}_{\mu\mu}}{4} = & \; |U_{\mu 3}|^2 |U_{\mu 1}|^2 \sin^2 \Delta_{31} \\ & + |U_{\mu 3}|^2 |U_{\mu 2}|^2 \sin^2 \Delta_{32} \\ & + |U_{\mu 4}|^2 \left(|U_{\mu 1}|^2 + |U_{\mu 2}|^2 + |U_{\mu 3}|^2 \right) \sin^2 \Delta_{41} \, . \end{aligned} \tag{3.52}$$

We now want to expand $\sin^2 \Delta_{32} = \sin^2(\Delta_{31} - \Delta_{21})$. Using trigonometric identities we get

$$\begin{aligned} \sin^2(\Delta_{31} - \Delta_{21}) = & \frac{1}{2} - \frac{1}{2} \sin^2 \Delta_{31} \sin^2 \Delta_{21} - \frac{1}{2} \cos^2 \Delta_{31} \cos^2 \Delta_{21} \\ & + \frac{1}{2} \sin^2 \Delta_{31} \cos^2 \Delta_{21} + \frac{1}{2} \cos^2 \Delta_{31} \sin^2 \Delta_{21} \\ & - 2 \sin \Delta_{31} \cos \Delta_{31} \sin \Delta_{21} \cos \Delta_{21} \, . \end{aligned} \tag{3.53}$$

We then discard terms proportional to $\sin^2 \Delta_{21}$ as before so,

$$\begin{aligned} \sin^2(\Delta_{32}) = & \frac{1}{2} - \frac{1}{2} \cos^2 \Delta_{31} \cos^2 \Delta_{21} + \frac{1}{2} \sin^2 \Delta_{31} \cos^2 \Delta_{21} \\ & - 2 \sin \Delta_{31} \cos \Delta_{31} \sin \Delta_{21} \cos \Delta_{21} \, . \end{aligned} \tag{3.54}$$

To simplify this we use the formulae:

$$-\frac{1}{2} \cos^2 \Delta_{31} + \frac{1}{2} \sin^2 \Delta_{31} = -\frac{1}{2} \cos 2\Delta_{31} \, , \tag{3.55}$$

$$2 \sin \Delta_{31} \cos \Delta_{31} \sin \Delta_{21} \cos \Delta_{21} = \frac{1}{2} \sin 2\Delta_{31} \sin 2\Delta_{21} \tag{3.56}$$

and approximate $\cos \Delta_{21} \approx 1 \implies \cos^2 \Delta_{21} \approx 1$ and $\sin 2\Delta_{21} \approx 2\Delta_{21}$ due to the small angle Δ_{21}. This gives

$$\sin^2(\Delta_{32}) = \frac{1}{2} \left(1 - \cos 2\Delta_{31} - 2\Delta_{21} \sin 2\Delta_{31} \right) \, . \tag{3.57}$$

We now want to expand the $\sin^2 \Delta_{31}$ and $\sin^2 \Delta_{41}$ terms in equation (3.52) using the trigonometric double-angle formula

$$\sin^2 \Delta_{i1} = \frac{1}{2} \left(1 - \cos 2\Delta_{i1} \right) \, . \tag{3.58}$$

Therefore equation (3.52) becomes

$$\begin{aligned}\frac{1-P^{4\nu}_{\mu\mu}}{4} = & \ \frac{1}{2}|U_{\mu 3}|^2|U_{\mu 1}|^2\left(1-\cos 2\Delta_{31}\right) \\ & +\frac{1}{2}|U_{\mu 3}|^2|U_{\mu 2}|^2\left(1-\cos 2\Delta_{31}-2\Delta_{21}\sin 2\Delta_{31}\right) \\ & +\frac{1}{2}|U_{\mu 4}|^2\left(|U_{\mu 1}|^2+|U_{\mu 2}|^2+|U_{\mu 3}|^2\right)\left(1-\cos 2\Delta_{41}\right)\ .\end{aligned} \tag{3.59}$$

We now simplify by defining the terms:

$$a \equiv |U_{\mu 3}|^2|U_{\mu 1}|^2\,, \tag{3.60}$$

$$b \equiv |U_{\mu 3}|^2|U_{\mu 2}|^2\,, \tag{3.61}$$

$$c \equiv |U_{\mu 4}|^2\left(|U_{\mu 1}|^2+|U_{\mu 2}|^2+|U_{\mu 3}|^2\right)\ . \tag{3.62}$$

Then collecting terms simplifies the probability

$$\frac{1-P^{4\nu}_{\mu\mu}}{4} = \frac{1}{2}\left[(a+b+c)-(a+b)\cos 2\Delta_{31}-2b\Delta_{21}\sin 2\Delta_{31}-c\cos 2\Delta_{41}\right]\ . \tag{3.63}$$

Then we further define:

$$a' \equiv \frac{a}{a+b+c}\,, \tag{3.64}$$

$$b' \equiv \frac{b}{a+b+c}\,, \tag{3.65}$$

$$c' \equiv \frac{c}{a+b+c}\,, \tag{3.66}$$

such that $a'+b'+c'=1$. So we further refine our equation

$$\frac{1-P^{4\nu}_{\mu\mu}}{4} = \frac{1}{2}(a+b+c)\left[1-(a'+b')\cos 2\Delta_{31}-2b'\Delta_{21}\sin 2\Delta_{31}-c'\cos 2\Delta_{41}\right]\ . \tag{3.67}$$

We can average over Δ_{41} fast oscillation terms using

$$\langle\cos 2\Delta_{41}\rangle = 0\,, \tag{3.68}$$

to give the even simpler

$$\frac{1-P^{4\nu}_{\mu\mu}}{4} = \frac{1}{2}(a+b+c)\left[1-(a'+b')\cos 2\Delta_{31}-2b'\Delta_{21}\sin 2\Delta_{31}\right]\ . \tag{3.69}$$

We now wish to combine our oscillation factors into one sine squared term so we can equate our expression to the two-flavour approx. To do this we define:

$$\cos\beta = \frac{a'+b'}{\sqrt{(a'+b')^2+4b'^2\Delta_{21}^2}} \approxeq \frac{a'+b'}{\sqrt{(a'+b')^2}} \approx 1, \tag{3.70}$$

$$\sin\beta = \frac{2b'\Delta_{21}}{\sqrt{(a'+b')^2+4b'^2\Delta_{21}^2}} \approxeq \frac{2b'\Delta_{21}}{\sqrt{(a'+b')^2}} = \frac{2b'\Delta_{21}}{a'+b'}\,. \tag{3.71}$$

Then solving for β

$$\beta = \tan^{-1}\left(\frac{\sin\beta}{\cos\beta}\right), = \tan^{-1}\left(\frac{2b'\Delta_{21}}{a'+b'}\right). \tag{3.72}$$

Note however that as the term c includes small sterile phase terms

$$c \propto |U_{\mu 4}|^2 \approx 0\,, \tag{3.73}$$

then we can further approximate some of our terms in the denominator of equation (3.72)

$$a'+b' = \frac{a+b}{a+b+c} \approx 1\,, \tag{3.74}$$

which means that (3.72) further reduces to

$$\beta = \tan^{-1}(2b'\Delta_{21}) \approxeq 2b'\Delta_{21}\,. \tag{3.75}$$

The probability will then become

$$\frac{1-P_{\mu\mu}^{4\nu}}{4} = \frac{1}{2}(a+b+c)\left[1-(\cos\beta\cos 2\Delta_{31} - \sin\beta\sin 2\Delta_{31})(a'+b')\right]. \tag{3.76}$$

We can further collect some sine and cosine factors

$$\cos a\cos b + \sin a\sin b = \cos(a-b) \tag{3.77}$$

to give the probability

$$\frac{1-P_{\mu\mu}^{4\nu}}{4} = \frac{1}{2}(a+b+c)\left[1-\cos(2\Delta_{31}-\beta)(a'+b')\right],$$

$$
\begin{aligned}
&= (a+b+c)\left[\frac{1}{2} - \frac{1}{2}\cos(2\Delta_{31} - \beta)\right] \,, \\
&= (a+b+c)\sin^2\left(\Delta_{31} - \frac{1}{2}\beta\right) \,. \qquad (3.78)
\end{aligned}
$$

So finally, after substituting for β we have a relatively simple probability

$$P^{4\nu}_{\mu\mu} = 1 - 4(a+b+c)\sin^2\left(\Delta_{31} - b'\Delta_{21}\right) \,. \qquad (3.79)$$

We then equate this to the effective two flavour probability

$$P_{\mu\mu} = 1 - \sin^2 2\theta^{4\nu}_{\mu\mu}\sin^2\Delta^{4\nu}_{\mu\mu} \qquad (3.80)$$

to give our effective mixing terms:

$$
\begin{aligned}
\sin^2 2\theta^{4\nu}_{\mu\mu} &= 4(a+b+c) \,, && (3.81)\\
\therefore\ \theta^{4\nu}_{\mu\mu} &= \frac{1}{2}\sin^{-1} 2\sqrt{a+b+c} \,, && (3.82)\\
\Delta^{4\nu}_{\mu\mu} &= \Delta_{31} - b'\Delta_{21} \,. && (3.83)
\end{aligned}
$$

So the mixing parameter in full is

$$\sin^2 2\theta^{4\nu}_{\mu\mu} = |U_{\mu3}|^2|U_{\mu1}|^2 + |U_{\mu3}|^2|U_{\mu2}|^2 + |U_{\mu4}|^2\left(|U_{\mu1}|^2 + |U_{\mu2}|^2 + |U_{\mu3}|^2\right) \,, \qquad (3.84)$$

with the explicit forms of the parameters:

$$\theta^{4\nu}_{\mu\mu} = \frac{1}{2}\sin^{-1} 2\sqrt{|U_{\mu3}|^2|U_{\mu1}|^2 + |U_{\mu3}|^2|U_{\mu2}|^2 + |U_{\mu4}|^2\left(|U_{\mu1}|^2 + |U_{\mu2}|^2 + |U_{\mu3}|^2\right)} \,, \qquad (3.85)$$

$$\Delta^{4\nu}_{\mu\mu} = \Delta_{31} - \frac{|U_{\mu3}|^2|U_{\mu2}|^2}{|U_{\mu3}|^2|U_{\mu1}|^2 + |U_{\mu3}|^2|U_{\mu2}|^2 + |U_{\mu4}|^2\left(|U_{\mu1}|^2 + |U_{\mu2}|^2 + |U_{\mu3}|^2\right)}\Delta_{21} \,. \qquad (3.86)$$

This seems to be reasonable because we can see that for vanishing sterile mixing $|U_{\mu4}|^2 \to 0$ and (3.86) will approach the three flavour case from (3.43). Further studies need to be performed to see if this is sufficient to model the four flavour case accurately or if sterile terms need to be kept at higher order.

3.4.2 Measured Mass Differences in Different 4ν Hierarchies

Identifying which numerical mass splitting corresponds to what measured oscillation can be complicated by non-standard hierarchies. Here we show some illustrative examples to clearly point out the reasons that the measured experimental splittings shouldn't be directly associated with the underlying analytical ones. As such, these should only be definitively related when the hierarchy is known (potentially averaging between multiple close splittings). Note that in the literature the measured experimental mass splittings are often labelled with abbreviated names of their sources. For example the measured splittings considered in our four flavour case are Δm^2_{sol}, Δm^2_{atm} and Δm^2_{SBL} corresponding to the solar, atmospheric and SBL oscillations. These are effective parameters as discussed earlier in chapter 3.4 and as such do not necessarily correspond to the numbered splittings Δm^2_{ij} in a straightforward manner.

We define the measured splittings to be positive-definite due to the sign ambiguity of the splitting in the effective two-flavour terms measured at experiments. For example, the probabilities for appearance $P_{\alpha\beta} \propto \sin^2 \Delta_{\alpha\beta}$ and survival $1 - P_{\alpha\alpha} \propto \sin^2 \Delta_{\alpha\alpha}$. The sign part is left to the ordering dependence of the underlying Δm^2_{ij} terms. Obviously due to our conventional ordering of the numerical mass differences $\Delta m^2_{ij} = m^2_i - m^2_j$ these themselves may be positive or negative depending on the ordering.

3+1 NO/IO

This corresponds to the standard 3ν NO/IO with a large mass splitting to a relatively heavy ν_4. A schematic can be seen in figure 3.3. These are the only two 4ν orderings we consider fully in our analysis due to them being the most simple solution for standard oscillations + SBL anomaly resolution without bumping the neutrino mass hierarchy up to potentially conflict with cosmology measurements.

In this hierarchy the measured solar and atmospheric splittings Δm^2_{sol} and Δm^2_{atm} correspond to Δm^2_{21} and an average of Δm^2_{31} and Δm^2_{32} respectively, as with the standard 3ν case. It can be seen that the introduced ν_4 state adds a much larger independent splitting Δm^2_{41} which can be attributed to the measured Δm^2_{SBL} for the oscillation interpretation of SBL anomalies. Note that this correspondance will also likely not be exact and theoretically the measured SBL splitting may actually be an average of Δm^2_{41}, Δm^2_{42} and Δm^2_{43}. To fit the SBL anomalies the choice of splitting is

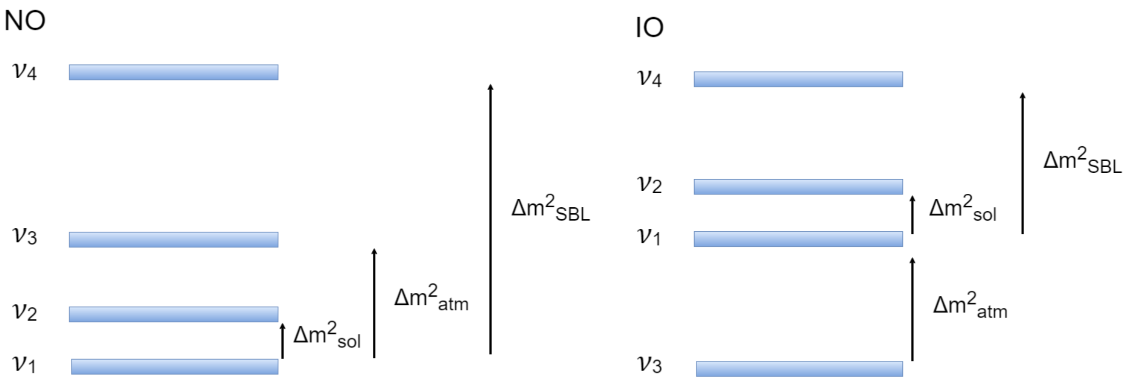

FIG. 3.3 Schematic of the 3+1 hierarchy in 4ν for NO and IO with sizes of splittings not to scale.

such that $\Delta m^2_{41} \gg \Delta m^2_{31} > \Delta m^2_{21}$, because of this all three of the new splittings are all quite similar in scale despite the difference in the size of Δm^2_{31} and Δm^2_{21}.

1+3 NO/IO

This choice is also a straightforward extension of the standard case, with no new close pairs of states being introduced. Compared to the 3+1 case however, this time the new mass eigenstate ν_4 is the lightest state, bumping up the overall mass scale of the original mass states ν_1, ν_2 and ν_3 by Δm^2_{41} for NO and Δm^2_{43} for IO (see figure 3.4). In this case the solar and atmospheric splittings are defined as in the 3ν or $3+1$

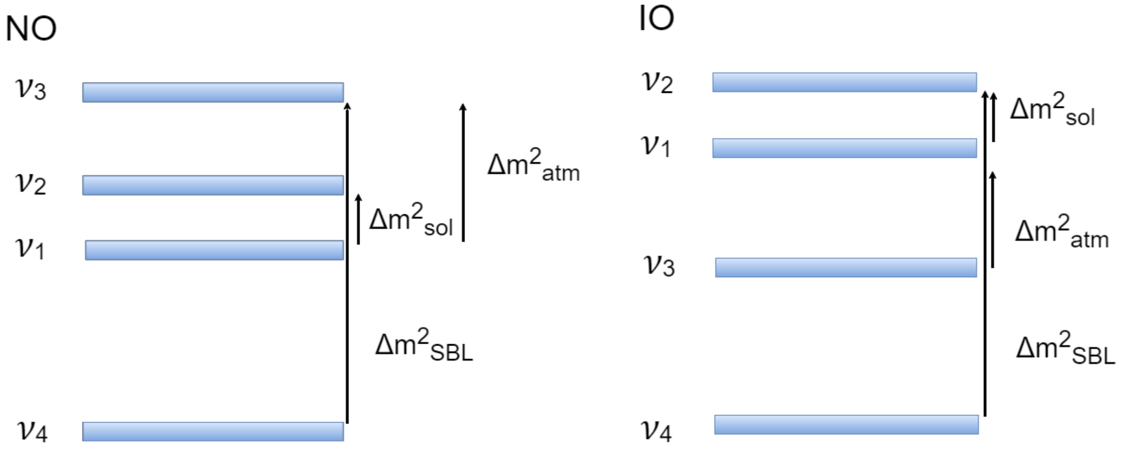

FIG. 3.4 Schematic of the 1+3 hierarchy in 4ν for NO and IO with sizes of splittings not to scale.

case and again, similar to before $\Delta m^2_{41} \approx \Delta m^2_{42} \approx \Delta m^2_{43}$. The key difference is in this case the limiting cases of largest possible SBL splittings are $\Delta m^2_{SBL} = -\Delta m^2_{43}$ and $\Delta m^2_{SBL} = -\Delta m^2_{41}$ for NO and IO respectively. Similar to 3+1 the measured SBL splitting theoretically corresponds to an average of all three large splittings though will likely be averaged out regardless. It can also be seen that in this case the lightest possible mass state being ν_4 implies that the scale of the first three neutrino masses is dependent on the SBL splitting and exact mass of ν_4. If we are certain that SBL splitting exists then this can make the astrophysical constraints on the sum of active neutrino masses hard to fit with this hierarchy. For example, even if ν_4 is massless ($m_4 = 0$) and $\Delta m^2_{\text{SBL}} \approx 1\text{ eV}^2$, then $\Sigma_i \nu_i \approx 3\text{ eV}$ which would be well outside current estimates.

2+2 A+S/S+A

These examples place ν_4 much closer in mass to ν_3 and the splitting between them becomes associated with the Δm^2_{atm} splitting. This clearly gives two closely spaced pairs of mass eigenstates (hence 2+2), rather than the small, medium and large gap of our other four flavour examples. The labels 2_S and 2_A refer to the solar and atmospheric mass splittings respectively. The two possible orderings of this hierarchy can be referred to as $2_S + 2_A$ and $2_A + 2_S$ with the former and latter corresponding to being the lower and higher mass pairings respectively as seen in figure 3.5. In this case the small mass splitting corresponding to solar mixing is the same as the standard case. The other two splittings are very different however, with the the atmospheric splitting corresponding to Δm^2_{43} for both orderings, while the SBL splitting will

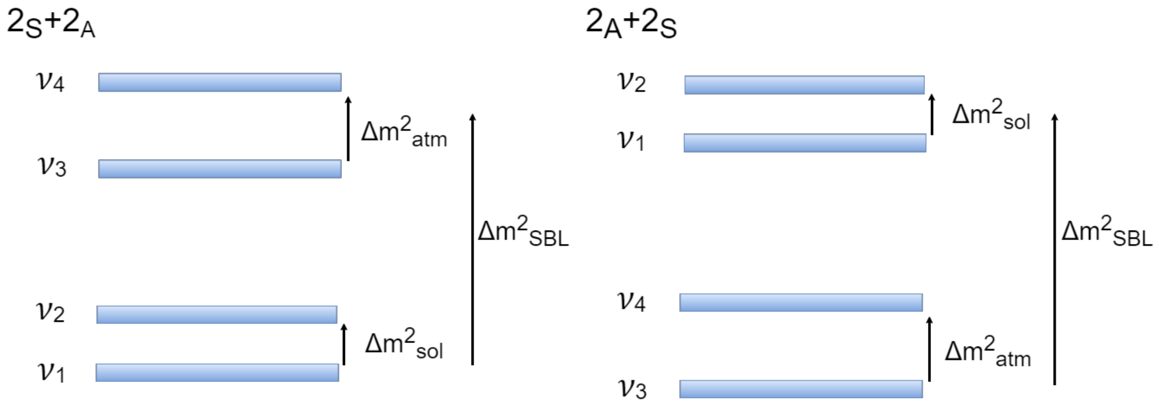

FIG. 3.5 Schematic of the 2+2 hierarchy in 4ν for S+A and A+S with sizes of splittings not to scale.

correspond to one of the large differences between the 1-2 and 3-4 pairings with maximum size defined by Δm^2_{41} in S+A and $-\Delta m^2_{32}$ in A+S (and in general might involve an average of all four possible splittings in each case).

3.5 Models With More Than One Sterile Neutrino

Here we briefly touch on the prospects and formalism of further extensions where the number of extra states is greater than one. Sometimes this is done to attempt to fit several models at once by including several mass scales. An example common in the literature is the 3+3 extension. This is similar to the previous $3+1$ extension but adds one 'light' ($\sim 10^{-5}$eV - 10^2eV) sterile neutrino and two 'heavy' (~ 1eV - 10^9GeV) sterile neutrinos. The light neutrino is usually intended to facilitate SBL oscillations while the heavy neutrinos cater for neutrino mass via a see-saw mechanism (we briefly outline this in section 3.6.2). The heavy neutrino mass is essentially unconstrained in terms of affecting the SM, and as such depends almost entirely on the requirements of the mass model.

3.5.1 3+n_s Extension

Let us now investigate a more general extension where we add n_s new (mostly sterile) mass eigenstates. We obviously have a whole range of extensions to the SM if we allow n_s new sterile flavours. The more of these we add, the more we can fine tuning our mixing and neutrino mass parameters. Not to mention potential contributions and candidates for dark matter. Of course the more states we add, the more easily they may be dismissed via naturalness arguments.

Regardless of real applications, lets investigate the n flavour formalism, where the total number of neutrino states is related to the number of additional states by $n = 3 + n_s$. Some of the formalism presented here is adapted from section 2 of [116]. So as we saw in section 1.10, in the SM we have 3 active neutrino fields: $\nu_{eL}, \nu_{\mu_L}, \nu_{\tau L}$ from the standard $SU(2)_L$ lepton doublets. We then add n_s sterile neutrino fields: $\nu_{s_1 R}, \nu_{s_2 R}, \cdots, \nu_{s_{n_s} R}$ which are $SU(2)_L \times U(1)_\gamma$ singlets. So the general Lagrangian in flavour basis becomes

$$\mathcal{L} = \frac{1}{2} \nu_L^{(F)^T} C^\dagger M \nu_L^{(F)} + \text{h.c.}\,, \tag{3.87}$$

where the full $n \times 1$ column flavour matrix is defined

$$\nu_L^{(F)} = \begin{pmatrix} \nu_{eL} \\ \nu_{\mu L} \\ \nu_{\tau L} \\ {\nu_{s_1 R}}^c \\ \vdots \\ {\nu_{s_{n_s} R}}^c \end{pmatrix} \equiv \begin{pmatrix} \nu_L^{(a)} \\ \nu_R^{(s)^c} \end{pmatrix} \tag{3.88}$$

and we have defined the 3×1 (active) and $n_s \times 1$ (sterile) respective sub arrays:

$$\nu_L^{(a)} = \begin{pmatrix} \nu_{eL} \\ \nu_{\mu L} \\ \nu_{\tau L} \end{pmatrix}, \quad \nu_R^{(s)^c} = \begin{pmatrix} {\nu_{s_1 R}}^c \\ \vdots \\ {\nu_{s_{n_s} R}}^c \end{pmatrix}. \tag{3.89}$$

We can then change into the mass basis via some unitary $n \times n$ matrix $\mathcal{U}$:

$$\nu_L^{(F)} = \mathcal{U} \nu_L^{(M)}, \quad \text{where} \quad \nu_L^{(M)} = \begin{pmatrix} \nu_{1L} \\ \vdots \\ \nu_{nL} \end{pmatrix} \tag{3.90}$$

and $\mathcal{U}$ is defined such that

$$\mathcal{U}^T M \mathcal{U} = \text{diag}(m_1, \cdots, m_n). \tag{3.91}$$

Then the Lagrangian mass term becomes

$$\begin{aligned} \mathcal{L}_{\text{mass}} = & \ \frac{1}{2} \sum_{k=1}^{n} m_k (\nu_{kL})^T C^\dagger \nu_{kL} + \text{h.c.}, \\ = & -\frac{1}{2} \sum_{k=1}^{n} m_k \overline{\nu_{kL}^c} \nu_{kL} + \text{h.c.}, \\ = & -\frac{1}{2} \sum_{k=1}^{n} m_k \overline{\nu_k} \nu_k + \text{h.c.}, \end{aligned} \tag{3.92}$$

where the elements ν_k are the Majorana neutrino fields $\nu_k = \nu_{kL} + \nu_{kL}^c$ which follow the Majorana constraint: $\nu_k = \nu_k^c$. We can now write the leptonic charged-current (CC) lagrangian in the flavour basis where the mass matrix of the charged leptons

$l_e = e$, $l_\mu = \mu$ and $l_\tau = \tau$ is diagonal

$$\begin{aligned} \mathcal{L}_{\rm CC} =& -\frac{g}{\sqrt{2}} \sum_{\alpha=e,\mu,\tau} \overline{l_{\alpha L}} \gamma^\rho \nu_{\alpha L} W^\dagger_\rho + \text{h.c.}\,, \\ =& -\frac{g}{\sqrt{2}} \sum_{\alpha=e,\mu,\tau} \overline{l_{\alpha L}} \gamma^\rho \nu_{\alpha L} W^\dagger_\rho + \text{h.c.}\,. \end{aligned} \tag{3.93}$$

Written in matrix form this becomes

$$\begin{aligned} \mathcal{L}_{\rm CC} =& -\frac{g}{\sqrt{2}} \overline{l_L} \gamma^\rho \nu_L^{(a)} W^\dagger_\rho + \text{h.c.}\,, \\ =& -\frac{g}{\sqrt{2}} \overline{l_L} \gamma^\rho U \nu_L^{(M)} W^\dagger_\rho + \text{h.c.}\,, \end{aligned} \tag{3.94}$$

with the charged lepton array defined as

$$l_L = \begin{pmatrix} e \\ \mu \\ \tau \end{pmatrix} . \tag{3.95}$$

The truncated flavour array and mixing matrix are:

$$\nu_L^{(a)} = U \nu_L^{(M)} \quad \text{and} \quad U = \mathcal{U}|_{3\times n}. \tag{3.96}$$

The matrix U is the $3 \times n$ rectangular matrix formed by taking the first 3 rows of $\mathcal{U}$. This is because the only CC interactions occur with the 3 active flavour eigenstates but can involve mixing via all of the n mass eigenstates. The rectangular matrix U can be parametrised in terms of: $3 + 3n_s$ mixing angles, $3 + 3n_s$ physical phases, of which $1 + 2n_s$ are Dirac phases and $n - 1$ Majorana phases λ_{i1} (so clearly U reduces to the standard 3ν PMNS matrix when $n_s = 0$). This can be expressed as

$$U = \left[\left(\prod_{a=1}^{3} \prod_{b=4}^{n} \tilde{R}^{ab} \right) \underbrace{R^{23} \tilde{R}^{13} R^{12}}_{3\nu \text{ PMNS}} \right]_{3\times n} \text{diag}\left(1, e^{i\lambda_{21}}, \cdots, e^{i\lambda_{n1}}\right) , \tag{3.97}$$

where we have defined the shorthand for the individual rotation matrices from equation (2.2)

$$\tilde{R}^{ab} = R(\theta_{ab}, \delta_{ab})\,, \tag{3.98}$$

$$R^{ab} = R(\theta_{ab}, 0) \tag{3.99}$$

and truncated to $3 \times n$ as we did with the diagonalised mass matrix $\mathcal{U}$ beforehand. The Majorana phases are of course not relevant in oscillation physics but we leave them in here because they important are in other extended neutrino theories like neutrinoless double beta decay. An example n flavour parametrisation is

$$U = \Big[R^{3n} \tilde{R}^{2n} R^{1n} \cdots R^{34} \tilde{R}^{24} R^{14} R^{23} \tilde{R}^{13} R^{12} \Big]_{3\times n} \mathrm{diag}\left(1, e^{i\lambda_{21}}, \cdots, e^{i\lambda_{n1}}\right) , \tag{3.100}$$

This sort of rectangular mixing matrix is how our simulations using GLoBES (section 4) handle extra neutrino states, given that we only care about observable flavours. Note however that $UU^\dagger = I_{3\times3}$ but $U^\dagger U \neq I_{n\times n}$. We can also write the neutrino NC Lagrangian corresponding to (3.94) in terms of the mass eigenstates using the same rectangular matrix

$$\begin{aligned} \mathcal{L}_{\mathrm{NC}} &= -\frac{g}{2\cos\theta_{\mathrm{W}}} \bar{\nu}_L^{(a)} \gamma^\rho \nu_L^{(a)} Z_\rho \\ &= -\frac{g}{2\cos\theta_{\mathrm{W}}} \bar{\nu}_L^{(M)} \gamma^\rho U^\dagger U \nu_L^{(M)} Z_\rho \, . \end{aligned} \tag{3.101}$$

Hopefully we have shown that it is relatively simple to keep adding more neutrinos to such models. Going any further with these parametrisations is outside the scope of this work, but example studies are easy to find. Many authors have attempted to resolve tensions in MiniBooNE, LSND and other SBL experiments using 3+2 [124–126] and $3+1+1$ [127, 128] five neutrino models, as well as 3+3 [124] and general 3+n [129, 130]. Unfortunately even these models with extra neutrinos are hard-pressed to explain the appearance-disappearance tension present in this sector as mentioned in section 3.1.1.

3.6 Neutrino Mass Models

Neutrino oscillations give us solid evidence that neutrinos do have mass and that the SM needs to be expanded to account for this. There are a few methods in which neutrinos can gain their physical mass, these depend on whether neutrinos have Majorana and/or Dirac masses as we briefly mentioned when discussing SM leptons in section 1.10.

In this work so far we have primarily discussed light sterile neutrinos due to the fact that mass splittings in the eV^2 scale will affect oscillations, therefore are the concern of modern oscillation experiments. That said, the parameter space for sterile neutrinos is rather broad, with the number of extra neutrinos and their mass scales mostly unconstrained. It is in the interest of many fields then to know as much as possible about any extra heavy neutral leptons.

In this section where we discuss mass models we will mention extra neutrinos (some authors prefer the more generic ‘neutral leptons’) in a more general sense. With the unconstrained number and mass range of extra neutrinos, models can be concocted where the existence of heavy sterile neutrinos can explain the light active masses e.g. see-saw type models. More conventional mass models are also discussed.

The nature of neutrinos as particles is still somewhat unknown due to having an unknown method of mass generation. If neutrinos have mass as oscillations suggest, then an extension to the SM must be made including terms that account for these neutrino masses. Examples of such terms are ‘Dirac’ or ‘Majorana’ masses corresponding to Dirac or Majorana fermion properties. Dirac particles are the norm in the SM with most particles gaining their bare mass from a Higgs-Yukawa coupling. However, because of the incredibly light neutrino mass, the same method of mass generation applied to neutrinos results in incredibly small Yukawa couplings which are suggested to be unphysical via a naturalness argument. So now that we have an introduction to extra and/or RH neutrinos, we can approach Dirac and Majorana mass terms specifically in the case of neutrinos.

3.6.1 Dirac Mass Models

Neutrinos, like all the other SM fermions can be Dirac particles, in this case the Lagrangian contains the relevant term

$$\mathcal{L} \supset -Y_\nu \bar{l}_L i\sigma_2 H^* \nu_R + \mathrm{h.c.} \tag{3.102}$$

If the neutrinos are conventional Dirac particles then the sterile, right-handed neutrinos (ν_R's) are, in a sense, not distinct new particles (but what makes a particle distinct anyway?). These RH neutrinos are merely non-interacting spin states and thus there will only be 3 distinct masses which would correspond to the known mass eigenstates. The consequences of such a case however mean that the Yukawa couplings corresponding to these neutrinos are of order $F \approx 10^{-12}$ which can be argued to be unnaturally small and too "fine-tuned". This model does not allow for neutrinoless double beta decay ($0\nu\beta\beta$), which is a strictly Majorana property. See section 3.7 for an overview of this phenomena and potential experimental detection.

The mass basis term in the Lagrangian associated with Dirac mass will be

$$\bar{\nu}_L m_D \nu_R + \text{h.c.} \tag{3.103}$$

However we know the relation between particles and antiparticles terms is

$$\bar{\nu}_L m_D \nu_R = \bar{\nu}_R^c m_D^T \nu_L^c \,. \tag{3.104}$$

So the Dirac mass term is often written "expanded" as

$$-\frac{1}{2}\left(\bar{\nu}_L m_D \nu_R + \bar{\nu}_R^c m_D^T \nu_L^c\right) + \text{h.c.} \tag{3.105}$$

where the factor of $1/2$ and conjugate terms make it more obvious how these can be incorporated into a general mass matrix. We will see this in the next section 3.6.2.

3.6.2 Majorana Neutrinos

Majorana particles have the unique property that they are their own antiparticles, thus only neutral particles of this sort are possible. Majorana neutrinos are perhaps the more interesting of the two, simply because they would be the only such elementary particles we know of in the SM with these properties. Some facts and properties of Majorana neutrinos are:

- For Majorana neutrinos $\nu = \bar{\nu}$ [131]. That is neutrinos are their own antiparticles.

- This violates conservation of total lepton number L.

- Neutrino particles can no longer be classified as 'neutrino' or 'antineutrino'.

- Because weak interactions are chiral we can define neutrinos and antineutrinos in the ultra relativistic limit when chirality coincides with helicity [132].
- Particles are now defined by the helicity, hence this defines the particles they produce in CC interactions.
- So a left-handed (negative helicity), l-type neutrino will produce a (left-handed) l^- lepton while a right-handed (positive helicity), l-type neutrino will produce a (right-handed) l^+ lepton.
- So the CC interactions involve $\nu_{lL} \to l^-$ and $\nu_{lR} \to l^+$.
- In this sense, we can say that for Majorana neutrinos, $\nu_{lL} \equiv \nu_l$ and $\nu_{lR} \equiv \bar{\nu}_l$.

Majorana neutrinos are favoured in some models because the mostly sterile heavy mass eigenstates can have large Majorana masses which, via the see saw mechanism raise the light mass eigenstate masses without requiring small Yukawa couplings. An aside to this is that clearly $\beta\beta$ (neutrinoless double-beta) decay is allowed, searches will be performed at facilities such as KamLAND and the proposed SNO+.

What follows is not intended to be a full discussion of mass models featuring Majorana neutrinos, rather a rough outline of the formalism of so called ‘See Saw Mechanisms’. For more thorough reviews of neutrino mass models, including variants of see saw theories, see [133, 134]. Adding a term to the SM lagrangian of the form

$$\frac{1}{2}\overline{\nu}_L m_\nu \nu_L^c + h.c. \tag{3.106}$$

does not add any degrees of freedom. This term does break gauge invariance however. The term associated with Majorana mass is:

$$-\frac{1}{2}\left(\bar{\nu}_L m_M \nu_L^c + \bar{\nu}_R M_M \nu_R^c\right) + \text{h.c.} \tag{3.107}$$

In general, neutrinos can have both mass terms, so combining the equations (3.105) and (3.107) we may express these as

$$-\frac{1}{2}\begin{pmatrix} \bar{\nu}_L & \bar{\nu}_R^c \end{pmatrix} \mathcal{M} \begin{pmatrix} \nu_L^c \\ \nu_R \end{pmatrix} + \text{h.c.} \equiv -\frac{1}{2}\begin{pmatrix} \bar{\nu}_L & \bar{\nu}_R^c \end{pmatrix} \begin{pmatrix} 0 & m_D \\ m_D^T & M_M \end{pmatrix} \begin{pmatrix} \nu_L^c \\ \nu_R \end{pmatrix} + \text{h.c.} \tag{3.108}$$

Where we have assumed that the Majorana mass associated with the left handed neutrinos is close to zero ($m_M \approx 0$). This means that the active neutrinos behave entirely as Dirac particles, or at least close to it. To get the physical masses from this equation we must diagonalise $\mathcal{M}$ and the eigenvalues will be the physical masses of the LH and RH neutrinos. For a matrix of the form:

$$\begin{pmatrix} 0 & A \\ A^T & B \end{pmatrix}, \tag{3.109}$$

where $A << B$, we have two highly disproportionate eigenvalues:

$$\lambda_1 = \frac{A^2}{B}, \tag{3.110}$$

$$\lambda_2 = B. \tag{3.111}$$

From this we can see that the physical masses are:

$$m_L = \frac{m_D^2}{M_M}, \tag{3.112}$$

$$m_R = M_M. \tag{3.113}$$

Note: these are actually matrices, so the true form of m_L in (3.112) is $m_L = -m_D M_M^{-1} m_D^T$. So a large Majorana sterile neutrino mass, can be responsible for the tiny active neutrino mass even if their Yukawa couplings with the Higgs are of a reasonable order. This would imply further that

$$m_L = \frac{(v y_\nu)^2}{M_M}, \tag{3.114}$$

for neutrino Yukawa coupling y_ν and Higgs VEV v. So if M_M is on the order of the GUT scale (at least 10^{16} eV in string models) and $v = 246$ GeV, then the Yukawa coupling required for a physical neutrino mass of order ~ 1 eV is

$$y_\nu \sim 1 \text{ eV} \frac{10^{16} \text{ eV}}{(246 \times 10^9 \text{ eV})^2} \sim \frac{1}{2.46} \times 10^{-4}. \tag{3.115}$$

This size is more within reason considering naturalness as motivation. Such a form of mass generation is known as a see-saw mechanism due to the fact that large Majorana mass terms can lead to small physical mass eigenstates. Unfortunately the ranges of m_D and M_M are almost entirely unconstrained, ranging from massless, up to the

GUT scale ($\sim 10^{16}$ eV) [84]. This can make the see-saw case seem rather fine tuned, but the motivation behind them is reasonable.

3.7 Double Beta Decay

Double beta ($\beta\beta$) decay is a process available to some unstable nuclei wherein the nucleus undergoes two standard beta decay events simultaneously, as visualised in figure 3.6(a). This interaction contains two weak vertices so is second order and as such is very rare. However some nuclei are energetically forbidden from decaying via single beta decay but can via double beta decay. Double beta decay has directly been observed in 11 nuclei [135]. Related phenomena have also been seen such as two neutrino double electron capture. Experiments in this area have been around for a while, for example the NEMO (Neutrino Ettore Majorana Observatory) collaboration started in 1989. The latest experiment by the collaboration was NEMO-3, situated in the Fréjus Underground Laboratory off the Fréjus road tunnel connecting France and Italy. It started in 2003 and saw 219,000 $2\nu\beta\beta$ events as of 2005 [135, 136]. The collaboration is currently constructing a new detector known as SuperNEMO which should improve on NEMO-3 Majorana mass constraints by more than one order of magnitude [137].

For Dirac neutrinos, double beta decay events will always emit two neutrinos i.e. two neutrino double beta decay ($2\nu\beta\beta$), but in the Majorana neutrino case there is an additional possibility which is neutrinoless double beta decay ($0\nu\beta\beta$) as seen in figure 3.6(b). Double beta decay is therefore a test of the Dirac/Majorana nature of neutrinos. Such a process also breaks the baryon number minus lepton number (or $B - L$) symmetry of the SM [138]. Originally the process was know as 'Double Beta Disintegration' [139] and was already understood to potentially occur when neither emission itself is possible (via conservation of energy) but both simultaneously are. It wasn't long before it was noticed that for Majorana neutrinos, less overall particles (only two e^- or e^+) would need to be emitted in the final state [140], with the neutrino being virtual. An important point was that this would not change the behaviour of standard beta decay, simply provide an additional pathway. The most important feature overall is that if the neutrino exhibits this Majorana property, then decays kinematically forbidden in the Dirac case may occur, hence the rate of detected double beta decays would increase. The smoking gun however, would be seeing a deficit in an associated neutrino/antineutrino rate measurement. Methods other than light Majorana neutrino exchange that would also contribute to $\beta\beta$ decays have been considered, including new unconventional operators and heavy neutrinos [132].

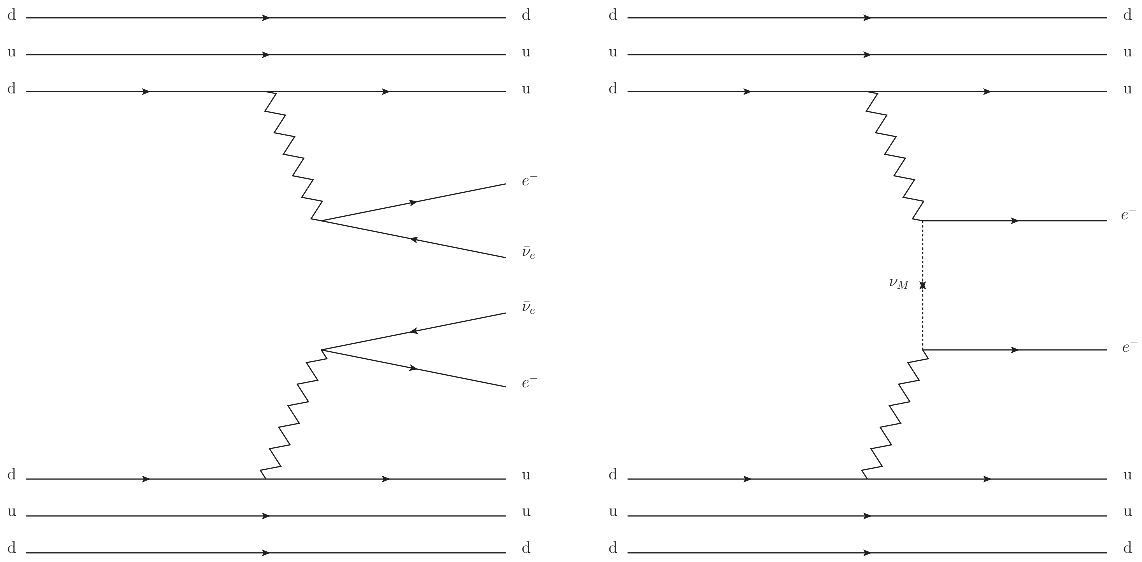

(a) $2\nu\beta\beta$ (b) $0\nu\beta\beta$

FIG. 3.6 Both double beta decay possibilities for two neutrons going to protons. In (a) two neutrinos are emitted while in (b) there is an intermediate Majorana neutrino. The neutrinoless case relies on Majorana neutrinos while the other can have Dirac or Majorana neutrinos.

The observable that is considered in $0\nu\beta\beta$ analyses is the half life, notated $T^{0\nu}_{1/2}$. If this is indeed mediated by a Majorana light neutrino then it can be related to the effective mass of such a neutrino $m_{\beta\beta}$ [141].

$$T^{0\nu}_{1/2} = G^{0\nu}(Q,Z)|M^{0\nu}|^2 \left(\frac{m_{\beta\beta}}{m_e}\right)^2 \tag{3.116}$$

where m_e is the mass of the electron, $G^{0\nu}$ is the lepton phase space integral, $M^{0\nu}$ is a nuclear matrix element to describe any effects due to structure and the effective neutrino mass $m_{\beta\beta}$ is defined

$$m_{\beta\beta} \equiv \left|\sum_j U^2_{ej} m_j\right| . \tag{3.117}$$

The matrix elements U_{ej} in equation (3.117) are not those of the standard PMNS matrix, but rather the more fundamental version including Majorana phases (recall section 2.1) in an extra diagonal matrix of the form $P_{\text{Maj}} = \text{diag}\left\{e^{i\alpha_1}, e^{i\alpha_2}, e^{i\alpha_3}\right\}$

postmultiplied onto U_{PMNS}. Adding these phases explicitly will give

$$m_{\beta\beta} \equiv \left| \sum_j e^{i\alpha_j} |U_{ej}|^2 m_j \right| \tag{3.118}$$

where the moduli of elements $|U_{ej}^2|$ will directly correspond to standard oscillation PMNS elements. Note that as discussed in 2.1, one of the Majorana phases can be set to zero without loss of generality (due to lack of physical significance), leaving $P_{\text{Maj}} = \{1, e^{i\alpha_2}, e^{i\alpha_3}\}$. Approximating $G^{0\nu}$ and $M^{0\nu}$ gives rough, hierarchy dependent limits on $T_{1/2}^{0\nu}$.

$$T_{1/2}^{0\nu} \begin{cases} > 10^{28} \text{ yr}, & \text{for Normal Hierarchy}, \\ \sim 10^{26}\text{--}10^{28} \text{ yr}, & \text{for Inverted Hierarchy}. \end{cases} \tag{3.119}$$

In a ton scale detector these possibilities would account for less than one event per year in NH to a few events per year in IH [138]. Thus measurement is very difficult but not impossible with current detector technology and the greatest challenge seems to be background mitigation. For an up to date full review of the status of experiments in this area see Cardani 2018 [138].

In some cases we can relate the effective neutrino mass from this decay with other physics involving Majorana neutrinos, for example seesaw mass generation [142]. If we have a mass term such as in equation (3.108), then we have a mass matrix of the form

$$\begin{pmatrix} 0 & m_D \\ m_D^T & M_M \end{pmatrix} \tag{3.120}$$

with Dirac and Majorana mass terms m_D and M_M as before. In this case the mass of the ν_e will come from the small eigenvalue of the matrix (see 3.6.2), which is

$$m_{\nu_e} = -\frac{m_D^2}{M_M}\,. \tag{3.121}$$

This will be related to the effective mass $m_{\beta\beta}$.

$$m_{\beta\beta} = |m_{\nu_e}| \left(1 + \frac{\langle q^2 \rangle}{M_M^2}\right)\,. \tag{3.122}$$

Time will tell if such searches for $0\nu\beta\beta$ bear fruit or not. For now, as with many neutrino studies, we will just have to wait for more data.

CHAPTER 4

GLoBES SIMULATION

4.1 Introduction to GLoBES

GLoBES (General Long Baseline Experiment Simulator) is a C library containing algorithms associated with neutrino oscillation and statistics as well as experiment definition via AEDL ("Abstract Experiment Definition Language") text files. GLoBES can calculate oscillation probabilities analytically as well as matter effects by evolving the matter Hamiltonian through small layers of constant matter density. Once set up with an appropriate AEDL file, GLoBES works as a self contained program so the user can call probabilities and hypothesis tests without calculating any effective oscillation terms or matrix elements. A schematic of this idea is shown in figure 4.1. GLoBES has built in capability to used modified probabilities and read in extra parameters to simulate non-standard physics.

GLoBES uses channels that are defined via reconstructed detector event rates which will depend on oscillation probabilities and detection efficiency. These are each dependent on one actual physical observable, for example the observation of an excess or deficit in the amount of NC or CC events. A schematic of this is shown in figure 4.2. Which channels are important will depend on the experiment beam composition and baseline. For example NOνA primarily attempts to 'see' electrons produced in CC events from oscillated electron neutrinos in a neutrino beam initially of muon flavour, these can be directly detected above background events. NOνA also can analyse the muon flavour disappearance channel by comparing the number of predicted muon CC events to the measured CC event count. This channel will expect a deficit of events compared to predicted for the non-oscillation case and combined with the electron appearance data can give an idea of tau oscillation. The NC channel

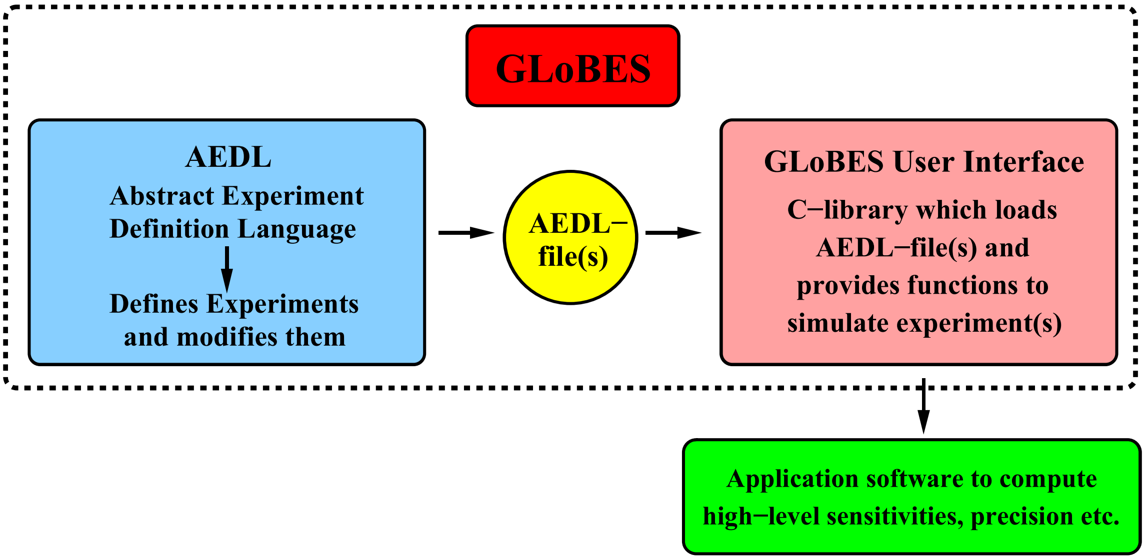

FIG. 4.1 Rough definition of the GLoBES interface and AEDL (from the GLoBES user manual available at the documentation page on the GLoBES website [143]).

is insensitive to neutrino flavour so can be used to test detection efficiency compared to expected number of events. In some cases a deficit in NC events, after accounting for efficiencies and rates, can potentially indicate sterile oscillations since these lack CC *and* NC interactions of possibly other interesting new physics. It is important to note that GLoBES can't output $P_{\alpha s}$ probabilities at all. Though these don't make much experimental sense anyway since they should be entirely invisible. If one wants to print sterile appearance for illustrations sake they will have to calculate it from the other probabilities. This is related to the fact that after calculating the PMNS matrix GLoBES will truncate it because we only care about transitions between active flavours. See the discussion on rectangular mixing matrices in section 3.5.1 for a similar idea.

Once we have defined channels they are then grouped into rules which consist of signal and background channels. These define what an experiment 'sees' overall once all separate channels are accounted for. Figure 4.3 shows the flowchart of signal+background to rule to χ^2 value. This is similar to how a physical experiment requires analysis to convert relatively useless direct particle/interaction counts into useful signals or rates above background. This allows for an output of oscillation probability or comparison between multiple test/true hypotheses.

GLoBES is limited in its ability to describe experiments and cannot take into account geometrical/directional source effects e.g. in the sun or the atmosphere or

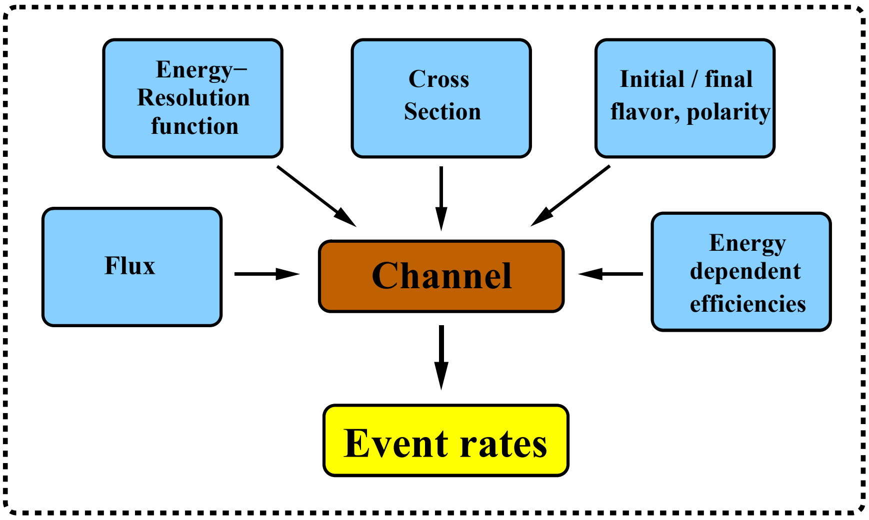

FIG. 4.2 Schematic describing AEDL channel definition showing several inputs (from the GLoBES user manual [143]).

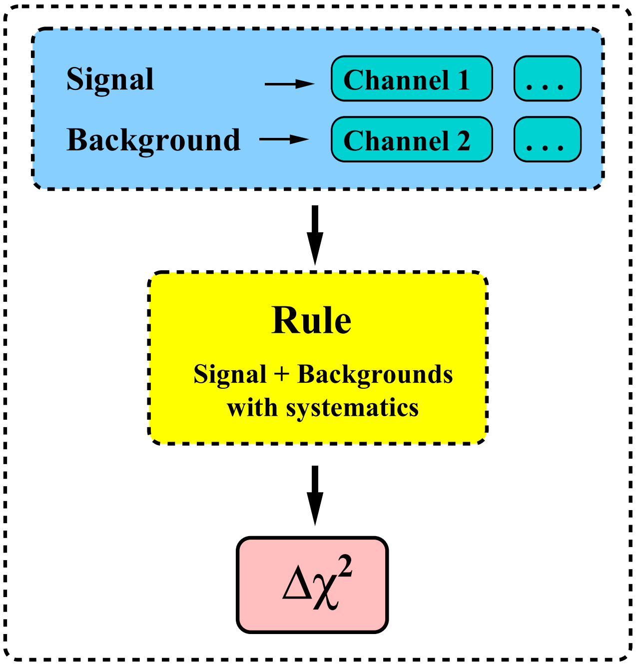

FIG. 4.3 Definition of rules in AEDL (from the GLoBES user manual [143]).

time dependent physics e.g. supernovae. However experiments which in principle have geometric effects, such as reactor experiments featuring multiple reactors as sources can be approximated. In addition, experiments where beams are pulsed to better veto background events (which are technically time dependent), can also be simulated, since the time dependence doesn't have physical significance to the actual oscillations. Figure 4.4 shows how a set of rules is combined in an experiment to give a sum of $\Delta\chi^2$ values that can be used for hypothesis tests. The standard install of GLoBES comes with files for simulating experiments including the commonly studied T2K and NOνA as well as some generic cases such as neutrino factories and β beams. In addition, files for proposed experiments T2HK and SPL (Superconducting Proton Linac), as well as reactor experiments DoubleCHOOZ (named after its two detectors near the Chooz Nuclear Power Plant in France, so not an acronym!) and RENO (Reactor Experiment for Neutrino Oscillation) are available.

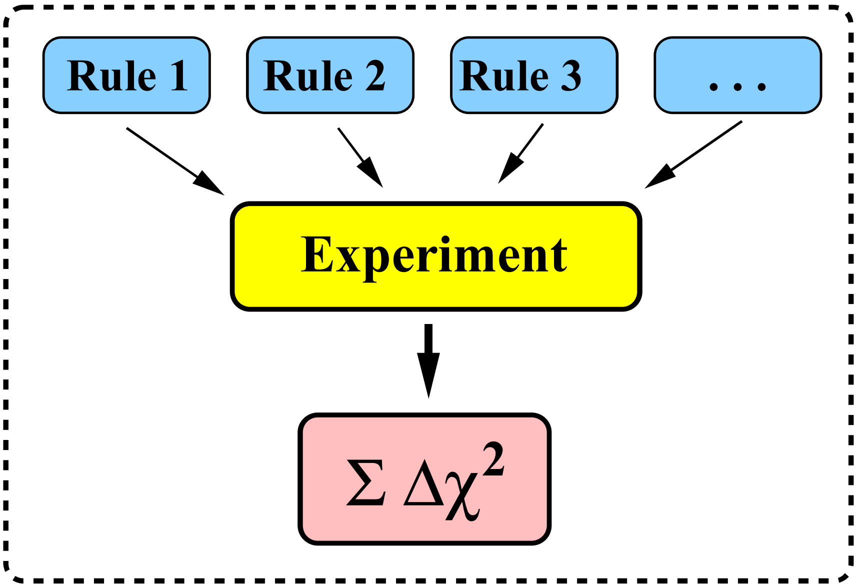

FIG. 4.4 AEDL experiment definition (from the GLoBES user manual [143]).

4.2 Simulation In 3+1 Scenario

Now that we have an idea of how we use GLoBES to simulate experiments, lets have a look at how we structure an analysis based on the $3+1$ hypothesis. To perform this analysis we will have to take true values from best fits for standard and extra parameters, these are specified in table 4.1. We also will need to know how to average our probabilities to represent finite detector resolution. Remember the sterile induced terms in our probability can be averaged because their oscillations will be rapid. So for $j = 1,2,3$ we have the averaged terms $\langle \sin^2 \Delta_{4j} \rangle \approx 1/2$ and $\langle \sin 2\Delta_{4j} \rangle \approx 0$ for all ν_4 induced oscillation factors Δ_{4j}. How do we implement this in our GLoBES probabilities?

Parameter	**True Value**	**Marginalisation Range**
$\sin^2\theta_{12}$	0.304	Fixed
$\sin^2 2\theta_{13}$	0.085	Fixed
$\sin^2\theta_{23}$	0.50	[0.34, 0.68]
$\sin^2\theta_{14}$	0.025	Fixed
$\sin^2\theta_{24}$	0.025	Fixed
$\sin^2\theta_{34}$	0.0	Fixed
δ_{13}	$[-180°, 180°]$	$[-180°, 180°]$
δ_{14}	$[-180°, 180°]$	$[-180°, 180°]$
δ_{34}	$0°$	Fixed
Δm^2_{21}	7.50×10^{-5} eV^2	Fixed
Δm^2_{31} (NH)	2.475×10^{-3} eV^2	Fixed
Δm^2_{31} (IH)	-2.400×10^{-3} eV^2	Fixed
Δm^2_{41}	1.0 eV^2	Fixed

TABLE 4.1 True value input parameters and marginalisation ranges in 3+1.

4.2.1 Averaging Probabilities in 3+1

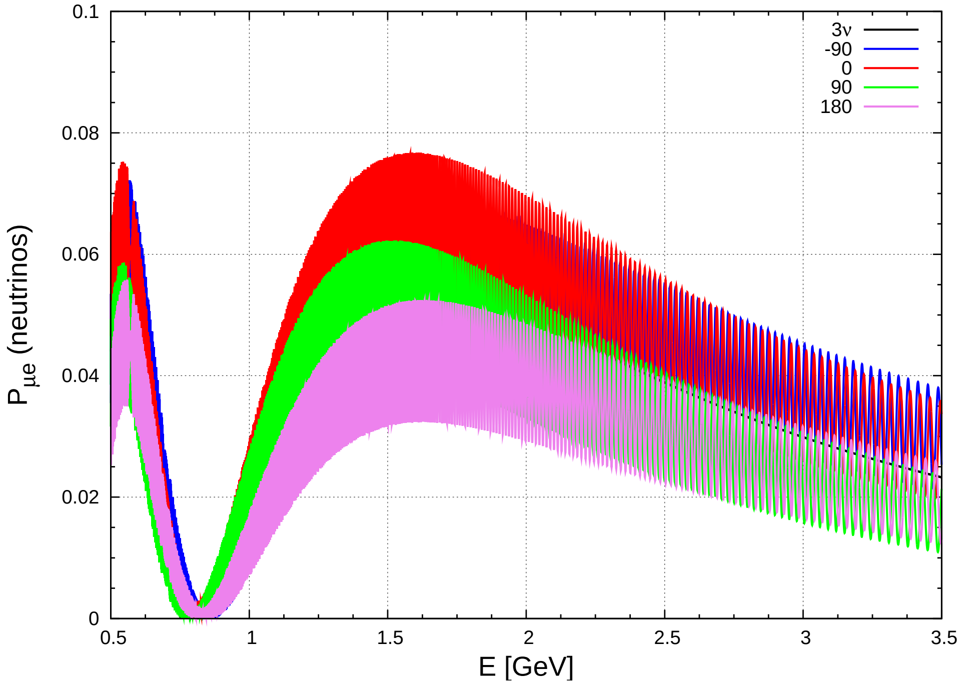

FIG. 4.5 Example oscillation probabilities for NOνA with various values of δ_{14}. Clearly we have not averaged over fast oscillations induced by ν_4 resulting in a rather messy plot!

Due to the finite resolution of the NOνA (or similar LBL experiment) detector in reality, these oscillations will inherently be averaged over. In GLoBES however we only obtain *exact* results according to the formula, as in figure 4.5. Therefore we will need to manually average these out to obtain nice smooth probabilities like those of figure 4.6.

We now outline how this can be performed during calculation of the unaveraged case. To do this we first run the standard probability function to output $P_i(E_i)$ where $i = 0, \cdots, N-1$ (indexing from zero due to our use of the C programming language) and N is the total number of data points. We define our energy axis as $E_i \in [E_{\min}, E_{\max}]$ where the minimum and maximum energies considered are experiment dependent (for NOνA, $E \in [0, 3.5]$ GeV while for DUNE, $E \in [0, 8]$ GeV)[1].

To temporarily store these outputs they are put into vectors $\vec{E}$ and $\vec{P}$ which have length N. To smooth our probability we want some form of averaged output $\vec{P}^A$ with corresponding energy axis points $\vec{E}^A$. Note we label $\vec{E}^A$ separately from the unaveraged $\vec{E}$ because the number of points N^A in $\vec{P}^A$ and $\vec{E}^A$ is actually less than N due to the width of the averaging window, in fact $N^A = N - n^A + 1$ where n^A is the number of points per average. This can be seen by observing that the first point in $\vec{P}^A$ will come from the average centred on the index $(n^A - 1)/2$ in $\vec{P}$, (which may not be an integer because it can be between two of the points in $\vec{P}$) with while the final point in $\vec{P}^A$ is an average including the final $(N-1)^{\text{th}}$ point in $\vec{P}$, hence is centred on $(N-1) - (n^A - 1)/2$. Taking the difference between these indices and adding one to account for the indexing from zero gives the length of $\vec{P}^A$ as $(N-1) - (n^A - 1)/2 - (n^A - 1)/2 + 1 = N - n^A + 1$. This clearly increases to the same length as the unaveraged case when $n^A = 1$, i.e., each point is only averaged with itself and hence no average is actually performed. The equation for our box windowed averages are:

$$D_j^A = \frac{1}{n^A} \sum_{i=j}^{j+n^A-1} D_i\,, \tag{4.1}$$

where $D_j(D_i^A)$ is $P_j(P_i^A)$ or $E_j(E_i^A)$ depending on which vector we are averaging and $j = 0, \cdots, N^A - 1$. The width of the averaging window is proportional to n^A which must be chosen such that $N > n^A > \tau$ where τ is the characteristic length of these sub oscillations i.e. we don't want to smooth out the larger scale behaviour

---

[1] Of course detectors will not see neutrinos with zero energy, their cutoff will clearly be way higher! We simply plot from zero (or close to it) to ensure we see the various peaks and troughs associated with the oscillation energy spectrum.

but also don't want to resolve small scale bumps and troughs. Rather than trying to find an exact size for this window we simply make a guess, especially as these plots are mostly used for demonstration purposes and varying the window size around a reasonable region barely affects the plot. In our case $N = 10000$ and $n^A = 550$, hence $N^A = 9451$. To compensate for the fact that $\vec{E}^A, \vec{P}^A$ are shorter than $\vec{E}, \vec{P}$ we often take the range of $\vec{E}$ to be larger than necessary. This ensures that our average can run the full range of E we are interested in and we don't run into any edge effects where the average starts to fail. Note that we clearly do not actually have to average the energy $\vec{E}$ and could simply set each point of $\vec{E}^A$ to the midpoint of the energies in each average, but because of the way the code is written and the fact that speed of execution is no issue this turns out to be more straightforward.

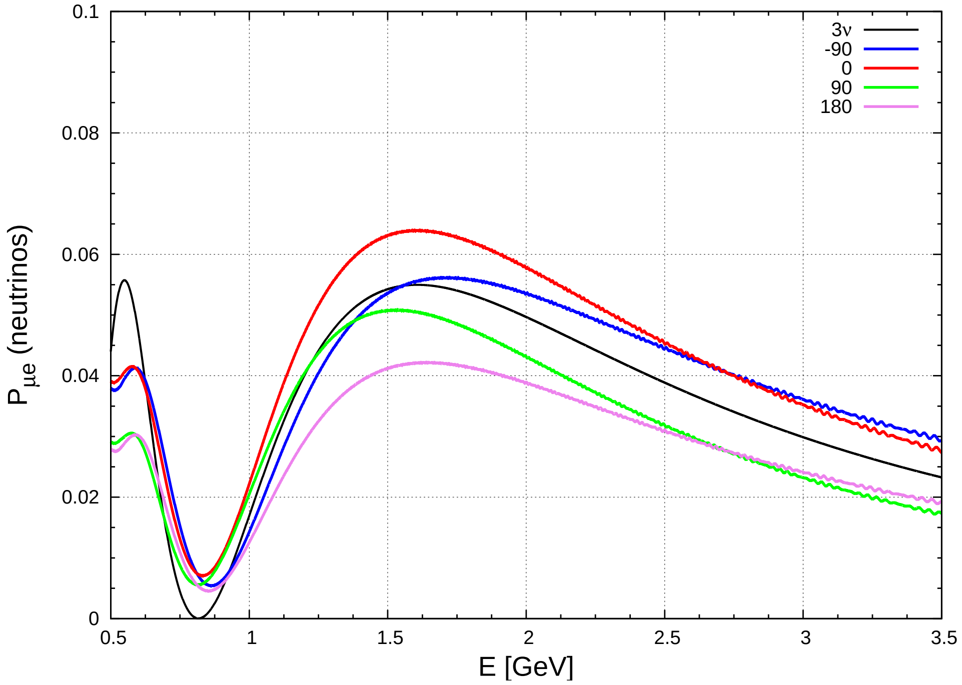

FIG. 4.6 Example oscillation probabilities for NOνA with $\delta_{13} = 0°$ and various values of δ_{14}. This is averaged over fast oscillations though some dithering can be seen on the right side of the plot.

These averaging algorithms only become necessary when we have fast oscillations relative to the primary oscillations our detector is designed to see, in our case this only occurs for Δm^2_{41} driven oscillations. In the standard case this approach is unnecessary though should, in principle, not affect the results greatly if at all.

4.2.2 Example Oscillation Probabilities

Several example probabilities for a given experiment can be compared on the same axes to give an 'at a glance' test of whether degenerate solutions might be measured at said experiment. To see a standard oscillation example we plot NH and IH bands for various δ_{13} in figure 4.7. Figure 4.7 clearly outlines favoured and unfavoured regions of parameter space to resolve the hierarchy in 3ν. True values corresponding to areas far from the overlap (NH, $\delta_{13} = -90°$) and (IH, $\delta_{13} = 90°$) will be favoured while areas that are overlapping such as (NH, $\delta_{13} = 90°$) and (IH, $\delta_{13} = -90°$) will be disfavoured. To get an idea in 4ν we perform additional computations based on the averaged plot 4.6 to give several iterations based on values of δ_{13}, the mass hierarchy and whether we are simulating neutrinos or antineutrinos. As with figure 4.6 we plot five traces on each plot, the 3ν probability and the 4ν probabilities for $\delta_{14} = 0°, 90°, -90°, 180°$.

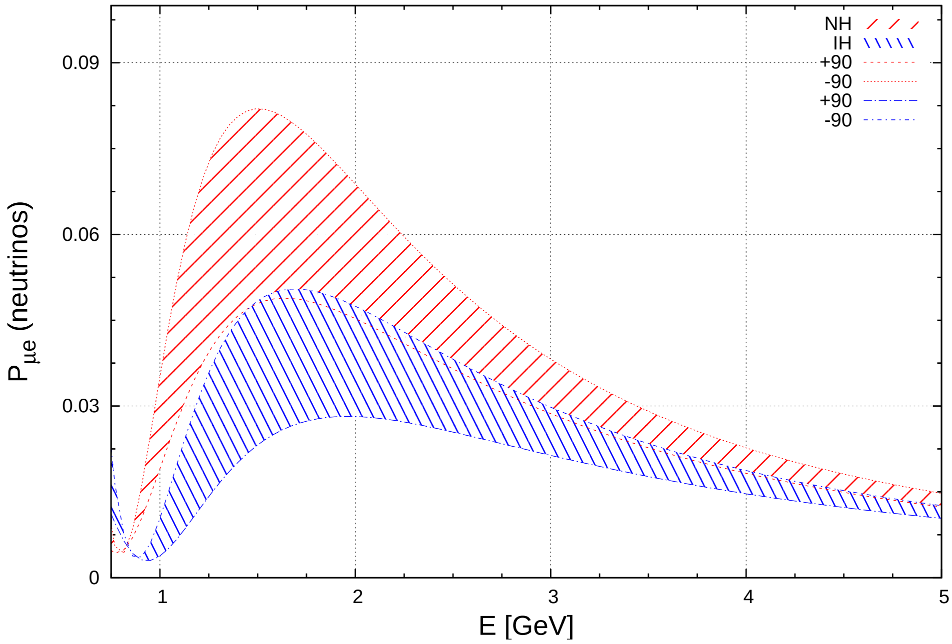

FIG. 4.7 Three flavour probability bands for NOνA showing the overlap of NH (red) and IH (blue) probability bands for $\delta_{13} = 90°$ (bottom line of each band) and $-90°$ (top line of each band).

Figure 4.8 contains several NH cases for $\delta_{13} = 0°, 90°, -90°, 180°$ with neutrinos(antineutrinos) notated by the unprimed(primed) labels. It can be seen at a glance that different combinations of δ_{13} and δ_{14} are maximal and minimal in each case for a given hierarchy e.g. 4.8(a) has $\delta_{14} = 0°$ maximal, while the plot for the other CP conserving value of δ_{13}, 4.8(d) has the $\delta_{14} = 0^\circ$ curve as the lowest. It can also be seen that the trend for probabilities lowers in general when we move from neutrinos to antineutrinos in NH with the exception of (b) to (b′). We expect the opposite to be true for IH as, recalling this is related to the reason for the MH-δ_{13} degeneracy in 3ν as we will see in figure 4.7. Figure 4.9 validates this prediction. Unfortunately it can be seen that the same δ_{14} curves overlap in each case so it is unlikely that this will assist in the same way for MH-δ_{14} degeneracies. We explore this in section 4.3.2.

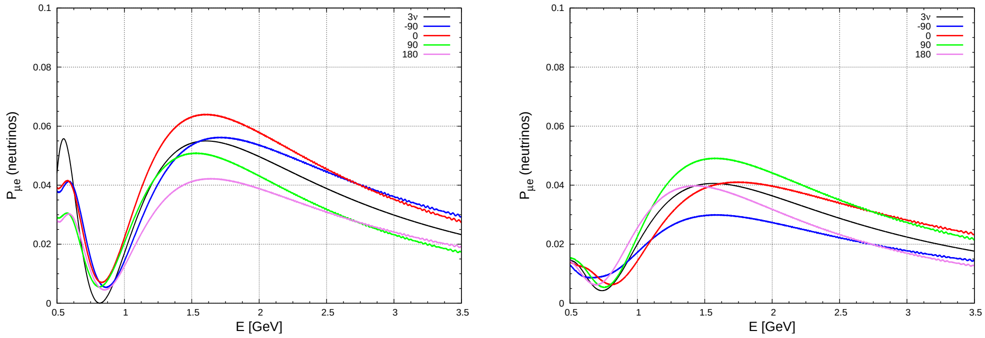

(a) NH, $\delta_{13} = 0°$ (b) NH, $\delta_{13} = 90°$

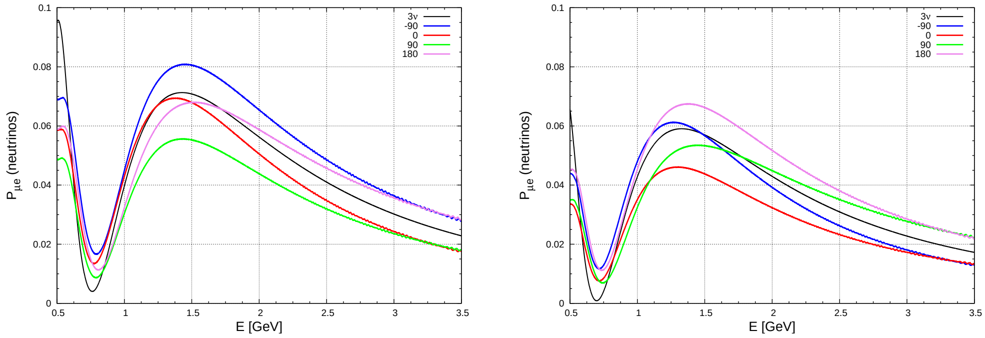

(c) NH, $\delta_{13} = -90°$ (d) NH, $\delta_{13} = 180°$

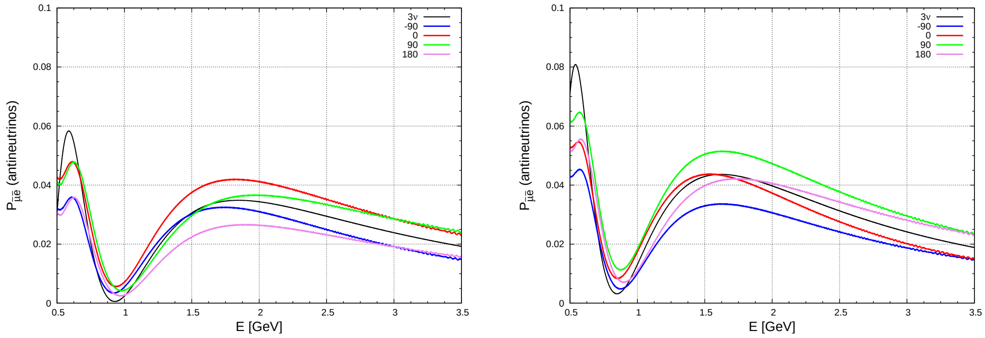

(a′) NH, $\delta_{13} = 0°$ (b′) NH, $\delta_{13} = 90°$

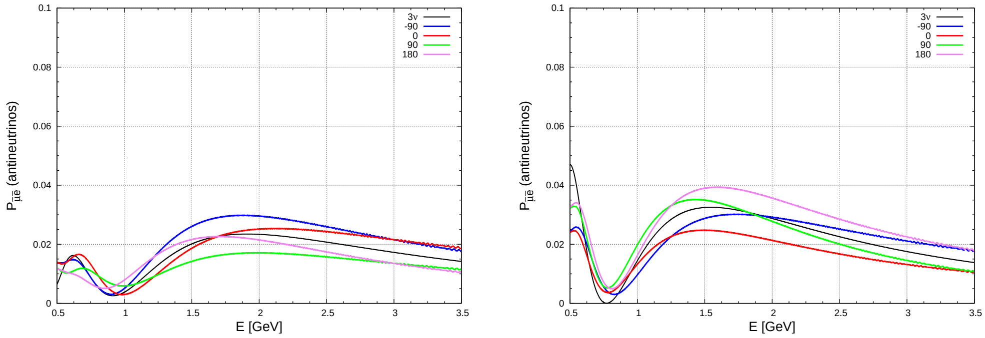

(c′) NH, $\delta_{13} = -90°$ (d′) NH, $\delta_{13} = 180°$

FIG. 4.8 Probability plots with NH as true hierarchy for NOνA with various values of δ_{13} and δ_{14}. Unprimed(primed) plots are for neutrinos(antineutrinos). The relative heights of each probability with a given δ_{14} choice changes depending on the value of δ_{13}. Going from neutrino to antineutrino (e.g. (a) to (a′)) does not change this relative ordering. This will have consequences for degeneracy resolution when we marginalise over δ_{13} and δ_{14} in hypothesis tests. Note that figure 4.8(a) is 4.6 repeated.

Figure 4.9 is the same as 4.8 but for IH. Flipping the hierarchy interestingly, shows the same relative ordering for the lowest and highest curves in each case, but opposite ordering for the intermediate ones in some cases. The fact that not all of the intermediate values flip implies that this is likely based on sub-leading effects and that the MH has no direct effect on these orderings at first order.

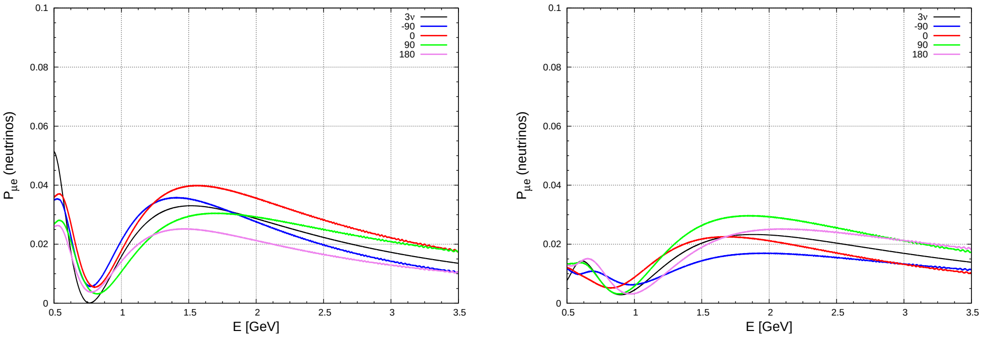

(a) IH, $\delta_{13} = 0°$

(b) IH, $\delta_{13} = 90°$

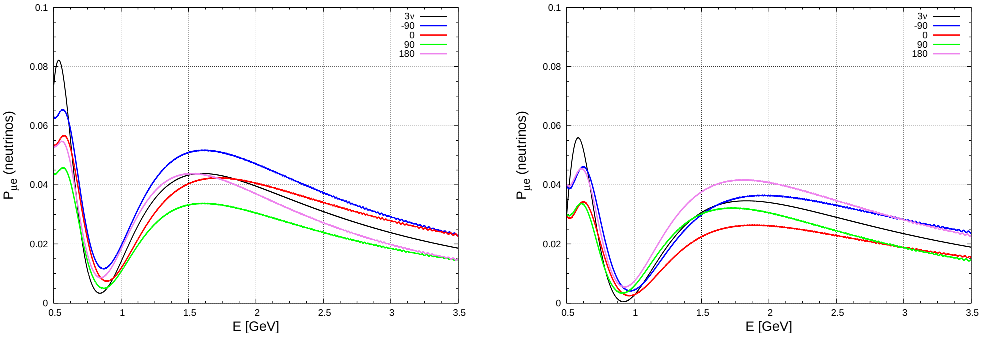

(c) IH, $\delta_{13} = -90°$

(d) IH, $\delta_{13} = 180°$

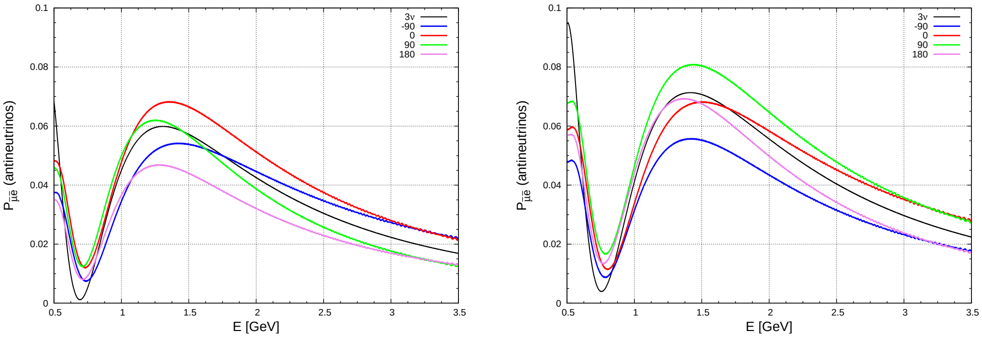

(a′) IH, $\delta_{13} = 0°$

(b′) IH, $\delta_{13} = 90°$

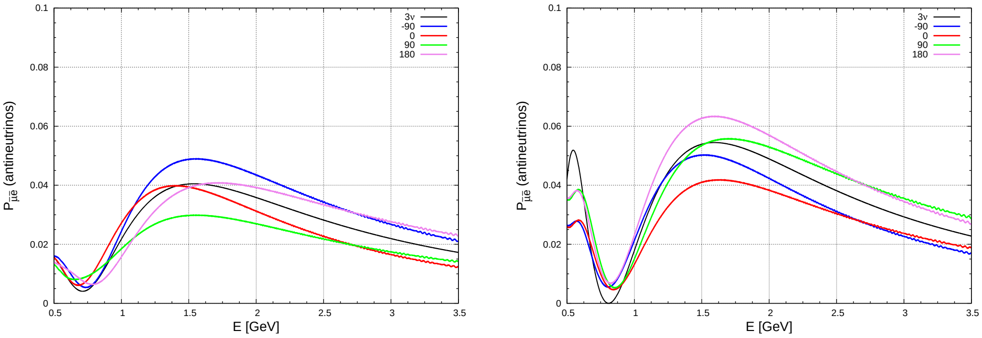

(c′) IH, $\delta_{13} = -90°$

(d′) IH, $\delta_{13} = 180°$

FIG. 4.9 Probability plots similar to figure 4.8 except with IH as true hierarchy. Comparing to figure 4.8 shows that almost exactly the same relative ordering of probability curves are present, this implies that extra 4ν terms in the probability don't flip sign under hierarchy change. Conversely, the overall heights do vary between NH and IH. Therefore allowing δ_{14} to float when fitting an experimental measurement will increase the amount of wrong solutions for a given true MH and δ_{13}.

Between the plots 4.8 and 4.9, any two curves that have around the same probability within the NOνA beam energy window (around 2 GeV) have the potential to produce degenerate solutions. Trying to pick degenerate values out of these plots by eye is perhaps not the most exact or efficient way of investigating detector response, especially due to the lack of any statistical effects or combined neutrino-antineutrino runs. In general, plots with degenerate curves in neutrinos can be quite non-degenerate in antineutrinos. This is potentially the most useful comparative tool these probability plots give us because they can directly inform experimentalists on how to balance the runtimes of either mode in such an experiment. Our examples do seem to show that such differences are much less pronounced in our 4ν case, which is why we expect the effect of extra flavours to be a net degradation in sensitivity.

Because looking at these individual probabilities overlaid is not always the best way of visualising degenerate values, often we will instead plot a band of probabilities and inspect how such bands overlap. Using bands shows more clear comparison between the two binary options chosen, usually NH/IH or LO/HO. For an example of this see figure 5.1 in our sterile analysis, which corresponds to the specific probabilities in 5.2. This also naturally leads us to our statistical analyses involving true and test hypotheses.

4.3 Parameter Degeneracies

Soon after oscillation was verified to occur precision measurements of mixing parameters began. Not long after it was found that the parameter space is fraught with degeneracies due to multiple sign flipping invariant terms as well as angular ambiguities [144]. It is around this time that the beam experiments of today started to be dreamt up and simulated for the first time with the hope of solving said degeneracies [144, 145]. First we investigate the theoretical underpinning of these degeneracies directly from equations, then we investigate the historical and current attempts to solve these problems with global fits and combined analyses. We will take an aside here to properly describe degeneracies in a general sense before we go further with our studies.

4.3.1 Degenerate Properties of Mixing

For a given oscillation process and experiment we can specify an effective two-flavour mixing (see 3.4) that is specific to this case as

$$P_{\alpha\beta} \equiv \sin^2 2\theta_{\alpha\beta} \sin^2 \Delta_{\alpha\beta}\,, \text{ for } \alpha \neq \beta \tag{4.2}$$

for β flavour appearance, and

$$P_{\alpha\alpha} \equiv 1 - \sin^2 2\theta_{\alpha\alpha} \sin^2 \Delta_{\alpha\alpha}\,, \tag{4.3}$$

for α flavour survival. We will focus on the appearance probability for now. It is clear from equation (4.2) that for a given value of $P_{\alpha\beta}$ we can solve for two solutions of $\Delta_{\alpha\beta}$, one positive and one negative. Hence this individual channel only constrains the overall size of the term $|\Delta_{\alpha\beta}|$. Furthermore, for simplicity's sake lets say we are at an accelerator and we can specify the conditions such that $\sin^2 \Delta_{\alpha\beta} \approx 1$ by tuning L/E. Then we have the simplified probability for this case

$$P_{\alpha\beta} \approx \sin^2 2\theta_{\alpha\beta}\,, \tag{4.4}$$

which also appears to have a sign degeneracy. However because the probability must be positive and unlike the mass splitting, the underlying mixing parameter is not a physical measurable so recalling section 2.1 we simply define the positive angle to be our choice.

This is not the end of our problems however, if we see the probability to be maximal $P_{\alpha\beta} \approx 1$ then $\sin^2 2\theta_{\alpha\beta} = 1$ and hence the solution for $\theta_{\alpha\beta}$ will be $\theta_{\alpha\beta} \approx 45°$. But for values close, but not equal to maximal, we will have the so-called octant degeneracy. This is where the probabilities for $45° \pm \phi$ will be the same due to the points $45° - \phi$ and $45° + \phi$ in the $\sin^2 2\theta$ plot being on opposite sides of a peak. For example for $\phi = 5°$, $\sin^2(2 \times 40°) = \sin^2(2 \times 50°)$. This can be more generally expressed as $P(\theta) = P(90° - \theta)$.

The name octant degeneracy comes from the fact that solutions for $\sin^2 2\theta = 1$ divide the θ parameter space into four sections i.e. 'quadrants', which are then further split into eight sections or 'octants' when we take $\sin^2 2\theta_{\alpha\beta}$ to be slightly off maximal. It unfortunately turns out that this is the case in the atmospheric neutrino $P_{\mu\mu}$ channel. Using the form of the survival channel in this case from equation (4.3), this channel can be expressed as:

$$P_{\mu\mu} = 1 - \sin^2 2\theta_{\mu\mu} \sin^2 \Delta_{\mu\mu} \,, \tag{4.5}$$

where the effective mixing angle and oscillation factor are

$$\sin^2 2\theta_{\mu\mu} = 4\cos^2\theta_{13} \sin^2\theta_{23} \left(1 - \cos^2\theta_{13}\sin^2\theta_{23}\right) \tag{4.6}$$

and

$$\Delta_{\mu\mu} = \Delta_{31} - \left(\cos^2\theta_{12} - \cos\delta_{13}\sin\theta_{13}\sin 2\theta_{12}\tan\theta_{23}\right)\Delta_{21} \,, \tag{4.7}$$

at first order in small terms. Because we wish to show clearly that this probability will experience the octant degeneracy in θ_{23} we will make the assumption that θ_{13} is small such that $\cos^2\theta_{13} \approx 1$. This is not well motivated with real parameters as it turns out that θ_{13} is relatively large (see section 4.3.2), but will demonstrate the behaviour. These assumptions allow us to simplify the mixing parameter via

$$\begin{aligned} \sin^2 2\theta_{\mu\mu} &= 4\sin^2\theta_{23}\left(1 - \sin^2\theta_{23}\right) \,, \\ &= 4\sin^2\theta_{23}\cos^2\theta_{23} \,, \\ &= \sin^2 2\theta_{23} \,. \end{aligned} \tag{4.8}$$

Where we used $\sin^2\theta + \cos^2\theta = 1$ from first to second line and the squared version of the double angle formula $\sin 2\theta = 2\sin\theta\cos\theta$ from the second to third. With these simplifying assumptions we get to a probability which displays the essence of our degeneracy similar to the previous effective case,

$$P_{\mu\mu} \approx 1 - \sin^2 2\theta_{23}\sin^2\Delta_{31} \,, \tag{4.9}$$

the oscillatory part of which is of the same form as the effective parameter equation (4.2). Note that for $\theta_{13} \neq 0°$, $\theta_{23} \neq \theta_{\mu\mu}$ so the atmospheric angle measured does not exactly correspond to the underlying parameter θ_{23} [146] but the degeneracy still appears in almost exact form. This is the muon flavour appearance probability, hence the term controlling the amplitude of muon disappearance must be

$$A_{\mu}^{\text{disapp}} = \sin^2 2\theta_{23} \,. \tag{4.10}$$

Note that the equations (4.6, 4.7) are accurate approximations at accelerator experiments designed to be sensitive to the atmospheric channel but not necessarily at atmospheric experiments themselves. This is because the L/E value can be tuned at accelerators such that Δ_{21} is very small compared to Δ_{31} so the related terms can be treated as a small perturbation [147]. Conversely, because atmospheric oscillations have an uncertain L/E, then $\sin^2 \Delta_{\mu\mu} \neq 1$ in general so we cannot assume an equation similar to (4.4) or that (4.6, 4.7) apply to $P_\mu^{\rm disapp}$ when measured by such experiments. The lack of an easy approximation means that there is uncertainty in relating measured atmospheric effective mixing parameters to the underlying three flavour parameters. Despite this, early fits of such measurements showed that disappearance of muon flavour was around maximal, implying $\theta_{\mu\mu} \approx 45^\circ$ and that, at least from the naive assumption, $\theta_{23} \approx 45^\circ$. Therefore an octant degeneracy for θ_{23} appeared in the data [148]. This problem persists in recent data [88] and may be resolved in the coming years, potentially by new detectors. We refer to the possible solutions around maximal as lower octant ($\theta < 45^\circ$), maximal mixing ($\theta = 45^\circ$) and higher octant ($\theta > 45^\circ$). These are then usually abbreviated to LO, MM and HO respectively. Fortunately the other mixing angles are much further from maximal so do not have this ambiguity.

Recall that in section 1.9 we claimed that sometimes it is useful to refer to the mass ordering somewhat incorrectly as the mass hierarchy. This is because when simultaneously discussing the octant we can reduce the confusion in abbreviations e.g. NO-LO versus NH-LO. Sometimes we also will refer to octant and/or hierarchy solutions in parameter space as right or wrong depending on their relation to the true values. These will be abbreviated in the form WO-RH, RO-WH, WO-WH (for degenerate regions) and RO-RH (for the region surrounding the true value). If we were using the word ordering instead, we then have abbreviations such as RO-RO. This is a poorly chosen, ambiguous shorthand because we have to remember the convention for referring to our parameters. This notation will be used extensively in chapters 5 and 6.

When we expand this to the three flavour case we introduce the first CP phase, δ_{13} (often simply δ_{CP} when there are no other phases to confuse it with). This parameter is also highly degenerate due to interplay with the sign of Δ_{31} where it comes into several probabilities. For example the expanded and simplified muon to electron appearance probability $P_{\mu e}$ from equation (3.6) has two terms dependent on $\sin^2 \Delta_{31}$ and one term dependent on $\Delta_{31} \times \sin \Delta_{31} \times \cos(\Delta_{31} - \delta_{13})$. So for an entirely degenerate term we need to transform $\delta_{13} \rightarrow 90^\circ - \delta_{13}$ in addition to flipping the sign of Δ_{13} to account for all of the sign flips necessary. This is called the MH-CP or MH-δ_{13} degeneracy and it extends the MH degeneracy to terms also involving the CP phase δ_{13} which are often not sensitive to MH alone.

4.3.2 Degeneracies at Experiments

It was quickly observed that due to the interplay between matter effects, mass ordering and CP, a long baseline experiment with the capability of running neutrino and antineutrino beams has some chance of solving the MH-CP degeneracy. The matter effect modifies oscillation probabilities in the opposite way for neutrinos and antineutrinos. In the NOνA case, where matter effects are reasonably significant this separates the NH and IH probabilities such that less possible combinations of δ_{13} and MH are degenerate. An example of this in the $3+1$ case can be seen from the bands in figure 4.10. In this case the matter effect enhances probability of ν_e appearance more for NH than IH. Conversely the probability for $\overline{\nu}_e$ appearance is diminished more for NH than IH for the same mixing parameters. It can be seen that the bands do not totally overlap which is what we'd expect from the vacuum case given the MH-CP degeneracy. Most of the parameter space of either mass ordering is separated except for the parts of the bands near (NH, 90°)/(IH, -90°) for neutrinos and (NH, -90°)/(IH, 90°) which will remain degenerate at the probability level and will likely show degenerate values in allowed region plots. The range of δ_{13} is usually separated into upper and lower half plane sections (UHP and LHP) so we can categorise which sets of true values are favoured and unfavoured regions for degeneracy resolution. So again from figure 4.10 we can conclude that (NH, LHP) and (IH, UHP) are favoured combinations for MH-CP degeneracy resolution, while (NH, UHP) and (IH, LHP) are unfavoured.

Accelerator experiments such as NOνA can measure $P_{\mu\mu}$ and $P_{\mu e}$ it is interesting to see what sensitivity to θ_{23} can be gained from either channel. Unfortunately due to degeneracy $P_{\mu\mu}$ has no sensitivity to the octant, though it can put limits on $\Delta_{\mu\mu}$ and $\sin^2 2\theta_{\mu\mu}$. So from (4.6), these limits will have two corresponding regions (which can intersect in parameter space) for $\sin^2\theta_{23}$, one for each possible octant. The $P_{\mu e}$ channel on the other hand does have sensitivity to octant depending on how well we know the CP phase, as can be seen in figure 4.11. Similarly, in the $3+1$ case the additional phase δ_{14} can modify this overlap as seen in figure 4.12 for $\delta_{13} = -90^\circ$.

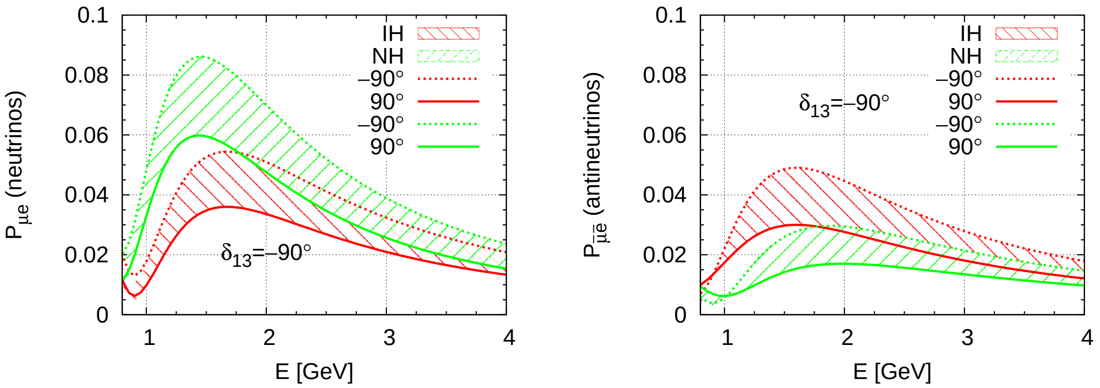

FIG. 4.10 Probability band plot showing overlap of different mass-ordering solutions at NOνA for neutrino and antineutrino. In both cases δ_{13} is fixed at $-90°$ and bands are drawn between the curves corresponding to $\delta_{14} = -90°$ and $90°$.

Unfortunately for these experiments, the octant degeneracy sensitivity is not affected by the difference between neutrino and antineutrino matter effects. This is because the contribution of the matter effects flip when the sign of Δ or δ changes as well as between neutrino and antineutrinos. This allows combined runs to distangle effects. No such behaviour exists for the octant. This can be seen in figure 4.12 where the same parts of the bands are degenerate for both neutrinos and antineutrinos. This implies that if present, this octant-CP degeneracy will likely have to be solved using combined statistics or similar methods.

Overall the three neutrino parameter space has three degeneracies, the MH-CP, octant and intrinsic θ_{13}-CP. The combination of degeneracies leads to the so called 'eightfold' degeneracy due to the total $2 \times 2 \times 2 = 8$ possible binary combinations of each degenerate pair of solutions. However, nowadays θ_{13} is known to be non-zero and relatively large, somewhat reducing the possible combinations of parameter degeneracies to four. From equation (4.6) it could be surmised that this non-small value could somewhat break the exactness of the octant degeneracy. It has been shown that this is not the case and indeed the LO and HO solutions will instead merely be slightly shifted when accounting for this by using the full equations (4.6, 4.7) for the effective parameters rather than assuming $\theta_{\mu\mu} = \theta_{23}$ and $\Delta_{\mu\mu} = \Delta_{32}$ or Δ_{31} which was the norm when θ_{13} was thought to be zero [146].

The likely solution to these problems, especially given the current abundance of experiments, is the combination of statistics from several detectors measuring the same interactions but with differing baselines. The reason this is useful is because the true values should line up in parameter space but the degenerate values may differ

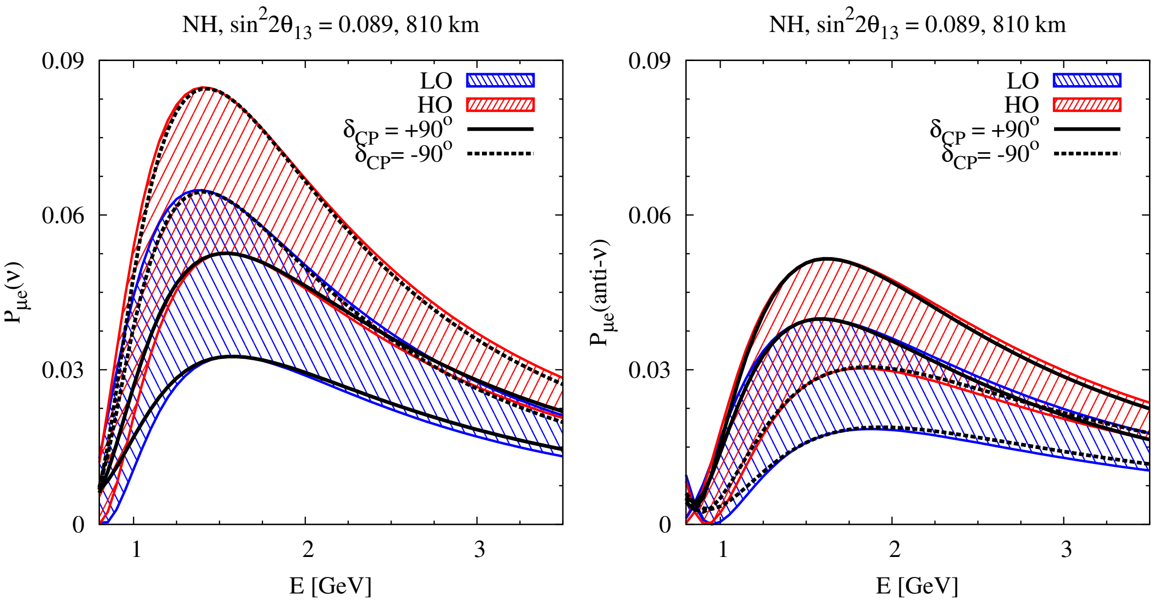

FIG. 4.11 Probability band plot showing overlap of different octant solutions at NOνA for neutrino and antineutrino in 3ν with varied δ_{13}. Taken from Agarwalla et al. 2013, Figure 1 [147].

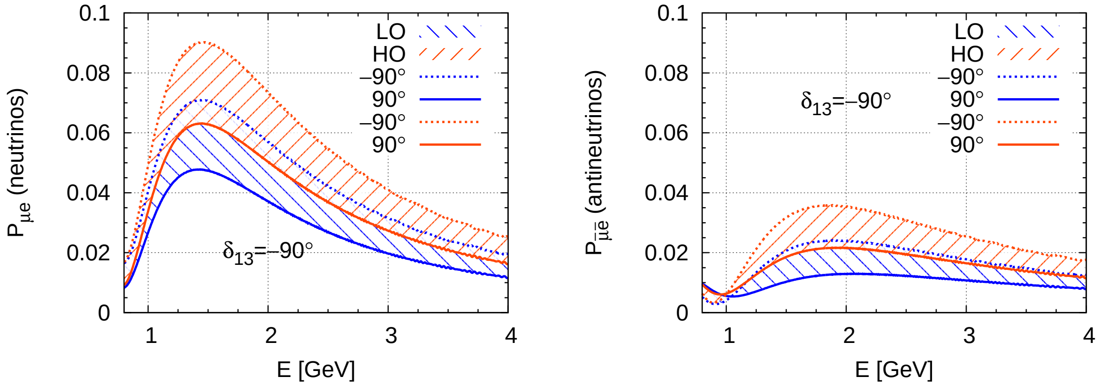

FIG. 4.12 Probability band plot showing overlap of different NH octant solutions at NOνA for neutrino and antineutrino with the same variations in δ_{13} and δ_{14} as figure 4.10. Note how for δ_{14} variation the octant bands *don't* flip, unlike δ_{13} in figure 4.11.

in exact position between experiments due to the differing matter effects. This can allow experiments to disentangle these degenerate regions.

4.4 Example Analyses

Here we outline a few examples of analyses commonly performed with GLoBES. In general the outputs used for analysis can either be raw numbers such as oscillation probability/number of events or statistical χ^2 hypothesis tests. Comparing event rates and probabilities is useful for determining what models will be degenerate at the probability level. It is obvious when this is the case because their curves will overlap or be nearby in such plots. With hypothesis tests we sometimes will pick one true value and vary the test parameters over their full allowed range to see what values agree at some confidence interval. This will highlight what values will appear degenerate given experiment combination, setup and runtime at this chosen level.

Another common analysis involves varying one or two parameters in the true hypothesis (often CP phase or phases and θ_{23}) and explicitly setting the test hypothesis to the same model except with a degenerate value flipped e.g. mass hierarchy, CP phase or octant of θ_{23}. This will show the level of confidence we can reject that explicit degeneracy for the particular value of the varied parameter(s). In general this confidence level will change, even if these parameters do not appear to contribute to the degeneracy from equations via sign flips etc.

Common hypothesis tests can be one or two dimensional. One dimensional plots are commonly used to compare true models differing by one parameter such as different values of CP violating phases. Two dimensional tests are often more useful in comparing test hypotheses with entangled degeneracies such as MH-CP (see allowed region plots). Another use of two dimensional tests is viewing the true regions where such cases are resolvable (see MH exclusion plots in chapters 5 and 6). Hypothesis tests will usually be performed by choosing a true set of oscillation parameters and comparing a set of test parameters with some degree of variation in the ones considered free. Such free parameters are marginalised to find the minimum χ^2 value for each location in the parameter space to ensure that we are looking at the lowest χ^2 values when we plot curves or confidence regions. These results will therefore correspond to the worst possible case for telling the true and test hypotheses apart. To fully account for neutrino+antineutrino combined runs, as well combining statistics of multiple experiments, hypothesis tests must be performed. It is also possible that highly degenerate regions in probability may not be degenerate at reasonable confidence level when a χ^2 test is performed due to statistics. This is why hypothesis tests are where real conclusions can be made.

4.4.1 Hierarchy Determination (3ν)

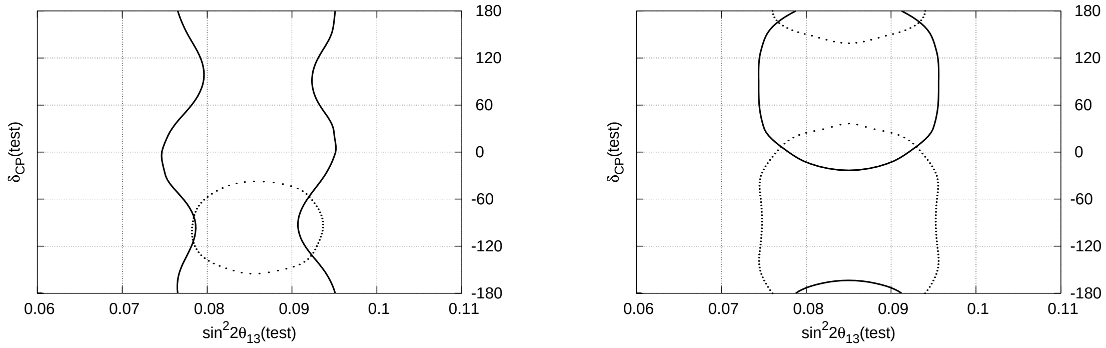

(a) NH, $\delta_{13} = 0°$ (b) NH, $\delta_{13} = 90°$

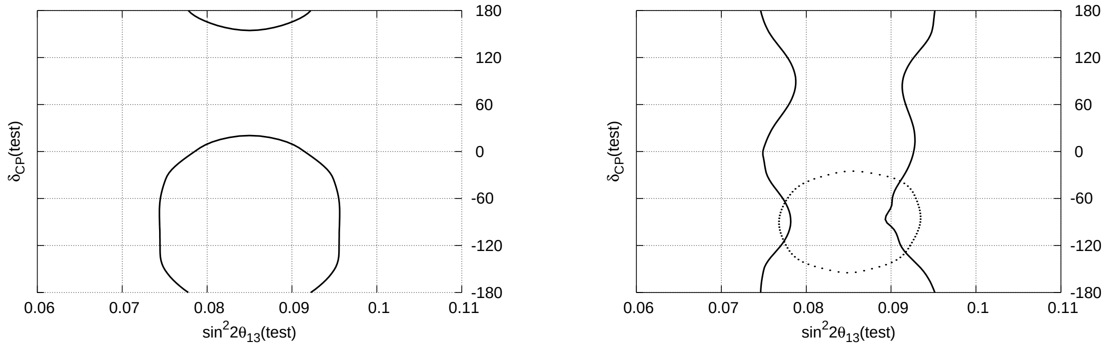

(c) NH, $\delta_{13} = -90°$ (d) NH, $\delta_{13} = 180°$

FIG. 4.13 Hierarchy determination plots for NOνA in the standard 3ν case. NH is the true hierarchy and δ_{13} takes various values these are labelled below each plot. The areas included in the regions are allowed at 90% C.L. where the solid(dotted) lines represent NH(IH) test solutions. We can conclude that for any true values other than those of (c), degenerate IH regions can appear in NOνA analyses at this confidence level.

Presented here are several example plots that demonstrate the idea of test solutions in the $\sin^2 2\theta_{13}$(test)/δ_{13}(test) plane for a specific underlying true set of parameters. In the plots 4.13 to 4.20 the smooth lines demonstrate the test NH solution which is the correct guess for the true ordering. The dashed lines represent test IH solutions which also appear at the chosen significance due to degeneracies. Both are drawn at 90% C.L. and should be taken as illustrative only because they do not encompass current values for parameters. We again use NH/IH rather than NO/IO to clearly separate ordering/hierarchy solutions from octant ones. From the four different true values of δ_{13} the position and significance of the correct and incorrect regions changes. For example, notice how the degenerate solution vanishes for figure 4.13 (c) due to it being the favoured true parameter combination for NOνA to resolve the ordering/hierarchy. The correct guess for the ordering creates a region that includes the true solution and should usually be centred over it. Conversely, the region corresponding to the incorrect guess can appear anywhere in the parameter space where the degeneracy is such that the significance of this wrong guess is high. The plots with CP conserving δ_{13}, 4.13 (a) and (d) are very similar with an extended NH solution including the respective true values and a degenerate value for IH and $\delta_{13} = -90^\circ$. The plot for the specifically disfavoured region, 4.13 (b) has almost mirrored solutions about $\delta_{13} = 0^\circ$, with the wrong IH solution having flipped sign in CP as expected from the hierarchy-CP degeneracy due to these two sign flips cancelling out in several leading order terms in the probability.

4.4.2 Hierarchy Determination (4ν)

The analysis from before can be extended with the additional parameter space of the 3+1 case, we wish to see how the correct guess and (perhaps more interestingly) the degenerate incorrect guess change. Due to the extra parameter space we have another CP-phase, which is δ_{14} in our parametrisation (we actually have two, δ_{14} and δ_{34}, but as can be seen in section 2.2.3 only one of these new ones comes into the μ and e matrix elements). This additional phase is the least constrained of the 4-flavour induced parameters and perhaps the most impactful. Therefore we will vary this between the same two CP conserving and two violating phase angles as δ_{13}. This gives us four times the plots which we arrange into figures 4.14 and 4.15 for conserving and violating values respectively.

4.4.3 Octant Determination (3ν)

To test the octant determination potential in 3ν we perform a similar analysis as in figure 4.13 but we choose true $\theta_{23} \neq 45^\circ$ and plot in the test $\delta_{13} - \theta_{23}$ plane instead. If we utilise similar combinations of parameters to before, then plotting each again except with LO and HO inputs will double our number of subplots. In the resulting plot 4.16 we can clearly see the right and wrong octant solutions reflected about $\theta_{23} = 45^\circ$ in every subplot but 4.16 (d). Some plots have wrong hierarchy solutions located only in the right octant such as 4.16 (d), (A) and (D) where we can see degeneracies already existed by comparing to 4.13 (a) and (d). This would imply that in cases like these the octant uncertainty doesn't introduce additional MH uncertainty. However for 4.16 (a), (b) and (B) we have wrong MH solutions for right and wrong octant simultaneously. This gives us three regions at our chosen confidence, or even four in the case of (a) and (B). This would lead to multiple best fits obviously which illustrates the essence of these compounding degeneracies.

So to summarise, there can in general be three spurious solutions in addition to the true solution which are the: (i) right hierarchy-wrong octant (RH-WO), (ii) wrong hierarchy-right octant (WH-RO) and (iii) wrong hierarchy-wrong octant (WH-WO) solutions. The 'right guess' or true solution will clearly be the right hierarchy-right octant (RH-RO) one, which is perhaps less useful as an abbreviation than just 'true'.

4.4.4 Octant Determination (4ν)

Similar to the 4ν hierarchy extension in 4.14 and 4.15, we can extend the octant analysis of 4.16 into the sterile parameter space. For plots 4.17, 4.18, 4.19 and 4.20 we vary the ordering between normal and inverted, octant between LO and HO and the CP phases between four values: $0°, 180°, 90°$ and $-90°$. The combinatorics of even this limited ($\delta_{13}, \delta_{14} = \pm 90°$) situation give us many ($2 \times 2 \times 4 \times 4 = 64$) potential sets of true parameters to plot, which is more than we care to analyse. It is for this reason that we neglect inverted ordering true solutions in this demonstration. What we really care about demonstrating is the appearance of right and wrong test solutions corresponding to the true and degenerate parameters respectively. Such regions should be present for a decent subset plots regardless of which ordering is set to be true. In realistic analyses the number of combinations considered will usually shrink based on best fits of parameters from previous works and plots can be tailored to suit.

We directly compare lowercase(uppercase) figures in 4.16 to 4.17(4.19) and 4.18(4.20). Note that the unprimed/primed nature of plots in the 4ν case is used to notate which of the CP values is used. So we match up letters to compare values other than θ_{23} and capitalisation to match LO/HO. The primes are used to denote specific values of δ_{14} in each plot. For example, true NH, HO $\delta_{13} = 90°$ corresponds to the 3ν subplot 4.16(B′) and the 4ν subplots (B) and (B′) in 4.19 and 4.20 for the four total δ_{14}. It can be seen that as soon as we allow the additional parameter space, every region immediately expands (as expected) regardless of the value of δ_{14}. This gives the rather trivial immediate conclusion that our sensitivity in the 4ν

case is worse that 3ν. In terms of analysing specifics, we are interested in seeing how the wrong solutions change in the parameter space, more so than the right solution, because these indicate degeneracy resolution power, not just the width of error bars.

In the true LO case we can see that only 4.17(c′) has no WH solution and 4.17(d) has the smallest WO solutions which would imply that these true values would be the most favoured for MH and octant degeneracy resolution respectively. It is clear at a glance that there are no true values in this array that yields a plot with no WH and WO solutions.

With CP-violating values of δ_{14}, figure 4.18 shows resultant plots similar to 4.17. The most obvious changes are the reduction of the WO solution in (c) and the expansion of it in (d). The cases 4.18(c) and (c′) both have insignificant WH solutions and in general the WH solutions seem to be smaller e.g. 4.18(d) and (a′) though considerable WH solutions still exist for many of the cases. Overall the octant sensitivity with CP violating δ_{14} seems slightly worse, while the hierarchy sensitivity may be slightly higher. But from these plots it is not clear whether there is any underlying explicit mathematical connection, and if so it is probably minor.

The true HO plots differ greatly from the LO ones, as both 4.19 and 4.20 have many plots where allowed regions do not clearly separate into LO and HO. This is similar to the corresponding 3ν plots (the primed plots in 4.16) but to a much greater degree. This would imply that experiments would have wider θ_{23} best fit ranges rather than split solutions, potentially further obfuscating any maximal mixing or octant information. Most of the subplots in 4.20 have MH solutions that span the entire range of δ_{13} implying that true CP violating δ_{14} leads to particularly poor δ_{13} resolution. Plots 4.19(C′) and 4.20(C′) are remarkably similar and both have no wrong hierarchy solution and a small excluded δ_{13} region making these the most favoured of the δ_{14} conserving and violating cases for MH and CP resolution.

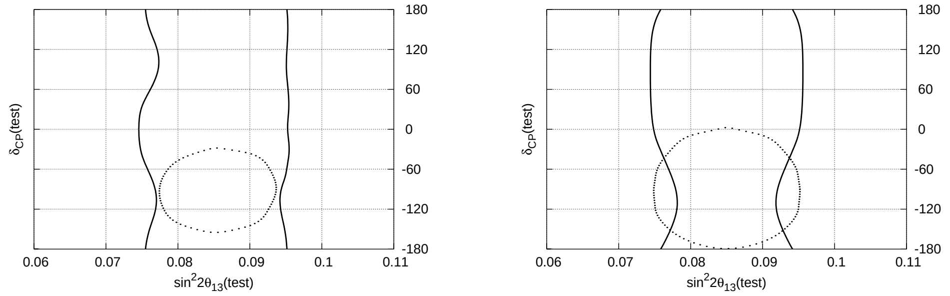

(a) NH, $\delta_{14} = 0°$, $\delta_{13} = 0°$ (b) NH, $\delta_{14} = 0°$, $\delta_{13} = 90°$

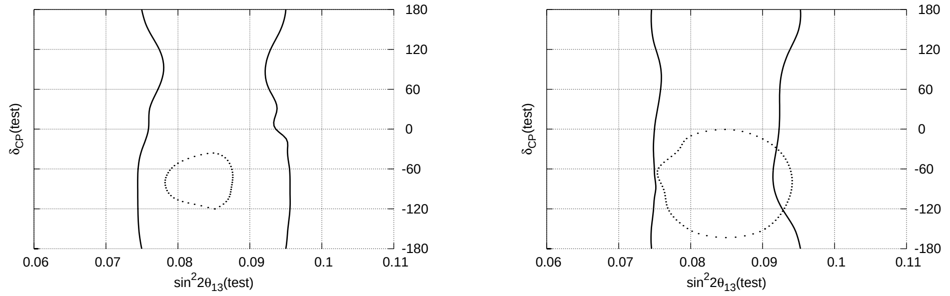

(c) NH, $\delta_{14} = 0°$, $\delta_{13} = -90°$ (d) NH, $\delta_{14} = 0°$, $\delta_{13} = 180°$

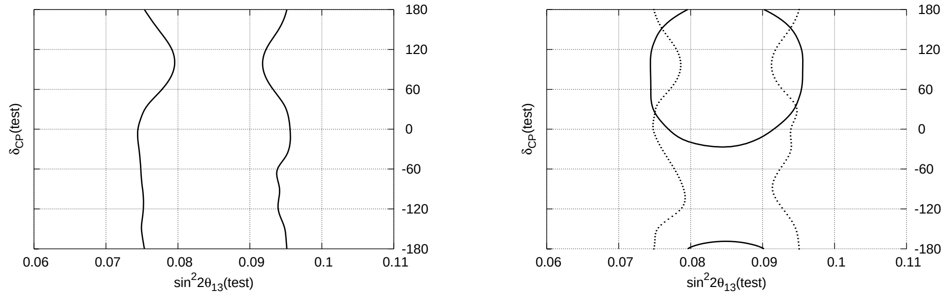

(a′) NH, $\delta_{14} = 180°$, $\delta_{13} = 0°$ (b′) NH, $\delta_{14} = 180°$, $\delta_{13} = 90°$

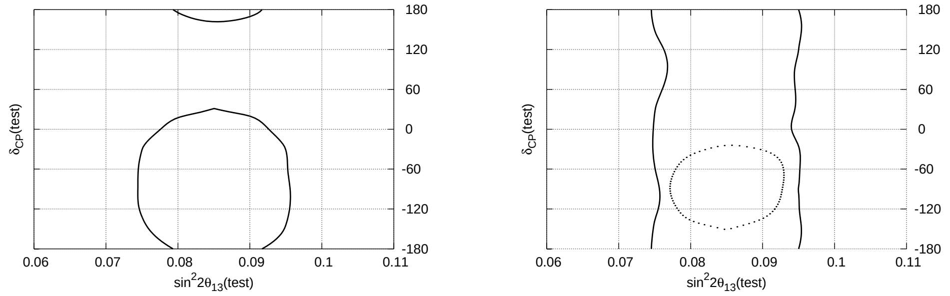

(c′) NH, $\delta_{14} = 180°$, $\delta_{13} = -90°$ (d′) NH, $\delta_{14} = 180°$, $\delta_{13} = 180°$

FIG. 4.14 Hierarchy discrimination plots with NH as true hierarchy for NOνA with various values of δ_{13}. $\delta_{14} = 0°$ for the unprimed plots and $\delta_{14} = 180°$ for the primed plots. Out of these extended 4ν cases with CP conserving δ_{14}, only (a′) and (c′) will have no degenerate MH solutions.

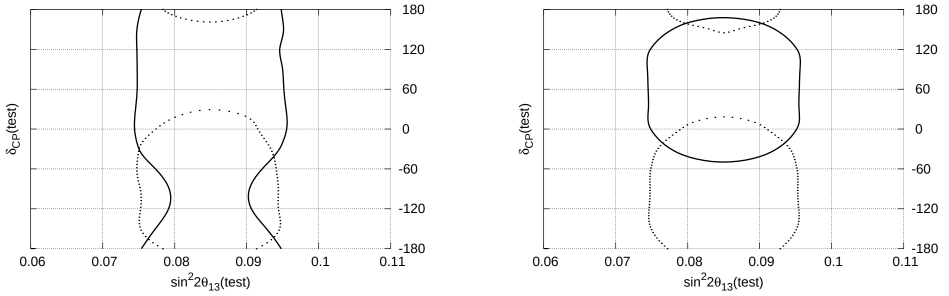

(a) NH, $\delta_{14} = 90°$, $\delta_{13} = 0°$ (b) NH, $\delta_{14} = 90°$, $\delta_{13} = 90°$

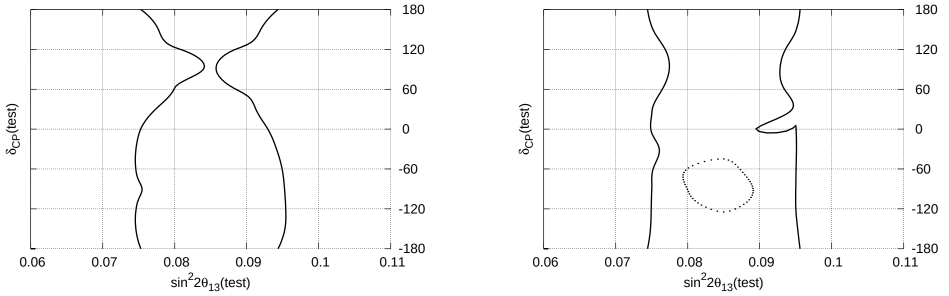

(c) NH, $\delta_{14} = 90°$, $\delta_{13} = -90°$ (d) NH, $\delta_{14} = 90°$, $\delta_{13} = 180°$

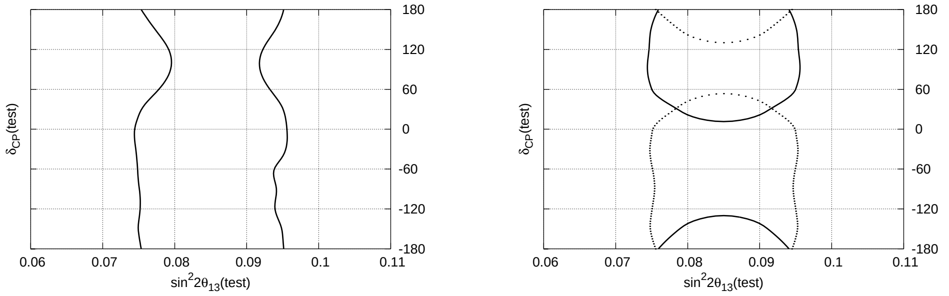

(a′) NH, $\delta_{14} = -90°$, $\delta_{13} = 0°$ (b′) NH, $\delta_{14} = -90°$, $\delta_{13} = 90°$

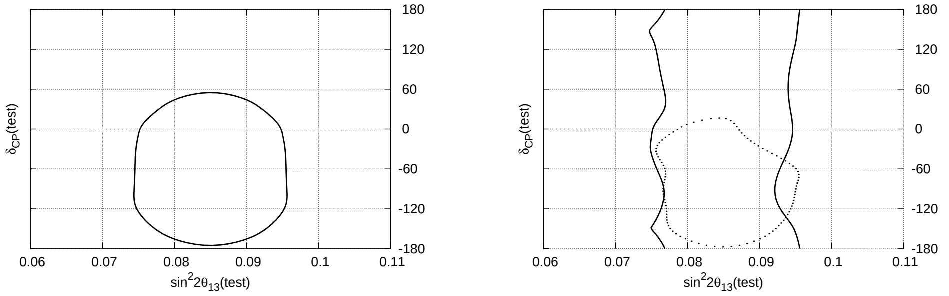

(c′) NH, $\delta_{14} = -90°$, $\delta_{13} = -90°$ (d′) NH, $\delta_{14} = -90°$, $\delta_{13} = 180°$

FIG. 4.15 Hierarchy discrimination plots similar to figure 4.14 but with $\delta_{14} = 90°$ for the unprimed plots and $\delta_{14} = -90°$ for the primed plots. Compared to the 4ν CP conserving cases, CP violating δ_{14} leads to (c), (a′) and (c′) having no degenerate MH solutions. The trade off is that the IH solutions in (a), (b) and (d′) are all larger.

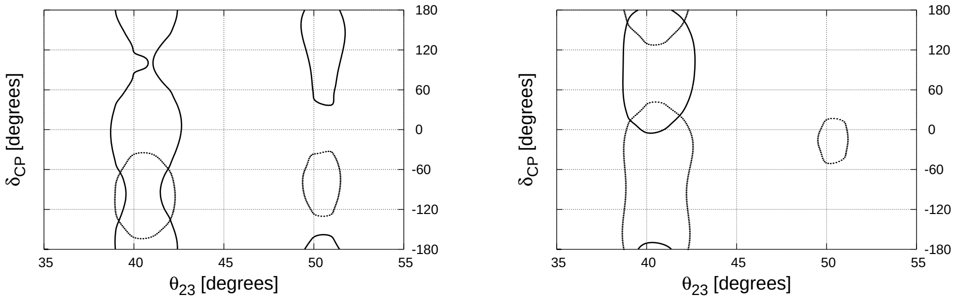

(a) NH, LO, $\delta_{13} = 0°$ (b) NH, LO, $\delta_{13} = 90°$

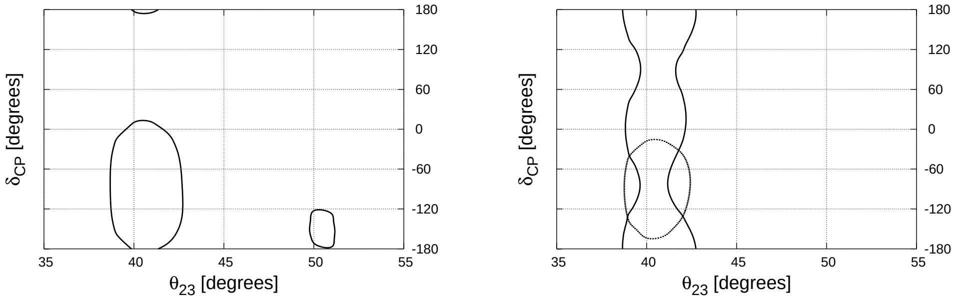

(c) NH, LO, $\delta_{13} = -90°$ (d) NH, LO, $\delta_{13} = 180°$

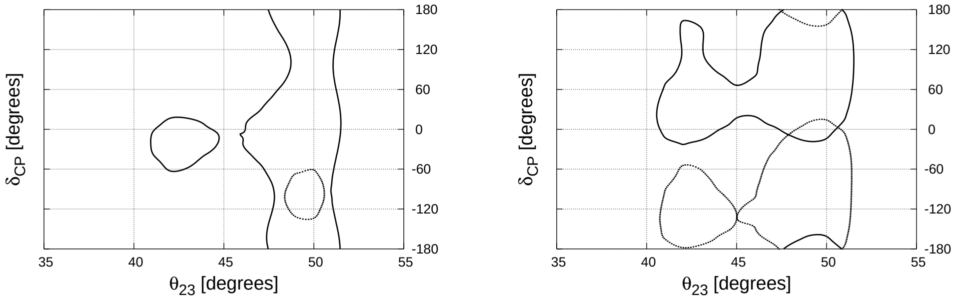

(A) NH, HO $\delta_{13} = 0°$ (B) NH, HO $\delta_{13} = 90°$

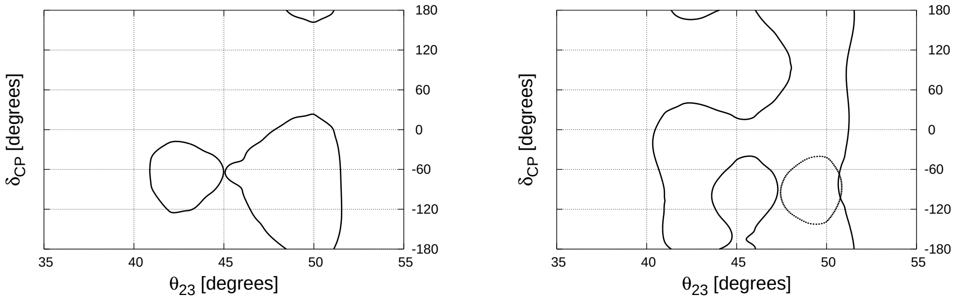

(C) NH, HO $\delta_{13} = -90°$ (D) NH, HO $\delta_{13} = 180°$

FIG. 4.16 Octant discrimination plots for NOνA in the standard 3ν case. NH is true hierarchy, various values of δ_{13} and LO (HO) for lowercase (uppercase) as true octant.

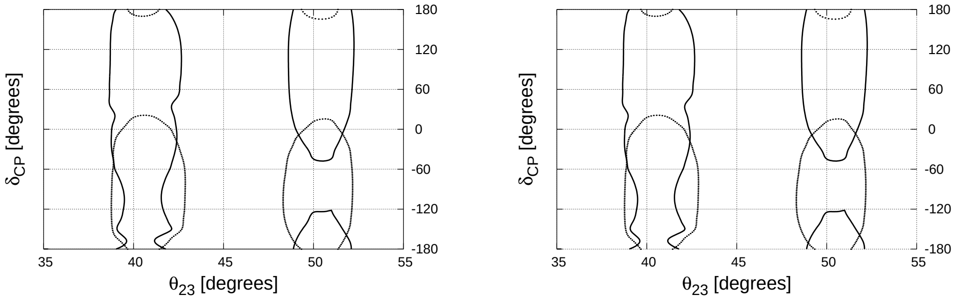

(a) NH, LO, $\delta_{14} = 0°$, $\delta_{13} = 0°$ (b) NH, LO, $\delta_{14} = 0°$, $\delta_{13} = 90°$

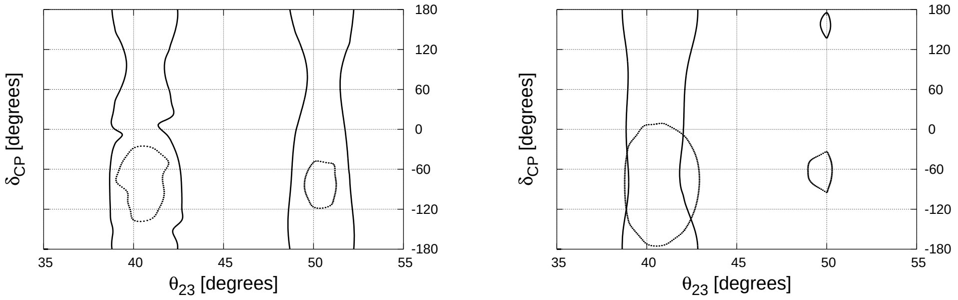

(c) NH, LO, $\delta_{14} = 0°$, $\delta_{13} = -90°$ (d) NH, LO, $\delta_{14} = 0°$, $\delta_{13} = 180°$

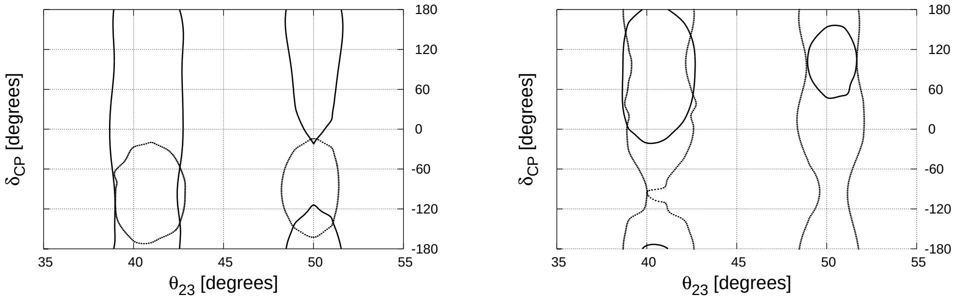

(a′) NH, LO, $\delta_{14} = 180°$, $\delta_{13} = 0°$ (b′) NH, LO, $\delta_{14} = 180°$, $\delta_{13} = 90°$

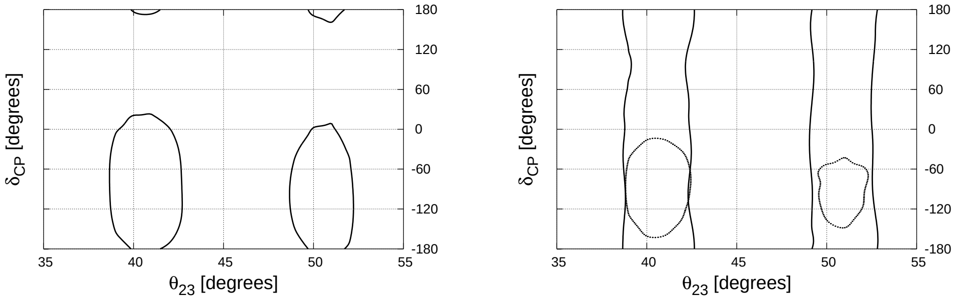

(c′) NH, LO, $\delta_{14} = 180°$, $\delta_{13} = -90°$ (d′) NH, LO, $\delta_{14} = 180°$, $\delta_{13} = 180°$

FIG. 4.17 Octant discrimination plots with NH as true hierarchy and LO as true octant for NOνA with various values of δ_{13} and CP conserving δ_{14}. For unprimed(primed) plots $\delta_{14} = 0°$ ($\delta_{14} = 180°$).

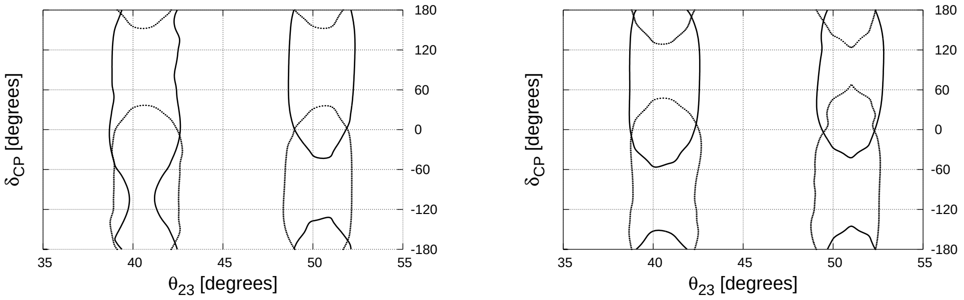

(a) NH, LO, $\delta_{14} = 90^\circ$, $\delta_{13} = 0^\circ$ (b) NH, LO, $\delta_{14} = 90^\circ$, $\delta_{13} = 90^\circ$

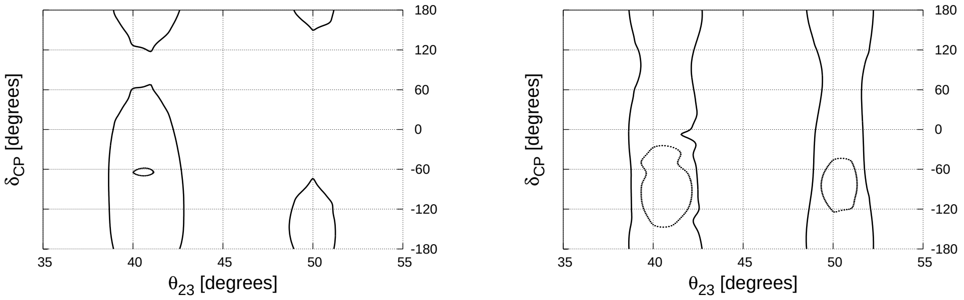

(c) NH, LO, $\delta_{14} = 90^\circ$, $\delta_{13} = -90^\circ$ (d) NH, LO, $\delta_{14} = 90^\circ$, $\delta_{13} = 180^\circ$

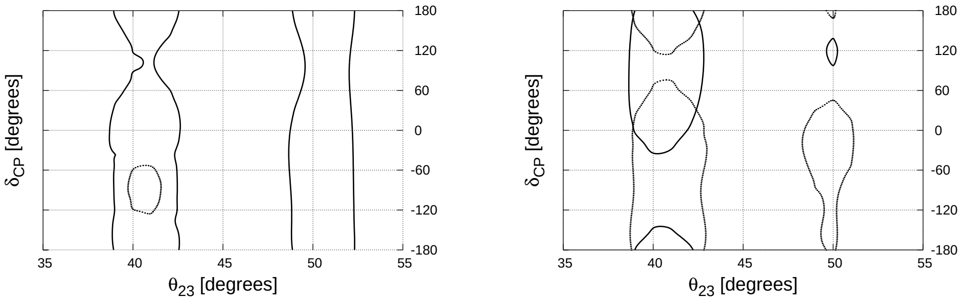

(a′) NH, LO, $\delta_{14} = -90^\circ$, $\delta_{13} = 0^\circ$ (b′) NH, LO, $\delta_{14} = -90^\circ$, $\delta_{13} = 90^\circ$

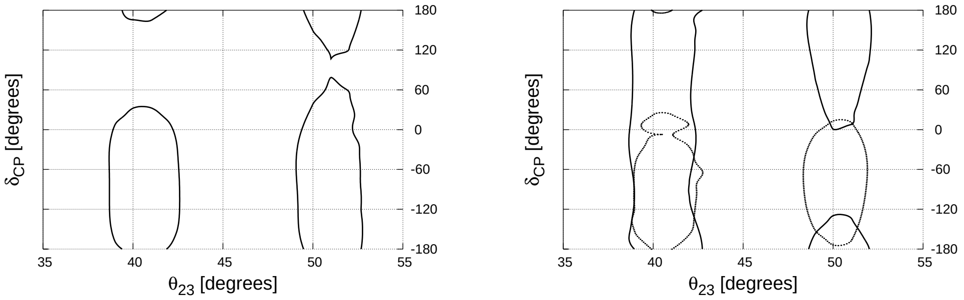

(c′) NH, LO, $\delta_{14} = -90^\circ$, $\delta_{13} = -90^\circ$ (d′) NH, LO, $\delta_{14} = -90^\circ$, $\delta_{13} = 180^\circ$

FIG. 4.18 Octant discrimination plots similar to figure 4.17 except with CP violating values of δ_{14}. For unprimed(primed) plots $\delta_{14} = 90^\circ$ ($\delta_{14} = -90^\circ$).

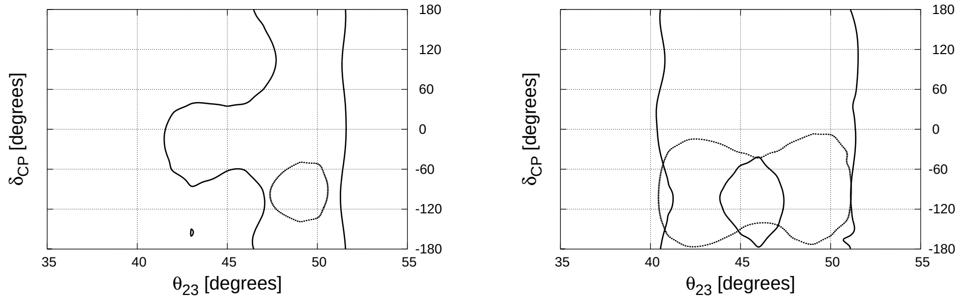

(A) NH, HO $\delta_{14} = 0°$, $\delta_{13} = 0°$ (B) NH, HO $\delta_{14} = 0°$, $\delta_{13} = 90°$

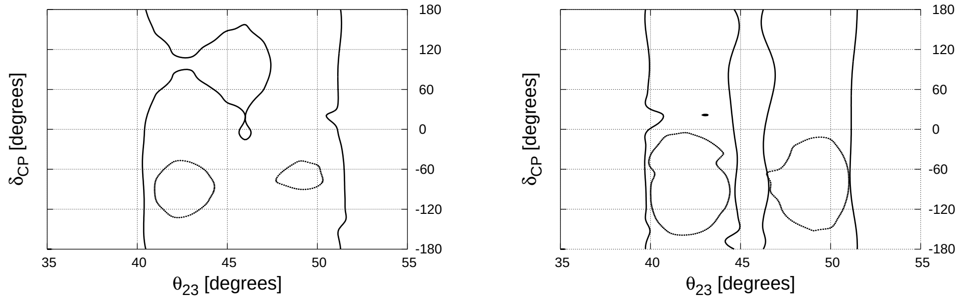

(C) NH, HO $\delta_{14} = 0°$, $\delta_{13} = -90°$ (D) NH, HO $\delta_{14} = 0°$, $\delta_{13} = 180°$

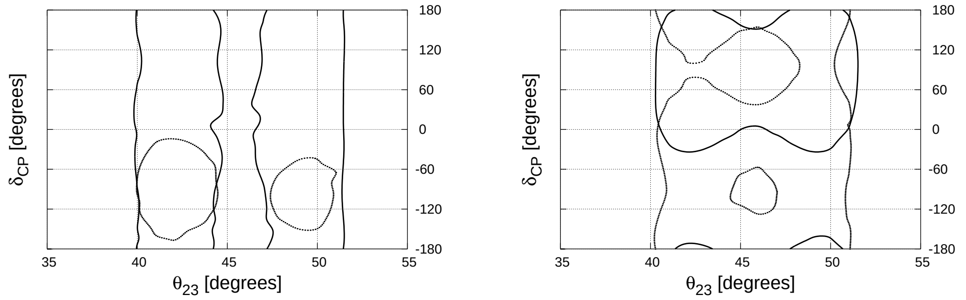

(A) NH, HO $\delta_{14} = 180°$, $\delta_{13} = 0°$ (B) NH, HO $\delta_{14} = 180°$, $\delta_{13} = 90°$

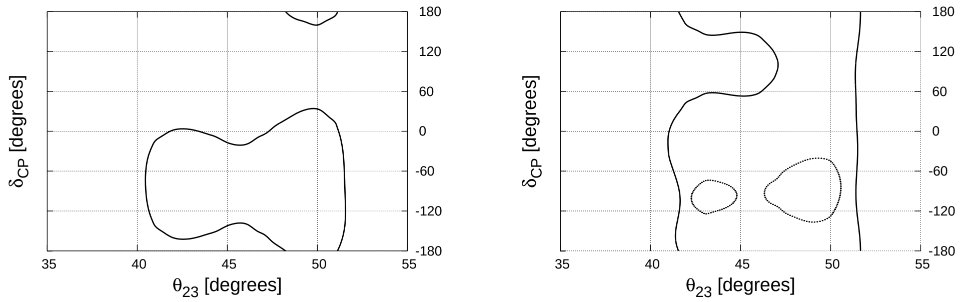

(C) NH, HO $\delta_{14} = 180°$, $\delta_{13} = -90°$ (D) NH, HO $\delta_{14} = 180°$, $\delta_{13} = 180°$

FIG. 4.19 Octant discrimination plots with NH as true hierarchy and HO as true octant for NOνA with various values of δ_{13} and CP conserving δ_{14}. For unprimed(primed) plots $\delta_{14} = 0°(\delta_{14} = 180°)$.

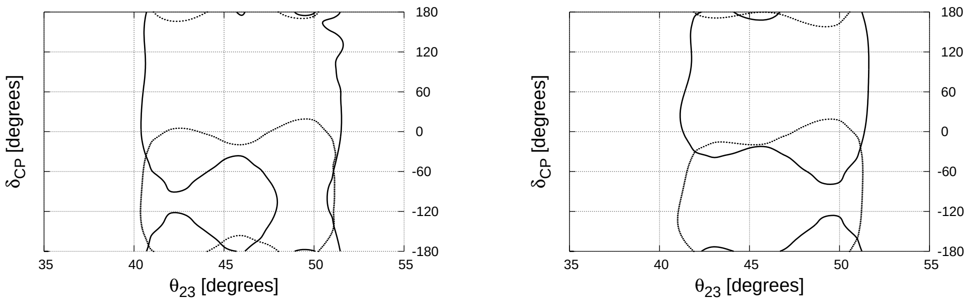

(A) NH, HO $\delta_{14} = 90^\circ$, $\delta_{13} = 0^\circ$ (B) NH, HO $\delta_{14} = 90^\circ$, $\delta_{13} = 90^\circ$

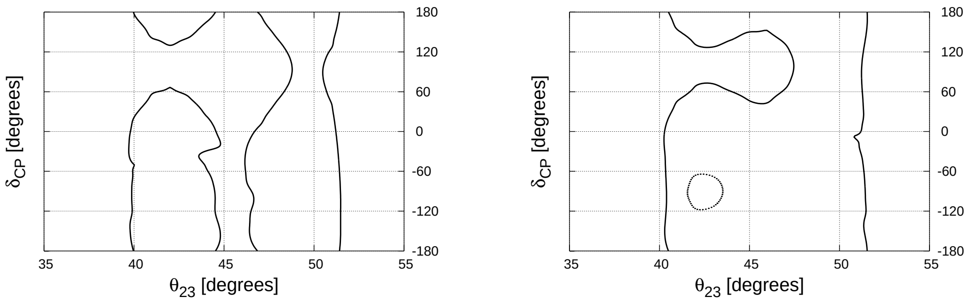

(C) NH, HO $\delta_{14} = 90^\circ$, $\delta_{13} = -90^\circ$ (D) NH, HO $\delta_{14} = 90^\circ$, $\delta_{13} = 180^\circ$

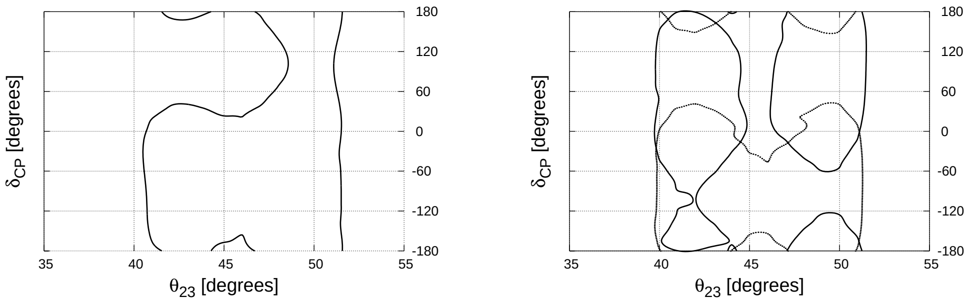

(A′) NH, HO $\delta_{14} = -90^\circ$, $\delta_{13} = 0^\circ$ (B′) NH, HO $\delta_{14} = -90^\circ$, $\delta_{13} = 90^\circ$

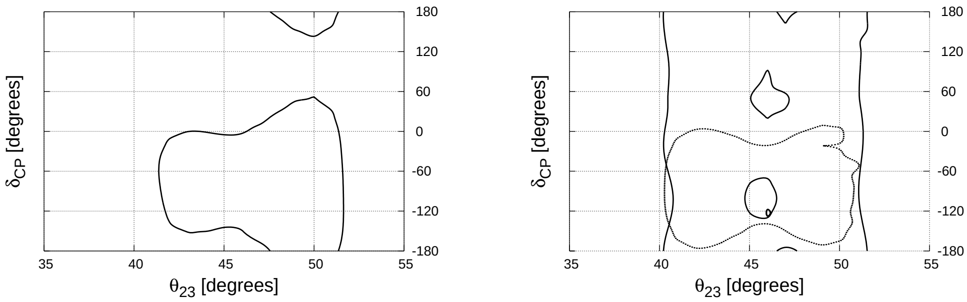

(C′) NH, HO $\delta_{14} = -90^\circ$, $\delta_{13} = -90^\circ$ (D′) NH, HO $\delta_{14} = -90^\circ$, $\delta_{13} = 180^\circ$

FIG. 4.20 Octant discrimination plots similar to figure 4.19 except with CP violating values of δ_{14}. For unprimed(primed) plots $\delta_{14} = 90^\circ$ ($\delta_{14} = -90^\circ$).

4.5 Global Fits for Mixing Parameters

Our current knowledge of neutrino mixing parameters comes from a variety of sources which can be summarised roughly:

- θ_{12} - Solar neutrino experiments
- θ_{13} - Reactor neutrino experiments
- θ_{23} - Atmospheric and accelerator experiments
- Δm^2_{21} - Solar neutrino experiments
- Δm^2_{31} - Atmospheric and accelerator experiments
- δ_{13} - Accelerator experiments.

In addition to these, we also have additional parameters, including potential sterile mixing:

- θ_{14} - LSND, MiniBooNE, other SBL experiments
- θ_{24} - SBL
- θ_{34} - SBL
- Δm^2_{41} - SBL
- δ_{13} - SBL
- δ_{14} - SBL
- Σ (the sum of active neutrino masses) - Cosmology, decay width of Z boson.

These global fits help motivate our simulations so it is important to be up to date. There are also neutrino mass scale measurements that can be taken from beta decay and neutrinoless double beta decay (if it occurs) but like the sum of active neutrino masses, these do not correspond to single mass eigenstates.

Early data released from NOνA featured disconnected LO and HO regions with no allowance for MM at 90% C.L. contrary to what was seen at MINOS and T2K [58]. This was important when we were performing our work seen in chapter 5 and 6. This constraint has since relaxed and NOνA has potential solutions in all three areas [60].

Parameter	NH best fit	IH best fit
$\sin^2\theta_{12}$	0.310	0310
θ_{12}	33.82°	33.82°
$\sin^2\theta_{23}$	0.580	0.584
θ_{23}	49.6°	49.8°
$\sin^2\theta_{13}$	0.02241	0.02264
θ_{13}	8.61°	8.65°
δ_{13}	215°	284°
Δm^2_{21}	7.39×10^{-5} eV^2	7.39×10^{-5} eV^2
$\Delta m^2_{3\ell}$	2.525×10^{-3} eV^2	-2.512×10^{-3} eV^2

TABLE 4.2 table of best fits for standard mixing parameters in NH and IH from [89]. With $\Delta m^2_{3\ell}(\mathrm{NH}) = \Delta m^2_{31}$ and $\Delta m^2_{3\ell}(\mathrm{IH}) = \Delta m^2_{32}$.

4.5.1 Current Global Fits

The standard best fits from [89] are summarised in table 4.2. The authors present two fits, one without Super-K atmospheric data and one with[2], we have presented the latter, though both are reasonably close. The full table is **Table 1.** in [89]. Note that analyses in subsequent chapters 5 and 6 were performed prior to these fits so instead use the parameters in table 5.1 which have been somewhat superseded. The presented fit prefers normal ordered mass spectrum and high octant and the significance of both of these preferences is strengthened with the inclusion of Super-K data. At this point the degeneracy conclusions and precision angle measurements are reasonably strong, while the constraints on the CP phase are much more loose. Refer to the paper for the full table including 1σ and 3σ ranges. We can also take the midpoints of the presented 3σ ranges for PMNS elements to get an idea of the size of the matrix elements,

$$|U|^{\text{midpoints}}_{3\sigma} = \begin{pmatrix} 0.820 & 0.552 & 0.150 \\ 0.362 & 0.564 & 0.713 \\ 0.414 & 0.597 & 0.678 \end{pmatrix}. \tag{4.11}$$

---

[2] The reason the authors of [89] state for presenting both fits is because it is hard to reproduce atmospheric experimental data outside of the associated collaboration. This makes it is difficult to include in a global fit. The largest effect of including the Super-K data is the increase in significance toward disfavouring inverted ordering and lower octant. Refer to the paper for an in-depth discussion.

Note that these elements are constrained to be unitary. We can overall summarise the general position of three flavour global fits:

- Solar experiments place heavy constraints on θ_{12} and Δm^2_{21},
- Reactor experiments heavily constrain θ_{13} to be non zero ($\sim 9^\circ$) and the uncertainties in Δm^2_{31} but are insensitive to hierarchy,
- Atmospheric experiments constrain θ_{23} to near maximal, and put some constraints on Δm^2_{31} and hierarchy,
- Accelerator experiments have overlap with atmospheric ones but have better hierarchy and octant sensitivity though these are still uncertain.
- T2K and NOνA results on θ_{23} differ somewhat between neutrino ($\theta_{23} \approx 45^\circ$) and antineutrino ($\theta_{23} \approx 40^\circ/50^\circ$) runs while MINOS ones do not [89].
- Normal ordering is slightly favoured in global fits especially from Super-K, T2K and NOνA data.

4.5.2 3+1 Fits

Analyses usually use the fact that θ_{14} is constrained to be small (due to reactor constraints), therefore $\cos^2\theta_{14} \approx 1$. Hence θ_{24} and θ_{34} can be extracted from the aforementioned matrix elements via the relations

$$|U_{e4}|^2 = \cos^2\theta_{14}\sin^2\theta_{24} \approx \sin^2\theta_{24}\,, \tag{4.12}$$

$$|U_{\mu 4}|^2 = \cos^2\theta_{14}\cos^2\theta_{24}\sin^2\theta_{34} \approx \cos^2\theta_{24}\sin^2\theta_{34}\,. \tag{4.13}$$

Subsequent global fits involving the $3+1$ case [149, 150] indicate preference for non-zero Δm^2_{41} and $|U_{e4}|^2$ using data from $\nu_e/\overline{\nu}_e$ disappearance as well as SBL and LBL $\nu_\mu/\overline{\nu}_\mu \to \nu_e/\overline{\nu}_e$.

Constraints on $|U_{\tau 4}|^2$ are incredibly hard to constrain because ν_τ sources are unavailable in general. Constraints can come from observing both matter effects in ν_e/ν_μ disappearance experiments and deficits in neutral current events at any detector that can distinguish them. Matter effects and neutral currents are present for all active flavours but are not possible for sterile states due to lack of W and Z boson vertices. So in summary, we cannot study $P_{\tau s}$, $P_{\tau\alpha}$ or especially P_{ss} or $P_{s\alpha}$ (because by definition we can't directly create sterile neutrinos from weak decays), where

α is any active flavour, due to the lack of sources. Instead we must study $P_{\mu\alpha}$ and $P_{e\alpha}$ holistically via disappearance and use our prior knowledge of $P_{\mu e}$ and $P_{e\mu}$ from appearance experiments to narrow down the combined tau and sterile contribution to such disappearance. When we get enough statistics, we can use neutral current data to separate out the contributions due to $P_{e\tau}/P_{\mu\tau}$ and $P_{es}/P_{\mu s}$ to fill out the rest of the matrix elements.

One experiment that can potentially determine if active-sterile oscillations are boosted by matter effects is IceCube [151–153]. Any upward travelling atmospheric neutrinos seen in this detector will have travelled through the Earth and consequently will have been effected by a MSW resonance for a huge distance. Unfortunately due to the resonance acting on neutrinos and antineutrinos in the opposite manner, this resonance only affects the antineutrinos seen by IceCube which have roughly one third the cross section of neutrinos. Additionally, because IceCube is a simple neutrino telescope and cannot tell neutrinos and antineutrinos apart in the event by event level, this effect becomes even less pronounced in the data. Current IceCube results do place reasonable limits on mixing, but are relatively inconclusive in the area considered by LSND/MiniBooNE. IceCube is still taking data however, so more years of data will be interesting.

Sterile mixing can also potentially be constrained by the Planck cosmological $N_{\text{eff}} \approx 3.046$ (effective number of neutrino species in the early universe) measurements from the CMB. For example, to allow a certain mixing parameter value, a change in the size of N_{eff} from the Plank result (ΔN_{eff}) may be required. Hence, this can be used to constrain sterile mixing [154]. If NH is assumed to be true and the smallest neutrino mass eigenstate is assumed to be zero (i.e. the case in which Planck constraints on a fourth mixed neutrino are smallest) then we can approximate $m_1 = 0$ eV, $m_2 \approx 0$ eV and $m_3 = 0.06$ eV, with the fourth mass eigenstate being almost directly related to the active-sterile splitting $m_4^2 \approx \Delta m_{41}^2$. In this favourable case Planck rules out a large region of the parameter space, some of which IceCube and MINOS also cover. The results do rule out the high mass splitting range ($\Delta m_{41}^2 > 3$ eV) more thoroughly than other experiments. This is to be expected, because more mass makes any mixing this heavy eigenstate more significant in the early universe. Despite this, Planck does not seem to provide any remarkable conclusions in the area SBL experiments are interested in and has worse constraints in the low mass splitting range ($\Delta m_{41}^2 < 10^{-2}$ eV^2). Despite this, CMB data is still potentially an interesting extra source of information on potential sterile mixing, especially given this example of a particularly lenient case.

We can summarise the experimental status of the $3+1$ case:

- LSND results heavily skew fits toward 3+1 case. Including LSND results implies rejection of the no sterile oscillations case at $> 6\sigma$,
- Appearance-disappearance tension between $\nu_e \to \nu_e$, $\nu_\mu \to \nu_e$ and $\nu_\mu \to \nu_e$ channels potentially indicates that sterile oscillations cannot account for the all anomalies. This is especially true for the ν_μ source case, though if LSND ν_μ disappearance data were to be erroneous then the tension would be a lot less significant,
- Old MiniBooNE data wasn't really consistent with 3+1, it's anomaly may have been related to some non-oscillatory effect,
- Recent MiniBooNE data seems to further hint at an LSND-like anomaly with high significance,
- Gallium and Reactor anomalies give 2.6σ disfavouring of no-oscillations when LSND data is excluded i.e. still a hint for $\Delta m^2_{41} \sim 1 \text{ eV}^2$ even when ignoring LSND,
- Daya Bay reports different fluxes from the two dominant isotopes present: ^{235}U and ^{239}Pu [155]. It is unclear whether these measurements can be reconciled with sterile oscillations [89],
- Overall reactor data does preference the oscillation solution at around 3σ with best fit parameters $\Delta m^2_{41} \approx 1.3 \text{ eV}^2$ and $|U_{e4}| \approx 0.1$ [89].

CHAPTER 5

DEGENERACY SIMULATION WITH FOUR MASS STATES

At this point in time, the basic mechanics of neutrino oscillation are well known. This includes estimates of mixing parameter and mass difference values as seen in section 4.5. The next logical step is performing high precision experiments to ascertain the exact values of such parameters and reducing experimental uncertainties. Given the fact that some of these parameters are relatively well known, the most important problem to solve becomes that of degeneracies which we introduced previously in section 4.3. Before we jump into our analysis we'll first recap the current state of neutrino oscillation physics.

In addition to the aforementioned parameter uncertainties, several short baseline experiments have reported results inconsistent with the three flavour oscillation paradigm (presented in section 3.1.1), for an overview of the anomalies we refer to [85]. The key idea of the 3+1 case is assuming that this can be explained by oscillation effects. If we assume that short range oscillations are the culprit, then this implies that there is a third independent mass-squared difference which we label Δm^2_{41}. This additional mass splitting must be much larger than the other two (roughly $1\ \mathrm{eV}^2$) to get such a significant effect over such short distances. Then, recalling section 2.1, this additional mass splitting implies the existence of a fourth mass eigenstate ν_4 and hence, to avoid super heavy active flavours and non-unitarity, a new flavour eigenstate ν_s. Recall that the ν_s must be 'sterile' to not interfere with astrophysical and particle physics constraints on the sum of active neutrino masses from the decay width of the Z boson.

Once we have this new splitting we discover(from the equations in sections 2.1 and 2.2.3) that in turn we must introduce new oscillation parameters: $\theta_{14}, \theta_{24}, \theta_{34}, \delta_{14}, \delta_{34}$

and Δm^2_{41}[1]. Given the fact that these SBL anomalies still have statistical significance it is clearly worth considering the $3+1$ sterile hypothesis when investigating experimental results whether real or simulated.

5.1 Motivating Our Simulation

The particular goal of this analysis is to analyse the capability of LBL experiments to resolve degeneracies in the $3+1$ case. This is important because the $3+1$ hypothesis introduces extra possible degrees of freedom and this allows additional degeneracy and uncertainty (we saw illustrative examples of this in sections 4.2.2 and 4.4). We can add a fourth mass eigenstate with primarily sterile flavour mixing to account for the SBL anomalies but this will change the mixing observed at LBL experiments even if the primary effects of short range oscillations will not be observable at such distance.

Recall that in the standard three flavour scenario, neutrino oscillation is parametrised by three mixing angles: θ_{12}, θ_{23} and θ_{13}, two mass squared differences: Δm^2_{21} and Δm^2_{31} and one Dirac type CP phase δ_{13} (derived in section 2.1). Current unknowns to be studied at LBL experiments are: (i) the sign of Δm^2_{31} which gives rise to the normal and inverted orderings of the neutrino masses, the octant of the mixing angle θ_{23} which can be LO or HO, and finally (iii) the phase δ_{13}. The running experiments intending to discover these unknowns at the time this study was performed were T2K [156] in Japan and NOνA [59] in the USA. These experiments are primarily analysed based on the standard 3ν oscillation case which has so far fit the majority of experimental tests very well.

In the standard three flavour scenario, there are currently two extant degeneracies: (i) MH-δ_{13} degeneracy [157] and (ii) octant-δ_{13} degeneracy [147]. The dependence of MH-δ_{13} degeneracy is same in neutrinos and antineutrinos but the octant-δ_{13} degeneracy behaves differently for neutrinos and antineutrinos [158, 159]. Thus the octant-δ_{13} degeneracy can be resolved with a balanced run of neutrinos and antineutrinos but a similar method cannot remove the MH-δ_{13} degeneracy. However, despite the MH-δ_{13} degeneracy being unremovable in general, the parameter space can be divided into a favourable region where it is completely absent for long-

---

[1] Of course the choice of which splitting to treat as independent and which CP phases to use is up to the physicist. For example, some papers parametrise with δ_{24} instead of δ_{14}. The choices we use appear to be the most common amongst LBL analyses.

baseline experiments, and an unfavourable region where it is present. For NOνA, the favourable parameter space is around {NH, $\delta_{13} = -90°$} and {IH, $\delta_{13} = +90°$} whereas the unfavourable parameter space is around {NH, $\delta_{13} = 90°$} and {IH, $\delta_{13} = -90°$} (this can be seen illustratively in section 4.2.2, figure 4.7). Recent data from NOνA shows a mild preference towards $\delta_{13} = -90°$ and NH [59]. From the above discussion we understand that for these combinations of true hierarchy and true δ_{13}, NOνA can have good hierarchy sensitivity and thus it is believed that the first evidence for the neutrino mass hierarchy will come from the NOνA experiment. However the understanding of degeneracies can completely change in new physics scenarios such as the 3+1 case we are interested in.

Early results for NOνA on active-sterile mixing show no evidence for ν_s oscillations [160] (as do most other non-SBL experiments) but can only put mild constraints on $|U_{e4}|^2$ and $|U_{\mu 4}|^2$. Though recently there has been some significant experimental evidence from MiniBooNE supporting the existence of a light sterile neutrino at the eV scale based on the LSND result [161]. This has motivated re-examination of oscillation analyses of the long-baseline experiments in the presence of sterile neutrinos [121, 162–171] with [163] and [165] dealing with a similar analysis to us but discussing the more general case where δ_{13} is varied rather than fixed at the best fit at the time of $-90°$. For details regarding the first hints of the existence of sterile neutrinos and for the current status we refer to the references [85, 153, 172–181].

From the probability level analyses in figure 5.1 we find, at a glance, that in the 3+1 case two new degeneracies are present at NOνA. These are the (i) MH-δ_{14} and (ii) octant-δ_{14} degeneracies. Note that we will refer to the degeneracies involving the sign of Δm^2_{31} as mass hierarchy rather than mass ordering as discussed in 1.9 to avoid confusing terminology that can arise if we abbreviate ordering and octant the same way. Our results also show that in this case the scenario is different to that of the hierarchy and octant degeneracy arising with δ_{13} in that the MH-δ_{14} degeneracy is opposite for both neutrinos and antineutrinos but the octant-δ_{14} degeneracy behaves similarly in neutrinos and antineutrinos. Thus unlike octant-δ_{13} (see figure 4.11), the octant-δ_{14} degeneracy can not be resolved by a combination of neutrino and antineutrino runs while the MH-δ_{14} degeneracy can be resolved with a balanced combination of neutrino and antineutrinos which was not the case for the MH-δ_{13} degeneracy . To show the degenerate parameter space in terms of χ^2, we present our results in the $\theta_{23}(\mathrm{test})$-$\delta_{13}(\mathrm{test})$ plane taking different values of δ_{14}. We do this for two values of θ_{23} (true), one in LO and one in HO. The rest of the parameters are defined by the current best-fit of NOνA which is $\delta_{13} = -90^\circ$ and NH, thus coinciding with the favourable parameter space. We show this for considering (i) NOνA running for six years in pure neutrino mode (6+$\bar{0}$) and (ii) NOνA running in equal neutrino and equal antineutrino mode (3+$\bar{3}$). Next we discuss the effect of these degeneracies on the hierarchy sensitivity of NOνA. We find that because of the existence of the new degeneracies, the hierarchy sensitivity of NOνA is highly compromised at the current best-fit value of NOνA (i.e. $\delta_{13} = -90^\circ$ and NH). To show this we plot hierarchy sensitivity of NOνA in the θ_{23}(true)-δ_{13}(true) plane taking different true values of δ_{14} for NH. We also identify the values of δ_{14} for which the hierarchy sensitivity of NOνA gets affected. We discuss these curves more thoroughly in the discussion section 5.4.1.

5.2 Oscillation Theory

Let us do a quick recap of the basics of 4ν oscillation parametrisation and probability. In this analysis we use our standard PMNS parametrisation defined in equation (2.36) of section 2.2.2

$$U^{3\nu}_{\mathrm{PMNS}} = R(\theta_{23}, 0)R(\theta_{13}, \delta_{13})R(\theta_{12}, 0)\,. \tag{5.1}$$

using the conventions from 2.1. When we extend our simulations to have four mass eigenstates we use the other previously defined parametrisation from in equation (2.40) of section 2.2.3

$$U^{4\nu}_{\mathrm{PMNS}} = R(\theta_{34}, \delta_{34})R(\theta_{24}, 0)R(\theta_{14}, \delta_{14})U^{3\nu}_{\mathrm{PMNS}}\,. \tag{5.2}$$

Remembering that the three new matrices introduce the new mixing angles: $\theta_{14}, \theta_{24}, \theta_{34}$ and phases: δ_{14}, δ_{34}. The final new oscillation parameter is the fourth independent mass-squared difference which comes into the probability and is chosen to be Δm^2_{41} to remain consistent with the 3ν parameters. Assuming that $\Delta m^2_{41} \gg \Delta m^2_{31}$, and that we are operating near the oscillation maximum where $\sin^2 \Delta_{31} \approx 1$, then the sterile-induced oscillations from $\sin^2 \Delta_{41}$ terms will be very rapid. Hence the four flavour vacuum ν_μ to ν_e oscillation probability can be averaged over the sterile oscillation factor Δ_{41} i.e.

$$\langle \sin^2 \Delta_{41} \rangle = \langle \cos^2 \Delta_{41} \rangle = \frac{1}{2} \tag{5.3}$$

$$\langle \sin \Delta_{41} \rangle = \langle \cos \Delta_{41} \rangle = 0 \tag{5.4}$$

this reflects the inherent averaging that the long-baseline detectors see due to the very short wavelength of the sterile induced oscillations and their limited energy resolution.

Once the averaging has been done the probability expression can be written using the conventions and approach from [121] which we previously covered in section 3.2

$$P_{\mu e}^{4\nu} = P_M^{\mathrm{ATM}} + P_{\mathrm{I}}^{\mathrm{INT}} + P_{\mathrm{II}}^{\mathrm{INT}}, \tag{3.27}$$

which, in the limit of low matter effects and small δ_{14} and δ_{24} mixing, can be written out as

$$\begin{aligned} P_{\mu e}^{4\nu} = \quad & 4\mathrm{s}_{23}^2\mathrm{s}_{13}^2 \sin^2\Delta_{31} \\ & + 8\mathrm{s}_{13}\mathrm{s}_{12}\mathrm{c}_{12}\mathrm{s}_{23}\mathrm{c}_{23} \sin\Delta_{21} \sin\Delta_{31} \cos(\Delta_{31} + \delta_{13}) \\ & + 4\mathrm{s}_{14}\mathrm{s}_{24}\mathrm{s}_{13}\mathrm{s}_{23} \sin\Delta_{31} \sin(\Delta_{31} + \delta_{13} - \delta_{14}). \end{aligned} \tag{5.5}$$

Note that the above expression is for vacuum and free from the sterile induced parameters θ_{34} and δ_{34} but will be sufficient to explain our probabilities.

From this probability we can see that the Δ_{31}, δ_{13} and δ_{41} dependent terms are responsible for the MH-CP degeneracies. This is due to the unconstrained sign of Δ_{31} and the (mostly) unconstrained CP phases δ_{13} and δ_{14}, which can compensate for sign changes in Δ_{31}. The above formula is for neutrinos, recall from 2.4 that to get from a neutrino formula to the antineutrino equivalent we replace δ_{13} by $-\delta_{13}$ and δ_{14} by $-\delta_{14}$.

5.3 Experimental Specification

For our analysis we consider the currently running long-baseline experiment NOνA. For NOνA we assume $3 + \bar{3}$ (three years neutrino and three years antineutrino running) unless specified otherwise. The detector is 14 kt liquid argon detector. Our experimental specification of coincides with that presented in [182]. To perform analysis we use the GLoBES software package along with files for 3+1 case PMNS matrices and probabilities [183–186]. We have set θ_{34} and δ_{34} to zero throughout our analysis due to them not appearing in the vacuum equation for $P_{\mu e}$. These may in principle show up in matter effects that GLoBES simulates but the contributions will be small. Our choices for the neutrino oscillation parameters are listed in table 5.1.

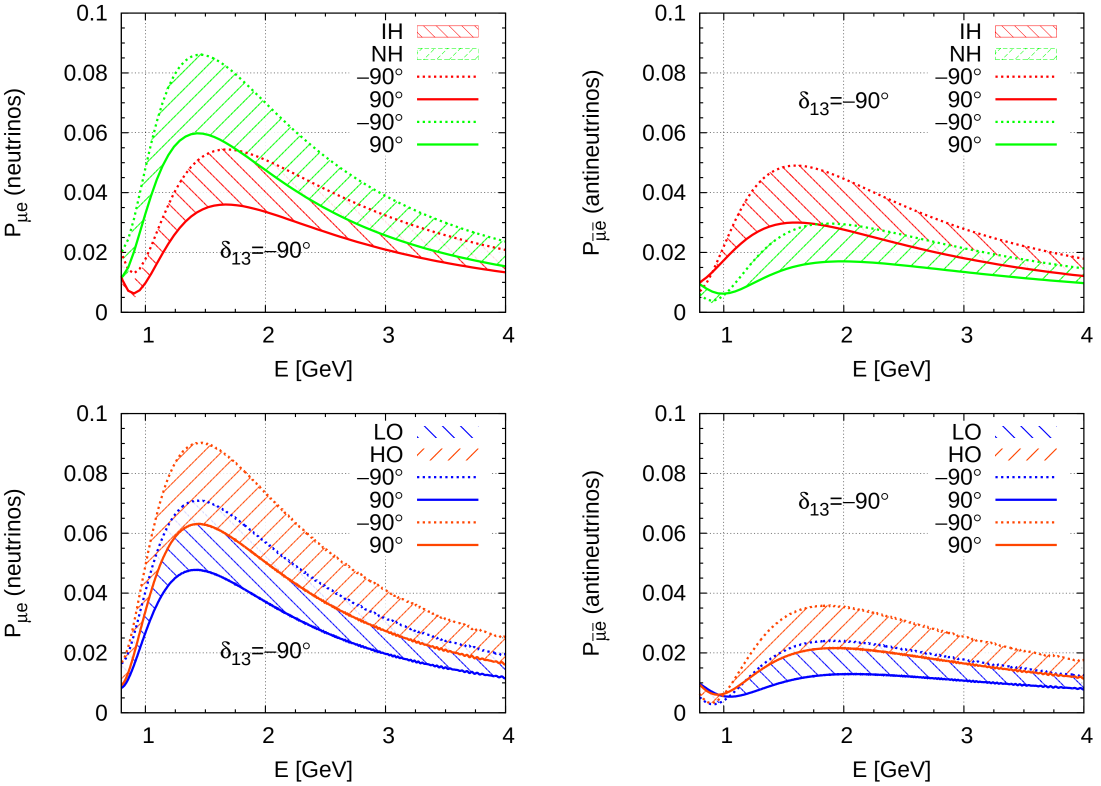

FIG. 5.1 $\nu_\mu \to \nu_e$ oscillation probability bands for $\delta_{13} = -90°$. Left panels are for neutrinos and right panels are for antineutrinos. The upper panel shows the MH-δ_{14} degeneracy and the lower panels shows the octant-δ_{14} degeneracy. These figures are 4.10 and 4.12 repeated from section 4.3.2. This is for convenience and because they were originally presented this way as part of this analysis.

5.4 Identifying New Degeneracies in the Presence of a Sterile Neutrino

For this analysis, the information for the standard oscillation parameters came from the latest global analyses of world neutrino data at the time [187–189]. For the sterile neutrino parameters θ_{14}, θ_{24} and Δm^2_{41} our best-fit values are consistent with the studies presented in [125, 180, 190, 191].

5.4.1 Identifying degeneracies at the probability level

In this section we will discuss parameter degeneracies in 3+1 case at the probability level. In figure 5.1 we plot the appearance channel probability $P_{\mu e}$ vs energy for the NOνA baseline. For plotting the probabilities we have averaged the rapid oscillations

4ν Parameters	True Value	Test Value Range
$\sin^2\theta_{12}$	0.304	N/A
$\sin^2 2\theta_{13}$	0.085	N/A
$\theta_{23}^{\mathrm{LO}}$	40°	$(40^\circ, 50^\circ)$
$\theta_{23}^{\mathrm{HO}}$	50°	$(40^\circ, 50^\circ)$
$\sin^2\theta_{14}$	0.025	N/A
$\sin^2\theta_{24}$	0.025	N/A
θ_{34}	0°	N/A
δ_{13}	-90°	$(-180^\circ, 180^\circ)$
δ_{14}	$-90^\circ, 0^\circ, 90^\circ$	$(-180^\circ, 180^\circ)$
δ_{34}	0°	N/A
Δm^2_{21}	7.5×10^{-5} eV^2	N/A
Δm^2_{31}	2.475×10^{-3} eV^2	$(2.2, 2.6) \times 10^{-3}$ eV^2
Δm^2_{41}	1 eV^2	N/A

TABLE 5.1 Expanded 4ν parameter true values and test marginalisation ranges used in our simulation. Parameters with N/A are not marginalised over.

due to Δm^2_{41}. The left column corresponds to neutrinos and the right column corresponds to antineutrinos. In all the panels δ_{13} is taken as -90° and the bands are due to the variation of δ_{14}.

The upper panels of figure 5.1 show the MH-δ_{14} degeneracy. For these panels θ_{23} is taken as 45°, i.e. the maximal mixing case. NH (IH) corresponds to $\Delta m^2_{31} = +(-)2.4 \times 10^{-3}$ eV^2. In both the panels the green bands correspond to NH and the red bands correspond to IH. Note that in the neutrino probabilities, the green band is above the red band and it is opposite in the antineutrinos. This is because, the matter effect enhances the probability for NH for neutrinos and IH for antineutrinos. For each given band, $\delta_{14} = -90^\circ$ corresponds to the maximum point in the probability and $+90^\circ$ corresponds to the minimum point in the probability, for both neutrinos and antineutrinos. These features in the probability can be understood in the following way. From equation (5.5), we see the neutrino appearance channel probability depends on the phases as: $a + b\cos(\Delta_{31} + \delta_{13}) + c\sin(\Delta_{31} + \delta_{13} - \delta_{14})$, where a, b and c are positive quantities. At the oscillation maxima we have $\Delta_{31} = 90^\circ$. As our probability curves correspond to $\delta_{13} = -90^\circ$, for neutrinos we obtain $a + b - c\sin\delta_{14}$. Now it is easy to understand that the contribution to the probability will be maximum for $\delta_{14} = -90^\circ$ and minimum for $\delta_{14} = +90^\circ$. Now let us see what happens for antineutrinos. For antineutrinos, we change sign of δ_{13} and δ_{14} in equation (5.5) and we obtain for $\delta_{13} = -90^\circ$ as $a - b - c\sin\delta_{14}$. Thus even for the antineutrinos, the probability is maximum for $\delta_{14} = -90^\circ$ and minimum for $\delta_{14} = +90^\circ$. This is in stark contrast to the behaviour of δ_{13}, as in the standard three flavour case, $\delta_{13} = -90^\circ$ corresponds to the maximum probability while $\delta_{13} = +90^\circ$ corresponds the minimum probability for neutrinos (vice-versa for antineutrinos). From the plots we see that there is overlap between {NH, $\delta_{14} = 90^\circ$} and {IH, $\delta_{14} = -90^\circ$} for the neutrinos and {NH, $\delta_{14} = -90^\circ$} and {IH, $\delta_{14} = +90^\circ$} for antineutrinos. This is why we can state that unlike the nature of MH-δ_{13} degeneracy, the MH-δ_{14} degeneracy is different in neutrinos and antineutrinos. Therefore as we mentioned earlier, in principle a balanced combination of neutrino and antineutrino runs should be able to resolve this degeneracy.

In the lower panels of figure 5.1, we depict the octant-δ_{14} degeneracy. In these panels LO corresponds to $\theta_{23} = 40^\circ$ and HO corresponds to 50°. Here the hierarchy is chosen to be normal with $\Delta m^2_{31} = +2.4 \times 10^{-3}$ eV^2. In both the panels, the blue band correspond to LO and the red band correspond to HO. Note that in both the panels, the red band is above the blue band. This is because the appearance channel oscillation probability increases as θ_{23} increases for both neutrinos and antineutrinos. As already explained for the MH case in the above paragraph, for each given band, $\delta_{14} = -90^\circ$ corresponds to the maximum value in the probability and $\delta_{14} = +90^\circ$ to the minimum point in the probability for both neutrinos and antineutrinos. From the panels we see that (LO, $\delta_{14} = -90^\circ$) is degenerate with (HO, $\delta_{14} = +90^\circ$). It is interesting to note that this degeneracy is same in both neutrinos and antineutrinos [165]. So to reiterate, this is a remarkable difference compared to the octant-δ_{13} degeneracy which is different for neutrinos and antineutrinos. Thus we understand that in the 3+1 scenario, it is impossible to remove the octant degeneracy by combining neutrino and antineutrino runs.

5.4.2 Identifying Degeneracies at the Event Level

Now we analyse the relevant degeneracies at the χ^2 level. In figure 5.2 we have given the contours in the $\theta_{23}(\text{test})$-$\delta_{13}(\text{test})$ plane for three different values of δ_{14} at 90% C.L. The first and second column correspond to the case when NOνA runs in pure neutrino mode and the third and fourth column correspond to the case when NOνA runs in equal neutrino and antineutrino mode. Note that though the current plan for NOνA is to run in the equal neutrino and antineutrino mode, we have

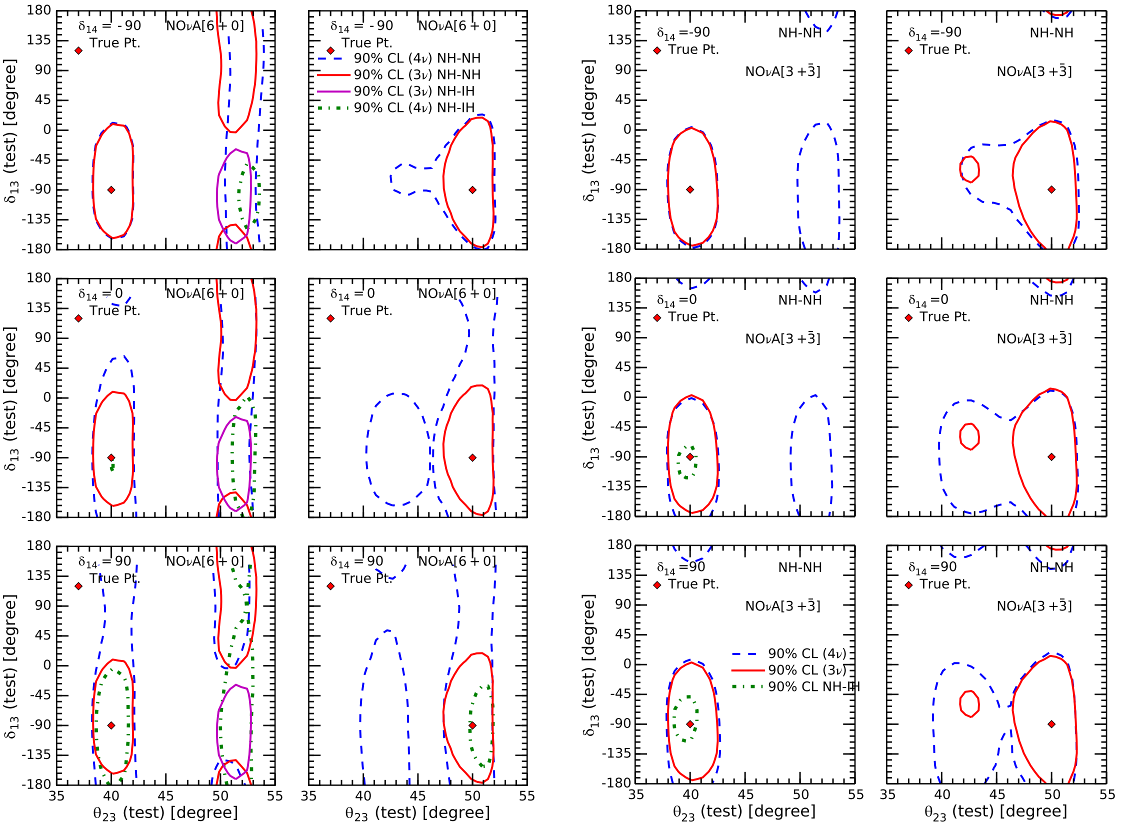

FIG. 5.2 Contour plots in the $\theta_{23}(\text{test})$ vs $\delta_{13}(\text{test})$ plane for two different true values of $\theta_{23} = 40^\circ$ (first and third column) and 50° (second and fourth column) for NOνA $(6+\bar{0})$ (first and second column) and $(3+\bar{3})$ (third and fourth column). The first, second and third rows are for $\delta_{14} = -90^\circ$, 0° and 90° respectively. The true value for the δ_{13} is taken to be -90°. The true hierarchy is NH. We marginalise over the test values of δ_{14}. Also shown are the contours for the 3ν flavour scenario.

produced plots corresponding to the pure neutrino run of NOνA to understand the role of antineutrinos in resolving the degeneracies. Again we have chosen the true parameter space to coincide with the latest best-fit of NOνA which is $\delta_{13} = -90^\circ$ and NH. While generating the plots we have marginalised over δ_{14} and $|\Delta m^2_{31}|$ in the test parameters while all the other relevant parameters are kept fixed in both the true and test spectrum. The top, middle and bottom rows correspond to $\delta_{14} = -90^\circ$, 0° and $+90^\circ$ respectively. In each row the first and third panel correspond to LO ($\theta_{23} = 40^\circ$) and the second and fourth panel correspond to HO ($\theta_{23} = 50^\circ$). These values of θ_{23} are nice round values closest to the current best-fits according the latest global analyses. For comparison we also have given the contours for the standard 3ν case. Note that because of the existence of MH-δ_{14} and octant-δ_{14} degeneracies, the three incorrect solutions from section 4.4.3 (i) right hierarchy-wrong octant (RH-WO), (ii) wrong hierarchy-right octant (WH-RO) and (iii) wrong hierarchy-wrong octant (WH-WO) solutions are even more likely to be present. Also both the MH-δ_{14} and octant-δ_{14} degeneracy occur for any given value of δ_{13} (which is -90° in this case). This will imply that at least at the event level, all three spurious solutions should appear at the correct value of $\delta_{13}(\text{test}) = -90^\circ$. Below we discuss the appearance of these spurious solutions in detail.

Let us start with the three generation case. The red contour is for RH solutions and the purple contour is for WH solutions. For NOνA $(6 + \bar{0})$ and LO (first column), we see that apart from correct solution (the contour around the true point), there is a RH-WO solution around $\delta_{13}(\text{test}) = +90^\circ$ and a WH-WO solution around $\delta_{13}(\text{test}) = -90^\circ$. Note that both of these wrong solutions vanish in the NOνA $(3 + \bar{3})$ case (third column). This is because as we mentioned earlier, the octant degeneracy in the standard three flavour scenario behaves differently for neutrinos and antineutrinos and a combination of them can resolve this degeneracy. On the other hand for NOνA $(6 + \bar{0})$ and HO (second column), there are no wrong solutions apart from the true solution but in NOνA $(3 + \bar{3})$ (fourth column), a small RH-WO solution appears around $\delta_{13}(\text{test}) = -90^\circ$. This can be understood by thinking about the statistics in the following way. Running antineutrinos helps in the sensitivity only if there is degeneracy in the pure neutrino mode. But if there is no degeneracy, then replacing neutrinos with antineutrinos causes a reduction in the total statistics because the neutrino cross section is almost three times higher than the antineutrino cross section. As {$\delta_{13} = -90^\circ$, NH, HO} does not suffer from degeneracy in the pure neutrino mode, addition of antineutrinos makes the precision of θ_{23} worse as compared to NOνA $(6+\bar{0})$ and a WO solution appears for NOνA $(3+\bar{3})$.

Now let us discuss the case for the 3+1 scenario for $\delta_{14}=-90^\circ$ (first row). In these figures the blue contours correspond to the RH solution and the green contours correspond to the WH solutions. For NOνA $(6+\bar{0})$ and LO (first panel), we see that there is a RH-WO solution for the entire range of $\delta_{13}(\text{test})$. Note that NH and $\delta_{14}=-90^\circ$ don't suffer from the MH-δ_{14} degeneracy but we find a WH solution appears with WO around $\delta_{13}(\text{test})=-90^\circ$ which disappears in the NOνA $(3+\bar{3})$ case (third panel). The RH-WO solution around $\delta_{13}(\text{test})=-90^\circ$ on the other hand, remains unresolved even in the NOνA $(3+\bar{3})$ case. This is because that the octant - δ_{14} degeneracy is same for neutrinos and antineutrinos. This is one of the major new features of the 3+1 case when compared to the three generation case. In the three generation case, NOνA $(3+\bar{3})$ is free from all degeneracies for $\delta_{13}=-90^\circ$, NH and LO but if we introduce a sterile neutrino, then there will be an additional WO solution at the 90% confidence level. For HO, we see that $(6+\bar{0})$ configuration is almost free from any degeneracies except for a small RH-WO solution (second panel). For NOνA $(3+\bar{3})$, the lack of statistics decrease the θ_{23} precision and there is a growth in the WO region (fourth panel).

Next let us discuss the case for $\delta_{14}=+90^\circ$ (third row). For $6+\bar{0}$ and LO (first panel) we see that there is a WH-RO solution around $\delta_{13}(\text{test})=-90^\circ$, a WH-WO solution for the entire range of $\delta_{13}(\text{test})$ and RH-WO solution around $\delta_{13}(\text{test})=+90^\circ$. In this case the inclusion of the antineutrino run of NOνA (third panel) almost resolves all the degenerate solutions but a small WH solution remains unresolved. This indicates that in this case the statistics of the antineutrino run are not sufficient to remove the RH-WO solution. For HO, we have the RH-WO and WH-RO solutions, both at $\delta_{13}(\text{test})=-90^\circ$ for NOνA$(6+\bar{0})$ (second panel). For NOνA $(3+\bar{3})$ we see that the WH solution gets removed but the WO solution remains unresolved (fourth panel).

For $\delta_{14}=0^\circ$ (middle row), we see that there is a RH-WO solution in the entire range of $\delta_{13}(\text{test})$ and WH-WO solution around $\delta_{13}(\text{test})=-90^\circ$ for NOνA $(6+\bar{0})$ in LO (first panel). By the inclusion of antineutrino run, the WH-WO region gets resolved but the RH-WO solution remains unresolved at $\delta_{13}(\text{test})=-90^\circ$ (third panel). Apart from that, there is also the emergence of a WH-RO solution at $\delta_{13}(\text{test})=-90^\circ$. For the HO, we see that apart from the true solution, there is a RH-WO region for both

NOνA $(6+\bar{0})$ and $(3+\bar{3})$ configurations around at $\delta_{13}(\text{test}) = -90^\circ$ (second and fourth panel respectively).

5.5 Results for hierarchy sensitivity

We now discuss the hierarchy sensitivity of NOνA $(3+\bar{3})$ in the presence of a sterile neutrino. In the figure 5.3 we have given the 2σ hierarchy contours in the $\delta_{14}(\text{true})$ - $\theta_{23}(\text{true})$ plane for three values of δ_{14}. The red contours are for standard three flavour case and the blue contours are for 3+1 case. For the region inside the contours (to the right of the lines) one can exclude the wrong hierarchy at 2σ. Here the true hierarchy is NH. While generating these plots we have marginalised over test values of δ_{13}, δ_{14} and $|\Delta m^2_{31}|$. We have assumed the octant to be unknown and known in the left and right panels respectively, while the top, middle and bottom rows corresponds to $\delta_{14} = -90^\circ$, 0° and 90° in turn.

For the standard three flavour scenario we see NOνA has 2σ hierarchy sensitivity around -90° for all the values of θ_{23} ranging from 35° to 55°. This is irrespective of the information of the octant. This is because for NOνA $(3+\bar{3})$, the $\delta_{13} = -90^\circ$ case does not suffer from hierarchy degeneracy in NH. This can be understood from figure 5.2 by noting the absence of purple (3ν test IH) contours in NOνA $(3+\bar{3})$ for both LO and HO.

In the 3+1 case, if δ_{14} is -90° then the hierarchy sensitivity is lost when θ_{23} is less than 43° in the known octant case (top left panel). Note that though NOνA $(3+\bar{3})$ does not have a WH solution at 90%, the loss of hierarchy sensitivity implies that this degeneracy re-appears at 2σ. If the octant is known then the sensitivity of 3+1 coincides with the standard 3 flavour case (top right panel). This signifies that the loss of sensitivity in the 3+1 case for the value of $\delta_{14} = -90^\circ$ is mainly due to the WH-WO solution. In the middle row we see that in the 3+1 case, one cannot have hierarchy sensitivity at 2σ for true $\delta_{14} = 0^\circ$ if θ_{23} is less than 46° (42°) when the octant is unknown (known) as can be seen from the middle panels. This implies that for this value of true δ_{14} the hierarchy sensitivity of NOνA is affected by the WH solution occurring with both right and wrong octant. But the most remarkable result is found for $\delta_{14} = 90^\circ$ (bottom panels). For this value of δ_{14} we see that the hierarchy sensitivity of NOνA is completely lost. This is mainly due to the WH-RO solution. Thus we understand that if there exists a ~ 1 eV sterile neutrino in addition to the three active neutrinos and the value of δ_{14} chosen by nature is $+90^\circ$, then NOνA can

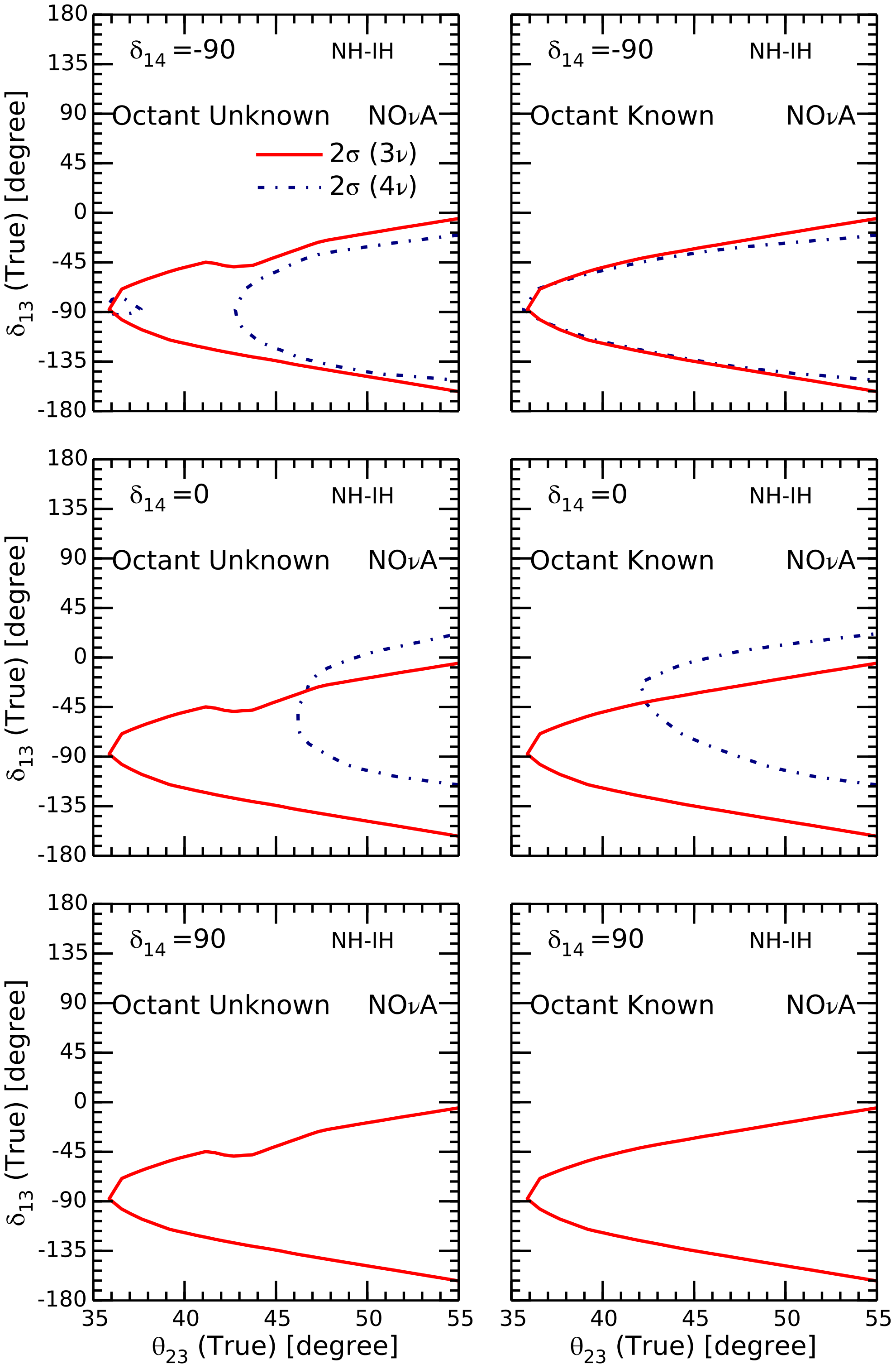

FIG. 5.3 Wrong hierarchy exclusion 3ν and 4ν contour plots for NOνA $(3+\bar{3})$ at 2σ C.L. in the $\delta_{13}(\text{true})$-$\theta_{23}(\text{true})$ plane. Left and right panels correspond to octant unknown and known. The first, second and third rows are for $\delta_{14} = -90°$, $0°$ and $90°$ respectively. The true MH is NH and test MH is IH. Note that the 4ν contours in the bottom panels are pushed entirely off the page.

not have even a 2σ hierarchy sensitivity for $\delta_{13} = -90^\circ$ and NH which is present best fit of NOνA.

5.6 Conclusion

In this analysis we studied the parameter degeneracy and hierarchy sensitivity of NOνA in the presence of a SBL motivated sterile neutrino. Apart from the MH-δ_{13} and octant-δ_{13} degeneracy in the standard three flavour scenario, we have identified two new degeneracies appearing with the new phase δ_{14} which occur for every value of δ_{13}. These are MH-δ_{14} degeneracy and octant-δ_{14} degeneracy. Unlike the standard three generation case, here the octant degeneracy behaves similarly for neutrinos and antineutrinos and the hierarchy degeneracy behaves differently. Thus a combination of neutrinos and antineutrinos are unable to resolve the octant-δ_{14} degeneracy but can resolve the MH-δ_{14} degeneracy. To identify the degenerate parameter space we present our results in $\theta_{23}(\mathrm{test})$ - $\delta_{13}(\mathrm{test})$ plane for three values of $\delta_{14}(\mathrm{true})$ assuming (i) NOνA runs in pure neutrino mode and (ii) NOνA runs in equal neutrino and antineutrino mode. We have chosen NH and $\delta_{13} = -90^\circ$ motivated by the latest fit from NOνA data. In those plots we find that there are different RH-WO, WH-RO and WH-WO regions depending on the true nature of the octant of θ_{23} and true value of δ_{14}. From these plots we find that the addition of antineutrinos helps to resolve the WH solutions but fails to remove the WO solutions appearing at $\delta_{13}(\mathrm{test}) = -90^\circ$. However we find that for $\delta_{14}(\mathrm{true}) = 90^\circ$ and LO, the antineutrino run of NOνA is unable to resolve the WH solution appearing with right octant at 90% C.L. While for $\delta_{14}(\mathrm{true}) = 0^\circ$, the WH-RO solution grows in size for NOνA $(3 + \bar{3})$ as compared to NOνA $(6 + \bar{0})$. Comparing these with that of standard three flavour case we find that apart from the small RH-WO regions for the true higher octant, there are no other degenerate allowed regions for this choice of $\delta_{13}(\mathrm{true})$ and hierarchy in the three flavour case for NOνA $(3 + \bar{3})$. Note the region $\delta_{13} = -90^\circ$ and NH is the favourable parameter space of NOνA which does not suffer from MH-δ_{13} degeneracy in the standard three flavour scenario where NOνA can have good hierarchy sensitivity. But now in the 3+1 case, the hierarchy sensitivity of NOνA for this parameter value can suffer due to the existence of the new degeneracies. To study that we plot the 2σ hierarchy contours in the $\theta_{23}(\mathrm{true})$-$\delta_{13}(\mathrm{true})$ plane for three values of true δ_{14} in NH. While in the standard three flavour case one can have 2σ hierarchy sensitivity for all the values of θ_{23} ranging from 35° to 55°, in the 3+1 case we find that for $\delta_{14} = -90^\circ$

and $\theta_{23} = 43^\circ$ the hierarchy sensitivity of NOνA is lost. For the value of $\delta_{14} = 0^\circ$, the hierarchy sensitivity of NOνA is also compromised if θ_{23} is less than 46°. But the most serious deterioration in hierarchy sensitivity occurs if the value of δ_{14} chosen by nature is $+90^\circ$. At this value of δ_{14}, NOνA suffers from hierarchy degeneracy and thus it has no hierarchy sensitivity for any value of θ_{23}. Therefore if: (i) the hint of $\delta_{13} = -90^\circ$ persists; (ii) the data begins to show a preference towards LO; and (iii) the observed hierarchy sensitivity is less than the expected sensitivity, then this can be a signal from NOνA towards existence of a sterile neutrino with $\delta_{14} \neq -90^\circ$.

The original work described in this chapter was originally published as 'Study of parameter degeneracy and hierarchy sensitivity of NOνA in presence of sterile neutrino' in Phys.Rev. D96 (2017) no.7, 075018.

CHAPTER 6

A LIGHT STERILE NEUTRINO AT NOνA AND DUNE

As a follow up to our $3+1$ study of NOνA in the previous chapter 5 we perform an extension of that work including the future experiment DUNE and some new best fits including $\theta_{23} = 45°$. For this analysis we focus our attention the MH-δ_{13} and octant-δ_{13} degeneracies. As before these conditions imply that for certain combinations of $\theta_{23}, \Delta m^2_{31}$ and δ_{13} we will have multiple sets of parameters that give the same oscillation probability, thus an experiment may not be able to tell these situations apart. The true and test parameters we investigate can be roughly divided into upper and lower ranges. So we continue to use the abbreviations NH/IH (normal hierarchy/inverted hierarchy), LO/HO (lower octant/higher octant), with the midpoint of the octant range corresponding to maximal-mixing (MM). These ranges are defined by:

$$\text{NH} \implies |\Delta m^2_{31}| > 0, \tag{6.1}$$

$$\text{IH} \implies |\Delta m^2_{31}| < 0, \tag{6.2}$$

$$\text{LO} \implies \theta_{23} < 45°, \tag{6.3}$$

$$\text{HO} \implies \theta_{23} > 45°, \tag{6.4}$$

$$\text{MM} \implies \theta_{23} = 45°, \tag{6.5}$$

while δ_{13} and δ_{14} can be anywhere in their full $-180°, 180°$ range, so we do not define named regions. Similarly, when discussing test ranges, we also extend the previously used shorthand: WO/RO (wrong octant/right octant), WH/RH (wrong hierarchy/right hierarchy) and Wδ_{13}/Rδ_{13} (wrong δ_{13}/right δ_{13}) to describe the test solutions surrounding the correct or incorrect regions in the parameter space.

For an overview of the phenomenology and experimental constraints on a fourth neutrino at this time we refer to references [85, 153, 161, 172–181, 191–193]. Similarly, for LBL analyses featuring sterile neutrinos see references [121, 162–171]. For a more thorough analysis of θ_{23} and δ_{13} in the 3ν case for DUNE see [194].

For true values, we use the three best fits from The NOνA Collaboration 2017 results [59] which are good examples of degenerate results, as well as the same results but with $\theta_{23} = 45°$. Note that the significance of some of these results dropped in the 2018 release [60] but all are still allowed at around 2σ. These solutions are outlined in table 6.1 with the rest of the oscillation parameters identical between each case. We aim to expand on our analysis [1] as well as [195] to analyse all three true solutions in the case where a sterile neutrino is introduced. We also produce plots with $\theta_{23} = 45°$ (which was previously ruled out by NOνA but is now allowed [60]) in each case to examine how the degeneracies and allowed regions change.

We will refer to these three solutions using the shorthand from table 6.1. It is important to analyse these results because they are examples of solutions degenerate in probability and thus must be resolved by detector effects or combined analyses. We also analyse hypotheses with $\theta_{23} = 45°$ because these 'maximal-mixing' solutions are allowed by MINOS, T2K and recently NOνA at 90% C.L. [156, 196]. However, we do not fully explore the maximal-mixing parameter space because it is beyond the scope of this analysis and in general should have less issues with degeneracies.

Solution	δ_{13}	octant	hierarchy
A	$-90°$	LO	NH
B	$135°$	HO	NH
C	$-90°$	HO	IH
A′	$-90°$	MM	NH
B′	$135°$	MM	NH
C′	$-90°$	MM	IH

TABLE 6.1 The three HO/LO and three MM true solutions considered in this analysis.

The main part of our analysis is introducing the sterile parameters then varying the new sterile phase δ_{14} between several values and investigating its effect on the octant and mass hierarchy sensitivity, specifically their degeneracies. The standard three neutrino (3ν) and the extended 3+1 parameters with the three representative values for θ_{23} are in table 6.2.

3ν Parameters	True Value	Test Value Range
$\sin^2\theta_{12}$	0.304	N/A
$\sin^2 2\theta_{13}$	0.085	N/A
$\theta_{23}^{\mathrm{LO}}$	$40°$	$(35°, 55°)$
$\theta_{23}^{\mathrm{HO}}$	$50°$	$(35°, 55°)$
$\theta_{23}^{\mathrm{MM}}$	$45°$	$(35°, 55°)$
δ_{13}	$-90°, 135°$	$(-180°, 180°)$
Δm^2_{21}	7.5×10^{-5} eV^2	N/A
Δm^2_{31}(NH)	2.475×10^{-3} eV^2	$(2.300, 2.500) \times 10^{-3}$ eV^2
Δm^2_{31}(IH)	-2.400×10^{-3} eV^2	$(-2.425, -2.225) \times 10^{-3}$ eV^2
4ν Parameters		
$\sin^2\theta_{14}$	0.025	N/A
$\sin^2\theta_{24}$	0.025	N/A
θ_{34}	$0°$	N/A
δ_{14}	$-90°, 90°$	$(-180°, 180°)$
δ_{34}	$0°$	N/A
Δm^2_{41}	1 eV^2	N/A

TABLE 6.2 3ν and 4ν true and test parameter values and marginalisation ranges. Parameters with N/A are not marginalised over.

6.1 Oscillation Theory

Extending to 4ν requires modification to the standard neutrino oscillation equations, it is important to pay attention to the parametrisation chosen, because comparing mixing angles and CP phases between different choices is non-trivial. We utilise the same parametrisation and probability as presented in section 5.2.

Recall that if these degeneracies can be solved at all with the current experiments T2K [156] and NOνA [59] then they may give the first hints of the values of δ_{13}, θ_{23} and the sign of Δm^2_{31} at some significant confidence level.

The addition of sterile neutrinos to the oscillation model can greatly lower sensitivity to degeneracies for NOνA and T2K [163], and DUNE is already predicted to have very good degeneracy resolution [197, 198] for 3ν so it's important to see how much a new $\sim 1\ \mathrm{eV}^2$ splitting affects this. In addition, to see the how the sensitivity scales for runtime, we simulate DUNE for $2+\bar{2}$ and $5+\bar{5}$.

It is predicted that DUNE, along with other proposed next generation long-baseline experiments such as T2HK (Tokai to Hyper-Kamiokande) [199] and/or T2HKK (Tokai to Hyper-Kamiokande and Korea) [200] (which we introduced in sections 1.3.1 and 1.4.1), will be very sensitive to sterile induced CP phases [201, 202]. As such, they will contribute much further to oscillation physics once the current degeneracies and issues are resolved, and will be increasingly important if sterile neutrinos are present.

6.2 Identifying Degeneracies in the 3+1 Case

We will use a similar approach to previously in section 6.4, firstly analysing probability plots by eye then moving on to various hypothesis tests.

6.2.1 Degeneracies at the Probability Level

We take the standard best fits for oscillation parameters from sources such as global fits and oscillation experiments [187–189] and then choose sterile parameters consistent with [125, 180, 190, 191]. As in chapter 5 we then set θ_{34} and δ_{34} to zero because they are not present in the vacuum equation for $P_{\mu e}$ (5.5), and we are under the assumption that matter interactions will not add any significant dependence to these terms. Finally we smooth our curves with a moving box-windowed average to represent the small oscillations that will be present but cannot be seen in real data, as mentioned in section 4.2.1.

When we plot the probability plots for our three true values into the 4ν sector and vary δ_{14} from -90° to $+90^\circ$, our lines will become bands. This may cause additional overlap where there was none before, thus introducing or re-introducing specific degenerate solutions. This is the primary feature we are interested in as it will determine the sensitivity degradation that would be present in the $3+1$ case.

For the plots where they are not axis variables we marginalise $|\Delta m^2_{31}|$, $\delta_{13}^{\text{test}}$ and $\delta_{14}^{\text{test}}$ to minimise χ^2 in the fit. All of the marginalisation ranges are summarised in table 6.2.

It can be seen from figure 6.2 that the curve separation for antineutrinos relative to the neutrino case seen in HO/LO is lessened for MM. This implies that it will be less important to run antineutrinos to distinguish these three values. This is due to the octant-δ_{13} degeneracy vanishing as θ_{23} approaches 45°. The MH degeneracy for results B′ and C′ is still significant in all cases as with B and C.

NOνA

It can be seen in figure 6.1 that for the 3ν unprimed parameter case, all three probability curves for NOνA running neutrinos are almost entirely degenerate, though in the antineutrino case only the B and C solutions are degenerate. This is clearly the reason they cropped up in real data! In the primed case (figure 6.2) the B′ and C′ solutions are distinct from the A′ solution for neutrinos and antineutrinos. Extending to 4ν shows bands that are also almost totally overlapping for neutrinos while for antineutrinos, 4ν the bands get closer together again but solution A is still mostly separate (figure 6.3). For the primed solutions the A′ band is still mostly distinct but now has gained significant overlap with B′ and C′ both neutrinos and antineutrinos (figure 6.4). So overall true MM is superior to LO/HO for distinguishing these parameter sets, aside from a small overlap increase in antineutrinos.

DUNE

In contrast with the NOνA plot, the 3ν DUNE plots (figure 6.5) show only the A and B neutrino curves overlapping and no overlap for the antineutrino case, as shown in [195]. This points to much better degeneracy resolution than NOνA, especially while running antineutrinos. The 4ν plots (figure 6.7) do show overlap, specifically A, B

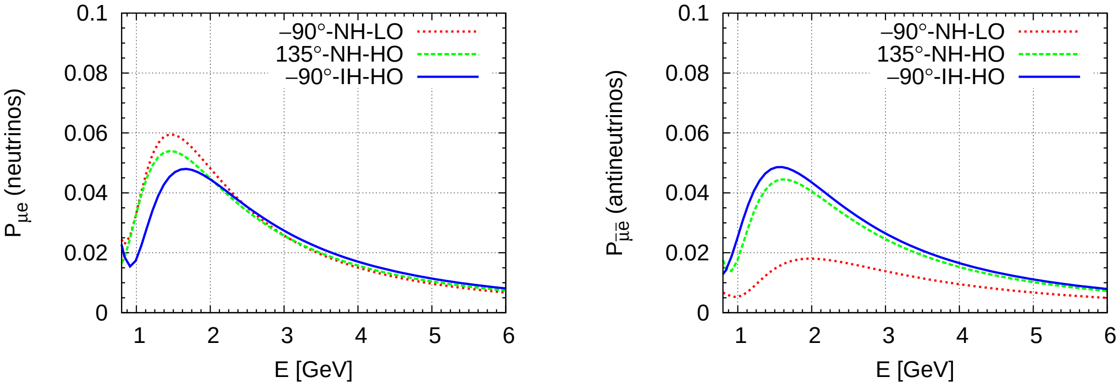

(a) Neutrinos. (b) Antineutrinos.

FIG. 6.1 Three-flavour probability plots with all three true value lines overlaid for NOνA showing the largely degenerate curves except in the antineutrino case where the LO curve is distinct. The dotted red, dashed green and solid blue probabilities come from the A, B and C parameter sets respectively.

and some C for neutrinos; and B and C for antineutrinos. So comparing 3ν lines to 4ν bands shows it is possible that some degeneracies can be reintroduced by extending our parameter space, even with the DUNE detector. Comparing these plots with the NOνA ones shows that solution A is still the favoured solution for degeneracy resolution. The probability plots do not tell the whole story however as they do not reflect the statistics of the detector, therefore we must do more analysis to get an idea of what significance degeneracies arise at. The primed MM case curves (figure 6.6) are widely spaced and have no overlap for DUNE in the 2-3 GeV range. So if MM is the true case, DUNE should have better resolution power when running neutrinos and slightly worse power when running antineutrinos, similar to NOνA. Thus the MM case does not have a disparity in neutrino/antineutrino degeneracy resolution power unlike the octant cases. Similar to NOνA, in the 4ν case (figure 6.8) the neutrino overlap improves slightly, while the antineutrino overlap gets slightly worse though DUNE is still overall vastly superior to NOνA in terms of overall band separation.

6.2.2 Degeneracies at the detector level

We now analyse our test hypotheses using several χ^2 type analyses to see for which values we can resolve the MH degeneracy, see what regions are allowed at 90% C.L. and also to look at the CP sensitivity for a variety of true values. This is necessary because we need to account for statistical effects and combined neutrino/antineutrino

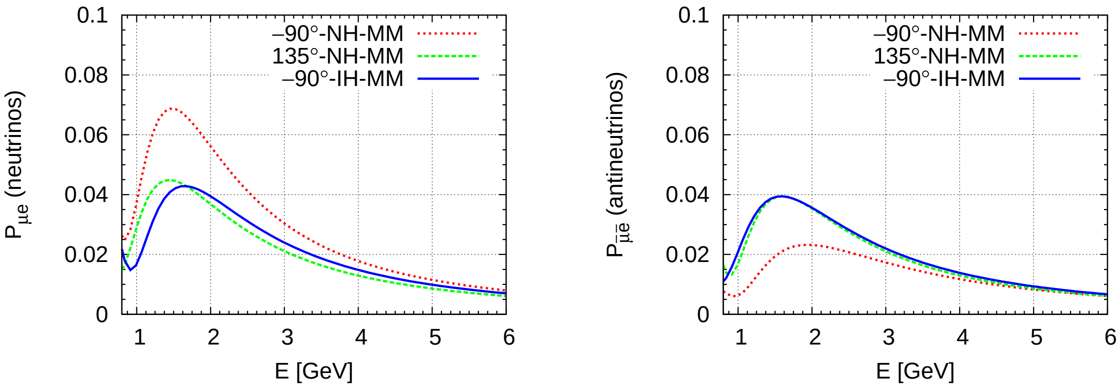

(a) Neutrinos.

(b) Antineutrinos.

FIG. 6.2 Three-flavour probability plots for NOνA as with figure 6.1 but for $\theta_{23} = 45^\circ$ so in this case the red, green and blue probabilities come from the A′, B′ and C′ instead.

runs. When performing the χ^2 analysis we take the true parameters to be A, B or C (then A′, B′ and C′) and the test parameters to be as specified in table 6.2 including marginalisation ranges for the free parameters.

NOνA

Exclusion Plots To investigate the explicit range of true values for which the MH can be resolved we can create hierarchy exclusion plots. As usual we vary the true oscillation parameters, flip the hierarchy in the test hypothesis and marginalising over every other variable. When we examine the exclusion plots for NOνA (figure 6.9) we can see that the excluded region for true NH (true IH) includes the $\delta_{13} = +90^\circ$ ($\delta_{13} = -90^\circ$) favoured region, this should be expected because for the favoured parameters it is predicted that in the 3ν case NOνA alone can resolve the mass hierarchy. Extending into 4ν changes these regions somewhat, e.g. for true NH, $\delta_{14} = 90^\circ$ the exclusion zone retreats towards the HO side of our plot, indicating that the MH degeneracy can only be solved for true values roughly in the ranges: $\theta_{23} > 45^\circ$ and $\delta_{13} \in (-45^\circ, -135^\circ)$. The change in the corresponding true IH plot with $\delta_{14} = 90^\circ$ is much less extreme, still allowing MH resolution for some LO true values. On the other hand for $\delta_{14} = -90^\circ$ both NH and IH are mostly similar to the 3ν case and as such the favoured half planes are mostly excluded.

So to summarise, true NH is ok for 3ν and $4\nu(\delta_{14} = -90^\circ)$ but $4\nu(\delta_{14} = 90^\circ)$ is a lot worse. True IH on the other hand has decent MH resolution in 3ν and $4\nu(\delta_{14} = \pm 90^\circ)$

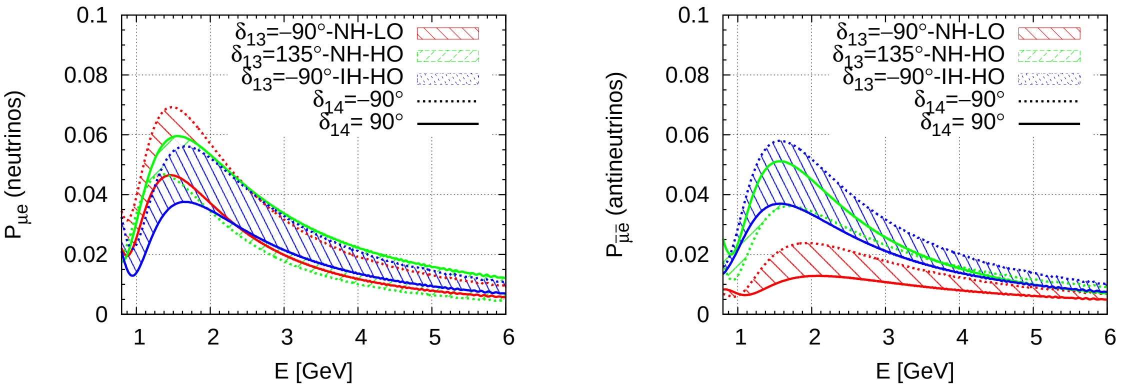

(a) Neutrinos.

(b) Antineutrinos.

FIG. 6.3 Four-flavour probability plots with all three true value bands overlaid for NOνA. The comparison between the neutrino and antineutrino cases is similar to the 3ν case, but the LO and HO curves in the antineutrino case do get closer. The red, green and blue probabilities come from the A′, B′ and C′ as with figure 6.1 but now the dotted lines correspond to $\delta_{14} = -90°$ and solid ones to $\delta_{14} = 90°$.

with the regions wher we can exclude the wrong MH moving higher and lower in δ_{13} respectively.

Allowed Region Plots From figure 6.10 it can be seen that in the 3ν case, the plot for A shows one allowed region surrounding the true value, while the B and C plots have WO-WH-Wδ_{13}, RO-WH-Wδ_{13} and WO-RH-Rδ_{13} regions as well as the correct solution. For the 4ν cases, in general the regions are broadly the same, though for $\delta_{14} = +90°$ true value A gains a WH region while for $\delta_{14} = -90°$ it gains a WO region. More significantly, for true values B and C the regions mostly get larger (though the WO-WH-Wδ_{13} solution for C vanishes). Overall figure 6.10 shows that solution A can be resolved more easily than the other cases, by relating the probability plots to the allowed regions, the particularly large separation of the curves for antineutrinos compared to neutrinos contributes strongly to this.

Similarly in figure 6.11 the A′ case is still the one with the least degeneracy having only a small WH solution when $\delta_{14} = +90°$. In the other MM cases the MH degeneracy exists with regions almost reflected about $\delta_{13} = 0°$. For most of these cases the LO and HO solutions we tested ($\theta_{23} = 40°, 50°$) are just outside the 90% C.L. regions, though $\theta_{23} \approx 42.5°, 49°$ are included in all regions, implying that some HO/LO solutions with less extreme values can't be ruled out by NOνA in the MM case.

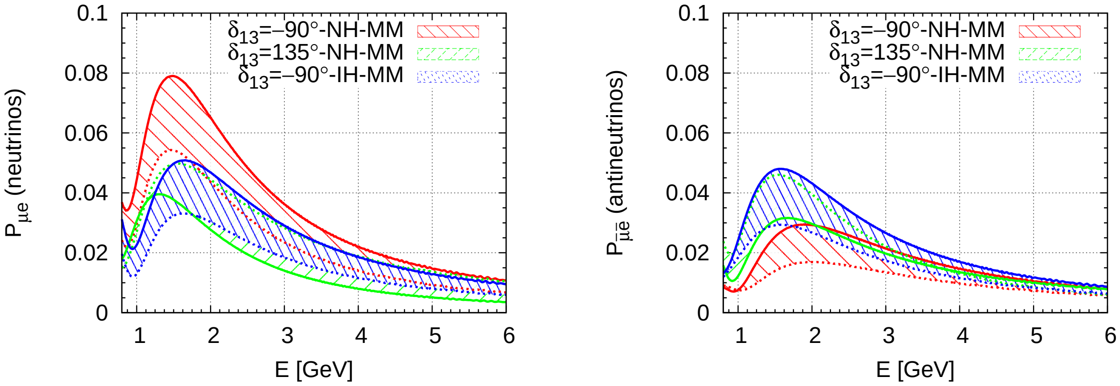

(a) Neutrinos.

(b) Antineutrinos.

FIG. 6.4 Four-flavour probability plots for NOνA as with figure 6.3 but for the primed parameters with $\theta_{23} = 45°$.

DUNE

Exclusion Plots Evaluating the exclusion plots for the reduced or partial run of DUNE $2 + \bar{2}$ (figure 6.12) and comparing to NOνA shows that the excluded region expands to include much of the unfavoured half plane. On the $\theta_{23} < 45°$ side of the plots there are reasonable sized areas still allowed, this implies that true LO is unfavoured for degeneracy resolution, even at DUNE. In the $\delta_{14} = -90°$ cases there are still small sections at ($\theta_{23} = 45°, \delta_{13} \approx 90°$, NH) and ($\theta_{23} = 45°, \delta_{13} \approx -90°$, IH) in which MH degenerate solutions will still exist.

Extending the DUNE run to $5 + \bar{5}$ further increases the parameter space for which the wrong mass hierarchy can be excluded (figure 6.13) and only small areas in the unfavoured half-planes remain for $\theta_{23} < 40°$ which is roughly 2σ to 3σ outside of NOνA's current fits depending on the value of $|\Delta m^2_{31}|$. Because these non-excluded values are only valid for θ_{23} well below current LO estimates this reinforces the prediction that after it's full run, DUNE will be capable of resolving the MH degeneracy independently of other experiments, regardless of θ_{23}, even in the case of small sterile mixing.

Allowed Region Plots Evaluating the allowed regions for DUNE $2 + \bar{2}$ shows an almost complete disappearance of WH solutions. Many of the WO solutions are gone too, for example the 3ν IH plots in figure 6.14 have almost none. Though some cases are still particularly bad, for example true value B has a degenerate octant solution that almost spans the entire range of δ_{13}.

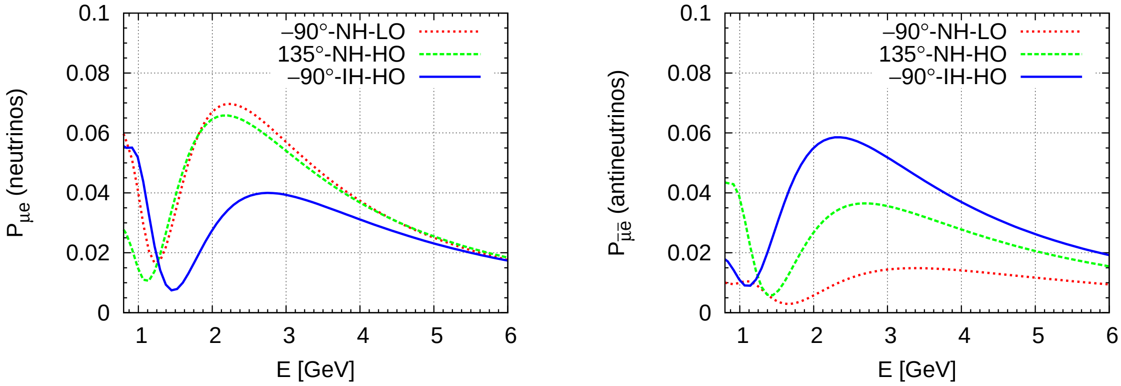

(a) Neutrinos.

(b) Antineutrinos.

FIG. 6.5 Three-flavour probability plots with all three true value lines overlaid for DUNE, highlighting the larger separation of curves for the longer baseline detector. Parameter sets are arranged the same as with figure 6.1.

For the MM case with only $2 + \bar{2}$ running (figure 6.15) the MH degenerate regions present for NOνA vanish for most cases and only remain for B′ in 3ν and $\delta_{14} = -90°$ as small regions. The size of the regions does not change much compared to NOνA so the allowed θ_{23} range is roughly the same, though the allowed regions do avoid $\theta_{23} = 40°, 50°$ in more of the cases. Overall for DUNE $(2 + \bar{2})$ the trade off is between octant true values with degenerate solutions or max-mixing true values with more uncertainty in the exact value of θ_{23}.

From figure 6.16 it can be seen that despite the additional probability overlap induced by the sterile parameters, for DUNE $5 + \bar{5}$ the degeneracies are practically resolved at 90% C.L. aside from small wrong octant regions for values A and C with $\delta_{14} = -90°$ and for B with $\delta_{14} = +90°$. We would expect this following what we have seen in the probability bands and exclusion plots. This is due to the fact that hierarchy resolution ability is related to the baseline of the experiment and as seen in figure 6.7 (b) at 2.5 GeV neutrino energy, DUNE has no overlap for our three parameter bands when running antineutrinos, this allows excellent degeneracy resolution.

In the MM case (figure 6.17) the allowed regions for DUNE get larger but have no MH degenerate regions. In all cases the HO/LO solutions are outside the 90% C.L. regions implying good rejection of HO/LO solutions and a good contribution to the precision measurement of θ_{23}. This means that the small MH overlap in antineutrinos must be resolved by statistics or the combined runs.

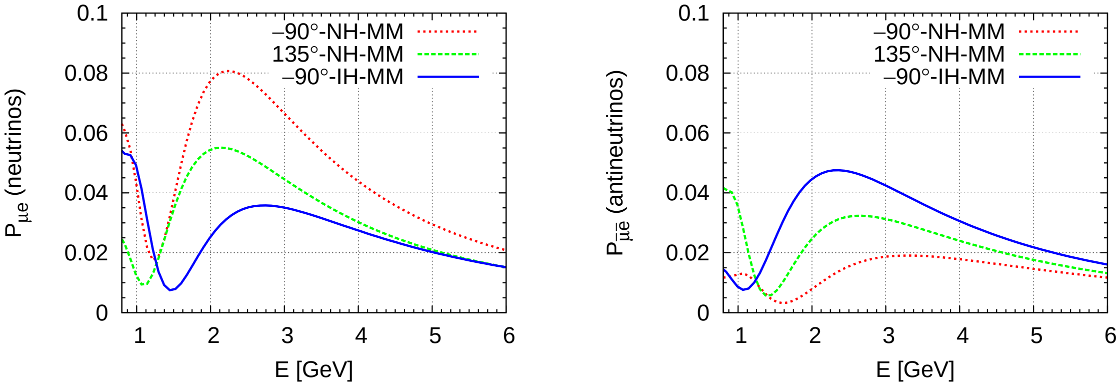

(a) Neutrinos. (b) Antineutrinos.

FIG. 6.6 Three-flavour probability plots for DUNES as with figure 6.5 but for $\theta_{23} = 45°$.

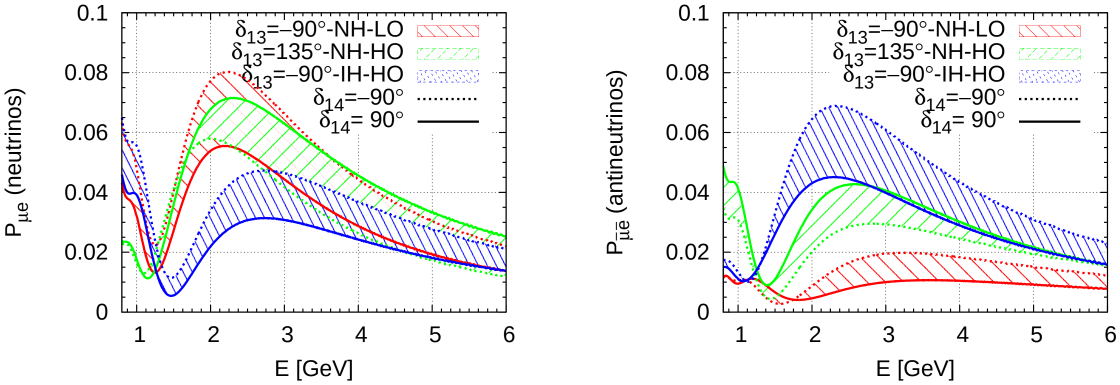

(a) Neutrinos. (b) Antineutrinos.

FIG. 6.7 Four-flavour probability plots as with figure 6.3 but for DUNE. The minimal overlap introduced by the sterile CP phase δ_{14} can be seen.

6.3 Conclusion

We have extended the analysis from chapter 5 in light of the discussions from [195] regarding the results in [59]. We include a light sterile neutrino specified as such to rectify the short baseline oscillation anomalies. From our analysis we see that the degenerate solutions are predicted to be worse at the probability level for the 4ν case due to the additional free parameters. We find that for certain values of δ_{14} the sensitivity of NOνA to the octant degeneracy and (to a much lesser extent) hierarchy degeneracy may be reduced. We also predict that DUNE $2 + \bar{2}$ can solve the MH degeneracy at 90% C.L. while some octant ambiguity still exists. However, extending

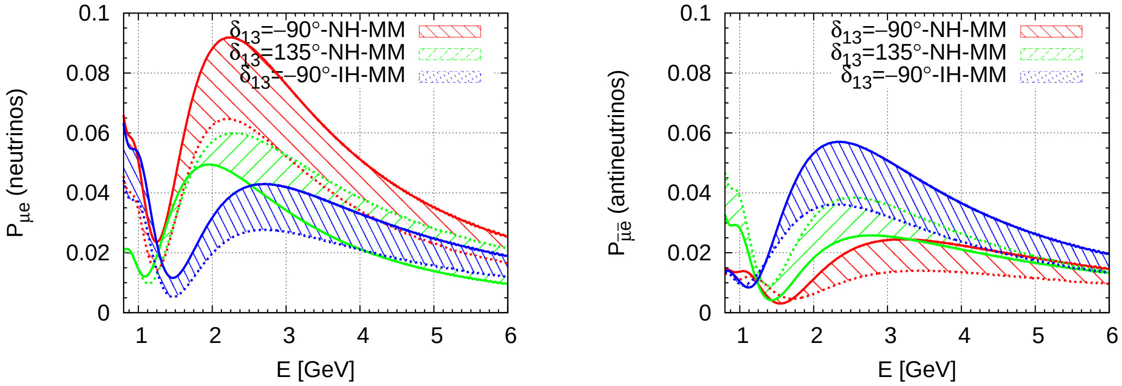

(a) Neutrinos. (b) Antineutrinos.

FIG. 6.8 Four-flavour probability plots for DUNE asimilar to figure 6.7 but for $\theta_{23} = 45°$.

to the full DUNE $5 + \bar{5}$ run removes almost all ambiguity at 90% C.L. in all cases regardless of δ_{14}. So it can be seen that for any of these true values with the sterile hypothesis being correct or not, that DUNE can resolve these degeneracies at 90% C.L. whilst NOνA alone loses some potential for degeneracy resolution in the sterile case.

We also find that if the θ_{23} value chosen by nature is $45°$, then the need for combined neutrino/antineutrino analysis to distinguish certain results is diminished. This leads to increased MH resolution power but less precision for the exact value of θ_{23}. However it can be seen that DUNE has similar MH resolution power at 90% C.L. no matter the case. It remains to be seen over the next few years how important DUNE will be in this field, depending on what best fit parameters NOνA and T2K favor.

The original work described in this chapter was originally published as ‘The Effect of a Light Sterile Neutrino at NOνA and DUNE’ in Phys.Rev. D98 (2018) no.3, 035042.

6.4 Additional Notes

New results from NOvA have been published recently [60, 203, 204] and indicate new 1σ parameter ranges:

$$\Delta m^2_{32} = 2.444^{+0.079}_{-0.077} \times 10^{-3}\ \mathrm{eV}^2 \tag{6.6}$$

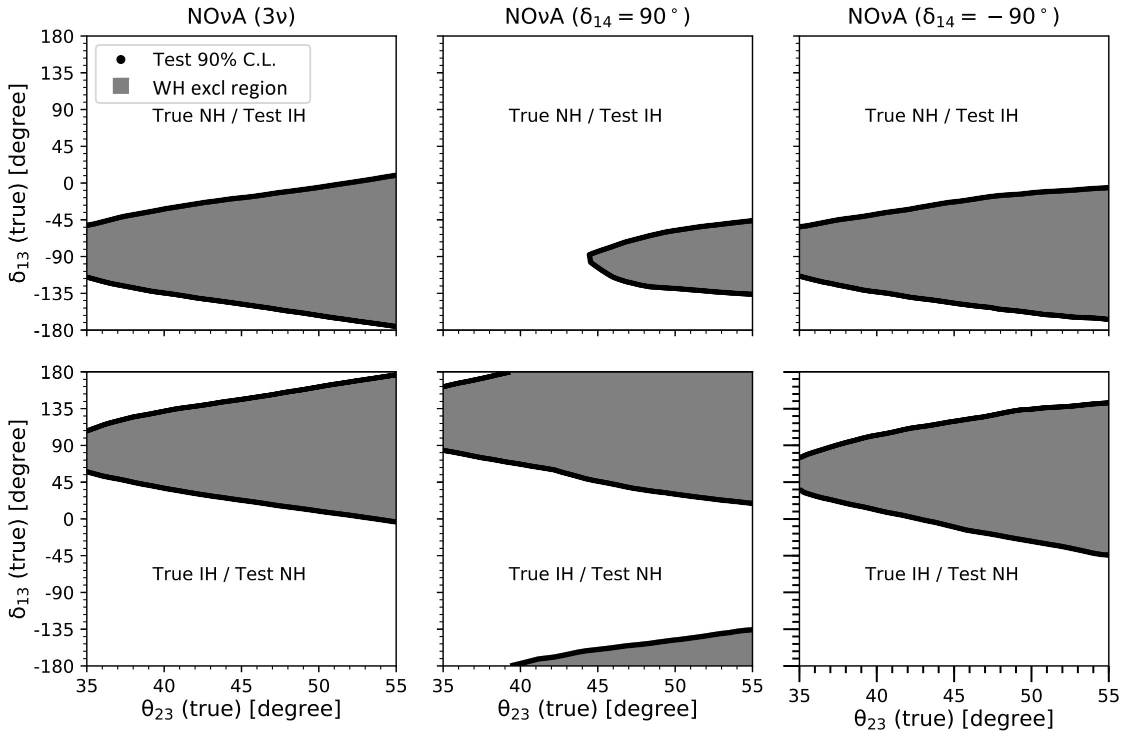

FIG. 6.9 MH exclusion plots for NOνA $\left(3+\bar{3}\right)$. Upper plots are for true NH/test IH and the lower plots are for true IH/test NH. These plots contain similar information to the octant unknown plots from figure 5.3 but we also analyse IH-NH and omit the $\delta_{14} = 0°$ case. For ease of comparison we have also shaded the true parameter region for which the wrong test hierarchy can be excluded.

$$\sin^2\theta_{23} = \begin{cases} 0.558^{+0.041}_{-0.033}\,(\mathrm{HO}) \\ 0.475^{+0.036}_{-0.044}\,(\mathrm{LO}) \end{cases} \tag{6.7}$$

with best fits of: $\delta_{13} = 1.21\pi \approx -142.2°$, HO, NH. These align somewhat better with previous T2K and MINOS results and no-longer explicitly rule out $\theta_{23} = 45°$ at 90% C.L. We will still continue to analyse our three values despite the fact that neither A or B are fully favoured and C is disfavoured, because we are interested purely in degeneracy resolution. With regards to these new preliminary best fits from NOνA, our sensitivity predictions do not really change, these results still fall into the favoured area for mass hierarchy resolution and as such the NOνA only loses MH sensitivity in the specific 4ν case with $\delta_{14} = -90°$ (figure 6.18). The octant region does have more spread for this true value, but the allowed region doesn't include the wrong octant, instead including the maximal-mixing ($\theta_{23} = 45°$) case. For DUNE

$\left(2+\bar{2}\right)$ the results are similar (figure 6.19). Therefore in this case MM can not be ruled out at 90% C.L. and may require a combined analysis to differentiate.

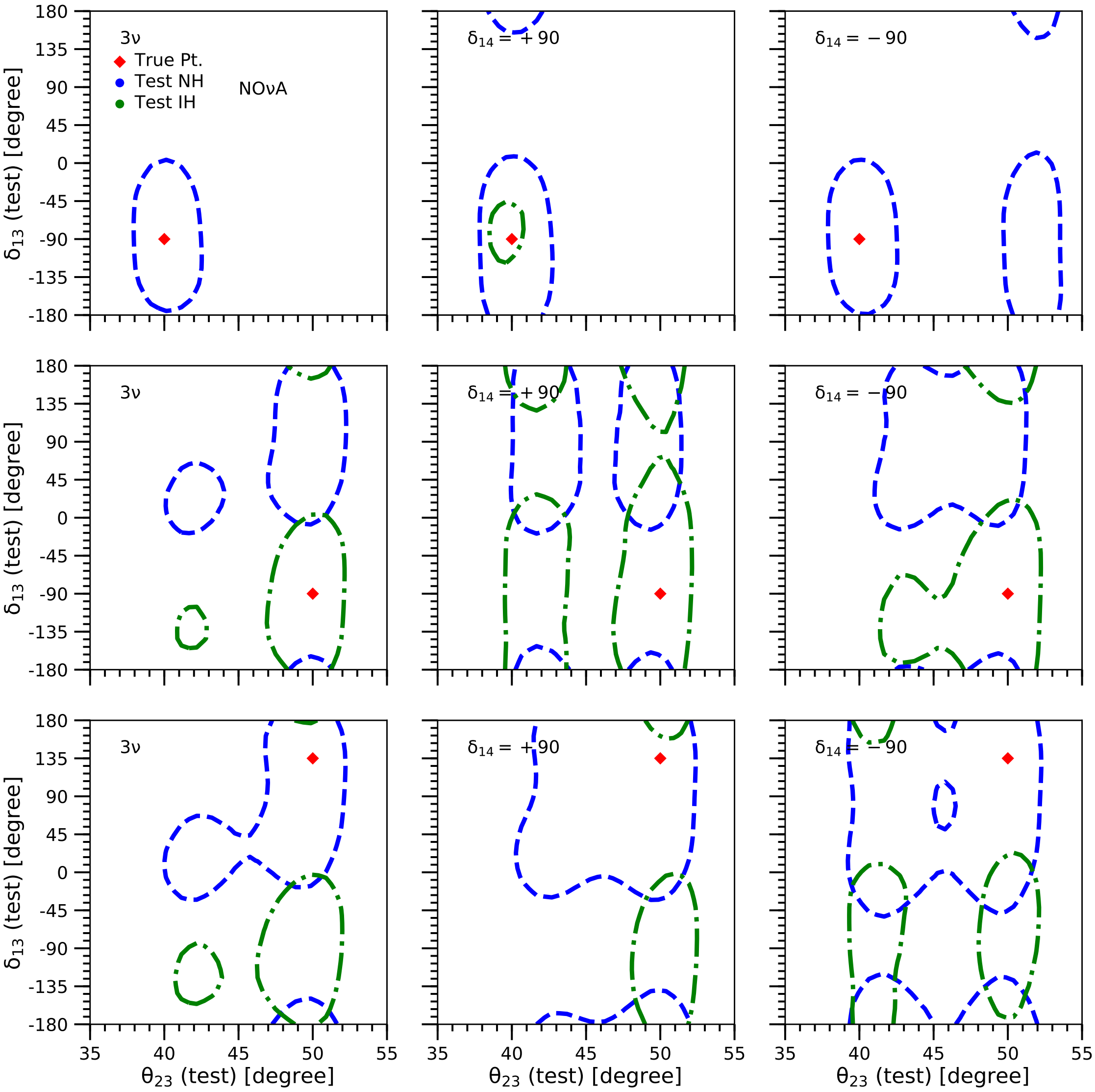

FIG. 6.10 Allowed region plots in the test θ_{23}-δ_{13} plane for three different true values of δ_{13}, θ_{23}, MH for 3ν (first column) as well as $\delta_{14} \pm 90^{\circ}$ in 4ν (second and third columns) all for NOνA. The top, middle and bottom rows are for true values based off parameter sets A, B and C respectively.

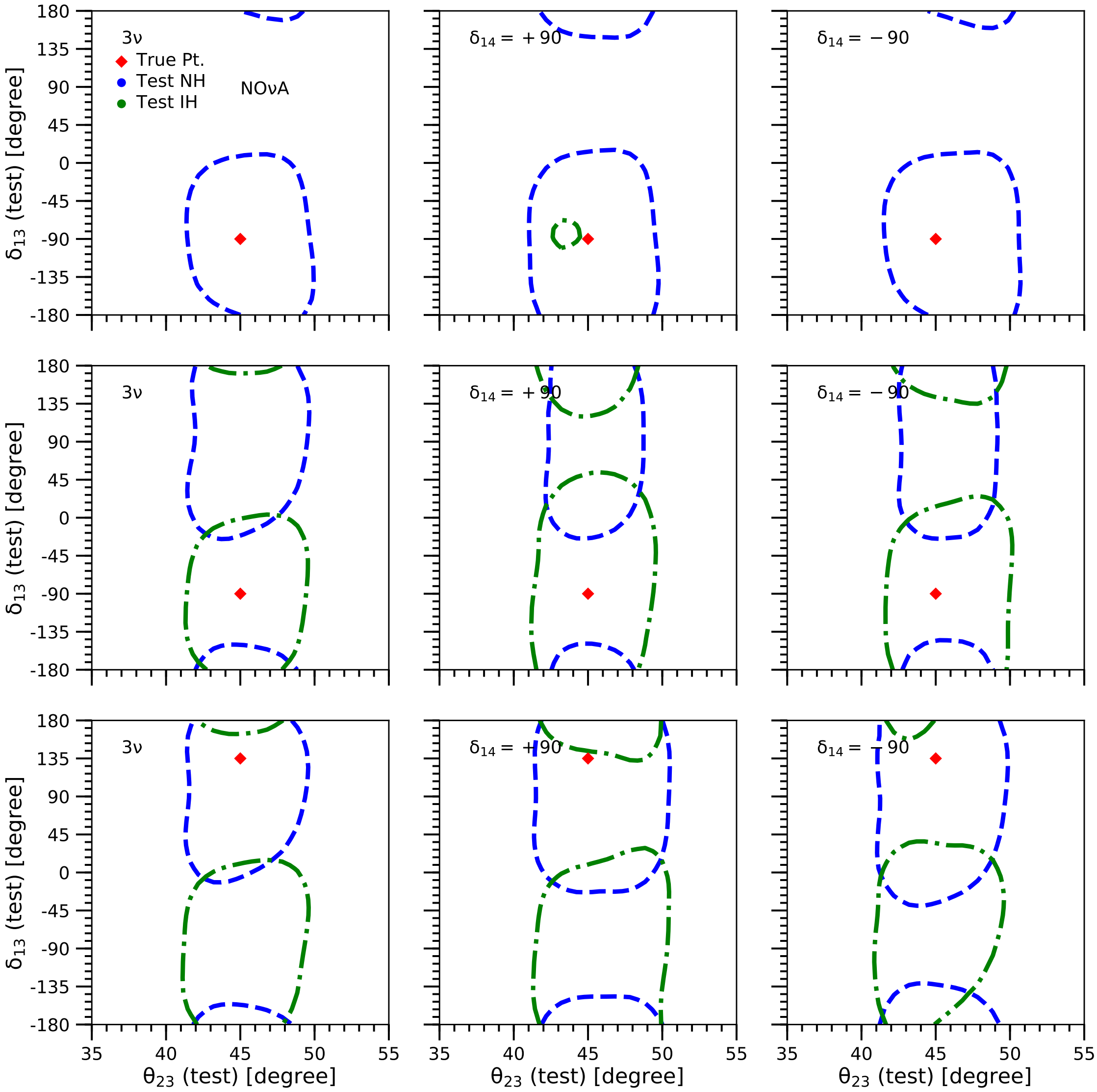

FIG. 6.11 Allowed region plots for NOνA similar to figure 6.10 but for $\theta_{23} = 45°$. Therefore top, middle and bottom rows are for parameter sets A′, B′ and C′ respectively.

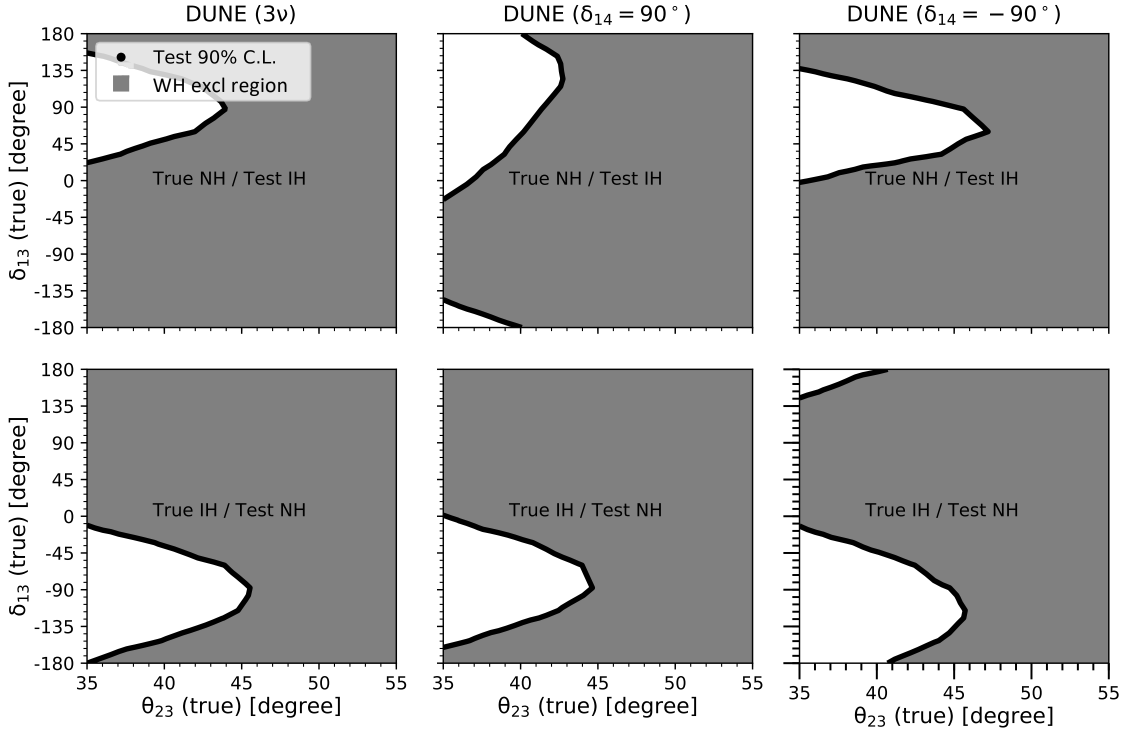

FIG. 6.12 MH exclusion plots for DUNE $\left(2+\bar{2}\right)$. Notice that compared with the NOνA case in figure 6.9, the WH hypothesis can be excluded in much more of the true parameter space.

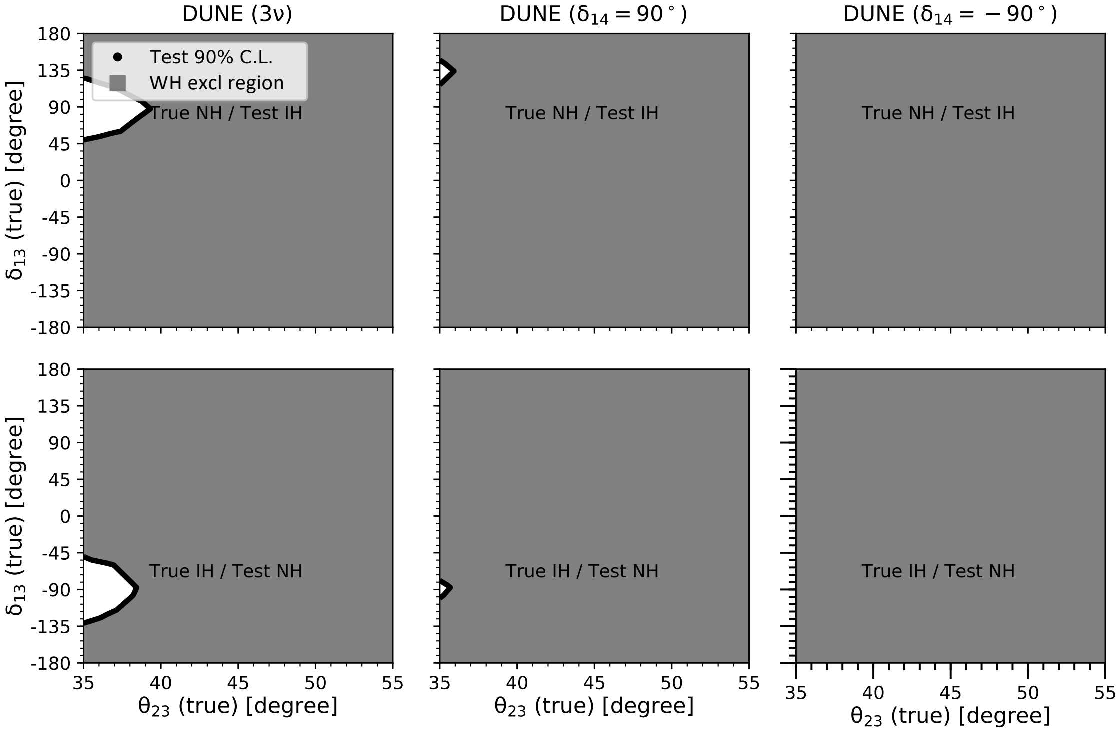

FIG. 6.13 MH exclusion plots for DUNE $\left(5+\bar{5}\right)$. Showing that the true parameter regions in which the wrong hierarchy can be excluded almost cover the entire allowed range of θ_{23} and δ_{13} for all considered CP phase value ranges.

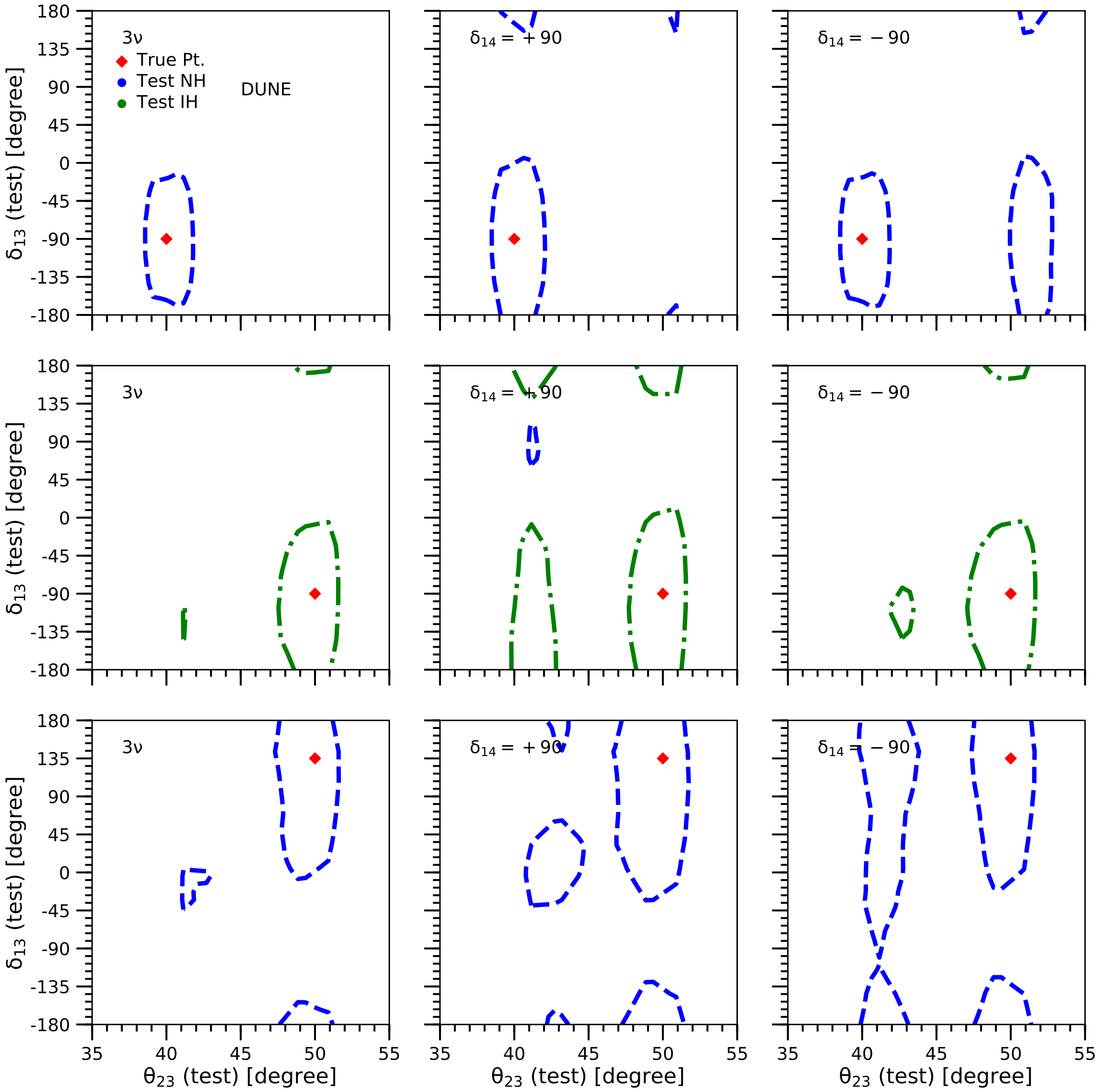

FIG. 6.14 Allowed region plots similar to figure 6.10 but for DUNE $\left(2+\bar{2}\right)$. Few WH solutions are seen but the octant degeneracy is still prevalent.

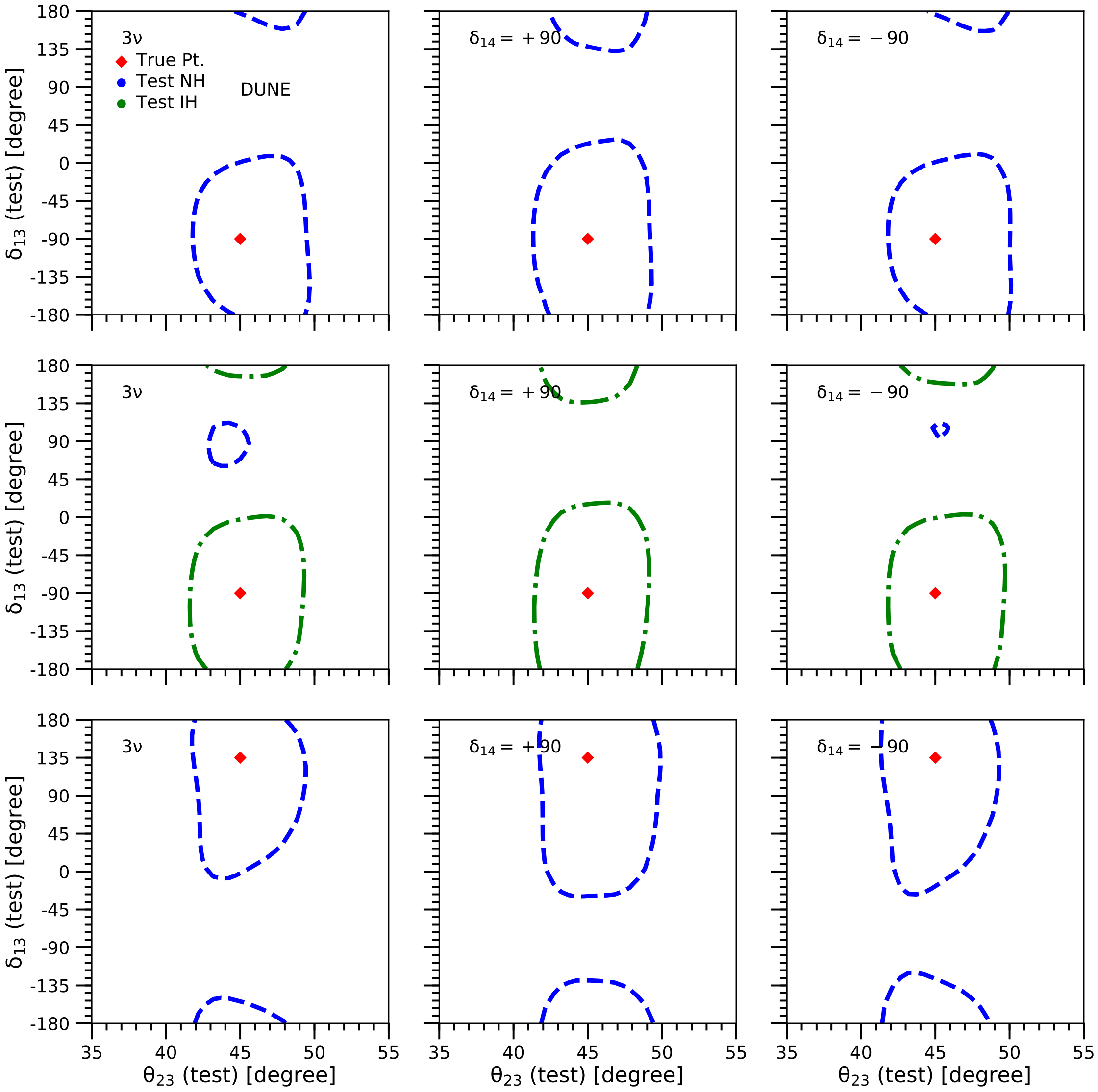

FIG. 6.15 Allowed region plots similar to 6.14 but for $\theta_{23} = 45^{\circ}$. Showing that even for only a $2 + \bar{2}$ run, DUNE has drastically better MH resolution than NOνA.

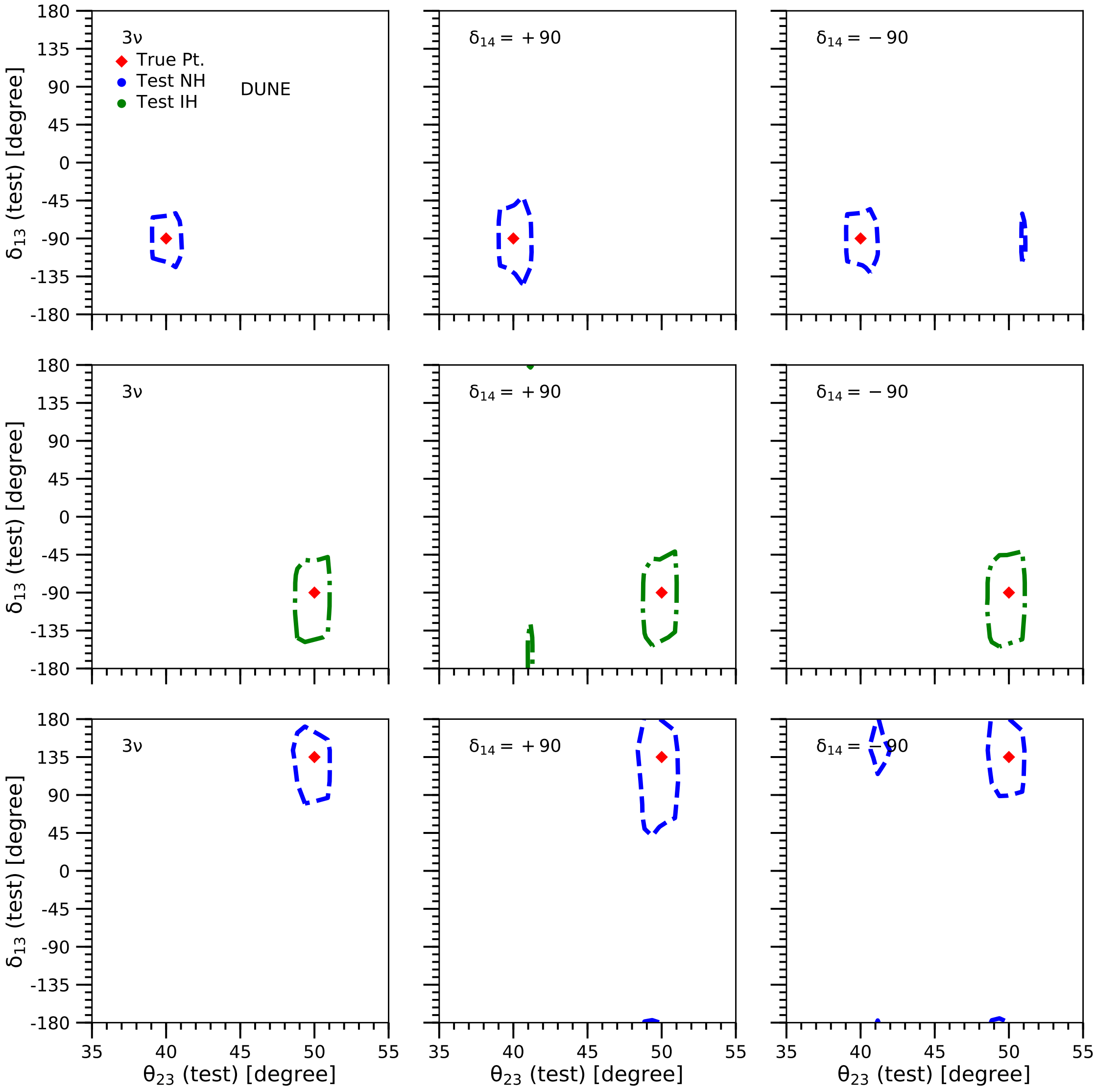

FIG. 6.16 Allowed region plots similar to figure 6.10 but for DUNE $\left(5+\bar{5}\right)$. Clearly showing that very few degenerate regions survive in the full DUNE run.

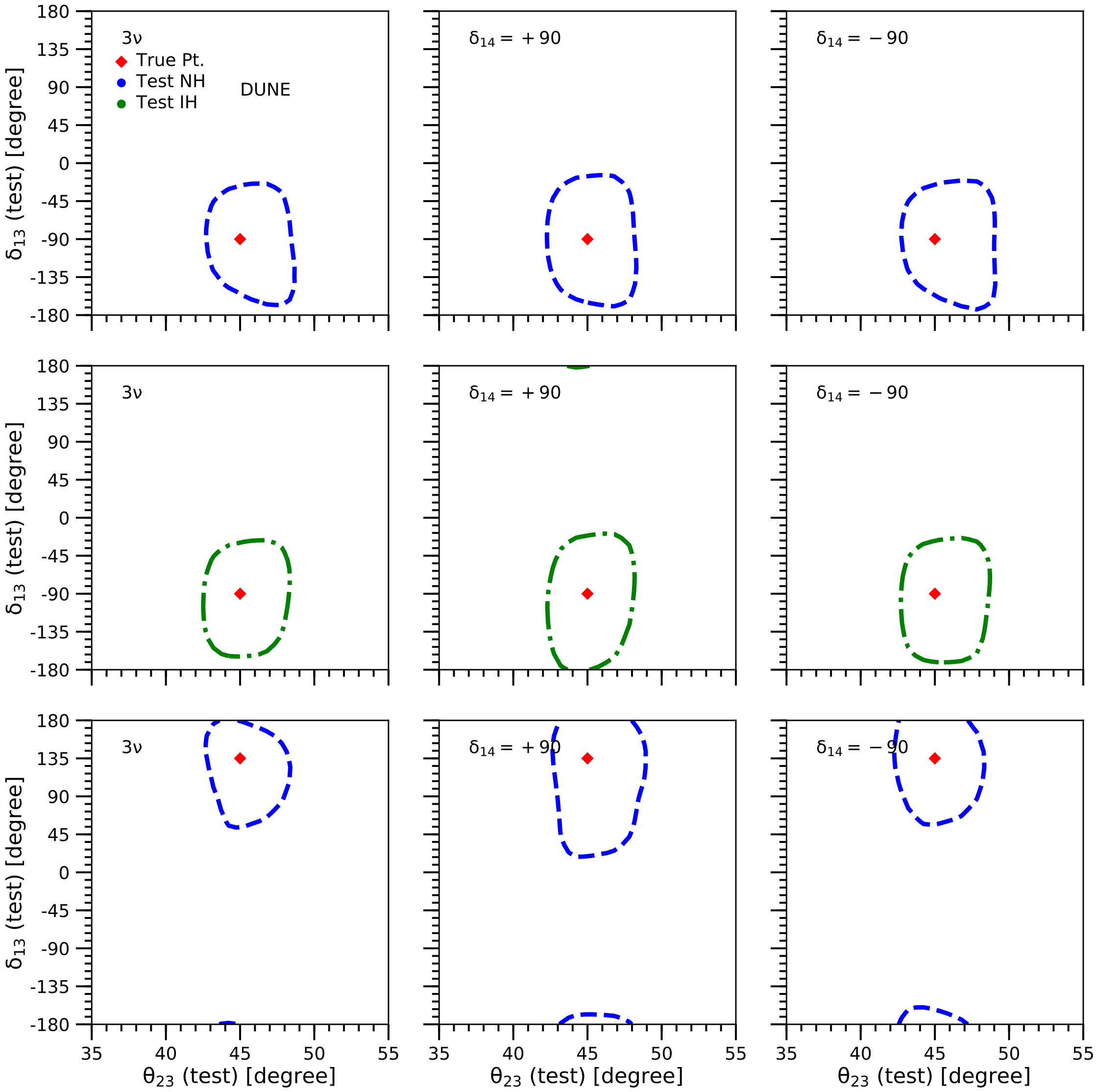

FIG. 6.17 Allowed region plots similar to figure 6.16 but for $\theta_{23} = 45°$. Clearly no degenerate regions are seen after the full DUNE rune if MM is the true θ_{23} mixing.

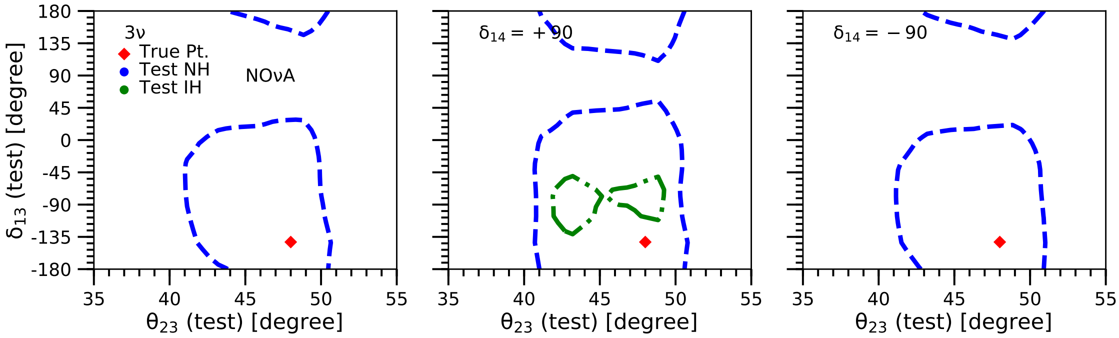

FIG. 6.18 Allowed regions for the new preliminary best fits for NOνA $\left(3+\bar{3}\right)$ with 4ν extension.

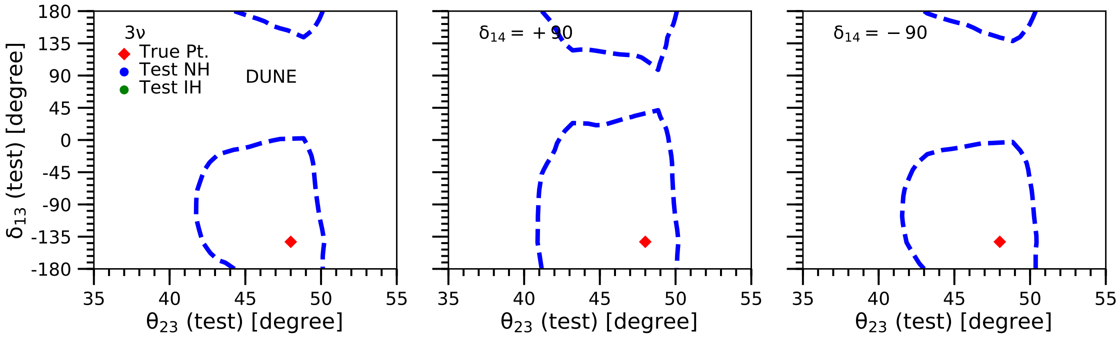

FIG. 6.19 Allowed regions for the new best fits same as figure 6.18 but for DUNE $\left(2+\bar{2}\right)$.

CHAPTER 7

SUMMARY, CONCLUSIONS AND OUTLOOK

During my PhD my focus has been on writing scripts for GLoBES calculations as well as contributing to or writing the associated analyses. At the beginning of study this involved installing and understanding the expanded $3 + N_s$ version of GLoBES. Once this was understood I adapted earlier work to such a formalism. This involved probability calculations as well as degenerate region and hierarchy exclusion hypothesis tests. The other focus of my work was to understand the more fundamental nature of neutrino oscillations and sterile neutrinos. This was communicated to my colleagues so that analyses could be proposed to explore the field in a phenomenological manner.

Once the motivation and application of the $3+1$ extension was well understood we performed the analysis from chapter 5. This used the code I developed for probability plots and test θ_{23}-Δ_{13} regions. In this analysis we found that the new phase δ_{14} in particular adds several degeneracies to the neutrino parameter space. The follow-up analysis presented in section 6 was primarily authored by me and covered revised fits from NOνA. This second analysis showed that DUNE has immense degeneracy resolution compared to NOνA even if a sterile neutrino is present. Additionally the possibility of maximal mixing leads to increased hierarchy resolution but less θ_{23} precision.

In this thesis I have attempted to provide an outline of neutrino physics, beginning with initial experiments and theories, up to possible extensions to the three active neutrino extended standard model. Hopefully it can be seen how the initial idea of ghostly neutral leptons invented to conserve energy and momentum, has led to this rich particle family with a plethora of interesting properties.

The major conclusion to be drawn from recent simulations and results for neutrinos is that we are poised to potentially solve most of the standard three neutrino degeneracies and to precisely measure all of the parameters. If we are fortunate we may only be left with the questions of additional mass eigenstates, sterile neutrinos and mass models by 2025 or so. However, depending on how convenient the mixing parameters turn out to be (not to mention potential non-standard interactions, see Appendix C) we could be battling with degeneracies for many years to come. This implies that the next generation DUNE and T2HK will perhaps at the very least reveal whether our neutrino situation is one of pessimism or optimism.

The matter of neutrino mass is likely to be a mystery for a while longer, especially given that cases involving heavy RH neutrinos are likely impossible to detect with standard methods. Nevertheless it is tempting to hold onto the hope that some all-encompassing model of RH neutrinos exists which would contain light mostly-steriles as well as heavy states to account for oscillation anomalies and light active masses simultaneously. Oscillation experiments are unlikely to help reveal the absolute mass scales of active neutrinos. But if somehow a method to determine the lightest mass can be found. The existence of such a method reduces the discovery of the absolute masses of ν_1, ν_2 and ν_3, to measuring the lightest state, determining the mass ordering and then simply performing precise measurements until uncertainties are low enough. Unfortunately this is pretty far-fetched and it is likely that double beta decay (see section 3.7) or direct kinematic decay experiments will shed some light on this eventually. The recently active KATRIN (Karlsruhe Tritium Neutrino Experiment) is of the latter type and uses tritium decay [205]. The KATRIN collaboration just released its first results which improved the upper limit of the neutrino mass scale to be ~ 1.1 eV [206]. Heavy RH neutrinos as dark matter candidates have been constrained somewhat but if they exist must likely contribute in some way. The mass ranges preferred by see-saw mass generation and dark matter candidates are different, so the discovery of a specific one of these doesn't necessarily solve the other.

As for sterile neutrinos themselves, we are still not likely to have a definite answer on their existence in the near future. Given the wide range of possible extra particles it can be hard to be certain whether any anomaly or phenomena is the result of sterile neutrinos or some other new physics phenomena. The inherent difficulties in carrying out precision neutrino experiments means that it is challenging to constrain their properties whether sterile or not. Light sterile neutrinos are promising candidates for oscillation anomalies but at the current time no strong conclusions can be made. For the future we need additional and more precise experiments to pin down the nature of the neutrino sector and any new physics that may be hiding there.

REFERENCES

[1] Monojit Ghosh, Shivani Gupta, Zachary M. Matthews, Pankaj Sharma, and Anthony G. Williams. Study of parameter degeneracy and hierarchy sensitivity of NOνA in presence of sterile neutrino. *Phys. Rev. D*, 96:075018, Oct 2017.

[2] Shivani Gupta, Zachary M. Matthews, Pankaj Sharma, and Anthony G. Williams. The Effect of a Light Sterile Neutrino at NOνA and DUNE. *Phys. Rev.*, D98(3):035042, 2018.

[3] Nobel Media AB. The Nobel Prize in Physics 1995. https://www.nobelprize.org/prizes/physics/1995/summary/.

[4] C. L. Cowan, F. Reines, F. B. Harrison, H. W. Kruse, and A. D. McGuire. Detection of the free neutrino: A Confirmation. *Science*, 124:103–104, 1956.

[5] John N. Bahcall. How the Sun Shines. https://www.nobelprize.org/prizes/themes/how-the-sun-shines-2.

[6] A. S. Eddington. The Internal Constitution of the Stars. *The Scientific Monthly*, 11(4):297–303, 1920.

[7] Aldo Serenelli. Alive and well: a short review about standard solar models. *Eur. Phys. J.*, A52(4):78, 2016.

[8] B. T. Cleveland, Timothy Daily, Raymond Davis, Jr., James R. Distel, Kenneth Lande, C. K. Lee, Paul S. Wildenhain, and Jack Ullman. Measurement of the solar electron neutrino flux with the Homestake chlorine detector. *Astrophys. J.*, 496:505–526, 1998.

[9] John N. Bahcall. *Neutrino Astrophysics*. Cambridge University Press, 1989.

[10] P. Anselmann et al. Solar neutrinos observed by GALLEX at Gran Sasso. *Phys. Lett.*, B285:376–389, 1992.

[11] V. N. Gavrin et al. First measurement of the integral solar neutrino flux by the Soviet-American Gallium Experiment (SAGE). In *High-energy physics. Proceedings, 25th International Conference, Singapore, August 2-8, 1990. Vol. I+II*, volume C900802V1, pages 693–697, 1990. [Conf. Proc.C900802V1,C900802V1:693(1990)].

[12] W. Hampel et al. GALLEX solar neutrino observations: Results for GALLEX IV. *Phys. Lett.*, B447:127–133, 1999.

[13] A. Yu. Smirnov. Solar neutrinos: Oscillations or No-oscillations? 2016.

[14] A. Y. Smirnov. The Mikheyev-Smirnov-Wolfenstein (MSW) Effect. In *International Conference on History of the Neutrino: 1930-2018 Paris, France, September 5-7, 2018*, 2019.

[15] Nobel Media AB. The Nobel Prize in Physics 2002. https://www.nobelprize.org/prizes/physics/2002/summary/.

[16] H. Ikeda et al. KAMIOKANDE: THE KAMIOKA NUCLEON DECAY EXPERIMENT. 1982.

[17] K. Hirata et al. Observation of a Neutrino Burst from the Supernova SN 1987a. *Phys. Rev. Lett.*, 58:1490–1493, 1987. [,727(1987)].

[18] Y. Oyama et al. A Search for High-energy Neutrinos From Sn1987a: First Six Months. *Phys. Rev. Lett.*, 59:2604, 1987.

[19] K. S. Hirata et al. Observation in the Kamiokande-II Detector of the Neutrino Burst from Supernova SN 1987a. *Phys. Rev.*, D38:448–458, 1988.

[20] M. Nakahata et al. Observation of solar neutrinos in KAMIOKANDE-II. In *In *Fujiyoshida 1988, Proceedings, Elementary-particle picture of the universe* 121-134.*, 1988.

[21] Evalyn Gates, Lawrence M. Krauss, and Martin J. White. Solar neutrino data and its implications. *Phys. Rev.*, D46:1263–1273, 1992.

[22] E. Akhmedov, P. Lipari, and Maurizio Lusignoli. Matter effects in atmospheric neutrino oscillations. *Phys. Lett.*, B300:128–136, 1993.

[23] T. Kajita, E. Kearns, and M. Shiozawa. Establishing atmospheric neutrino oscillations with Super-Kamiokande. *Nucl. Phys.*, B908:14–29, 2016.

[24] Y Fukuda, T Hayakawa, E Ichihara, K Inoue, K Ishihara, H Ishino, Y Itow, T Kajita, J Kameda, S Kasuga, et al. Evidence for oscillation of atmospheric neutrinos. *Physical Review Letters*, 81(8):1562, 1998.

[25] K.S. Hirata, T. Kajita, M. Koshiba, M. Nakahata, S. Ohara, Y. Oyama, N. Sato, A. Suzuki, M. Takita, Y. Totsuka, T. Kifune, T. Suda, K. Nakamura, K. Takahashi, T. Tanimori, K. Miyano, M. Yamada, E.W. Beier, L.R. Feldscher, E.D. Frank, W. Frati, S.B. Kim, A.K. Mann, F.M. Newcomer, R. Van Berg, W. Zhang, and B.G. Cortez. Experimental study of the atmospheric neutrino flux. *Physics Letters B*, 205(2):416 – 420, 1988.

[26] K.S. Hirata, K. Inoue, T. Ishida, T. Kajita, K. Kihara, M. Nakahata, K. Nakamura, S. Ohara, A. Sakai, N. Sato, Y. Suzuki, Y. Totsuka, Y. Yaginuma, M. Mori, Y. Oyama, A. Suzuki, K. Takahashi, M. Yamada, M. Koshiba, K. Nishijima, T. Kajimura, T. Suda, T. Tajima, K. Miyano, H. Miyata, H. Takei, Y. Fukuda, E. Kodera, Y. Nagashima, M. Takita, H. Yokoyama, K. Kaneyuki, Y. Takeuchi, T. Tanimori, E.W. Beier, E.D. Frank, W. Frati, S.B. Kim, A.K. Mann, F.M. Newcomer, R. Van Berg, and W. Zhang. Observation of a small atmospheric ν_μ/ν_e ratio in kamiokande. *Physics Letters B*, 280(1):146 – 152, 1992.

[27] D. Casper, R. Becker-Szendy, C. B. Bratton, D. R. Cady, R. Claus, S. T. Dye, W. Gajewski, M. Goldhaber, T. J. Haines, P. G. Halverson, T. W. Jones, D. Kielczewska, W. R. Kropp, J. G. Learned, J. M. LoSecco, C. McGrew, S. Matsuno, J. Matthews, M. S. Mudan, L. Price, F. Reines, J. Schultz, D. Sinclair, H. W. Sobel, J. L. Stone, L. R. Sulak, R. Svoboda, G. Thornton, and J. C. van der Velde. Measurement of atmospheric neutrino composition with the imb-3 detector. *Phys. Rev. Lett.*, 66:2561–2564, May 1991.

[28] M Koshiba. Observational neutrino astrophysics. *Physics Reports*, 220(5):229 – 381, 1992.

[29] D. Griffiths. *Introduction to elementary particles*. Wiley-VCH, 2008.

[30] S. Kasuga et al. A Study on the e / mu identification capability of a water Cherenkov detector and the atmospheric neutrino problem. *Phys. Lett.*, B374:238–242, 1996.

[31] S. Fukuda et al. Tau neutrinos favored over sterile neutrinos in atmospheric muon-neutrino oscillations. *Phys. Rev. Lett.*, 85:3999–4003, 2000.

[32] J. Hosaka et al. Solar neutrino measurements in super-Kamiokande-I. *Phys. Rev.*, D73:112001, 2006.

[33] K. Nishikawa. A Possible long baseline neutrino oscillation experiment using KEK PS and Super-Kamiokande. *Submitted to: J. Phys. Soc. Jap.*, 1992.

[34] M. H. Ahn et al. Measurement of Neutrino Oscillation by the K2K Experiment. *Phys. Rev.*, D74:072003, 2006.

[35] K. Abe et al. Hyper-Kamiokande Design Report. 2018.

[36] A. Bellerive, J. R. Klein, A. B. McDonald, A. J. Noble, and A. W. P. Poon. The Sudbury Neutrino Observatory. *Nucl. Phys.*, B908:30–51, 2016.

[37] P. C. de Holanda and A. Yu. Smirnov. Solar neutrinos: The SNO salt phase results and physics of conversion. *Astropart. Phys.*, 21:287–301, 2004.

[38] Q. R. Ahmad et al. Measurement of the rate of $\nu_e + d \to p + p + e^-$ interactions produced by ^8B solar neutrinos at the Sudbury Neutrino Observatory. *Phys. Rev. Lett.*, 87:071301, 2001.

[39] Nobel Media AB. The Nobel Prize in Physics 2015. https://www.nobelprize.org/prizes/physics/2015/summary/.

[40] K. Abe et al. The T2K Experiment. *Nucl. Instrum. Meth.*, A659:106–135, 2011.

[41] D. Beavis et al. Long Baseline Neutrino Oscillation Experiment at the AGS Approved by the HENPAC as AGS Experiment 889. 1995.

[42] Y. Itow et al. The JHF-Kamioka neutrino project. hep-ex/0106019, 2001.

[43] K. Abe et al. Measurements of the T2K neutrino beam properties using the INGRID on-axis near detector. *Nucl. Instrum. Meth.*, A694:211–223, 2012.

[44] K. Abe et al. Indication of Electron Neutrino Appearance from an Accelerator-produced Off-axis Muon Neutrino Beam. *Phys. Rev. Lett.*, 107:041801, 2011.

[45] E. Ables et al. P-875: A Long baseline neutrino oscillation experiment at Fermilab. 1995.

[46] P. Adamson et al. First observations of separated atmospheric nu(mu) and anti-nu(mu) events in the MINOS detector. *Phys. Rev.*, D73:072002, 2006.

[47] D. G. Michael et al. Observation of muon neutrino disappearance with the MINOS detectors and the NuMI neutrino beam. *Phys. Rev. Lett.*, 97:191801, 2006.

[48] P. Adamson et al. Combined analysis of ν_μ disappearance and $\nu_\mu \to \nu_e$ appearance in MINOS using accelerator and atmospheric neutrinos. *Phys. Rev. Lett.*, 112:191801, 2014.

[49] P. Adamson et al. Measurement of neutrino velocity with the MINOS detectors and NuMI neutrino beam. *Phys. Rev.*, D76:072005, 2007.

[50] M. Antonello. The ICARUS experiment and the neutrino velocity measurement. *Nucl. Phys. Proc. Suppl.*, 237-238:190–192, 2013.

[51] D.S. Ayres, G.R. Drake, M.C. Goodman, J.J. Grudzinski, V.J. Guarino, R.L. Talaga, A. Zhao, /Argonne, P. Stamoulis, E. Stiliaris, G. Tzanakos, and M. Zois. The NOvA Technical Design Report.

[52] D. S. Ayres et al. NOvA: Proposal to Build a 30 Kiloton Off-Axis Detector to Study $\nu_\mu \to \nu_e$ Oscillations in the NuMI Beamline. 2004.

[53] João A. B. Coelho. Status of NuMI experiments: MINOS+ and NOνA. *Nucl. Part. Phys. Proc.*, 260:178–181, 2015.

[54] F. P. An et al. Observation of electron-antineutrino disappearance at Daya Bay. *Phys. Rev. Lett.*, 108:171803, 2012.

[55] J. K. Ahn et al. Observation of Reactor Electron Antineutrino Disappearance in the RENO Experiment. *Phys. Rev. Lett.*, 108:191802, 2012.

[56] Y. Abe et al. Indication of Reactor $\bar{\nu}_e$ Disappearance in the Double Chooz Experiment. *Phys. Rev. Lett.*, 108:131801, 2012.

[57] P. Adamson et al. Improved search for muon-neutrino to electron-neutrino oscillations in MINOS. *Phys. Rev. Lett.*, 107:181802, 2011.

[58] P. Adamson et al. Measurement of the neutrino mixing angle θ_{23} in NOvA. *Phys. Rev. Lett.*, 118(15):151802, 2017.

[59] P. Adamson et al. Constraints on Oscillation Parameters from ν_e Appearance and ν_μ Disappearance in NOvA. *Phys. Rev. Lett.*, 118(23):231801, 2017.

[60] M. A. Acero et al. New constraints on oscillation parameters from ν_e appearance and ν_μ disappearance in the NOvA experiment. 2018.

[61] M. A. Acero et al. First measurement of neutrino oscillation parameters using neutrinos and antineutrinos by NOvA. 2019.

[62] R. Acciarri et al. Long-Baseline Neutrino Facility (LBNF) and Deep Underground Neutrino Experiment (DUNE). 2016.

[63] Jaret Heise. The Sanford Underground Research Facility. In *15th International Conference on Topics in Astroparticle and Underground Physics (TAUP 2017) Sudbury, Ontario, Canada, July 24-28, 2017*, 2017.

[64] B. Abi et al. The DUNE Far Detector Interim Design Report Volume 1: Physics, Technology and Strategies. 2018.

[65] André de Gouvêa, Kevin J. Kelly, G. V. Stenico, and Pedro Pasquini. Physics with Beam Tau-Neutrino Appearance at DUNE. 2019.

[66] Anish Ghoshal, Alessio Giarnetti, and Davide Meloni. On the Role of the ν_τ Appearance in DUNE in Constraining Standard Neutrino Physics and Beyond. 2019.

[67] N. Agafonova et al. Observation of a first ν_τ candidate in the OPERA experiment in the CNGS beam. *Phys. Lett.*, B691:138–145, 2010.

[68] N. Agafonova et al. Final Results of the OPERA Experiment on ν_τ Appearance in the CNGS Neutrino Beam. *Phys. Rev. Lett.*, 120(21):211801, 2018. [Erratum: Phys. Rev. Lett.121,no.13,139901(2018)].

[69] T. Adam et al. Measurement of the neutrino velocity with the OPERA detector in the CNGS beam. *JHEP*, 10:093, 2012.

[70] N. Yu. Agafonova et al. Determination of a time-shift in the OPERA set-up using high energy horizontal muons in the LVD and OPERA detectors. *Eur. Phys. J. Plus*, 127:71, 2012.

[71] Xinheng Guo et al. A Precision measurement of the neutrino mixing angle θ_{13} using reactor antineutrinos at Daya-Bay. 2007.

[72] J. K. Ahn et al. RENO: An Experiment for Neutrino Oscillation Parameter θ_{13} Using Reactor Neutrinos at Yonggwang. 2010.

[73] F. Ardellier et al. Letter of intent for Double-CHOOZ: A Search for the mixing angle theta(13). 2004.

[74] Xin Qian and Jen-Chieh Peng. Physics with Reactor Neutrinos. *Rept. Prog. Phys.*, 82(3):036201, 2019.

[75] G. L. Fogli, E. Lisi, A. Marrone, A. Palazzo, and A. M. Rotunno. Hints of $\theta_{13} > 0$ from global neutrino data analysis. *Phys. Rev. Lett.*, 101:141801, 2008.

[76] Michele Maltoni and Thomas Schwetz. Three-flavour neutrino oscillation update and comments on possible hints for a non-zero θ_{13}. *PoS*, IDM2008:072, 2008.

[77] P. A. N. Machado, H. Minakata, H. Nunokawa, and R. Zukanovich Funchal. Combining Accelerator and Reactor Measurements of θ_{13}: The First Result. *JHEP*, 05:023, 2012.

[78] G. L. Fogli, E. Lisi, A. Marrone, D. Montanino, A. Palazzo, and A. M. Rotunno. Global analysis of neutrino masses, mixings and phases: entering the era of leptonic CP violation searches. *Phys. Rev.*, D86:013012, 2012.

[79] Michael Wurm. Solar Neutrino Spectroscopy. *Phys. Rept.*, 685:1–52, 2017.

[80] E. Richard et al. Measurements of the atmospheric neutrino flux by Super-Kamiokande: energy spectra, geomagnetic effects, and solar modulation. *Phys. Rev.*, D94(5):052001, 2016.

[81] Abhijit Samanta. The Mass hierarchy with atmospheric neutrinos at INO. *Phys. Lett.*, B673:37–46, 2009.

[82] Laurie M. Brown. The idea of the neutrino. *Phys. Today*, 31N9:23–28, 1978.

[83] Nobel Media AB. The Nobel Prize in Physics 1988. https://www.nobelprize.org/prizes/physics/1988/summary/.

[84] Marco Drewes. The Phenomenology of Right Handed Neutrinos. *Int. J. Mod. Phys.*, E22:1330019, 2013.

[85] S. Gariazzo, C. Giunti, M. Laveder, Y. F. Li, and E. M. Zavanin. Light sterile neutrinos. *J. Phys.*, G43:033001, 2016.

[86] Dmitry V. Naumov. The Sterile Neutrino: A short introduction. *EPJ Web Conf.*, 207:04004, 2019.

[87] A. Diaz, C. A. Argüelles, G. H. Collin, J. M. Conrad, and M. H. Shaevitz. Where Are We With Light Sterile Neutrinos? 2019.

[88] M. Tanabashi, K. Hagiwara, K. Hikasa, K. Nakamura, Y. Sumino, F. Takahashi, J. Tanaka, K. Agashe, G. Aielli, C. Amsler, M. Antonelli, D. M. Asner, H. Baer, Sw. Banerjee, R. M. Barnett, T. Basaglia, C. W. Bauer, J. J. Beatty, V. I. Belousov, J. Beringer, S. Bethke, A. Bettini, H. Bichsel, O. Biebel, K. M. Black, E. Blucher, O. Buchmuller, V. Burkert, M. A. Bychkov, R. N. Cahn, M. Carena, A. Ceccucci, A. Cerri, D. Chakraborty, M.-C. Chen, R. S. Chivukula, G. Cowan, O. Dahl, G. D'Ambrosio, T. Damour, D. de Florian, A. de Gouvêa, T. DeGrand, P. de Jong, G. Dissertori, B. A. Dobrescu, M. D'Onofrio, M. Doser, M. Drees, H. K. Dreiner, D. A. Dwyer, P. Eerola, S. Eidelman, J. Ellis, J. Erler, V. V. Ezhela, W. Fetscher, B. D. Fields, R. Firestone, B. Foster, A. Freitas, H. Gallagher, L. Garren, H.-J. Gerber, G. Gerbier, T. Gershon, Y. Gershtein, T. Gherghetta, A. A. Godizov, M. Goodman, C. Grab, A. V. Gritsan, C. Grojean, D. E. Groom, M. Grünewald, A. Gurtu, T. Gutsche, H. E. Haber, C. Hanhart, S. Hashimoto, Y. Hayato, K. G. Hayes, A. Hebecker, S. Heinemeyer, B. Heltsley, J. J. Hernández-Rey, J. Hisano, A. Höcker, J. Holder, A. Holtkamp, T. Hyodo, K. D. Irwin, K. F. Johnson, M. Kado, M. Karliner, U. F. Katz, S. R. Klein, E. Klempt, R. V. Kowalewski, F. Krauss, M. Kreps, B. Krusche, Yu. V. Kuyanov, Y. Kwon, O. Lahav,

J. Laiho, J. Lesgourgues, A. Liddle, Z. Ligeti, C.-J. Lin, C. Lippmann, T. M. Liss, L. Littenberg, K. S. Lugovsky, S. B. Lugovsky, A. Lusiani, Y. Makida, F. Maltoni, T. Mannel, A. V. Manohar, W. J. Marciano, A. D. Martin, A. Masoni, J. Matthews, U.-G. Meißner, D. Milstead, R. E. Mitchell, K. Mönig, P. Molaro, F. Moortgat, M. Moskovic, H. Murayama, M. Narain, P. Nason, S. Navas, M. Neubert, P. Nevski, Y. Nir, K. A. Olive, S. Pagan Griso, J. Parsons, C. Patrignani, J. A. Peacock, M. Pennington, S. T. Petcov, V. A. Petrov, E. Pianori, A. Piepke, A. Pomarol, A. Quadt, J. Rademacker, G. Raffelt, B. N. Ratcliff, P. Richardson, A. Ringwald, S. Roesler, S. Rolli, A. Romaniouk, L. J. Rosenberg, J. L. Rosner, G. Rybka, R. A. Ryutin, C. T. Sachrajda, Y. Sakai, G. P. Salam, S. Sarkar, F. Sauli, O. Schneider, K. Scholberg, A. J. Schwartz, D. Scott, V. Sharma, S. R. Sharpe, T. Shutt, M. Silari, T. Sjöstrand, P. Skands, T. Skwarnicki, J. G. Smith, G. F. Smoot, S. Spanier, H. Spieler, C. Spiering, A. Stahl, S. L. Stone, T. Sumiyoshi, M. J. Syphers, K. Terashi, J. Terning, U. Thoma, R. S. Thorne, L. Tiator, M. Titov, N. P. Tkachenko, N. A. Törnqvist, D. R. Tovey, G. Valencia, R. Van de Water, N. Varelas, G. Venanzoni, L. Verde, M. G. Vincter, P. Vogel, A. Vogt, S. P. Wakely, W. Walkowiak, C. W. Walter, D. Wands, D. R. Ward, M. O. Wascko, G. Weiglein, D. H. Weinberg, E. J. Weinberg, M. White, L. R. Wiencke, S. Willocq, C. G. Wohl, J. Womersley, C. L. Woody, R. L. Workman, W.-M. Yao, G. P. Zeller, O. V. Zenin, R.-Y. Zhu, S.-L. Zhu, F. Zimmermann, P. A. Zyla, J. Anderson, L. Fuller, V. S. Lugovsky, and P. Schaffner. Review of particle physics. *Phys. Rev. D*, 98:030001, Aug 2018.

[89] Ivan Esteban, M. C. Gonzalez-Garcia, Alvaro Hernandez-Cabezudo, Michele Maltoni, and Thomas Schwetz. Global analysis of three-flavour neutrino oscillations: synergies and tensions in the determination of θ_23, δ_CP, and the mass ordering. *JHEP*, 01:106, 2019.

[90] C. Jarlskog. Commutator of the quark mass matrices in the standard electroweak model and a measure of maximal CP nonconservation. *Phys. Rev. Lett.*, 55:1039–1042, Sep 1985.

[91] M. Tanabashi et al. Review of Particle Physics. *Phys. Rev.*, D98(3):030001, 2018.

[92] Stephen F King. Discrete symmetries and models of flavour mixing. *Journal of Physics: Conference Series*, 631:012005, 07 2015.

[93] Boris Kayser. On the Quantum Mechanics of Neutrino Oscillation. *Phys. Rev.*, D24:110, 1981.

[94] Evgeny Akhmedov. Do non-relativistic neutrinos oscillate? *JHEP*, 07:070, 2017.

[95] Evgeny Kh. Akhmedov and Joachim Kopp. Neutrino oscillations: Quantum mechanics vs. quantum field theory. *JHEP*, 04:008, 2010. [Erratum: JHEP10,052(2013)].

[96] I Alekseev et al. Search for sterile neutrinos at the DANSS experiment. *Phys. Lett.*, B787:56–63, 2018.

[97] Luis Manzanillas. Status of the SoLid experiment: Search for sterile neutrinos at the SCK·CEN BR2 reactor. 2017.

[98] L. Wolfenstein. Neutrino oscillations in matter. *Phys. Rev. D*, 17:2369–2374, May 1978.

[99] S. P. Mikheev and A. Yu. Smirnov. Resonance enhancement of oscillations in matter and solar neutrino spectroscopy. *Soviet Journal of Nuclear Physics*, 1985.

[100] A. Yu. Smirnov. The MSW effect and matter effects in neutrino oscillations. *Phys. Scripta*, T121:57–64, 2005.

[101] J. Linder. Derivation of neutrino matter potentials induced by earth. *Submitted to: Am. J. Phys.*, 2005.

[102] Stefania Ricciardi. Lecture Notes on Neutrino oscillations in matter, 2013. http://hepwww.rl.ac.uk/ricciardi/Lectures/MSW-1.pdf.

[103] A. Yu. Smirnov. The MSW effect and solar neutrinos. In *Neutrino telescopes. Proceedings, 10th International Workshop, Venice, Italy, March 11-14, 2003. Vol. 1+2*, volume hep-ph/0305106, pages 23–43, 2003.

[104] S. P. Mikheev and A. Yu. Smirnov. Neutrino oscillations in a medium with variable density. *Sov. Phys. Usp.*, 29:1155–1157, 1986.

[105] S. P. Mikheev and A. Yu. Smirnov. Resonant amplification of neutrino oscillations in matter and solar neutrino spectroscopy. *Nuovo Cim.*, C9:17–26, 1986.

[106] S. Schael et al. Precision electroweak measurements on the Z resonance. *Phys. Rept.*, 427:257–454, 2006.

[107] Patrick Huber. On the determination of anti-neutrino spectra from nuclear reactors. *Phys. Rev.*, C84:024617, 2011. [Erratum: Phys. Rev.C85,029901(2012)].

[108] G. Mention, M. Fechner, Th. Lasserre, Th. A. Mueller, D. Lhuillier, M. Cribier, and A. Letourneau. Reactor antineutrino anomaly. *Phys. Rev. D*, 83:073006, Apr 2011.

[109] A. C. Hayes, J. L. Friar, G. T. Garvey, Gerard Jungman, and G. Jonkmans. Systematic uncertainties in the analysis of the reactor neutrino anomaly. *Phys. Rev. Lett.*, 112:202501, May 2014.

[110] John N. Bahcall. Gallium solar neutrino experiments: Absorption cross-sections, neutrino spectra, and predicted event rates. *Phys. Rev.*, C56:3391–3409, 1997.

[111] Carlo Giunti and Marco Laveder. Statistical significance of the gallium anomaly. *Phys. Rev. C*, 83:065504, Jun 2011.

[112] Joel Kostensalo, Jouni Suhonen, Carlo Giunti, and Praveen C. Srivastava. The gallium anomaly revisited. 2019.

[113] A. Aguilar-Arevalo et al. Evidence for neutrino oscillations from the observation of anti-neutrino(electron) appearance in a anti-neutrino(muon) beam. *Phys. Rev.*, D64:112007, 2001.

[114] Klaus Eitel. Compatibility analysis of the LSND evidence and the KARMEN exclusion for $\bar{\nu}_\mu \rightarrow \bar{\nu}_e$ oscillations. *New Journal of Physics*, 2:1–1, Jan 2000.

[115] Pedro AN Machado, Ornella Palamara, and David W Schmitz. The Short-Baseline Neutrino Program at Fermilab. 2019.

[116] Carlo Giunti and T. Lasserre. eV-scale Sterile Neutrinos. 2019.

[117] Manuel Drees and Fazlollah Hajkarim. Neutralino Dark Matter in Scenarios with Early Matter Domination. *JHEP*, 12:042, 2018.

[118] Xiangxiang Ren et al. Constraining Dark Matter Models with a Light Mediator at the PandaX-II Experiment. *Phys. Rev. Lett.*, 121(2):021304, 2018.

[119] Juan Herrero-Garcia, Andre Scaffidi, Martin White, and Anthony G. Williams. On the direct detection of multi-component dark matter: implications of the relic abundance. *JCAP*, 1901(01):008, 2019.

[120] A. Boyarsky, M. Drewes, T. Lasserre, S. Mertens, and O. Ruchayskiy. Sterile Neutrino Dark Matter. *Prog. Part. Nucl. Phys.*, 104:1–45, 2019.

[121] N. Klop and A. Palazzo. Imprints of c p violation induced by sterile neutrinos in t2k data. *Physical Review D*, 91(7), apr 2015.

[122] Katsuhiro Asano and Hisakazu Minakata. Large-Theta(13) Perturbation Theory of Neutrino Oscillation for Long-Baseline Experiments. *JHEP*, 06:022, 2011.

[123] Hiroshi Nunokawa, Stephen J. Parke, and Renata Zukanovich Funchal. Another possible way to determine the neutrino mass hierarchy. *Phys. Rev.*, D72:013009, 2005.

[124] Michele Maltoni and Thomas Schwetz. Sterile neutrino oscillations after first MiniBooNE results. *Phys. Rev.*, D76:093005, 2007.

[125] Carlo Giunti and Marco Laveder. 3+1 and 3+2 Sterile Neutrino Fits. *Phys. Rev.*, D84:073008, 2011.

[126] A. Donini, P. Hernandez, J. Lopez-Pavon, M. Maltoni, and T. Schwetz. The minimal 3+2 neutrino model versus oscillation anomalies. *JHEP*, 07:161, 2012.

[127] Eric Kuflik, Samuel D. McDermott, and Kathryn M. Zurek. Neutrino Phenomenology in a 3+1+1 Framework. *Phys. Rev.*, D86:033015, 2012.

[128] Jinrui Huang and Ann E Nelson. MeV dark matter in the 3+1+1 model. *Phys. Rev.*, D88:033016, 2013.

[129] C. Giunti and E. M. Zavanin. Appearance–disappearance relation in $3 + N_s$ short-baseline neutrino oscillations. *Mod. Phys. Lett.*, A31(01):1650003, 2015.

[130] Y. H. Ahn and Sin Kyu Kang. A Model of Neutrino Anomalies and IceCube data. 2019.

[131] Lincoln Wolfenstein. Different Varieties of Massive Dirac Neutrinos. *Nucl. Phys.*, B186:147–152, 1981.

[132] Stefano Dell'Oro, Simone Marcocci, Matteo Viel, and Francesco Vissani. Neutrinoless double beta decay: 2015 review. *Adv. High Energy Phys.*, 2016:2162659, 2016.

[133] S. F. King. Neutrino mass models. *Rept. Prog. Phys.*, 67:107–158, 2004.

[134] André de Gouvêa. Neutrino mass models. *Annual Review of Nuclear and Particle Science*, 66(1):197–217, 2016.

[135] A. S. Barabash. Average and recommended half-life values for two neutrino double beta decay. *Nucl. Phys.*, A935:52–64, 2015.

[136] R. Arnold, C. Augier, J. Baker, A. Barabash, G. Broudin, V. Brudanin, A. J. Caffrey, E. Caurier, V. Egorov, K. Errahmane, A. I. Etienvre, J. L. Guyonnet, F. Hubert, Ph. Hubert, C. Jollet, S. Jullian, O. Kochetov, V. Kovalenko, S. Konovalov, D. Lalanne, F. Leccia, C. Longuemare, G. Lutter, Ch. Marquet, F. Mauger, F. Nowacki, H. Ohsumi, F. Piquemal, J. L. Reyss, R. Saakyan, X. Sarazin, L. Simard, F. Šimkovic, Yu. Shitov, A. Smolnikov, L. Štekl, J. Suhonen, C. S. Sutton, G. Szklarz, J. Thomas, V. Timkin, V. Tretyak, V. Umatov, L. Vála, I. Vanushin, V. Vasilyev, V. Vorobel, and Ts. Vylov. First results of the search for neutrinoless double-beta decay with the nemo 3 detector. *Phys. Rev. Lett.*, 95:182302, Oct 2005.

[137] R. Arnold et al. Probing New Physics Models of Neutrinoless Double Beta Decay with SuperNEMO. *Eur. Phys. J.*, C70:927–943, 2010.

[138] L. Cardani. Neutrinoless Double Beta Decay Overview. *SciPost Phys. Proc.*, 1:024, 2019.

[139] M. Goeppert-Mayer. Double beta-disintegration. *Phys. Rev.*, 48:512–516, 1935.

[140] W. H. Furry. On transition probabilities in double beta-disintegration. *Phys. Rev.*, 56:1184–1193, 1939.

[141] Petr Vogel. Neutrinoless double beta decay. In *Proceedings of Theoretical Advanced Study Institute in Elementary Particle Physics : Exploring New Frontiers Using Colliders and Neutrinos (TASI 2006): Boulder, Colorado, June 4-30, 2006*, pages 577–608, 2006.

[142] Manimala Mitra, Goran Senjanović, and Francesco Vissani. Neutrinoless double beta decay and heavy sterile neutrinos. *Nuclear Physics B*, 856(1):26 – 73, 2012.

[143] Manfred Lindner Patrick Huber, Joachim Kopp and Walter Winter. Globes documentation. https://www.mpi-hd.mpg.de/personalhomes/globes/documentation.html.

[144] Hisakazu Minakata and Hiroshi Nunokawa. Exploring neutrino mixing with low-energy superbeams. *JHEP*, 10:001, 2001.

[145] V. Barger, D. Marfatia, and K. Whisnant. Breaking eightfold degeneracies in neutrino CP violation, mixing, and mass hierarchy. *Phys. Rev. D*, 65:073023, Mar 2002.

[146] Sushant K. Raut. Effect of non-zero theta(13) on the measurement of theta(23). *Mod. Phys. Lett.*, A28:1350093, 2013.

[147] Sanjib Kumar Agarwalla, Suprabh Prakash, and S. Uma Sankar. Resolving the octant of theta23 with T2K and NOvA. *JHEP*, 07:131, 2013.

[148] K Nakamura and. Review of particle physics. *Journal of Physics G: Nuclear and Particle Physics*, 37(7A):075021, jul 2010.

[149] G. H. Collin, C. A. Argüelles, J. M. Conrad, and M. H. Shaevitz. First Constraints on the Complete Neutrino Mixing Matrix with a Sterile Neutrino. *Phys. Rev. Lett.*, 117(22):221801, 2016.

[150] Mona Dentler, Álvaro Hernández-Cabezudo, Joachim Kopp, Pedro A. N. Machado, Michele Maltoni, Ivan Martinez-Soler, and Thomas Schwetz. Updated Global Analysis of Neutrino Oscillations in the Presence of eV-Scale Sterile Neutrinos. *JHEP*, 08:010, 2018.

[151] H. Nunokawa, O. L. G. Peres, and R. Zukanovich Funchal. Probing the LSND mass scale and four neutrino scenarios with a neutrino telescope. *Phys. Lett.*, B562:279–290, 2003.

[152] M. G. Aartsen et al. Searches for Sterile Neutrinos with the IceCube Detector. *Phys. Rev. Lett.*, 117(7):071801, 2016.

[153] M. G. Aartsen et al. Search for sterile neutrino mixing using three years of IceCube DeepCore data. *Phys. Rev.*, D95(11):112002, 2017.

[154] Sarah Bridle, Jack Elvin-Poole, Justin Evans, Susana Fernandez, Pawel Guzowski, and Stefan Soldner-Rembold. A Combined View of Sterile-Neutrino Constraints from CMB and Neutrino Oscillation Measurements. *Phys. Lett.*, B764:322–327, 2017.

[155] F. P. An et al. Evolution of the Reactor Antineutrino Flux and Spectrum at Daya Bay. *Phys. Rev. Lett.*, 118(25):251801, 2017.

[156] K. Abe et al. First combined analysis of neutrino and antineutrino oscillations at T2K. 2017.

[157] Suprabh Prakash, Sushant K. Raut, and S. Uma Sankar. Getting the Best Out of T2K and NOvA. *Phys. Rev.*, D86:033012, 2012.

[158] Monojit Ghosh, Srubabati Goswami, and Sushant K. Raut. Implications of $\delta_{CP} = -90^\circ$ towards determining hierarchy and octant at T2K and T2K-II. *Mod. Phys. Lett.*, A32(06):1750034, 2017.

[159] Monojit Ghosh. Reason for T2K to run in dominant neutrino mode for detecting CP violation. *Phys. Rev.*, D93(7):073003, 2016.

[160] P. Adamson et al. Search for active-sterile neutrino mixing using neutral-current interactions in NOvA. *Phys. Rev.*, D96(7):072006, 2017.

[161] A. A. Aguilar-Arevalo et al. Observation of a Significant Excess of Electron-Like Events in the MiniBooNE Short-Baseline Neutrino Experiment. 2018.

[162] David Hollander and Irina Mocioiu. Minimal 3+2 sterile neutrino model at LBNE. *Phys. Rev.*, D91(1):013002, 2015.

[163] Sanjib Kumar Agarwalla, Sabya Sachi Chatterjee, Arnab Dasgupta, and Antonio Palazzo. Discovery Potential of T2K and NOvA in the Presence of a Light Sterile Neutrino. *JHEP*, 02:111, 2016.

[164] Sanjib Kumar Agarwalla, Sabya Sachi Chatterjee, and Antonio Palazzo. Physics Reach of DUNE with a Light Sterile Neutrino. *JHEP*, 09:016, 2016.

[165] Sanjib Kumar Agarwalla, Sabya Sachi Chatterjee, and Antonio Palazzo. Octant of θ_{23} in danger with a light sterile neutrino. *Phys. Rev. Lett.*, 118(3):031804, 2017.

[166] Antonio Palazzo. 3-flavor and 4-flavor implications of the latest T2K and NOνA electron (anti-)neutrino appearance results. *Phys. Lett.*, B757:142–147, 2016.

[167] Raj Gandhi, Boris Kayser, Mehedi Masud, and Suprabh Prakash. The impact of sterile neutrinos on CP measurements at long baselines. *JHEP*, 11:039, 2015.

[168] Debajyoti Dutta, Raj Gandhi, Boris Kayser, Mehedi Masud, and Suprabh Prakash. Capabilities of long-baseline experiments in the presence of a sterile neutrino. *JHEP*, 11:122, 2016.

[169] Bhubanjyoti Bhattacharya, Arun M. Thalapillil, and Carlos E. M. Wagner. Implications of sterile neutrinos for medium/long-baseline neutrino experiments and the determination of θ_{13}. *Phys. Rev.*, D85:073004, 2012.

[170] Jeffrey M. Berryman, André de Gouvêa, Kevin J. Kelly, and Andrew Kobach. Sterile neutrino at the Deep Underground Neutrino Experiment. *Phys. Rev.*, D92(7):073012, 2015.

[171] Kevin J. Kelly. Searches for new physics at the Hyper-Kamiokande experiment. *Phys. Rev.*, D95(11):115009, 2017.

[172] P. Adamson et al. Active to sterile neutrino mixing limits from neutral-current interactions in MINOS. *Phys. Rev. Lett.*, 107:011802, 2011.

[173] K. N. Abazajian et al. Light Sterile Neutrinos: A White Paper. 2012.

[174] Antonio Palazzo. Phenomenology of light sterile neutrinos: a brief review. *Mod. Phys. Lett.*, A28:1330004, 2013.

[175] Thierry Lasserre. Light Sterile Neutrinos in Particle Physics: Experimental Status. *Phys. Dark Univ.*, 4:81–85, 2014.

[176] F. P. An et al. Search for a Light Sterile Neutrino at Daya Bay. *Phys. Rev. Lett.*, 113:141802, 2014.

[177] P. A. R. Ade et al. Planck 2015 results. XIII. Cosmological parameters. *Astron. Astrophys.*, 594:A13, 2016.

[178] Feng Peng An et al. Improved Search for a Light Sterile Neutrino with the Full Configuration of the Daya Bay Experiment. *Phys. Rev. Lett.*, 117(15):151802, 2016.

[179] Sandhya Choubey and Dipyaman Pramanik. Constraints on Sterile Neutrino Oscillations using DUNE Near Detector. *Phys. Lett.*, B764:135–141, 2017.

[180] Joachim Kopp, Pedro A. N. Machado, Michele Maltoni, and Thomas Schwetz. Sterile Neutrino Oscillations: The Global Picture. *JHEP*, 05:050, 2013.

[181] Y. J. Ko et al. Sterile Neutrino Search at the NEOS Experiment. *Phys. Rev. Lett.*, 118(12):121802, 2017.

[182] Sanjib Kumar Agarwalla, Suprabh Prakash, Sushant K. Raut, and S. Uma Sankar. Potential of optimized NOvA for large $\theta_(13)$ & combined performance with a LArTPC & T2K. *JHEP*, 12:075, 2012.

[183] Patrick Huber, M. Lindner, and W. Winter. Simulation of long-baseline neutrino oscillation experiments with GLoBES (General Long Baseline Experiment Simulator). *Comput. Phys. Commun.*, 167:195, 2005.

[184] Patrick Huber, Joachim Kopp, Manfred Lindner, Mark Rolinec, and Walter Winter. New features in the simulation of neutrino oscillation experiments with GLoBES 3.0: General Long Baseline Experiment Simulator. *Comput. Phys. Commun.*, 177:432–438, 2007.

[185] Patrick Huber, Joachim Kopp, Manfred Lindner, Mark Rolinec, and Walter Winter. GLoBES: General Long Baseline Experiment Simulator. *Computer Physics Communications*, 177(5):439 – 440, 2007.

[186] P Huber, M Lindner, T Schwetz, and W Winter. First hint for CP violation in neutrino oscillations from upcoming superbeam and reactor experiments. *arXiv*, hep-ph/0907.1896, 2009.

[187] D. V. Forero, M. Tortola, and J. W. F. Valle. Neutrino oscillations refitted. *Phys. Rev.*, D90(9):093006, 2014.

[188] Ivan Esteban, M. C. Gonzalez-Garcia, Michele Maltoni, Ivan Martinez-Soler, and Thomas Schwetz. Updated fit to three neutrino mixing: exploring the accelerator-reactor complementarity. *JHEP*, 01:087, 2017.

[189] F. Capozzi, G. L. Fogli, E. Lisi, A. Marrone, D. Montanino, and A. Palazzo. Status of three-neutrino oscillation parameters, circa 2013. *Phys. Rev.*, D89:093018, 2014.

[190] C. Giunti, M. Laveder, Y. F. Li, and H. W. Long. Pragmatic View of Short-Baseline Neutrino Oscillations. *Phys. Rev.*, D88:073008, 2013.

[191] S. Gariazzo, C. Giunti, M. Laveder, and Y. F. Li. Updated Global 3+1 Analysis of Short-BaseLine Neutrino Oscillations. *JHEP*, 06:135, 2017.

[192] Mona Dentler, Álvaro Hernández-Cabezudo, Joachim Kopp, Pedro A. N. Machado, Michele Maltoni, Ivan Martinez-Soler, and Thomas Schwetz. Updated global analysis of neutrino oscillations in the presence of eV-scale sterile neutrinos. 2018.

[193] H. L. H. Wong. Search for a Light Sterile Neutrino at Daya Bay. *J. Phys. Conf. Ser.*, 888(1):012130, 2017.

[194] Rahul Srivastava, Christoph A. Ternes, Mariam Tórtola, and José W. F. Valle. Zooming in on neutrino oscillations with DUNE. 2018.

[195] Srubabati Goswami and Newton Nath. Implications of the latest NOνA results. 2017.

[196] P. Adamson et al. First measurement of muon-neutrino disappearance in NOvA. *Phys. Rev.*, D93(5):051104, 2016.

[197] R. Acciarri et al. Long-Baseline Neutrino Facility (LBNF) and Deep Underground Neutrino Experiment (DUNE). 2015.

[198] Monojit Ghosh, Srubabati Goswami, and Sushant K. Raut. Economizing the LBNE configuration with current experiments. *arXiv*, hep-ph/1412.1744, 2014.

[199] K. Abe et al. Letter of Intent: The Hyper-Kamiokande Experiment - Detector Design and Physics Potential. 2011.

[200] K. Abe et al. Physics Potentials with the Second Hyper-Kamiokande Detector in Korea. 2016.

[201] Sandhya Choubey, Debajyoti Dutta, and Dipyaman Pramanik. Imprints of a light Sterile Neutrino at DUNE, T2HK and T2HKK. *Phys. Rev.*, D96(5):056026, 2017.

[202] Sandhya Choubey, Debajyoti Dutta, and Dipyaman Pramanik. Measuring the Sterile Neutrino CP Phase at DUNE and T2HK. 2017.

[203] Alexander Radovic. Results from nova. In *Fermilab Joint Experimental-Theoretical Physics Seminar, January 12, 2018*, Wilson Hall, Fermilab, Illinois. http://theory.fnal.gov/events/event/results-from-nova/.

[204] Alex Himmel for the NOvA Collaboration. New oscillation measurements from nova. In *Presented at a CERN Particle Physics Seminar January 30, 2018*, 222-R-001, CERN, Geneva. https://indico.cern.ch/event/696410/attachments/1586708/2518752/2018-01-30-CERN-Nova-Results.pdf.

[205] A. Osipowicz et al. KATRIN: A Next generation tritium beta decay experiment with sub-eV sensitivity for the electron neutrino mass. Letter of intent. 2001.

[206] M. Aker et al. An improved upper limit on the neutrino mass from a direct kinematic method by KATRIN. 2019.

[207] I. Ambats et al. $\mathrm{NO}\nu\mathrm{A}$ proposal to build a 30-kiloton off-axis detector to study neutrino oscillations in the Fermilab NuMI beamline. *arXiv*, hep-ex/0503053, 2004.

[208] T. Yang and S. Woijcicki. Study of physics sensitivity of ν_μ disappearance in a totally active version of NOvA detector. 2004.

Appendix A

GLoBES .glb Experiment Example

A typical .glb experiment file, in this case for our NOνA simulations [207, 208].

```
%!GLoBES

$version="3.0.0"

/* Copyright 2008, 2009 The GLoBES Team
*
* If you modify this file you have to rename it.
*
* If you are using this file for producing a scientific publication
* or a talk please cite the following references and check the
   supporting
* files for a similar comment.
*
* This file was used to produce the results in
*
#* @Article{Huber:2009xx,
#*  author = "Huber, P and Lindner, M and Schwetz, T and Winter, W",
#*  title = "First hint for CP violation in neutrino oscillations
#*           from upcoming superbeam and reactor experiments",
#*  year = "2009",
#*  eprint = "arXiv:0907.1896"
#* }
*
* The description of NoVA (concerning the nu_e appearance signal)
   follows
* the proposal as of March 15, 2005.
*
#* @Article{Ambats:2004js,
```

```
#*  author     = "Ambats, I. and others",
#*  collaboration = "NOvA",
#*  title      = "NOvA proposal to build a 30-kiloton off-axis detector to
#*                  study neutrino oscillations in the Fermilab NuMI beamline",
#*  year       = "2004",
#*  eprint     = "hep-ex/0503053",
#*  SLACcitation  = "%%CITATION = HEP-EX 0503053;%%"
#* }
*
* The description of the nu_mu disappearance signal is taken from
*
#* @Article{Yang_2004,
#*  author     = "T. Yang and S. Woijcicki",
#*  collaboration = "NOvA",
#*  title      = "Study of physics sensitivity of $\nu_mu$ disappearance in
#*                  a totally active version of NoVA detector",
#*  year       = "2004",
#*  eprint     = "Off-Axis-Note-SIM-30"
#* }
*
* Reduced detector mass to 15kt according to the outcome of the
* latest CD2 review.
*
* This an attempt to match the numbers in the October 2007 TDR. We
* try to be as close as possible to the their numbers given in tables
* 6.2-6.4. We have applied a correction factor for the different
* proton to neutron ratio in water and scintillator (our cross
* sections are for water). We had to apply an overall factor of 1.12
* to get the total event numbers right. The background efficiencies
* had to be increased to account for the effect of migrations. Also,
* at the current stage we do not account for neutrino BG in the
* anti-neutrino beam, which is not a good approximation, but we
* increase the BG effecienies as to match table 6.2.
*
* This an attempt to match the numbers in the October 2007 TDR. This
* file is to test the disappearance analysis. This analysis is termed
* preliminary in the TDR and there is very little information to go
* by.
*
```

```
* This file deviates at following points from the TDR:
*
*  - 2%/Sqrt(E) resolution plus a flat 0.085GeV for Fermi motion
*  - 2% signal error
*  - 0.1% of all NC as background
*  - 10% background error
*  - 1% energy scale error
*
* Besides that, we use 100% of all nu_mu QE events. We use an energy
* window from 1 to 3 GeV. We use ME beam tune.
*
* Last Update: 13/07/09 <pahuber@vt.edu>
*/


/* We need to correct for the fact that our cross sections are
 for water, i.e. a proton to neutron ratio of 5/4, whereas mineral oil
 has a proton qratio closer to 4/3. That is we get correction factor
 for nu ar of */

NUB=1.066

/* ####### Beam flux ####### */

 nuflux(#NoVA)<
 @flux_file="0709-nova-plus.dat"
 @time = 3 /* years (changed from 3) */
 @stored_muons = 6e20 /* POT yrs^-1 for 0.7 MW*/
 @norm = 1.12*6.47886918e-19 /* 1.12 is necessary to match the
 numbers in the 2007 TDR */
>


 nuflux(#NoVAanti)<
 @flux_file="0709-nova-minus.dat"
 @time = 3 /* years (changed rom 3) */
 @stored_muons = 6e20 /* POT yrs^-1 for 0.7 MW*/
 @norm = 1.12*NUB* 6.47886918e-19 /* 1.12 is necessary to match the
 numbers in the 2007 TDR */
>

```

```
/* ####### Detector settings ###### */

$target_mass =          15.0   /* kt */


/* ####### Energy window ####### */

$bins =      20

$emin =            0.5 /* GeV */
$emax =            3.5 /* GeV */

$sampling_points = 100
$sampling_min =        0.05   /* GeV */
$sampling_max =            4.0 /* GeV */


/* ####### Baseline setting ####### */

$profiletype =    3

/* The relatively larger signal is due to matter effects
* whereas the event numbers in the proposal assume two-flavour
* vacuum oscillations
*/

$densitytab =     {2.8}
$lengthtab =    {810} /* km */


/* ####### Technical information ####### */

$filter_state = 0
$filter_value = 1000000


/* ####### Energy resolution ####### */

energy(#electron)<
@type = 1
@sigma_e = {0.0,0.1,0.0}
>
```

```
energy(#muon)<
@type = 1
@sigma_e = {0.0,0.05,0.0}
>


energy(#muonQE)<
@type = 1
@sigma_e = {0.0,0.02,0.085}
>

/* ####### Cross sections ####### */

cross(#CC)<
@cross_file = "XCC.dat"
>

cross(#NC)<
@cross_file = "XNC.dat"
>

cross(#QE)<
@cross_file = "XQE.dat"
>


/* ####### Channel definitions ####### */

channel(#nu_mu_CC)<
@channel =  #NoVA:  +:  m:      m:      #CC:    #muon
>


channel(#nu_mu_NC)<
@channel =  #NoVA:  +:  NOSC_m: NOSC_m: #NC:    #electron
>

channel(#nu_e_beam)<
@channel =  #NoVA:  +:  e:      e:      #CC:    #electron
>

```

```
channel(#nu_e_signal)<
@channel =  #NoVA:   +:  m:   e:   #CC:     #electron
>

channel(#nu_bar_mu_CC)<
@channel =  #NoVAanti:   -:  m:   m:   #CC:     #muon
>

channel(#nu_bar_mu_NC)<
@channel =  #NoVAanti:   -:  NOSC_m: NOSC_m: #NC:     #electron
>

channel(#nu_bar_e_beam)<
@channel =  #NoVAanti:   -:  e:   e:   #CC:     #electron
>

channel(#nu_bar_e_signal)<
@channel =  #NoVAanti:   -:  m:   e:   #CC:     #electron
>




channel(#nu_mu_QE)<
@channel =  #NoVA:   +:  m:   m:   #QE:     #muonQE
>

channel(#nu_bar_mu_QE)<
@channel =  #NoVAanti:   -:  m:   m:   #QE:     #muonQE
>



/* ####### Setting the rules ####### */



rule(#Nu_E_Appearance)<
@signal = 0.26@#nu_e_signal
@signalerror = 0.05 : 0.025
```

```
@background =  0.001*1.3@#nu_mu_CC : 1.4*0.002@#nu_mu_NC : 0.074*2.2@#nu_e_beam
@backgrounderror = 0.10 : 0.025

@sys_on_function = "chiSpectrumCalib"
@sys_off_function = "chiNoSysSpectrum"

@energy_window= 1.0 : 3.0
>


rule(#Nu_E_Bar_Appearance)<
@signal = 0.409@#nu_bar_e_signal
@signalerror = 0.05 : 0.025

@background =  0.001*1.3@#nu_bar_mu_CC : 2.2*0.004@#nu_bar_mu_NC : 0.105*3.2@#nu_bar_e_beam
@backgrounderror = 0.10 : 0.025

@sys_on_function = "chiSpectrumCalib"
@sys_off_function = "chiNoSysSpectrum"

@energy_window= 1.0 : 3.0

>




rule(#Nu_Mu_Disappearance)<
@signal = 1.0@#nu_mu_QE
@signalerror = 0.02 : 0.01

@background =  0.001@#nu_mu_NC
@backgrounderror = 0.1 : 0.01

@sys_on_function = "chiSpectrumCalib"
@sys_off_function = "chiNoSysSpectrum"

@energy_window= 0.5 : 3.0
>
```

```

rule(#Nu_Mu_Bar_Disppearance)<
@signal = 1.0@#nu_bar_mu_QE
@signalerror = 0.02 : 0.01

@background =  0.001@#nu_bar_mu_NC
@backgrounderror = 0.1 : 0.01

@sys_on_function = "chiSpectrumCalib"
@sys_off_function = "chiNoSysSpectrum"
@energy_window= 0.5 : 3.0

>





/**********************END**********************/
```

APPENDIX B

GLOBES SCRIPT EXAMPLE

A typical script written in C used to generate data for a MH hypothesis test projected onto the θ_{13}-δ_{13} plane.

```

/* GLoBES -- General LOng Baseline Experiment Simulator
* (C) 2002 - 2004,  The GLoBES Team
*
* GLoBES is mainly intended for academic purposes. Proper
* credit must be given if you use GLoBES or parts of it. Please
* read the section 'Credit' in the README file.
*
* This program is free software; you can redistribute it and/or modify
* it under the terms of the GNU General Public License as published by
* the Free Software Foundation; either version 2 of the License, or
* (at your option) any later version.
*
* This program is distributed in the hope that it will be useful,
* but WITHOUT ANY WARRANTY; without even the implied warranty of
* MERCHANTABILITY or FITNESS FOR A PARTICULAR PURPOSE.  See the
* GNU General Public License for more details.
*
* You should have received a copy of the GNU General Public License
* along with this program; if not, write to the Free Software
* Foundation, Inc., 59 Temple Place, Suite 330, Boston, MA  02111-1307
   USA
*/

/*******************************************************************
    ****
*    *   Confidence regions in the th13-delta_CP plane             *
```

```
*************************************************************************
   ***/

#include <stdio.h>
#include <stdlib.h>
#include <math.h>
#include <string.h>
#include <globes/globes.h>   /* GLoBES library */

/* Output file */
char MYFILE[]="deltath13.dat";
char AEDLFILE[]="0709-nova.glb";
char AEDLFILE2[]="T2K.glb";
FILE *outfile = NULL;

int main(int argc, char *argv[])
{
/* Initialize libglobes */
glbInit(argv[0]);
glbSelectMinimizer(GLB_MIN_POWELL);

/* Initialize experiment(s) */
glbInitExperiment(AEDLFILE,&glb_experiment_list[0],&glb_num_of_exps); /*
     NOvA experiment */
//  glbInitExperiment(AEDLFILE2,&glb_experiment_list[0],&glb_num_of_exps
   ); /*T2K experiment */

/* Intitialize output */
outfile = fopen(MYFILE, "w");
if (outfile == NULL)
{
printf("Error opening output file.\n");
return -1;
}

/* Define "true" oscillation parameters (cf. hep-ph/0405172v5) */
double theta12 = asin(sqrt(0.3));
double theta13 = asin(sqrt(0.1))/2.0;
double theta23 = 45.0 * M_PI/180.0;
double deltacp = 90.0 * M_PI/180.0;
double sdm = 7.9e-5;
double ldm = 2.6e-3;
```

```
/* Define "true" oscillation parameter vector */
glb_params true_values = glbAllocParams();
//glbDefineParams(true_values,theta12,theta13,theta23,deltacp,sdm,ldm);//True NH
glbDefineParams(true_values,theta12,theta13,theta23,deltacp,sdm,-ldm+sdm);//True IH
glbSetDensityParams(true_values,1.0,GLB_ALL);

/* Define initial guess for the fit values */
glb_params test_values = glbAllocParams();
glbDefineParams(test_values,theta12,theta13,theta23,deltacp,sdm,ldm);
glbSetDensityParams(test_values,1.0,GLB_ALL);
glb_params test_valuesIH = glbAllocParams();
glbDefineParams(test_valuesIH,theta12,theta13,theta23,deltacp,sdm,-ldm+sdm);
glbSetDensityParams(test_valuesIH,1.0,GLB_ALL);

/* Define external input (1-sigma errors) on the parameters: 10% error
* on the solar parameters, 5% on the matter density, all other parameters free.
* External input is implemented as a prior of the form
*    (fit_value - central_value)^2 / input_error^2
*/
glb_params input_errors = glbAllocParams();
glbDefineParams(input_errors, theta12*0.1, 0, 0, 0, sdm*0.1, 0);
glbSetDensityParams(input_errors,0.05,GLB_ALL);
glbSetInputErrors(input_errors);
glbSetCentralValues(true_values);

/* Define projection onto th13 and delta, marginalizing over
* th23 and dm31. The solar parameters can be kept fixed to speed
* up the calculation without introducing large errors. */
glb_projection th13delta_projection = glbAllocProjection();
glbDefineProjection(th13delta_projection,GLB_FIXED,GLB_FIXED,GLB_FREE,
GLB_FIXED,GLB_FIXED,GLB_FREE);
glbSetDensityProjectionFlag(th13delta_projection, GLB_FIXED, GLB_ALL);
glbSetProjection(th13delta_projection);

/* Compute simulated data */
glbSetOscillationParameters(true_values);
glbSetRates();
```

```

/* Scan the th13-delta plane */
double this_th13, this_delta;
double th13_lower  = 5;   /*corresponds to roughly 0.1127 radians (6.46 degrees)*/
double th13_upper  = 150; /*corresponds to roughly 0.1989 radians (11.39 degrees)*/
double th13_steps  = 5;   /*step SIZE in this case*/
double delta_lower = -180*(M_PI/180); /*looks dumb but shows conversion from degrees to radians*/
double delta_upper =  180*(M_PI/180);
double delta_steps = 12; /*number of steps (see below)*/
double res, res2, prior, th13_test;

for(this_th13=th13_lower; this_th13<=th13_upper; this_th13+=th13_steps)/*loop over x axis unitless*/

{
//convert to radians for osc params call
th13_test=asin(sqrt(this_th13*0.001))/2.0; //calculate angle (in radians) corresponding to each x-axis pt.
glbSetOscParams(test_values,th13_test, GLB_THETA_13);
glbSetOscParams(test_valuesIH,th13_test, GLB_THETA_13);


for(this_delta=delta_lower; this_delta<=delta_upper; this_delta+=(delta_upper-delta_lower)/delta_steps)
{
/* Set vector of test=fit values */
glbSetOscParams(test_values, this_delta, GLB_DELTA_CP);
glbSetOscParams(test_valuesIH, this_delta, GLB_DELTA_CP);

/* Compute chi^2 assuming the normal mass hierarchy in the fit */
res = glbChiNP(test_values, NULL, GLB_ALL);
res2 = glbChiNP(test_valuesIH, NULL, GLB_ALL);

/*add prior manual prior */
prior=pow((0.1 - this_th13*0.001)/(0.1*0.05),2); // i.e. ((test guess - fit value)/inputerror)^2, ideal sin(2theta)^2=0.1 so subtract unitless value NOT angle, also inputerror=0.005

res=res+prior;
```

```
res2=res2+prior;

fprintf(outfile, "%g %g %g %g %g %g %g\n", this_th13*0.001, this_delta*
    (180.0/M_PI), res, res2, pow(sin(2*theta13),2),deltacp*(180.0/M_PI),
    prior); //print th13—> convert to sin^2 form, delta—> convert to
    degrees and true values of those

}
fprintf(outfile, "\n");
}
fclose(outfile);

/* Destroy parameter and projection vector(s) */
glbFreeParams(true_values);
glbFreeParams(test_values);
glbFreeParams(test_valuesIH);
glbFreeParams(input_errors);
glbFreeProjection(th13delta_projection);

return 0;
}
```

APPENDIX C

NON-STANDARD (MATTER) INTERACTIONS

Matter effects of neutrinos assume that only the electron flavour neutrinos experience the additional interactions with regular electronic matter. If, however neutrinos can experience some kind of additional interaction with matter, especially in the non-electron channels, then the oscillatory behaviour will be affected. NC or CC interactions between electrons or even quarks in matter are possible, what the exact nature of such interactions would be is unknown. These are grouped under the general framework of Non-Standard Interactions (NSI) and are a common theory brought up as potential explanations for oscillation anomalies as well as making degenerate solutions more difficult to disentangle.

C.0.1 Formalism

We start with an effective Hamiltonian to describe the propagation of ν's with an additional matrix of matter potentials added to the basic MSW oscillation Hamiltonian. This gives

$$\begin{aligned}\mathcal{H}_f =& \mathcal{H}_\nu + \mathcal{H}_{\rm SI} + \mathcal{H}_{\rm NSI} && \text{(C.1)}\\ =&\lambda \left\{ U \begin{pmatrix} 0 & & \\ & r_\lambda & \\ & & 1 \end{pmatrix} U^\dagger + r_A \begin{pmatrix} 1 & & \\ & 0 & \\ & & 0 \end{pmatrix} + r_A \begin{pmatrix} \varepsilon_{ee} & \varepsilon_{e\mu} & \varepsilon_{e\tau} \\ \varepsilon_{e\mu}^* & \varepsilon_{\mu\mu} & \varepsilon_{\mu\tau} \\ \varepsilon_{e\tau}^* & \varepsilon_{\mu\tau}^* & \varepsilon_{\tau\tau} \end{pmatrix} \right\}, && \text{(C.2)}\end{aligned}$$

in the flavour basis. With:

$$\lambda \equiv \frac{\Delta m^2_{31}}{2E}\,, \quad r_\lambda \equiv \frac{\Delta m^2_{21}}{\Delta m^2_{31}}\,, \quad r_A \equiv \frac{A(x)}{\Delta m^2_{31}}\,, \tag{C.3}$$

and

$$A(x) = 2\sqrt{2}EG_F n_e(x)\,, \tag{C.4}$$

is the Wolfenstein matter term with path dependence. U is the usual PMNS matrix.

C.0.2 NSI terms

The NSI parameters notated as

$$\varepsilon_{\alpha\beta} = |\varepsilon_{\alpha\beta}|e^{i\phi_{\alpha\beta}}, \tag{C.5}$$

are complex params. For the $\alpha = \beta$ the $\varepsilon_{\alpha\alpha}$'s are real, due to Hermiticity of $\mathcal{H}$. Therefore the three off diagonal terms have phases that will contribute to CP effects: $\phi_{e\mu}, \phi_{e\tau}, \phi_{\mu\tau}$. These introduce new "fake" CP effects (i.e. not from PMNS phases) as well as genuine new CP effects from these phases.

Matter propagation NSI terms obey unitarity (while source and detector NSI do not) therefore we still have an overall unitary matrix that diagonalises the effective Hamiltonian

$$\mathcal{H}_d = \hat{\mathrm{U}}^\dagger \mathcal{H}_f \hat{\mathrm{U}} = \mathrm{diag}(\lambda_1, \lambda_2, \lambda_3)\,, \tag{C.6}$$

where the λ_i's are the eigenvalues of the effective Hamiltonian, and

$$\sum_i \hat{\mathrm{U}}_{\alpha i}\hat{\mathrm{U}}^*_{\alpha i} = \delta_{\alpha\beta}\,. \tag{C.7}$$

There are some constraints on the NSI parameters we have introduced, they are

$$|\varepsilon_{\alpha\beta}| < \begin{pmatrix} 4.2 & 0.3 & 0.5 \\ 0.3 & 0.068 & 0.04 \\ 0.5 & 0.04 & 0.15 \end{pmatrix} \tag{C.8}$$

the phases however are not constrained

$$\phi_{\alpha\beta} \in (-\pi, \pi)\,. \tag{C.9}$$